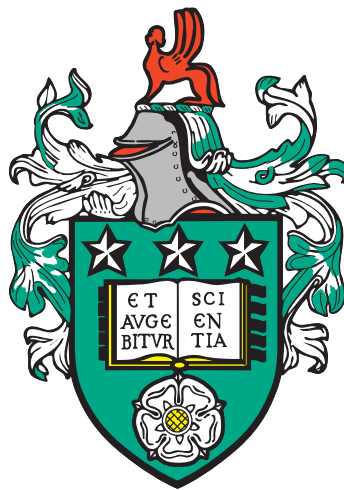# Optimisation of the electronic properties of graphene devices

Matthew Newman

Department of Physics and Astronomy

University of Leeds

Submitted in accordance with the requirements for the degree of

Doctor of Philosophy

September 2012

This thesis is dedicated to my grandparents
Beryl and Malcolm Ridley

Intellectual Property Statement

The candidate confirms that the work submitted is his own and that appropriate credit has been given where reference has been made to the work of others.

This copy has been supplied on the understanding that it is copyright material and that no quotation from the thesis may be published without proper acknowledgement.

The right of Matthew Newman to be identified as Author of this work has been asserted by him in accordance with the Copyright, Designs and Patents Act 1988.

Acknowledgements

Firstly, I would like to thank my supervisor, Dr Gavin Burnell, for his encouragement and guidance throughout the course of my PhD. I am also grateful for his willingness to debug LabVIEW code, even at the most inopportune times, without which much of the data presented in this thesis could not have been taken. I would also like to thank Prof. Bryan Hickey for his support and Dr Oscar Céspedes for use of the Raman spectrometer.

Much of the work was performed in the cleanroom here at Leeds, which was made possible thanks to the maintenance of equipment by Dr Li Chen and Mr Geoff Butterworth. I am also indebted to many of the Physics and Astronomy department technical staff. In particular, Mr John Turton and Mr Philip Cale have been incredibly helpful, ensuring that vacuum equipment worked without fail and that the cryostats were always filled. I would also like to thank Mr Richard Oliver and Mr Andrew Price from the electronics workshop, whom at one point I was visiting on an almost daily basis on the hunt for components.

I feel very fortunate to have worked with such a great group of PhD students and postdocs over the years. In particular, I would like to thank Dr Graham Creeth and Dr Nick Porter for the many valued discussions and cryostat advice and Mr Mark Elkin (soon to be Dr) and Dr Chris Allen for their guidance regarding electron beam lithography and transport measurements. I would like to make a special mention of Dr Mannan Ali who always went above and beyond to help me, whether it was helping to repair equipment late at night, getting a job done in the workshop quickly or acting as an endless source of advice, technical or otherwise.

I am very lucky to have a wonderful family, without whose love and support I could not have completed this PhD. I am also very grateful to my father for helping me proof read this thesis, it is certainly the better for it. Finally, I would like to thank Miss May Wheeler. Not only has she ensured that I was sheltered and nourished during the last few months of my PhD, but has also been a source of moral support. I am also thankful for her thesis proof reading skills, I look forward to returning the favour in the not too distant future.

Abstract

The isolation of graphene has generated a great deal of excitement because of its unique properties. From a fundamental physics standpoint the most exciting aspect of the material is its electronic properties. One interesting method available to explore this electronic system is to investigate how the material interacts with superconductors. This interaction has been investigated by several groups via the production of superconductor-graphene-superconductor devices, although their observed transport properties have been less than optimal.

This thesis explores the factors which can limit the performance of these graphene devices. Suggestions are made regarding possible methods of improving device performance through the optimisation of the fabrication procedures. Graphene field effect transistors are produced using a combination of mechanical exfoliation, lithography and sputtering techniques. These devices are then characterised using a combination of transport and optical measurements.

Two annealing methods are explored to reduce the concentration of charged impurities on the samples, using both an existing current annealing technique and a novel annealing technique using an on-chip platinum heater. Quantum Hall effect measurements are performed confirming the high quality of our graphene.

Making poor contact to graphene is a possible performance limiter. The transfer length method is used to measure the contact resistance in our devices directly. A large contact resistance is observed, attributed to amorphisation of the underlying graphene by the sputtered material. This is confirmed using Raman spectroscopy. Asymmetry in the electric field measurements are also explained using an existing contact induced doping model. Extension of this model to include alternative doping profiles is shown to improve the fit to data. Measurements of the opto-electronic response of our graphene devices using scanning photocurrent microscopy supports the observation of contact induced doping and carrier density inhomogeneity in graphene devices which can limit device performance.

Abbreviations

2DEG	Two Dimensional Electron Gas	LL	Landau Level
AC	Alternating Current	MAR	Multiple Andreev Reflections
AR	Andreev Reflection	MIBK	Methyl Isobutyl Ketone
BCS	Bardeen-Cooper-Schrieffer	MR	Magnetoresistance
BLG	Bi-Layer Graphene	OL	Optical Lithography
CCD	Charge Coupled Device	PC	Photocurrent
CNP	Charge Neutrality Point	PMMA	Poly(Methyl Methacrylate)
CVD	Chemical Vapour Deposition	QHE	Quantum Hall Effect
DAC	Digital-to-Analogue Converter	SdHO	Shubnikov de-Haas Oscillation
DC	Direct Current	SEM	Scanning Electron Microscope
DFT	Density Functional Theory	SGS	Superconductor-Graphene-Superconductor
EBL	Electron Beam Lithography	SIS	Superconductor-Insulator-Superconductor
EFE	Electric Field Effect	SLG	Single Layer Graphene
FET	Field Effect Transistor	SNS	Superconductor-Normal-Superconductor
FLG	Few Layer Graphene	SPCM	Scanning Photocurrent Microscopy
FWHM	Full Width Half Maximum	TK	Tuinstra-Koenig
h-BN	Hexagonal Boron Nitride	TLM	Transfer Length Measurement
IPA	Isopropyl Alcohol	UHV	Ultra High Vacuum
JJ	Josephson Junction	VTI	Variable Temperature Insert

Common Symbols

B	Applied Magnetic Field ($\mu_0 H$)
Δ	Superconducting Gap Parameter
E_F	Fermi Energy
e	Elementary Charge
ϵ_0	Permittivity of Free Space
h	Planck's Constant
$\hbar$	$h/2\pi$
I_c	Critical Current
μ	Carrier Mobility
n_s	Carrier Density
ω_c	Cyclotron Frequency
ρ	Resistivity
ρ_c	Contact Resistivity
σ	Conductivity
T	Temperature
T_c	Critical Temperature
V_{Dirac}	Dirac Point Gate Voltage
v_F	Fermi Velocity
V_{G}	Gate Voltage

CONTENTS

CHAPTER 1

Introduction

The isolation of graphene - a single layer of graphite one atom thick - in 2004[1] generated a great deal of excitement throughout the scientific community as a result of its unique properties. From a structural standpoint, despite representing the ultimate in thinness, the material is incredibly strong[2], owing to the strength of the carbon-carbon bond, while also very flexible. It is the electronic properties of graphene which are arguably the most exciting[3; 4]. The electronic band structure of graphene, first derived by Wallace[5] in 1947, features two conical points where band crossing occurs. Within a small energy range about these points the energy is linearly proportional to the wavevector, representing a linear dispersion relation which deviates greatly from the usual parabolic dispersion of almost all other condensed matter systems. This dispersion relation closely resembles that of relativistic spin 1/2 particles, such as high energy electrons, which are described not by the Schrödinger equation but by the Dirac equation[6].

One of the fundamental results of the Dirac formalism is the existence of antiparticles, indeed the Dirac equation predicted the electron antiparticle, the positron, before its experimental discovery. In graphene the role of the positron particle is replaced by the hole. While electrons and holes are usually described by separate wavefunctions, in the case of graphene they are both described by the positive and negative forms of the same two-component wavefunction. This analogue between charge carriers in graphene and relativistic fermions can be exploited by allowing otherwise high energy phenomena to be probed in a standard laboratory setting. New physical phenomena resulting from this unique electronic structure were observed very shortly after the isolation of graphene. The most striking observation was that of the anomalous integer quantum Hall effect (QHE) at high magnetic field[7; 8]. A shift of 1/2 in the sequence of steps in the Hall conductance was observed, compared to the standard result observed in a two-dimensional electron gas (2DEG) and provided direct evidence of Dirac physics.

Accompanying the interest in graphene from a fundamental physics perspective there has also been a great deal of research into possible practical applications of the material. Graphene samples have shown remarkably high carrier mobilities[9], exceeding those of state-of-the-art silicon transistors, demonstrating ballistic transport over sub-micrometer distance[10]. Consequently, graphene has been proposed as a possible replacement for silicon in electronic devices, which is currently approaching

the fundamental limits of the material. Many other practical uses have been described for graphene, including its use in gas sensors[11; 12], touch-screens[13] and photo-detectors[14; 15]. The definition of a resistance standard based on the anomalous QHE has also been proposed[16].

With the wide range of technological applications available, a large scale method of producing graphene is required. Two main methods have been proposed. Firstly, graphene has been grown via the controlled decomposition of a SiC substrate at high temperatures[17]. More recently large scale films of graphene have been grown on metallic substrates by a chemical vapour deposition (CVD) technique[13]. Despite the availability of high throughput fabrication methods, most fundamental studies into the properties of graphene have been performed on samples produced using the original mechanical exfoliation technique[1]. This top-down technique consists of the repeated peeling of graphene layers from a bulk graphite crystal, traditionally using Scotch tape, before deposition on a substrate. While SiO_2 has mostly been used as a substrate, owing to the relatively high visibility of graphene on its surface[18] and the ease in which it can be used as part of a global back gate for field effect measurements, it has more recently been found to limit the performance of graphene devices[19–21]. Graphene devices with astonishingly high mobilities have been shown in recent years using hexagonal boron-nitride (h-BN) as a substrate[22], while suspended graphene devices have also shown remarkable properties[23; 24]. Despite the marked improvement in device performance that these latter two techniques deliver, they require a high level of technical ability, which is currently only available to a select few groups world wide. Graphene on SiO_2 therefore remains one of the most commonly used combinations and is sufficient to explore many of the interesting properties of the material.

A particularly attractive proposition is to explore the interplay between the Dirac fermions in graphene with other transport phenomena. One of the most interesting phenomena is that of superconductivity, which in itself has been a source of intense theoretical and experimental research since its discovery over a century ago. The interaction between Dirac fermions and the charge carriers in a superconducting material - known as Cooper pairs[25] - is predicted to lead to new phenomena such as specular Andreev reflection[26; 27] and so is worthy of investigation. A great deal of research, both theoretical and experimental[28–44], has been performed in order to gain an insight into how the two classes of material interact. The most common

device geometry employed to investigate this interplay, is that of the superconductor-graphene-superconductor (SGS) Josephson junction (JJ). In this class of devices the graphene represents a weak link between the two superconductors. As a result of the Josephson effect - first proposed by Josephson in 1962[45] - a supercurrent can flow between these two superconductors, the properties of which depend on the weak link material itself. This device geometry can therefore be used to probe the properties of the weak link material.

In the years following the isolation of graphene several groups have managed to produce a supercurrent in SGS JJs. These devices typically consist of mechanically exfoliated graphene on SiO_2 with predominantly aluminium (Al) contacts, deposited via electron beam evaporation[31–36]. Given the very low temperatures required for operation of Al based devices, coupled to the instability of the materials superconducting properties in the presence of relatively weak magnetic fields, it would be beneficial to produce devices using superconductors with higher critical temperatures. One such material which should be ideal for incorporating into SGS devices is niobium (Nb) because of its relatively high critical temperature, $T_c = 9.2$ K, and critical magnetic field field[46]. Until recently Nb based SGS devices have been conspicuously absent from the literature[42; 43; 47], despite the obvious technological benefits of such an advancement. The devices that have been realised suffer from greatly reduced supercurrents than expected and operate at temperatures of tens of millikelvin, far below the critical temperature of Nb. In fact, almost all SGS devices, regardless of contact material, show sub optimal properties which cannot be explained by the fundamental properties of graphene alone.

1.1 Thesis Layout

This thesis aims to explain the poor performance of SGS devices by studying the properties of graphene devices, in the typical field effect geometry, contacted with superconducting electrodes. The contact material used in this study is a palladium-niobium bilayer which has previously been used to produce carbon based JJs in the form of superconductor-carbon nanotube- superconductor devices[48–52]. Through a combination of low temperature transport measurements and optical techniques the devices

are fully characterised and, where appropriate, the results interpreted in terms of the impact the properties will have on SGS devices.

The thesis layout is as follows. Chapter 2 presents an introduction to the theory and background physics underpinning the research performed. The structure and electronic properties of graphene are discussed with particular attention to the interesting consequences of its unique electronic band structure. Much of the initial excitement regarding graphene resulted from its anomalous QHE. In this work the QHE has been one of the methods used to characterise our graphene devices. The QHE in both 2DEGs and graphene is discussed, with the former discussed both for contrast and because it encompasses much of the physics involved. Raman spectroscopy has been used extensively as a complimentary technique for characterising our graphene thus the theory behind this technique is discussed. The original aim of the project was the realisation of a working SGS junction and so a review of the fundamental theory behind superconductivity is presented. Following this is a review of the work currently published on this class of devices, with particular focus on the factors which limit device performance.

Chapter 3 outlines the experimental methods used to produce and characterise the graphene devices. The lithographic and metal deposition techniques are discussed as well as the oxygen plasma method used to etch the graphene into a desired shape. The production of a finalised device for electric field effect measurements requires wire bonding of a finished device in a chip carrier, as well as making good contact to the silicon substrate for use as a global back gate, and so this is outlined. The device characterisation methods used include the electrical measurement set-up, the cryogenic environment employed for low temperature measurements as well as Raman spectroscopy and these techniques will also be discussed.

To optimise the transport properties of graphene devices it is necessary to minimise the concentration of impurities on the graphene itself. Chapter 4 shows experimental results from an investigation into annealing graphene devices, which is one method used to remove impurities. Two annealing methods are investigated, one consisting of an on-chip heater patterned alongside the graphene device and another involving the direct heating of the graphene by applying a large current to the device. Field effect measurements before and after the respective annealing procedures are shown and interpreted in terms of the possible changes the devices have undergone. Measurements

combining time resolved Raman spectroscopy and current annealing are also presented aiming to understand what changes occur during annealing.

Transport measurements are performed to characterise our graphene devices, with the results of these measurements presented in Chapter 5. Electric field effect measurements are performed in order to assess to what extent the graphene is doped by charged impurities and to determine the carrier mobility of our graphene. Following this, QHE measurements are presented taken both on unetched graphene flakes and those shaped into a Hall bar geometry via an etching technique. Through these measurements the graphene is proven to be a single layer and of high quality. An extensive investigation into the magnetic field dependence of the QHE allows estimates of the elastic scattering time and broadening of the quantised Landau levels. The Shubnikov de-Haas oscillations are also identified and the Berry's phase in a graphene sample measured directly.

Having validated the high quality of our graphene samples, Chapter 6 consists of an investigation into the contacting of graphene with metallic electrodes in order to identify factors which could limit device performance. The commonly used transfer length method (TLM) is implemented to measure directly the contact resistance as a function of applied gate voltage. A model based on doping of the graphene by the metal electrodes is then presented to explain the asymmetry observed in the TLM measurements and the resultant gate voltage dependence of contact resistance. Raman spectroscopy is then used to explore the possibility of damage to the graphene from sputtering of the contact material, followed by a comparison of our contact resistance measurements with those available in the literature.

The final experimental chapter, Chapter 7, shows measurements of the opto-electronic response of our samples using a scanning photocurrent microscopy (SPCM) technique. Maps of photocurrent versus excitation laser position are taken as a function of applied gate voltage. These measurements are used to assess contact induced doping of the graphene, as well as the carrier density inhomogeneity in the graphene, when the Fermi energy is close to the Dirac point. Finally, the findings of this work are concluded in Chapter 8.

CHAPTER 2

Theory and Background

In this chapter the necessary background theory is presented to aid the understanding of the experimental work presented in later chapters. The structure and electronic properties of graphene are outlined followed by a discussion of the electric field effect (EFE) in graphene. The QHE is then discussed, first in terms of the standard 2DEG model and then the specific case of the anomalous QHE in monolayer graphene.

Optical measurements have been performed during the course of this research as a complimentary tool, alongside transport measurements, to characterise the graphene samples. The basic theory behind Raman spectroscopy is presented in conjunction with discussing the specific Raman modes that are active in graphene samples.

Given the initial aim of the project was to produce a superconducting graphene device, it seems prudent to outline the basic theory behind superconductivity. The main results of the microscopic theory developed by Bardeen, Cooper, and Schrieffer (BCS theory) are presented, as well as a description of the processes that occur in devices where two superconducting electrodes are separated by a weak link, otherwise known as Josephson junctions.

Finally, an overview of the current state-of-the-art SGS devices produced is given. Particular attention is given to temperature and gate voltage dependence of the magnitude of the critical current, as well the impact of the superconductor-graphene interface transparency, in order to understand the limiting factors when trying to produce superconducting graphene devices.

2.1 Structure and Electronic Properties of Graphene

In this section an overview of the general properties of graphene are discussed. A comprehensive overview is difficult to give because of the number of publications on the topic in recent years, however, a good discussion of the electronic properties of graphene can be found in the complimentary review articles of Castro Neto *et al.* [3] and Das Sarma *et al.* [4]. The recent text by Katsnelson[53] also provides a solid basis for understanding the properties of graphene.
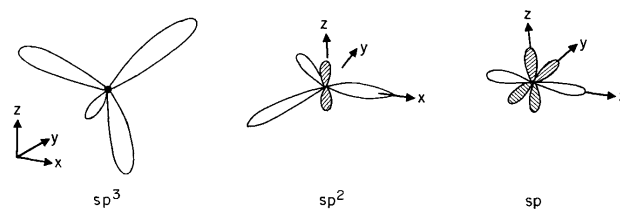
Figure 2.1: Schematic diagram showing the sp^3, sp^2 and sp bonding hybridisations. Shaded (unshaded) denote weak (strong) bonds[54].

2.1.1 Bonding in Carbon

A single carbon atom has six electrons with a ground state atomic configuration of $1s^2 2s^2 2p^2$. When forming molecular bonds with other species the s and p states in the valence shell hybridise, in order to lower the overall energy of the system forming what is known as sp^3, sp^2 or sp states as shown in Figure 2.1. In the sp^3 configuration both electrons in the 2s orbital hybridise with the $2p^2$ orbitals, forming tetrahedrally directed orbitals, which form strong σ bonds with four neighbouring atoms, giving rise to the structure of diamond. In the sp^2 configuration, the 2s orbital hybridises with the $2p_x$ and $2p_y$ orbitals, forming three strong covalent bonds with three neighbouring atoms in the plane, at an angle of $120°$ to one another. The remaining p_z orbital lies perpendicular to the plane and forms a weak π bond with neighbouring atoms. While the σ bonds are highly localised, electrons in these orbitals do not take part in conduction, the π bonds are de-localised and are responsible for electronic conduction through graphitic structures.

There are a range of structures that can be formed through sp^2 bonding in carbon, see Figure 2.2. Monolayer graphene, also referred to as single-layer graphene (SLG), consists of a single 2D sheet of sp^2 bonded carbon in a hexagonal structure while bilayer graphene (BLG) and few layer graphene (FLG) consist of two or more graphene sheets, stacked on top of one another respectively. Throughout this thesis, the term graphene shall be used to denote monolayer graphene unless otherwise stated. By cutting and folding the graphene, several other structures can be formed namely the 0D buckminsterfullerene (buckyball) and 1D nanotube. By stacking many graphene sheets on top of one another the common 3D graphite structure is produced.
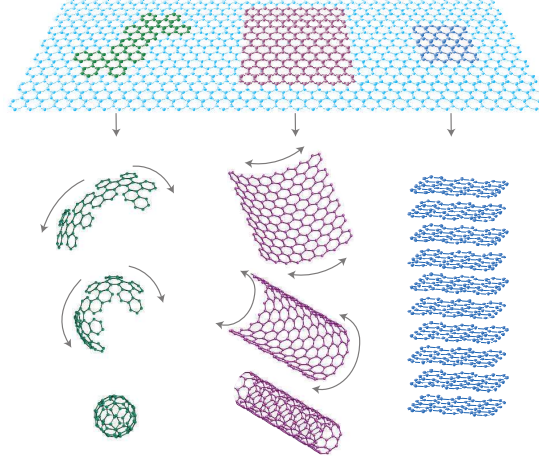
Figure 2.2: The allotropes of sp^2 bonded carbon with a single graphene sheet (top) and (from left to right) a buckyball, nanotube and graphite stack.[9]

2.1.2 Band Structure of Graphene

By considering the atomic structure of a graphene sheet, the band structure can be calculated, from which the electronic properties can be derived. The honeycomb lattice of a graphene sheet is shown in Figure 2.3(a). The Bravais lattice is triangular with two atoms per unit cell, each situated on one of two sub-lattices, often referred to as the A and B sublattices. The triangular reciprocal lattice is shown in Figure 2.3(b). The particularly interesting points of high symmetry, the K and K' points have wavevectors:

$$\vec{K} = (\frac{2\pi}{3a}, -\frac{2\pi}{3\sqrt{3}a}), \qquad \vec{K}' = (\frac{2\pi}{3a}, \frac{2\pi}{3\sqrt{3}a}), \tag{2.1}$$

The significance of the K and K' points is clear upon calculation of the band structure of graphene. This was first performed by Wallace[5] following a tight-binding model with a nearest neighbour approximation, whereby only hopping of electrons between nearest-neighbour atoms from sub-lattice A to B (or B to A) is considered. While consideration of the second- and third-nearest neighbours gives a more accurate description of the dispersion relation, for small wavevectors around the K and K' points the nearest-neighbour approximation is sufficient[55]. The tight-binding Hamiltonian for graphene assuming electrons can hop from one atom to its nearest neighbour is given:

$$H = -t \sum_{\langle i,j \rangle, \sigma} \left(a_{\sigma,i}^+ b_{\sigma,j} + \text{H.c.} \right), \tag{2.2}$$
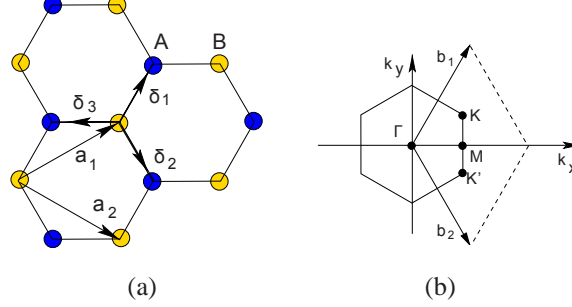
(a)   (b)

Figure 2.3: a) The honeycomb lattice of graphene with sublattices A and B shown in blue and yellow respectively. The lattice vectors are $\vec{a_1} = \frac{a}{2}(3, \sqrt{3})$ and $\vec{a_2} = \frac{a}{2}(3, -\sqrt{3})$ where $a \sim$ 1.42Å is the nearest-neighbour distance. The nearest-neighbour vectors are $\vec{\delta_1} = \frac{a}{2}(1, \sqrt{3})$, $\vec{\delta_2} = \frac{a}{2}(1, -\sqrt{3})$ and $\vec{\delta_1} = \frac{a}{2}(-1, 0)$. b) Brillouin zone and reciprocal lattice vectors of graphene. The reciprocal lattice vectors are $\vec{b_1} = \frac{2\pi}{3a}(1, \sqrt{3})$ and $\vec{b_2} = \frac{2\pi}{3a}(1, -\sqrt{3})$.[3]

where $a_{\sigma,i}$ ($a_{\sigma,i}^+$) annihilates (creates) an electron with spin $\sigma(\sigma = \uparrow, \downarrow)$ on site i on sublattice A, with an equivalent definition for sublattice B. The nearest-neighbour hopping energy is given by $t \approx 2.97$ eV[55] and H.c. is the Hermitian conjugate which corresponds to an electron hopping in the opposite direction. The energy bands derived from this Hamiltonian have the following form:

$$E(\vec{k}) = \pm t\sqrt{3 + f(\vec{k})}, \tag{2.3}$$

where,

$$f(\vec{k}) = 2\cos\left(\sqrt{3}k_y a\right) + 4\cos\left(\frac{\sqrt{3}}{2}k_y a\right)\cos\left(\frac{3}{2}k_x a\right). \tag{2.4}$$

The energy dispersion as given by Equation 2.3 is plotted in Figure 2.4. The origin of the upper band is the anti-bonding orbitals, π^*, and the lower band the bonding orbital, π. The two bands meet at the K-points at the edge of the first Brillouin zone and so graphene is a zero-gap semiconductor. Close to these points the dispersion relation is given by:

$$E = \pm v_f \hbar |\vec{k}|, \tag{2.5}$$

where v_f is the Fermi velocity in graphene (which is approximately 10^6 ms^{-1}), $\hbar$ is Planks constant over 2π and $\vec{k}$ is the wave vector with respect to K or K'. This linear dispersion relation is in stark contrast to the usual quadratic dispersion relation in solids ($E = \hbar^2 k^2/2m$) which has a dependence on the mass, m. In fact the linear relation is
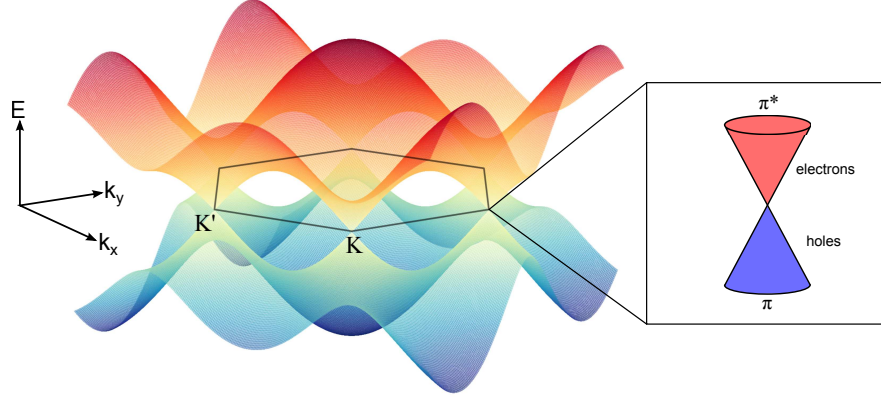
Figure 2.4: Electronic dispersion and Brillouin zone of graphene.

equivalent to that of photons in a vacuum only with the speed of light c replaced with v_f. As such, the carriers in graphene are said to be relativistic and massless.

A further point of interest is that the dynamics of the charge carriers in graphene are not described by the Schrödinger equation but by the 2D Dirac equation. From this, the two component wavefunctions in momentum space are found for the momentum around the K and K' points, and are given by:

$$\psi_{\pm,K}(\vec{k}) = \frac{1}{\sqrt{2}}\begin{pmatrix} e^{-i\theta_{\vec{k}}/2} \\ \pm e^{i\theta_{\vec{k}}/2} \end{pmatrix}, \qquad \psi_{\pm,K'}(\vec{k}) = \frac{1}{\sqrt{2}}\begin{pmatrix} e^{i\theta_{\vec{k}}/2} \\ \pm e^{-i\theta_{\vec{k}}/2} \end{pmatrix}, \tag{2.6}$$

where $\pm$ corresponds to the π^* and π bands respectively and the angle $\theta_{\vec{k}}$ is given by:

$$\theta_{\vec{k}} = \arctan\left(\frac{k_x}{k_y}\right). \tag{2.7}$$

The two components of the wavefunction correspond to the contributions from the A and B sublattices. It should be noted that under a rotation of 2π the wavefunction changes sign, indicating a phase change of π. This change in phase with geometry is otherwise known as a Berry's phase. A further point of note is that electrons and holes in graphene have pseudospin. The pseudospin denotes which of the sublattices the particle belongs and its direction is dependent on valley (K or K') and energy, see Figure 2.5. Pseudospin must be conserved which acts to prohibit back-scattering and leads to exotic phenomenon such as Klein tunnelling[56].
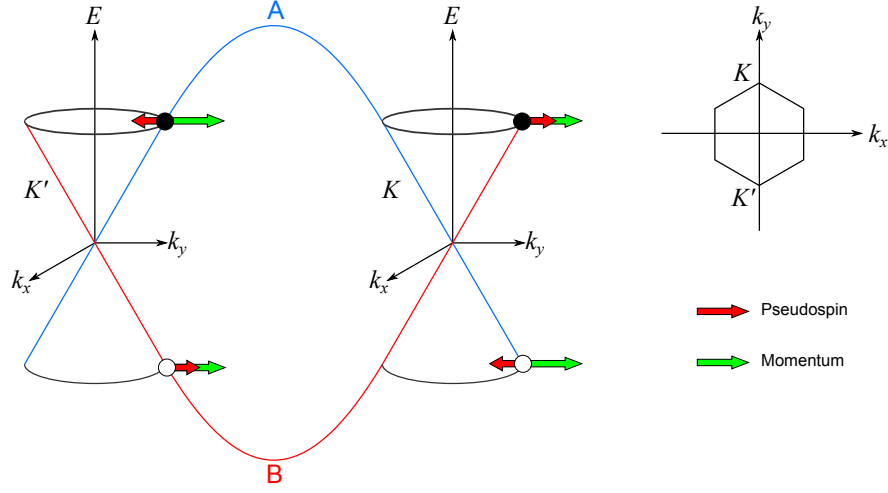
Figure 2.5: The relative contributions to the band structure from the A and B lattices are shown in blue and red respectively. The pseudospin (red arrows) indicates which sublattice the electron (filled circle) or hole (unfilled circle) is on. Electrons with the same momentum in the K and K' have opposite pseudospin as do electrons and holes in the same valley.

2.1.3 Electric Field Effect

The original motivation that led to the discovery of graphene, was the attempt to measure the EFE in a metal[57]. Ordinarily the conduction in a bulk sample is relatively impervious to the effects of an electric field because of charge screening. There is minimal screening of the charge carriers in graphene and so it is highly susceptible to nearby charge and so a dramatic field effect is observed. A common sample geometry employed in measuring the EFE in a graphene sample is shown in Figure 2.6. In this geometry a graphene flake contacted with metal contacts is situated on top of the oxide barrier of a highly doped Si substrate (which is conductive). By applying a voltage between the substrate (acting as a gate) and one of the electrodes, the device acts as a parallel plate capacitor and charge builds up at either side of the dielectric. The result is an increase (or decrease) in the carrier density n_s in the graphene, depending on the gate voltage applied. The resulting carrier density from this effect is given by:

$$n_s = \frac{\epsilon_0 \epsilon}{te} |V_G - V_{\text{Dirac}}|, \qquad (2.8)$$

where ϵ_0 is the permittivity of free space ($\sim 8.854 \times 10^{-12}$ Fm^{-1}), $\epsilon = 3.9$ the relative permittivity of silicon dioxide [58], t is the thickness of the oxide layer, e the elemen-
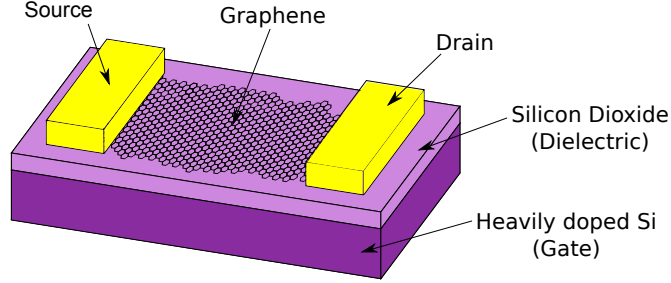
Figure 2.6: A simple graphene device. A graphene sheet is contacted by two electrodes, one acting as a source, the other a drain. An insulating Silicon dioxide layer separates the device from the conductive heavily doped Silicon substrate which is used as a global back gate.

tary charge and V_G the voltage applied to the gate. The gate voltage at which E_F is at the Dirac point, otherwise known as the charge neutrality point (CNP), is given by V_{Dirac}. In an extrinsic sample, external dopants act as either electron donors or acceptors, which shifts E_F away from the CNP and so an additional gate voltage $V_G = V_{\text{Dirac}}$ is required to overcome this shift.

An example of the EFE response of a typical graphene sample is shown in Figure 2.7. In an undoped sample $V_{\text{Dirac}} = 0$ and at $V_G = 0$ the Fermi level coincides with the point at which the conduction and valence band meet at the Dirac point (neutrality point). This coincides with a maximum in the resistivity of the sample because of there being a minimum of free states available at this point. As $V_G > 0$ V, E_F increases which coincides with a greater number of available states, a reduction in resistivity and charge carriers are electron-like. As $V_G < 0$ V E_F decreases which again increases the number of available states and a reduction in resistivity is observed, however the charge carriers are now hole like rather than electron-like.

The carrier mobility can be determined from EFE measurements by combining Equation 2.8 with the following relation:

$$\sigma = n_s e \mu. \tag{2.9}$$

Where σ is the conductivity of the sample and μ is the mobility of the carriers (in units of $\text{m}^2\text{V}^{-1}\text{s}^{-1}$). The mobility is thus given by:

$$\mu = \frac{t}{\epsilon_0 \epsilon} \frac{\sigma}{V_G}, \tag{2.10}$$
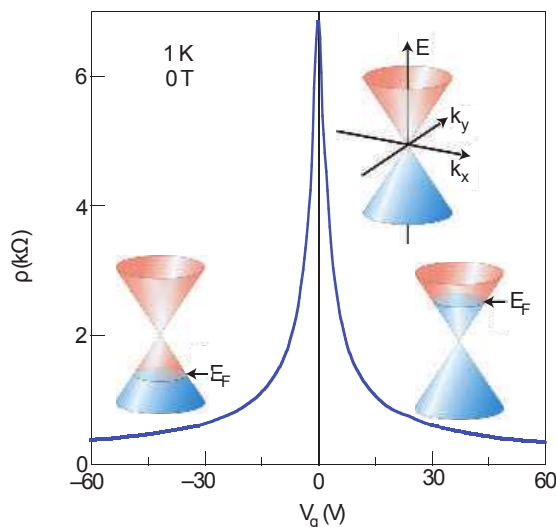
Figure 2.7: Electric field effect measurements taken on a monolayer graphene sample. The three Dirac cones indicate the shift in E_F that occurs as the gate voltage is varied.[9]

and can be found by taking the gradient of the conductivity with respect to the applied back gate voltage. Typical values of μ for graphene samples on SiO_2 are in the range of $1,000 - 20,000$ cm^{2}V^{-1}s^{-1}[9] close to the CNP which is more than an order of magnitude lower than theory predicts[59]. The limiting factor has been identified as scattering from charged impurities and structural deformations (ripples) in the graphene sheet. Values of μ exceeding 200,000 cm^{2}V^{-1}s^{-1} have been reported for suspended graphene samples[10; 23], where impurities such as trapped charges in the substrate are avoided. Flakes supported on exfoliated h-BN crystals have also shown mobilities in the range of 140,000 cm^{2}V^{-1}s^{-1}[22], which is attributable to the good lattice match between graphene and BN, which reduces structural deformations.

2.2 Quantum Hall Effect in a 2DEG

Much of the initial excitement generated by the discovery of graphene was fuelled by its demonstration of an unconventional QHE. While observation of the QHE confirmed that the material was truly two dimensional, the additional observation of half-integer filling factors confirmed that the charge carriers in monolayer graphene were behaving as massless Dirac fermions. In this section the QHE is introduced, following the

treatment of Singleton[60] before discussing the unusual QHE that is demonstrated by graphene.

2.2.1 Landau Levels and Shubnikov de-Haas Oscillations

In a two dimensional material the electrons are confined to the xy plane. If a magnetic field is applied in the z plane then the electrons will experience a Lorentz force:

$$\vec{F} = -e(\vec{E} + \vec{v} \times \vec{B}), \tag{2.11}$$

where e is the electron charge, $\vec{E}$ is the electric field, $\vec{v}$ the velocity of the electron and $\vec{B}$ the magnetic field. As a result, the electrons are driven in a circular orbit in the plane with an angular frequency known as the Larmor frequency given by:

$$\omega_c = eB/m^*, \tag{2.12}$$

where m^* is the effective mass of the electron. This leads to the generation of a series of discrete quantised energy levels known as Landau levels, LLs, which can be found in a 2DEG by solving the Schrödinger equation for an electron in a magnetic field giving:

$$E_n = \hbar\omega_c(n + 1/2), \tag{2.13}$$

where n is an integer. A diagram showing the energy of the discrete LLs in a 2DEG as a function of the density of states is shown in Figure 2.8(a). These discrete levels are broadened by δE from defect scattering as given by the uncertainty principle $\delta E \approx \hbar/\tau$, where τ is the scattering time. The broadened levels are shown in Figures 2.8(b) and 2.8(c) for two different values of E_F. When the Landau level is half filled, as in in Figure 2.8(b), there are lots of empty states available above E_F for electrons and so the sample will have high conductivity. Conversely, when the highest occupied Landau level is completely filled, as in in Figure 2.8(c), there are no available states above E_F and so the sample has low conductivity.

Broadening ensures that the individual LLs can only be resolved once a charge carrier can complete a single cyclotron orbit before scattering, which occurs when $\omega_c\tau \gg 1$, and can be achieved by increasing the magnetic field strength and/or reducing the temperature. Decreasing the temperature also sharpens the Fermi-Dirac distribution close to E_F and so makes it easier to resolve the discrete energy levels.
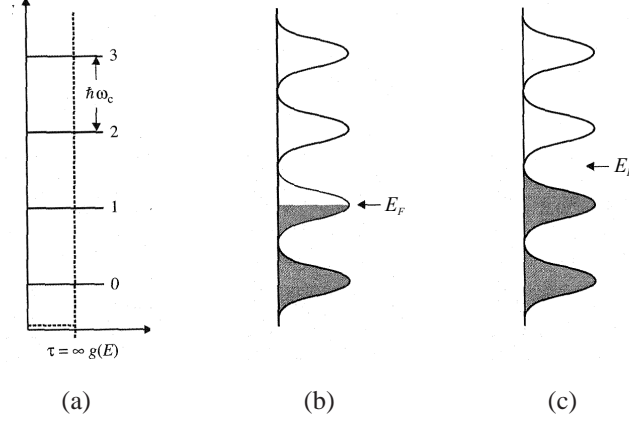
Figure 2.8: Landau levels in a 2DEG at high field. In a sample without scattering the levels are delta functions as in (a). With scattering the levels are broadened. The broadened case is shown in b) and c) where E_F is inside and outside a Landau level respectively.[60]

The maximum number of carriers per unit area per Landau level, n_s, can be calculated by dividing the 2D DOS by the area of a given Landau level. Doing so gives:

$$n_s = \frac{2eB}{h}. \tag{2.14}$$

Therefore, oscillations in the conductivity that are periodic in 1/B, will be observed as the field is swept with a period given by:

$$\Delta(1/B) = \frac{2e}{hn_s}. \tag{2.15}$$

These oscillations are otherwise known as the Shubnikov de-Haas oscillations (SdHO).

2.2.2 Resistivity and Conductivity Tensors for a 2D system.

Considering a 2D sample in the xy plane measured in the Hall geometry the current densities in the x and y plane, J_x and J_y, are given by:

$$J_x = \sigma_{xx}E_x + \sigma_{xy}E_y, \qquad J_y = -\sigma_{xy}E_x + \sigma_{xx}E_y, \tag{2.16}$$

where J is the current density, E the electric field and σ the conductivity tensor. If the sample is homogeneous and isotropic then $\sigma_{xx} = \sigma_{yy}$ and $\sigma_{xy} = -\sigma_{yx}$. Assuming all current flow is in the x direction then $J_y = 0$ and therefore:

$$\frac{E_y}{E_x} = \frac{\sigma_{xy}}{\sigma_{xx}}, \tag{2.17}$$

and the resistivity tensors are given by:

$$\rho_{xx} \equiv \frac{E_x}{J_x} = \frac{\sigma_{xx}}{\sigma_{xx}^2 + \sigma_{xy}^2}, \qquad \rho_{xy} \equiv \frac{E_y}{J_x} = \frac{\sigma_{xy}}{\sigma_{xx}^2 + \sigma_{xy}^2}. \qquad (2.18)$$

The motion of electrons taking into account the relaxation-time approximation is given by:

$$\frac{\partial \vec{v}}{\partial t} = -\frac{e}{m^*}\vec{E} - \frac{e}{m}\vec{v} \times \vec{B} - \frac{\vec{v}}{\tau}. \qquad (2.19)$$

In the steady state $\frac{\partial \vec{v}}{\partial t} = 0$ and so the electron velocity components are given by:

$$v_x = \frac{-e\tau}{m^*}E_x - \omega_c\tau v_y, \qquad v_y = \frac{-e\tau}{m^*}E_y - \omega_c\tau v_x. \qquad (2.20)$$

As there is no current in the y direction then $v_y = 0$ and so:

$$\frac{E_y}{E_x} = -\omega_c\tau. \qquad (2.21)$$

Using $J_x = -en_s v_x$, where n_s is the carrier density in carriers per unit area, and Equations 2.20 and 2.21 it can be shown that the Hall coefficient can be given by:

$$R_H \equiv \frac{E_y}{J_x B} = -\frac{1}{n_s e}. \qquad (2.22)$$

For a two dimensional system $J_x = I/w$ and $E_y = V_y/w$ where I is the current, V is the voltage and w is the width of the device. Therefore Equation 2.22 can be re-written as:

$$R_H = \frac{V_y}{IB}. \qquad (2.23)$$

Finally the resistivity tensors can be simplified by combining the high-field relationship $\omega_c\tau \gg 1$ with Equations 2.17 and 2.18 to give:

$$\rho_{xx} \approx \frac{\sigma_{xx}}{\sigma_{xy}^2}, \qquad \rho_{xy} \approx \frac{1}{\sigma_{xy}} = R_H B. \qquad (2.24)$$

The counter-intuitive result that ρ_{xx} is proportional to σ_{xx} is caused by the establishment of the Hall field. When the Fermi energy, E_F, is in an insulating state between two LLs σ_{xx} goes to zero. Because there are no states to scatter into the electrons will travel in cyclotron orbits with a drift in the y direction and hence no current flows in the direction of the applied electric field. Once the Hall field is established, from the

build up of charge at the edges of the sample, it balances the Lorentz force meaning that current can flow with a low probability of scattering and hence ρ_{xx} is small.

The longitudinal conductivity, σ_{xx} is at a minimum whenever the total carrier density coincides with some integer multiple of the number of states in a single Landau level ie:

$$n_s = j\frac{2eB}{h}, \tag{2.25}$$

where j is an integer. Given Equations 2.22 and 2.24 it is trivial to show that σ_{xy} is quantised:

$$\sigma_{xy} = \frac{1}{R_H B} = \frac{n_s e}{B} = j\frac{2e^2}{h}, \tag{2.26}$$

which manifests as the characteristic Hall plateaus.

2.3 Quantum Hall Effect in Graphene

In contrast to the standard QHE demonstrated in 2DEGs, graphene shows an anomalous QHE as a consequence of its unusual charge carrier dynamics. As in the 2DEG case, the energies of the LLs in monolayer graphene can be found by finding the eigenvalues of $H\Psi = E\Psi$ for a particle in a magnetic field. Rather than using the standard Schrödinger form, the Dirac Hamiltonian is now used with the two component wavefunction from Equation 2.7. This gives the following solution for the energies of the LLs in monolayer graphene:

$$E_n = \pm v_F\sqrt{2e\hbar Bn}, \tag{2.27}$$

where n is a positive integer. A similar method can be used to find the Landau level energies in bilayer graphene.

$$E_n = \pm\hbar\omega_c\sqrt{n(n-1)}, \tag{2.28}$$

where $\omega_c = |e|B/m$. A schematic showing the DOS of states as a function of energy for the LLs in mono- and bi-layer graphene as well as the conventional 2DEG is shown in Figure 2.9.

In both monolayer and bilayer graphene there is a zero-energy Landau level that is populated by both electrons and holes. In monolayer graphene the zero-energy Landau
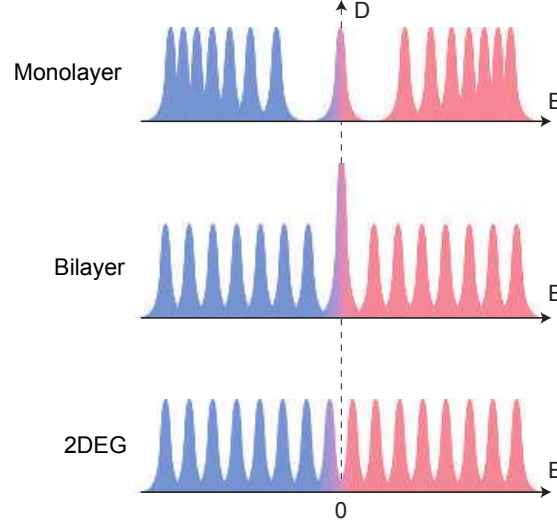
Figure 2.9: Density of states as a function of energy for monolayer graphene, bilayer graphene and standard 2D electron gas showing the various Landau level separations.[9]

level only has half as many states as the other LLs. The result is the observation of an anomalous half-integer QHE, with the Hall conductivity plateaus occurring at:

$$\sigma_{xy} = g_s g_v (n + \frac{1}{2}) \frac{e^2}{h}. \tag{2.29}$$

Where $g_s = 2$ and $g_v = 2$ are the spin and valley degeneracy in graphene, n is an integer, e is the elementary charge and h is the Planck constant. In bilayer graphene there are twice as many states in the zero-energy Landau level and so the integer Hall effect returns however there is still no Hall plateau at $E_F = 0$.

The first measurements confirming the unusual QHE in graphene were published simultaneously by Zhang *et al.* [7] and Novoselov *et al.* [61]. One of the results of Novoselov *et al.* is shown in Figure 2.10. The main figure shows ρ_{xx} (green) and σ_{xy} (red) as a function of carrier concentration for a monolayer of graphene etched into a Hall bar. The inset figure shows σ_{xy} for a similar device consisting of a bilayer of graphene. In both cases the zero-energy Landau level is clearly evident owing to the lack of a plateau when the carrier density is at a minimum.

The discovery of graphene also opened up the opportunity to observe the QHE at room temperature. This was achieved by Novoselov *et al.* [62] at a temperature of 300 K with a perpendicular applied field of 29 T. This is possible for a number of factors.
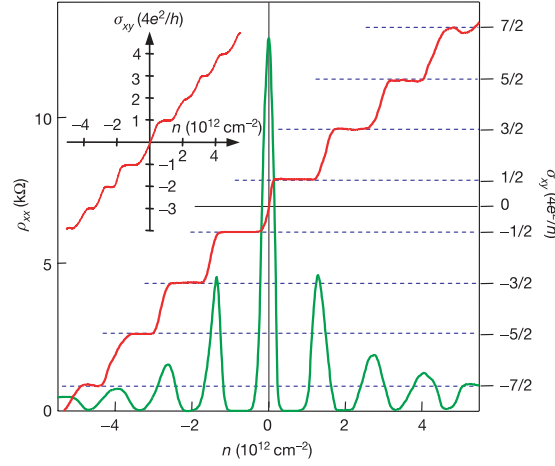
Figure 2.10: Hall conductivity σ_{xy} and longitudinal resistivity ρ_{xx} for a monolayer of graphene as a function of carrier concentration at B = 14 T and T = 4 K. (Inset) Same measurement in a bilayer sample.[61]

Firstly the high mobility of the Dirac fermions in graphene ensures a long scattering time τ and hence the $\omega_c\tau \gg 1$ condition is met at fields of several T. Secondly, the energy spacing of the first few LLs in monolayer graphene is so large that it can exceed k_BT even at room temperature.

2.4 Raman Spectroscopy

While it is possible to identify the flakes visually, using the optical microscope, establishing that monolayers have been produced requires an additional technique. Raman spectroscopy has been proven to be a rapid non-destructive technique capable of determining not only the number of layers in a graphene flake, but also gives information about the amount of disorder present [63], strain [64] or doping [65]. Here we outline the theory behind the technique and the characteristic spectra obtained from graphene.

2.4.1 Theory of Raman Spectroscopy

When photons are incident upon a molecule there can be a number of outcomes, namely the photon may be transmitted, absorbed or scattered[66]. The most common scattering event occurs when the electric field of the photon distorts only the electron
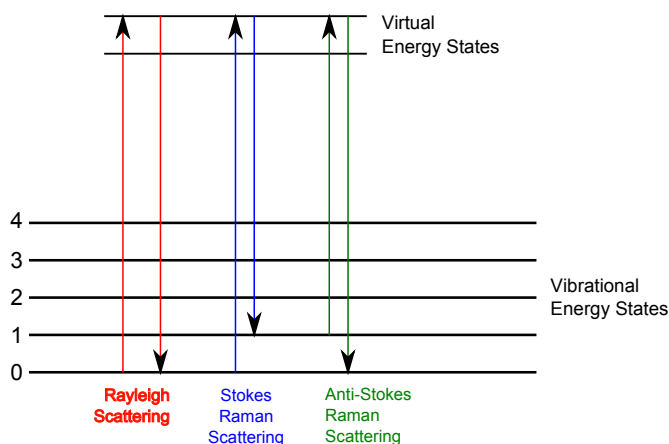
Figure 2.11: Energy level diagram showing possible scattering events that can occur because of an incident photon. Adapted from Ref. [66].

cloud of a molecule and scatters in an elastic process. In this process the photon does not change energy and is known as Rayleigh scattering. Another event is possible whereby the photon polarises the electron cloud and nuclear motion is induced. This is an inelastic process known as Raman scattering which was discovered in 1928 by Raman *et al.* [67]. It is a relatively weak phenomenon involving only one in $10^6 - 10^8$ photons[68], however it is experimentally viable even for small samples through the use of modern lasers with high power densities.

There are two possible outcomes of the Raman process, one in which the molecule absorbs energy from the photon and another in which the molecule transfers energy to the photon, known as the Stokes and anti-Stokes processes respectively. At room temperature Stokes scattering is the dominant event because there are more molecules in the energetically favourable ground state. Through these processes the energies of the scattered photons are increased or decreased with respect to the energies of the incident photons by a quantised amount, corresponding to vibrational and rotational energy states in the molecule[66], see Figure 2.11. Intense Raman scattering occurs from vibrations, which cause a change in the polarisability of the electron cloud of the molecule, with symmetric vibrations causing the largest changes, giving the greatest amount of scattering.

In a typical Raman experiment, a sample is illuminated with laser light of a known wavelength, λ (typically $\lambda = 633$ nm), and the scattered light (shifted in wavelength

because of the aforementioned Raman scattering events) is measured using a spectrometer. The measured Raman shifts indicate the change in photon frequency and are denoted by $\Delta\nu$ with units of cm^{-1} (i.e. wavenumber). The Raman shift is calculated using the following formula[66]:

$$\Delta\nu(\text{cm}^{-1}) = \frac{10^8}{\lambda_E} - \frac{10^8}{\lambda_R}. \tag{2.30}$$

Where λ_E and λ_R are the wavelength of the exciting line and Raman line in angstroms respectively. Equation 2.30 calculates the Raman shift for the Stokes lines, to obtain the anti-Stokes lines it is required to interchange λ_E and λ_R with one another.

2.4.2 Lineshape of the Raman Peaks

Peaks in the Raman spectra can be described using a forced damped harmonic oscillator model where an oscillator with a natural frequency, ω_q, is driven by an external force with a frequency ω. As such the characteristic line-shape is given by a Lorentzian of the form shown below[69]:

$$I(\omega) = \frac{I_0}{\pi\Gamma_q} \frac{1}{(\omega - \omega_q)^2 + \Gamma_q^2} + I_b, \tag{2.31}$$

where $I(\omega)$ gives the intensity of the Raman signal at a given frequency and Γ_q is the damping term. The full width at half maximum of the Lorentzian is equal to $2\Gamma_q$ and I_0 is the maximum intensity of the peak with respect to the background signal I_b. The relationship between phonon energy and phonon lifetime is given by the uncertainty principle $\Delta E \Delta t \sim \hbar$. The uncertainty in E is given by Γ_q and so Γ_q is the inverse of the phonon lifetime, with broader peaks indicating shorter phonon lifetimes which could be because of scattering events with other phonons or electrons.

2.4.3 Raman Spectroscopy of Graphene Samples

Figure 2.12 shows experimental Raman data taken on flakes, demonstrating that the number of graphene layers present can be established by comparing the relative intensities of the G peak and the 2D peak (also known as the G' peak). The G peak is located at $\sim$1580 cm^{-1} and in the molecular picture is caused by the doubly degenerate zone centre E_{2G} mode i.e. the bond stretching of all pairs of sp^2 bonded atoms, see Figure
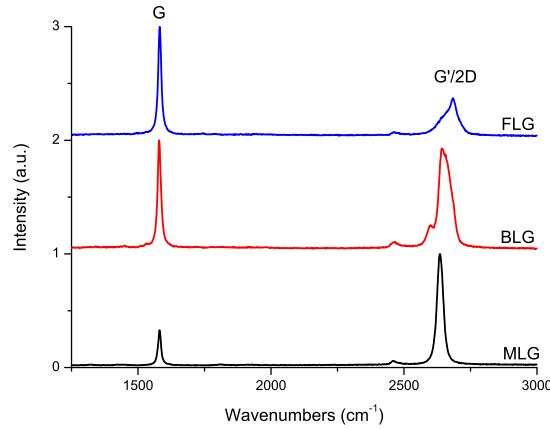
Figure 2.12: Raman measurements taken on flakes of different thickness using a laser wavelength = 633 nm. Spectra have been normalised and offset for clarity.

(a) E_{2G} (b) A_{1G}
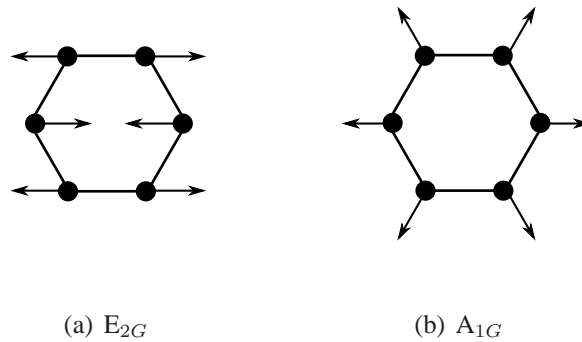
Figure 2.13: Vibrational modes of graphene showing a) G mode and b) D breathing mode. Black circles indicate carbon atoms with arrows indicating the direction of vibration.

2.13(a). The 2D peak is located at ~ 2700 cm^{-1} and can be attributed to the second harmonic of the A_{1G} breathing mode (the first harmonic occurring at ~ 1360 cm^{-1}), see Figure 2.13(b). While these molecular descriptions of the vibrational modes provide the simplest explanation for the observed peaks in graphene, they cannot explain for example, the appearance of the D-peak overtone (2D peak), despite the absence of the first harmonic D peak which is seen in high quality samples. A more fruitful approach identified primarily by Ferrari *et al.* [63; 70], is to consider the solid-state model of the excitation of an electron by the laser and the subsequent decay processes as shown in Figure 2.14.

(a) G

(b) G'/2D

(c) D

(d) D'
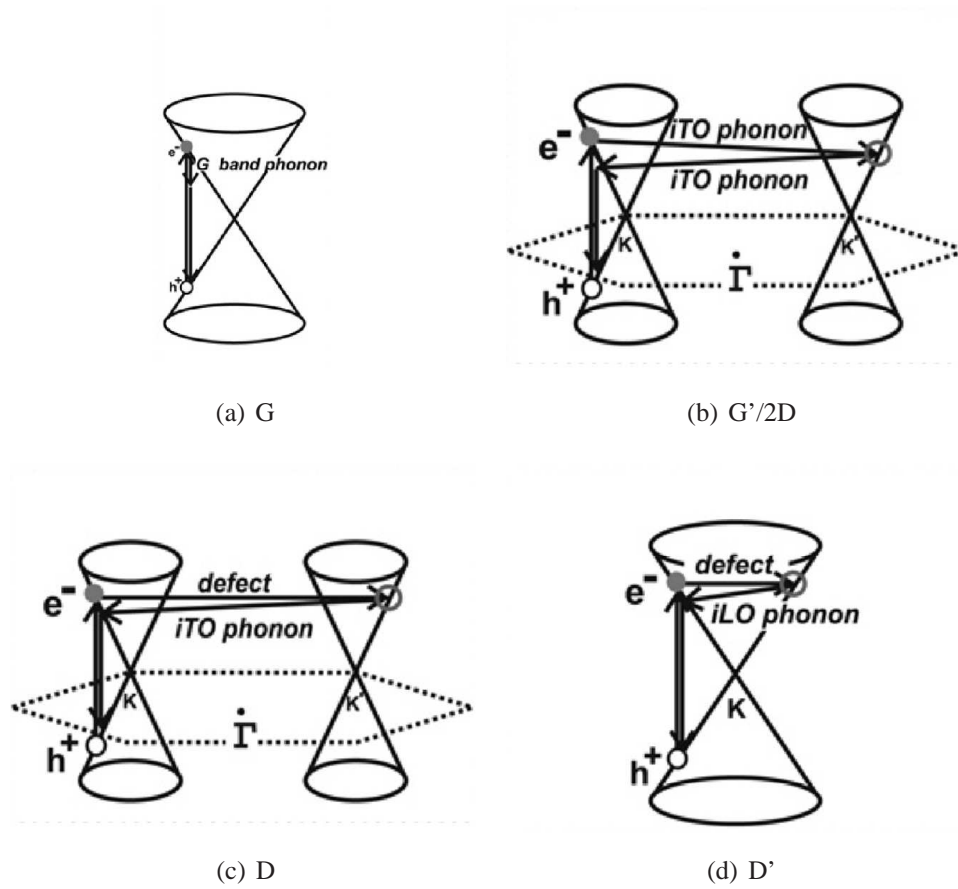
Figure 2.14: Various Raman processes in graphene. Only the G mode shown in a) is a first order process. Second order Raman processes are responsible for the G'/2D, D and D' modes. [71]

It is clear from Figure 2.14(a) that only the G band is attributable to a standard first order Raman process, with the other bands caused by second order Raman processes. In the case of the D peak, Figure 2.14(c), an electron-hole pair is generated by laser excitation followed by elastic scattering of the electron off a crystal defect. This is followed by an inelastic scattering event, where an in-plane transverse optical (iTO) phonon is absorbed or emitted, which allows the electron-hole recombination to occur, generating a photon with energy lower than the initial excitation energy. A similar case is observed in the 2D case, Figure 2.14(b), whereby following excitation the electron undergoes two inelastic scattering events by iTO phonons, which accounts for why the 2D band is observed at a frequency twice that of the D band. The absence of elastic defect scattering in the 2D band process explains why in defect free samples the 2D peak can be present without a D peak.

Another frequently observed feature in defected samples is the D' peak at about 1620 cm^{-1} from the process shown in Figure 2.14(d). Again an excited electron scatters off a defect, only this time remaining close to its original K point. The electron then inelastically scatters by the absorption or emission of an in-plane longitudinal optical (iLO) phonon before electron-hole recombination occurs.

2.5   Superconductivity

In this section, the basic properties of superconductivity are summarised along with the underlying microscopic theory of superconductivity. The related phenomenon of Andreev reflection and the Josephson effect are also discussed in some detail. Given the rich history of superconductivity research over the past century, a complete discussion of the phenomenon is beyond the scope of this thesis. For a more in depth discussion of the superconducting state the reader is directed towards Tinkham [72], as well as several other instructive texts written by Annet [73], Buckel[74] and Duzer[75].

2.5.1   Basic Properties

Superconductivity was discovered by Kamerlingh-Onnes over a century ago[74] while making low temperature measurements on mercury. Below temperatures of 4.2 K the unexpected observation was made that the resistance dramatically decreased to zero.

So large was the effect, that it implied that the mercury had entered into a new state, which has become known as the superconducting state. This phenomenon has been demonstrated in a large number of materials, from elemental metals to more complicated crystalline structures, such as ceramic cuprates and biological molecules. In addition, each material shows vanishing resistance at a material dependent temperature known as the critical temperature, T_c.

As the resistivity is zero below T_c the dissipative mechanisms that would normally degrade an electrical current are non-existent, hence a persistent current can be generated. This persistent current can be destroyed through a number of means, namely; applying a sufficiently large magnetic field (the critical field H_c), by generating a sufficiently large current (the critical current I_c) or applying a high frequency AC electric field[76].

2.5.2 Microscopic Theory

2.5.2.1 Attraction Between Electron Pairs

A compelling microscopic theory for superconductivity was formulated in 1957 by Bardeen, Cooper and Schrieffer, known as BCS theory[77]. According to the BCS theory, the superconducting state is a result of the pairing of electrons into a bound state, a Cooper pair. For this to occur a net attraction between electrons is required. Ordinarily this does not occur because of the mutual Coulomb repulsion, however, an attractive force between electrons can be realised if there is a coupling between the electrons and the lattice phonons. Figure 2.15 shows a Feynmann diagram for the exchange of a virtual phonon between electrons occupying states $\vec{k_1}$ and $\vec{k_2}$.

While it is required that the total momentum, $\vec{K}$, is conserved in this process the energy need not be conserved. As the scattering occurs in a very short time, t, the uncertainty Δt is also very small. As a result of the Heisenberg uncertainty principle $\Delta t \Delta E \geq \hbar$ and since Δt is small then the uncertainty in energy ΔE must be large. Therefore, the total energy after the scattering event can be less than before the scattering occurred, within $\Delta \epsilon$.

The effective reduction in energy from the formation of the bound pair is greatest when the scattering probability is at its greatest which occurs when $\vec{K} = \vec{k_1} + \vec{k_2} = 0$ i.e. when $\vec{k_1} = -\vec{k_2}$. As a result the electrons which form a Cooper pair always have
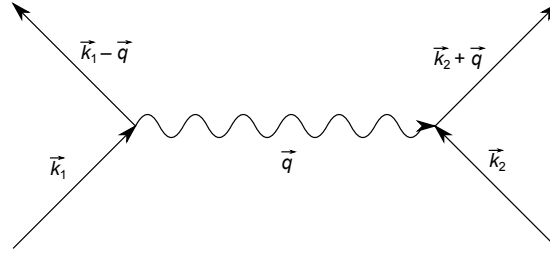
Figure 2.15: Exchange of a virtual phonon between two electrons.

equal but opposite momentum. By a similar argument the electrons also have opposite spins to one another. The attractive force between the electrons can be modelled using the interaction potential $V_{\vec{k}\vec{k}'}$. In BCS theory a simple form is used which assumes that, for $\hbar\omega < \hbar\omega_D$, $V_{\vec{k}\vec{k}'}$ is a negative constant $-V$ and zero otherwise. In this case, ω is the frequency difference between the initial and final states and ω_D is the Debye frequency, the theoretical maximum phonon frequency for the lattice.

2.5.2.2 BCS Wavefunction

The superconducting state is described by a macroscopic wavefunction, or condensate, of Cooper pairs. This macroscopic wavefunction can be written as a superposition of coherent wavefunctions which can be written as:

$$|\Psi_{\text{BCS}}\rangle = C \prod_k \left(1 + \alpha_k \hat{p}_k^+\right) |0\rangle, \tag{2.32}$$

where C is a normalisation constant, α_k is a complex number, $|0\rangle$ is the ground-state wavefunction and $\hat{p}_k^+$ creates a pair of electrons with equal but opposite spin and momentum. Normalising Equation 2.32 allows the BCS wavefunction to be re-written as:

$$|\Psi_{\text{BCS}}\rangle = \prod_k \left(u_k^* + v_k^*\hat{p}_k^+\right) |0\rangle, \tag{2.33}$$

where $|u_k^*|^2$ and $|v_k^*|^2$ give the probabilities that a state $\pm k$ is unoccupied or occupied respectively by a Cooper pair.

2.5.2.3 BCS Hamiltonian

The BCS Hamiltonian can be written as follows:

$$H = -V \sum_{|\epsilon_k - \epsilon_F| \leq \hbar\omega_D} \hat{p}_k^+ \hat{p}_k + 2 \sum_{k>k_F} |\epsilon_k| \hat{p}_k^+ \hat{p}_k + 2 \sum_{k<k_F} |\epsilon_k| \hat{p}_k \hat{p}_k^+, \qquad (2.34)$$

where ϵ_k is the kinetic energy of an electron (or hole) measured relative to the E_F. The first term is the contribution from pairing and the second and third term is the kinetic energy of the electrons and holes respectively. The energy of the superconducting ground state relative to the normal ground state can be found by calculating the expectation value of H. Minimising this energy enables the probabilities of a state being occupied or unoccupied to be found, which are given as follows:

$$|v_k|^2 = \frac{1}{2} \left[1 - \frac{\epsilon_k}{(\Delta^2 + \epsilon_k^2)^{1/2}} \right], \qquad (2.35)$$

$$|u_k|^2 = \frac{1}{2} \left[1 + \frac{\epsilon_k}{(\Delta^2 + \epsilon_k^2)^{1/2}} \right], \qquad (2.36)$$

where Δ is known as the gap parameter and is defined as:

$$\Delta = V \sum_k u_k v_k^* = V \sum_k \frac{\Delta}{2(\Delta^2 + \epsilon_k^2)^{1/2}}. \qquad (2.37)$$

This can be solved by integrating over the range of available energies:

$$\frac{2}{NV} = \int_{-\hbar\omega_D}^{\hbar\omega_D} \frac{d\epsilon}{(\Delta^2 + \epsilon^2)^2}, \qquad (2.38)$$

where N is the density of states. Finally this gives the gap parameter as:

$$|\Delta| = \hbar\omega_D \exp\left(-\frac{1}{NV} \right), \qquad (2.39)$$

which is the binding energy of one electron. To evaluate the temperature dependence of the gap parameter it is necessary to incorporate the standard Fermi function, f, which accounts for the removal of electrons from the pair by thermal fluctuations. Subsequently, the T dependence of Δ is:

$$\Delta(T) = V \sum_k u_k v_k^* (1 - 2f). \qquad (2.40)$$

29

Substituting Equation 2.37 into Equation 2.40 gives:

$$\Delta(T) = V\Delta(T) \sum_k \frac{1}{2E_k} \left(1 - 2f\right), \tag{2.41}$$

where E_k is the energy of a single quasiparticle in the superconducting state with wavevector $\vec{k}$ which is given by:

$$E_k^2 = \epsilon_k^2 + |\Delta|^2. \tag{2.42}$$

Equation 2.41 can be rearranged and solved by integrating over the available energy range:

$$\frac{1}{NV} = \int_0^{\hbar\omega_D} \frac{1}{E_k} \tanh\left(\frac{E_k}{k_B T}\right) d\epsilon. \tag{2.43}$$

Assuming $\Delta = 0$ when $T = T_c$, where T_c is the critical temperature gives the following result:

$$k_B T = 1.13\hbar\omega \exp\left(-\frac{1}{NV}\right). \tag{2.44}$$

By substituting Equation 2.39 into this equation the following result for the pair binding energy at $T = 0$ K, $\Delta(0)$, in terms of the critical temperature is achieved:

$$2\Delta(0) = 3.52 k_B T_c. \tag{2.45}$$

Consequently, materials with higher critical temperatures invariably have larger pair binding energies. This is intuitive as more thermal energy is required to break pairs which are more strongly bound together.

2.5.2.4 BCS Density of States

The density of BCS density of states can be derived assuming that during the transition from the normal state to the superconducting state only the energy of the electrons changes, not their values of $\vec{k}$. Hence, the following relation holds:

$$N_S(E) = N_N \frac{d\epsilon}{dE}, \tag{2.46}$$

where N_N and N_S are the density of states for the normal and superconducting state respectively. Combining this with Equation 2.42 results in the following expression for the BCS density of states.

$$N_S(E) = N_N(\epsilon) \frac{E_k}{\left(E_k^2 - \Delta^2\right)^{1/2}}. \tag{2.47}$$
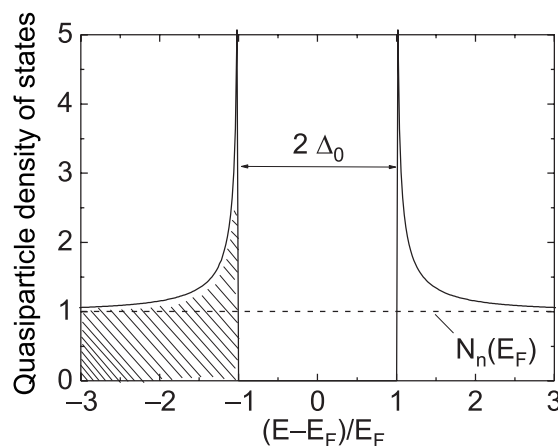
Figure 2.16: Normalised density of states of the quasiparticles in a superconductor according to BCS theory. At T = 0 K all states below E_F are occupied (hatched region). Modified from Ref. [74].

A plot of the density of states of a superconductor is shown in Figure 2.16. This clearly shows that there is an energy gap of 2Δ in which there are no single particle energy states, only pair bound states.

2.5.3 Andreev Reflection

A particularly interesting phenomenon that can occur at the interface between a superconductor and a normal conductor is Andreev reflection (AR). Consider an electron travelling in a normal conductor with an energy $E < \Delta_0$, arriving at the interface of a superconductor. As the electron is within the superconducting energy gap, there are no available energy states for it to enter and so it will be unable to penetrate the material. The electron can undergo strong inelastic scattering and reach thermal equilibrium with the ensemble of electrons within the superconductor, but this process is of little interest. If instead we consider that the electron retains its energy, there are two possible outcomes. Firstly, the electron can undergo a specular reflection, a familiar process that does not contribute to any current transfer across the interface. The second possibility is that the electron is absorbed into the superconductor forming a Cooper pair with a second electron taken from the superconductor. This process can only occur if the change in $\Delta_0(x)$ is small, compared to the wavelength of the incoming electron of the same length scale.
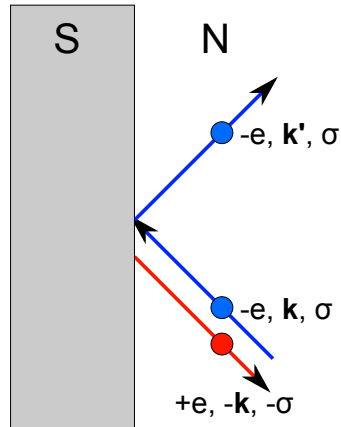
Figure 2.17: Andreev reflection of an electron in a normal metal. Two possible scattering processes are possible. The electron can undergo specular scattering at the superconductor-normal interface where its charge $(-e)$ and spin (σ) are maintained. Alternatively an Andreev reflection event can occur where a hole of opposite charge $(+e)$ and spin $(-\sigma)$ is retro-reflected. In this event a net charge of $-2e$ passes into the superconductor condensate as a Cooper pair. Adapted from Ref. [73].

In order for the Cooper pair to form, the second electron must be removed from an energy below E_F resulting in the generation of a hole. The Cooper pair has zero net momentum (each electron having a wavevector $\mathbf{k}$ and $-\mathbf{k}$ respectively) and so in order for momentum to be conserved during the process, the hole must have equal and opposite momentum to that of the original incident electron. The AR process is as such, an incident electron with wavevector $\mathbf{k}$ forms a Cooper pair with an electron in the superconductor and a hole is retro-reflected with wavevector $-\mathbf{k}$ in the normal conductor. It is important to note that during the process a charge of 2e has moved across the interface. This results in the measured current across such an interface being twice as large as would be expected when the voltages are below Δ_0/e.

2.5.4 Josephson Effect

In 1962 Josephson predicted that in a superconductor-insulator-superconductor (SIS) junction, in addition to observing standard electron tunnelling another tunnelling mechanism would manifest itself, consisting of a current carried by Cooper pairs provided the barrier was not too thick[74]. Josephson predicted that a consequence of this was
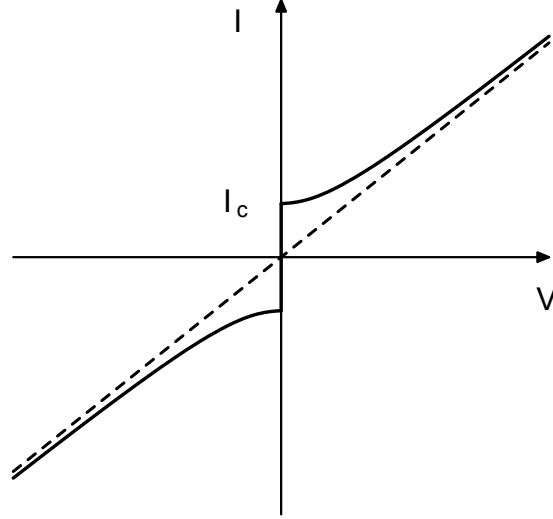
Figure 2.18: *IV* characteristic of an SNS Josephson junction. Provided $I < I_c$ there is no voltage drop. For large currents the *IV* relation approaches that given by Ohm's law, $V = IR$.[73]

that a supercurrent should flow, regardless of whether an electric field is applied (the DC Josephson effect)[76].

As the Andreev reflection amplitudes depend on the relative phase difference between the macroscopic wavefunctions describing the two superconductors, it is observed that the supercurrent across the weak link, known as the Josephson current, also shares this phase dependency. It can be shown to a first-order approximation that this current is given by:

$$I_s = I_c \sin \gamma, \tag{2.48}$$

$$\gamma = \varphi_2 - \varphi_1 - \frac{2\pi}{\Phi_0} \int_1^2 A \, dl, \tag{2.49}$$

which is known as the first Josephson equation. γ is the gauge-invariant phase difference, Φ_0 the magnetic flux quantum and $\int_1^2 A \, dl$ the path integral of the vector potential taken from superconductor 1 to superconductor 2. The quantity I_c is known as the critical current and is the maximum Josephson current that can flow through the junction. For $I < I_c$ there is no dissipation of the Josephson current, i.e. a supercurrent flows. When $I > I_c$ a finite voltage drops across the junction leading to the typical *IV* characteristic for a Josephson junction as shown in Figure 2.18.
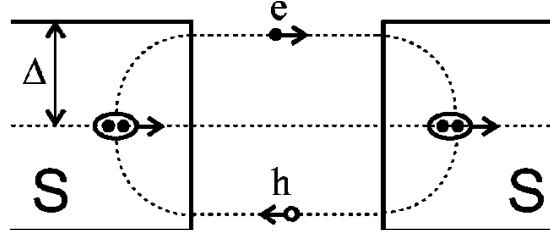
Figure 2.19: Andreev bound state in a Josephson junction. A cooper pair is transferred from the left superconductor to the right one, via the transmission of an electron e and reflection of a hole h, creating a supercurrent flow across the junction.[78]

For $I > I_c$ the finite voltage difference between the superconductors, V, results in a time dependent oscillation of the phase difference between the two superconductors. Consequently, a high-frequency alternating current is observed, known as the AC Josephson effect. The relationship between γ and V is given by the following equation:

$$\frac{\partial \gamma}{\partial t} = \frac{2eV}{\hbar}. \tag{2.50}$$

2.5.5 SNS Junctions

A supercurrent can also be observed flowing through a superconductor-normal metal-superconductor (SNS) junction. Rather than the direct tunnelling of Cooper pairs through the barrier as in an SIS junction, this process is mediated via the formation of Andreev bound states, consisting of repeated Andreev retro-reflection events as shown in Figure 2.19. In SNS junctions additional features can be observed in the IV characteristics, known as sub-harmonic energy gap structure. This is observed as peaks in the conductivity measurements at:

$$V_n = \frac{2\Delta_0}{ne}, \tag{2.51}$$

where $n = 1, 2, 3...$ and is because of the occurrence of multiple Andreev reflections (MAR), see Figure 2.20. When a voltage is applied to the junction, an electron is accelerated and gains an energy eV, subsequently when a hole is generated via an AR process, it too is accelerated across the junction (as it has a positive charge), gaining an energy eV. Each reflection event transfers a charge $(n+1)e$ corresponding to the $n+1$ particle current. If the applied voltage has the value $2\Delta_0/ne$ then $(n-1)$ reflections are
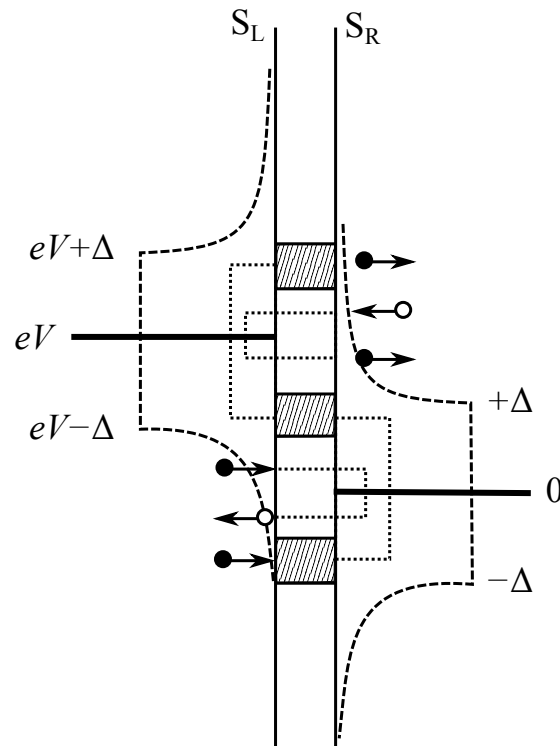
Figure 2.20: Schematic showing multiple Andreev reflections in a normal material between two superconductors (S_L and S_R) with a superconducting energy gap Δ. The filled circles are electrons, the open circles are holes, and the arrows indicate the direction of motion. The dashed lines (long) represent the Andreev reflection amplitudes. The electron is retro-reflected as a hole at the N-S_R interface via Andreev reflection. In the process a Cooper pair is generated in S_R. Subsequently at the S_L-N interface the hole undergoes an Andreev reflection event, annihilating a Cooper pair. With each successive pass the electron and holes acquire an energy eV from acceleration by the applied bias V. Reproduced from Ref. [72].

just enough for an electron (or hole) to reach an allowed energy state in the opposite electrode and so each time this condition is met a peak in the conductivity is measured, because of the availability of a new MAR harmonic.

2.6 Published Work on Superconductor-Graphene Interfaces

The tunable properties of graphene devices accessible through the field effect, coupled to its unique charge transport dynamics, make it an ideal candidate for incorporation into superconducting devices. Since its discovery, a wealth of experimental papers have emerged detailing superconducting phenomenon in graphene devices. While supercurrents have been generated in graphene decorated with Sn islands[28; 29] and Andreev bound states have been produced in graphene quantum dots[30], generally the bulk of the work has focussed on producing superconductor-graphene-superconductor (SGS) JJs, with graphene as the weak link between two superconducting contacts. As such the following discussion shall focus on this class of graphene device. A variety of superconducting materials have been employed, most devices were initially based on Al[31–36] deposited by electron beam evaporation followed by devices using Ta[37], Pb[38; 39], PbIn[40; 41], Nb[42], NbTiN[43], W[44] and ReW[42] deposited via a variety of deposition methods ranging from magnetron sputtering[37; 42; 43] and thermal evaporation to decomposition of an active gas by a focussed Ga ion beam[44], with varying degrees of success.

Heersche *et al.* [31] produced numerous SGS devices comprising of Ti/Al (10/70 nm) bilayers contacted to single- and few-layer graphene, via electron beam lithography and evaporation. Al was used as the principal superconductor with Ti used as an adhesion layer to improve contact to the graphene. Almost all subsequent studies have employed an adhesion layer with a few nm's of Pd or Ti being typical choices. Measurements were performed at a temperature of 30 mK which is well below the critical temperature of the electrodes ($T_c = 1.3$ K). Owing to the nanoampere range of I_c measured in these devices, extensive noise filtering is employed, with a standard set-up consisting of low pass π-filters at room temperature and RC-filters coupled to thermocoax cables or metal powder filters at low temperature (T = 4.2 K). Heersche
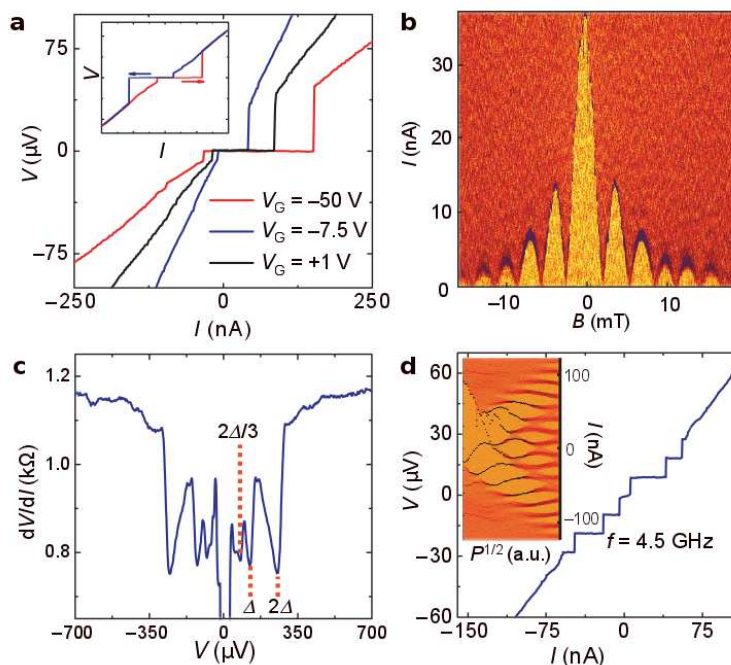
Figure 2.21: Josephson effects in a SGS junction with Ti/Al contacts. a) IV measurements at various values of V_G. Inset, current bias sweeps in both directions showing hysteretic behaviour typical of an underdamped junction. b) Colour-scale representation of differential resistance as a function of current and field for T = 30 mK (yellow-orange is zero resistance i.e. a supercurrent region, and red corresponds to finite resistance. c) Differential resistance versus V showing MAR dips below the superconducting gap. d) AC Josephson effect demonstrating Shapiro steps of 9.3 μV in the IV characteristics when the sample is irradiated with 4.5 GHz microwaves.[31]

et al. reported observing supercurrents in 17 devices, with 4 unambiguously identified as single layer flakes via QHE measurements. Electrode separations of these devices ranged from $100 - 500$ nm.

A variety of transport measurements clearly showing the Josephson effect in these devices are shown in Figure 2.21. IV measurements are shown at a variety of gate voltages. In this device V_{Dirac} was established to be between $-10 \rightarrow -20$ V and it was observed that a reduction in carrier density in the graphene channel corresponds to a reduction in I_c. The highly asymmetric IV curve, when sweeping from negative to positive current is established to be from a hysteretic junction response typical of

an underdamped junction. Similar hysteretic IVs have been shown in all supercurrent carrying SGS junctions at low temperature and was attributed by Jeong *et al.* [40] to a finite junction capacitance. To establish that the supercurrent is carried through the graphene and not by superconducting material bridging the weak link, a weak magnetic field is applied perpendicular to the junction. This results in an additional phase difference across the junction, see Equation 2.49, which results in a variation in supercurrent according to:

$$I_c \propto \frac{\sin\left(\pi\phi/\phi_0\right)}{\pi\phi/\phi_0}, \tag{2.52}$$

where ϕ is the flux penetrating the weak link and ϕ_0 is the flux quantum. The result of varying the field is a characteristic Fraunhofer diffraction pattern with minima in I_c when the amount of flux is equal to an integer number of flux quanta and so by determining the field at which a minima occurs, the junction area can be calculated. For the data shown the area was found to be 0.8 ± 0.2 μm^2 which compares favourably with the area determined by atomic force microscopy (0.7 ± 0.2 μm^2), confirming that the supercurrent is being carried by the graphene sheet. This measurement has been particularly useful in current annealed SGS devices to ensure that the diffusion of superconducting material across the graphene channel is not responsible for carrying the supercurrent.

At finite bias, multiple dips in differential resistance are observed at source-drain voltages $V = 2\Delta/en$ ($n = 1, 2, 3, ...$) because of MAR. From the MAR Δ is calculated to be 125 μeV which is a smaller energy gap than bulk Al as a result of the presence of the Ti adhesion layer. At voltages above 2Δ the normal state resistance is recovered. Under exposure of the junction to a radio frequency field a series of quantised steps in voltage (Shapiro steps) in the IV curves is observed, the manifestation of the AC Josephson effect. The steps have an amplitude of $\hbar\omega/2e$ where ω is the frequency of the microwave radiation. The observation of a supercurrent, Fraunhofer diffraction pattern and Shapiro steps makes it clear that the SGS junctions are operating as JJs.

In Figure 2.22(a) a colour plot of differential resistance as a function of both I and V_G is shown. It is immediately clear that the critical current is highly dependent on V_G with a minimum critical current at V_{Dirac}. Furthermore, about the CNP I_c versus V_G has a high degree of asymmetry, which correlates strongly to the normal state conductance G_N as indicated by the blue curve. The characteristic voltage $V_c = I_c R_N$ is plotted
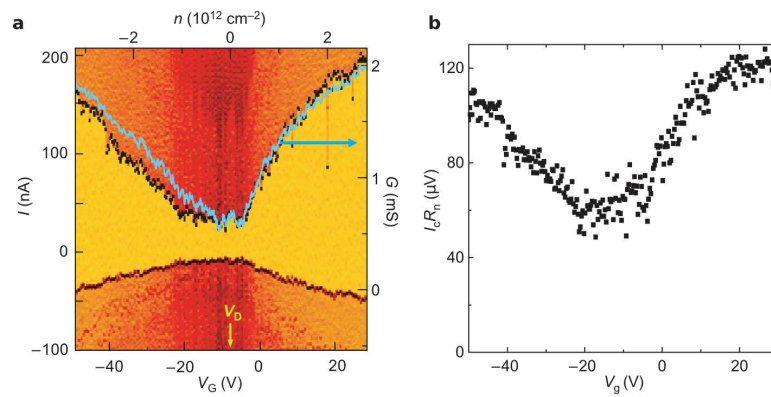
Figure 2.22: Bipolar supercurrent transistor behaviour and finite supercurrent at the Dirac point. a) Colour-scale plot of differential resistance as a function of I and V_G. Yellow means zero resistance i.e. a supercurrent region with orange to dark red representing increasing differential resistance. Current is swept from negative to positive values and demonstrates asymmetry caused by an underdamped junction. The top axis shows the carrier density calculated using the parallel plate capacitor model and the blue curve represents the normal state conductance. b) Product of the critical current and normal state resistance versus V_G. Normal state resistance is measured at T = 30 mK in a small magnetic field to drive the superconducting contacts normal.[31]

in Figure 2.22(b) and shows that V_c is suppressed around 2-3 times close to the Dirac point. The origin of this suppression has subsequently been a point of interest in SGS JJ devices.

Ojeda-Aristizabal *et al.* [37] explored annealing SGS devices as a means of improving the device so as to observe a supercurrent across the junction. They produced devices of a similar geometry to Heersche *et al.* but used Pt/Ta/Pt trilayer deposited using magnetron sputtering instead of evaporated Ti/Al as the contact material. The dimensions of the device investigated was $L = 330$ nm, $W = 2.7$ μm and T_c for the Ta was 2.5 K. Measurements were performed in a dilution refrigerator at $T = 60$ mK. Several R versus V_{G} profiles are shown in Figure 2.23 for this device. The numbered curves 0, 1, 2 and 3 correspond to a device before it was annealed and three subsequent anneals respectively. A current annealing procedure was performed, whereby application of a large current between the source and drain contacts results in an elevated sample temperature via Joule heating, as pioneered by Moser *et al.* [79]. This process is described in more detail in Chapter 4. The first, second and third anneals are performed for several minutes, each using currents $I = 3, 6$ and 10 mA respectively, with $J = 2 \times 10^8$ Acm^{-2} at 3 mA assuming a graphene thickness of 0.36 nm. Pre-anneal (curve 0) the graphene appears to be slightly doped by charged impurities with $V_{\mathrm{Dirac}} = 5$ V and at a high carrier density the extracted mobility is around 2,000 cm^2/Vs which is relatively low.

The inset figures show the resistance and mean free path at T = 4 K when the contacts are in the normal state. The mean free path was calculated using $l_e = h\sigma/(2k_F e^2)$, where k_F is determined from V_{G} using a plane capacitor model. Far away from V_{Dirac} $l_e \sim 15$ nm which corresponds to diffusive transport. An obvious reduction in resistance is observed following the second anneal (curve 2). As the two terminal resistance measurement includes both the sheet resistance and the contact resistance it is difficult to attribute the resistance drop to one or the other following the anneal. The generation of a supercurrent after the third anneal (curve 3), evident from $R \sim 0$ Ω across all values of V_{G}, suggests that the interface transparency has dramatically improved. Additional evidence for an improvement in interface transparency is given in measurements of dI/dV, see Figure 2.24, which features peaks in conductance because of MAR in the high bias regime. While the peak position seems invariant to the alteration
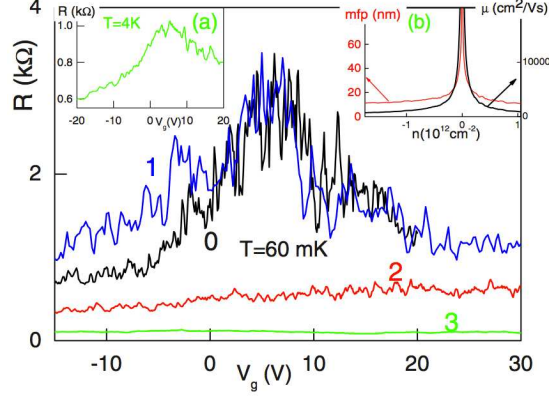
Figure 2.23: Gate voltage dependence of the two wire resistance of the sample before and after different annealing steps at 60 mK. The labels 1, 2 and 3 correspond to 3, 6 and 10 mA current anneals for several minutes each. The last anneal resulted in a supercurrent running through the graphene. Inset (a): resistance versus gate voltage before any annealing at 4.2 K. Inset (b): mobility and mean-free path of the graphene sheet before annealing deduced from inset (a) data. [37]

of V_G, the number of peaks observable does increase from 3 to 4 following an additional anneal step. This suggests that the interface transparency has improved, which enables higher order tunnelling processes to occur.

Further investigation of the supercurrent state of the SGS junction following the third anneal was performed, see Figure 2.25. At T = 60 mK the observed zero resistance state was established up to $I_s = 600$ nA at $V_G = 15.5$ V with a hysteretic IV response as reported previously attributed to the junction being underdamped. The characteristic voltage was measured to be of the order of 50 μV which is approximately $\Delta/5e$. Whether the junction is in the long or short limit is determined by the ratio of the junction length L to the superconducting coherence length, ξ, given by:

$$\xi = \sqrt{\frac{\hbar D}{\Delta}}, \tag{2.53}$$

where $D = v_F l_e/2$ is the diffusion constant of graphene and l_e is the elastic mean free path. At $V_G = 15.5$ V l_e was calculated to be 55 nm which corresponds to a coherence length $\xi = 260$ nm, placing the junction in the intermediate region between a long and short junction. As a result the Thouless energy, $E_{Th} = \hbar D/L^2$, a characteristic energy scale for diffusive processes, is at a similar energy to the superconducting gap.
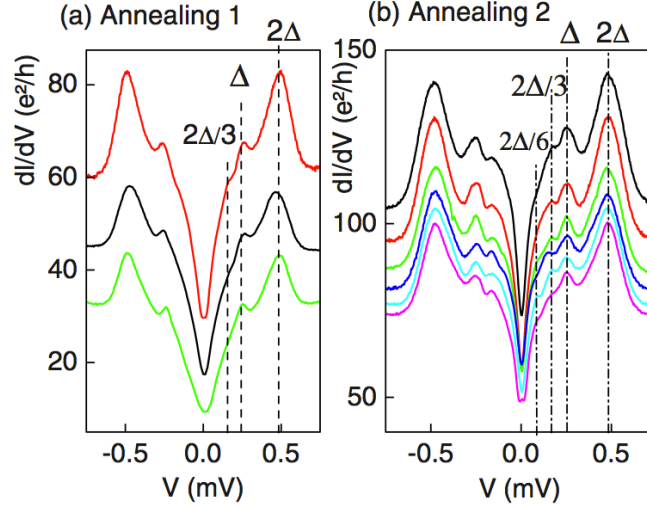
Figure 2.24: Evolution of MAR with annealing seen in the differential conductance curves as a function of bias voltage at 60 mK. Curves correspond to different gate voltage values with (from top to bottom) $V_G = -3, -8$ and 5 V in panel a) and $V_G = -24, -22, -18, -16, -15$ and -6 V in panel b). Up to 4 MAR peaks are seen after the annealing step 2.[37]

Measurement of I_s versus T also point to the device operating in the diffusive junction regime, displaying a trend that obeys the Kulik-Omelyanchuk law which describes short SNS junctions.

For a perfect interface a device with $L/\xi = 1.3$ is predicted to have a $V_c = 1.3\Delta/e$ which is ~ 6 times higher than what is measured experimentally. The authors stated that this was too large a discrepancy to be attributed to the interface resistance as such an explanation requires this resistance to be many times that of the graphene sheet. Instead they proposed that de-phasing fluctuators on and beneath the graphene are the main cause of the suppressed switching current. While such a mechanism will contribute to the suppression of I_s, they have not accounted for the increased contact resistance from damage to the graphene under the contact, as a result of the energetic metal deposition procedure used.

In the recent work of Popincuic *et al.* [43] graphene-NbTiN junctions were produced in SGS and SGN (one normal contact) configurations. Again the NbTiN ($T_c = 13$ K) was deposited using sputtering however the direct sputtering of this material onto the graphene resulted in contact resistance in the kilo-ohms range, which they
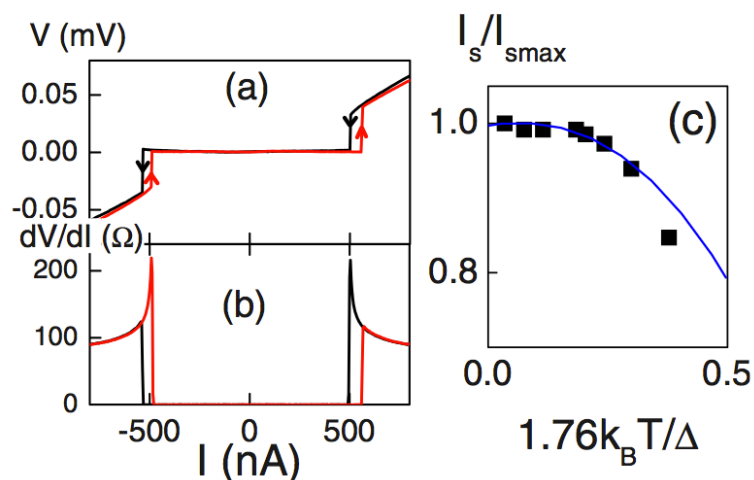
Figure 2.25: Full proximity effect after third annealing step. a) IV curve and b) $dV/dI(I)$ of the SGS junction taken at 60 mK, zero resistance state prevails at bias currents below switching current of 600 nA. c) Temperature dependence of the switching current (data points) fitted to a Kulik-Omelyanchuk law (continuous line) typical of a short SNS junction. $\Delta = 250$ μV is extracted from MAR features.[37]

attributed to damage to the underlying graphene by the bombardment of the energetic species during sputtering. To reduce this impact a 10 nm Ti adhesion layer was first deposited, using an electron beam evaporator, where the deposition energies are low (of the order of 1 eV). The sample was then transferred to the sputterer in air, which took 3 to 5 minutes so that the NbTiN could be deposited. To remove any oxide formed on the Ti during the transfer procedure, the Ti film was etched to 7 nm using an Ar RF plasma before sputtering. In another procedure the RF etch step was avoided by depositing Ti/Au first, where the Au acted as a capping layer to stop the formation of any oxide. The authors found that only upon increasing the thickness of the Ti, so that it was about 20 nm after RF plasma cleaning, could a supercurrent flow through their SGS junctions. This was attributed to the poor transparency of damaged graphene close to the contact, a conclusion supported by conductance measurements in the SGN devices. In Ti/Au/NbTiN devices only 2nm of Ti and 2.5 nm of Au were required to produce a working JJ, suggesting the cleaning step adversely affected the graphene. That being said they could not observe a supercurrent in these devices when $L > 280$ nm, which is relatively short, and even for a device with dimensions $L = 150$ nm and $W = 1.5$ μm at high carrier density, I_c did not exceed 4 nA at 50 mK.
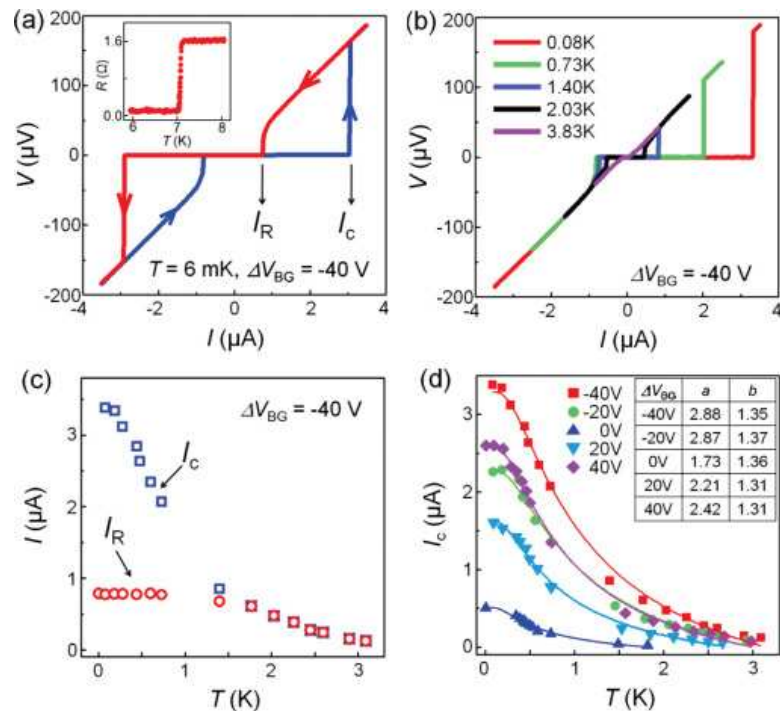
Figure 2.26: Transport measurements taken on a $Pb_{0.93}In_{0.07}$ based SGS junction. a) IV measurement at $V_G = -40$ V ($V_{Dirac} = -20$ V) with increasing and decreasing bias current. The critical (I_c) and retrapping (I_R) currents are indicated. Inset, resistance vs temperature curve of a single electrode showing $T_c = 7.0$ K. b) IV curves for five different temperatures. c) T dependencies of I_c and I_R. d) I_c as a function of temperature for different values of V_G. Solid lines are fits to a theoretical model. [40]

Jeong *et al.* produced SGS devices made using a PbIn alloy ($T_c = 7.0$ K) deposited via thermal evaporation [40]. Indium was included to reduce the granularity of the deposited Pd, which would otherwise reduce contact to the graphene sheet. The addition of a Ti adhesion layer was found to suppress the observation of low bias conductance enhancement, indicative of Andreev reflection processes and so PdIn was deposited directly. Transport measurements taken on one of these devices is shown in Figure 2.26. The IV curve in Figure 2.26(a) clearly shows the existence of a critical current at $T = 6$ mK, in addition to a pronounced re-trapping current, I_R. Subsequent IV measurements taken at various temperatures up to 3.83 K are shown in Figure 2.26(b), clearly showing a reduction in I_c with increasing temperature, while the normal state resistance in the high current regime remains unchanged. The extracted values of I_c and I_R are plotted as a function of temperature in Figure 2.26(c) which indicate that while I_c drops rapidly with increasing temperature, I_R remains constants until at $T > 1.5$ K $I_c = I_R$ and no IV hysteresis is observed. Most interestingly the temperature dependence of I_c at various gate voltages, see Figure 2.26(d), shows a very good fit to the theoretical prediction for a long diffusive JJ in the low temperature limit, as calculated by Dubos *et al.* [80], given by:

$$ eI_cR_N = aE_{TH} \left(1 - b \exp \left(\frac{-aE_{TH}}{3.2k_BT} \right) \right). \tag{2.54} $$

Here E_{TH} is the Thouless energy, R_N the normal state resistance, and a and b are fitting parameters. The theoretically predicted values of a and b are 10.8 and 1.30 respectively in a long junction where $E_{TH}/\Delta_{PbIn} \to 0$. The values of parameters a and b are found to be $a = 1.2 - 2.9$ and $b \sim 1.3$ with $E_{TH}/\Delta_{PbIn} = 0.083$. The reduced values of the fitting parameters are attributed in part to the junction being in the intermediate regime between the long- and short-junction limits.

The production of SGS devices with Nb or ReW contacts opens up the possibility of investigation of the interplay between superconductivity and exotic phenomenon that occur at high field, such as the QHE. Komatsu *et al.* produced SGS JJs with sputtered Nb contacts and ReW contacts with a thin (4 to 8 nm) Pd adhesion layer and capping layer (to be published in Phys. Rev. B [42]). Prior to the deposition of the contact material, the devices were annealing in vacuum at $100°$C for an hour. Out of the 12 samples produced, only 3 showed a full proximity effect at low temperature.
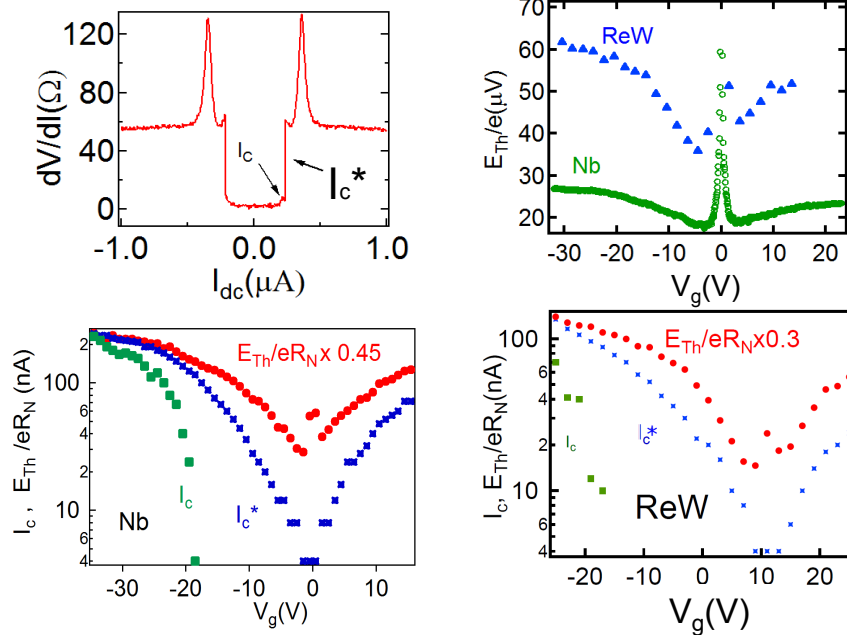
Figure 2.27: Comparison of switching current with Thouless energy. Upper left, two ways of defining switching current, I_c, the largest current for which the differential resistance dV/dI is zero, and I_c^*, the inflection point of the jump in dV/dI towards large resistance. Upper right, variations of the Thouless energy with V_G deduced using the sample resistance in the normal state for both ReW and Nb SGS junctions. The resistance of the Nb sample was measured at 1 K and the ReW sample at 55 mK at $I > I_c$. Bottom panels, comparison of I_c and I_c^* with E_{TH}/eR_N for the sample with Nb electrodes at 200 mK and ReW electrodes at 55 mK. [42]

The results presented by the authors were on a Nb device with dimensions $L = 1.2$ μm, $W = 12$ μm and a ReW device with $L = 0.7$ μm and $W = 2.6$ μm. Low temperature measurements were performed in a dilution refrigerator through low-pass filtered lines. Again the authors found that their junction to be operating in the diffusive regime with $L/\xi = 7$ and 5 for the Nb and ReW devices respectively, putting the devices in the long-junction limit.

Figure 2.27(a) shows the two possible ways of defining the switching current, I_c, which is the largest current at which $dI/dV = 0$, and I_c^*, which is the point of inflection when dI/dV jumps to a finite resistance. The evolution of E_{TH} with respect to V_G is shown in Figure 2.27(b) for both Nb and ReW contacted samples. According to the diffusive SNS theory as given by Equation 2.54, assuming the second term is

Figure 2.28: Temperature dependence of superconducting phenomenon in a ReW sample. Left, differential resistance curves for various temperatures ranging fro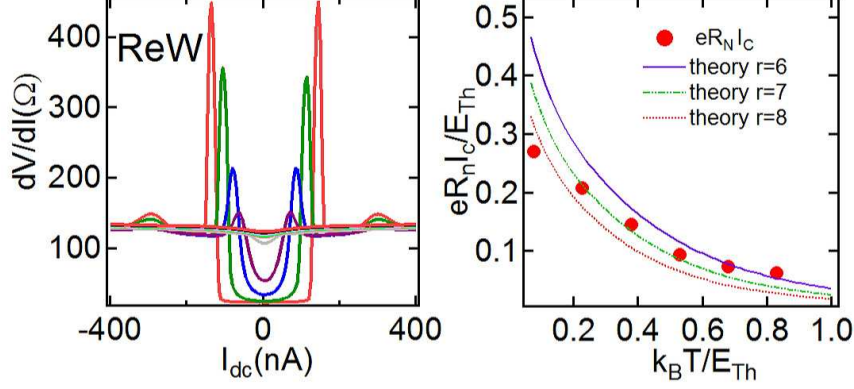m 100 mK to 800 mK. Right, comparison of the extracted critical currents as a function of temperature (solid points) and theoretical curves based on barriers with different ratios of contact resistance to graphene sheet resistance, r. Both the overall suppression of the critical current with respect to the Thouless energy at low temperature and the respective decay of I_c with temperature are accounted for assuming $r \sim 7$.[42]

small, there should be a constant factor, a, between I_c and E_{TH}/eR_N. It is clear from Figures 2.27(c) and 2.27(d) that this is not the case with enhanced suppression of I_c as $V_G \rightarrow V_{\text{Dirac}}$. The values of a giving the best fit to I_c are 0.45 and 0.3 for Nb and ReW respectively, compared to expected values of 9 and 8 at zero temperature. This difference is attributed to partial transmission at the SG interface, which can be experimentally shown by measuring I_c as a function of T, see Figure 2.28. The dependence of the characteristic voltage with respect to the temperature is shown to be in good agreement with the theory of a diffusive SNS junction developed by Hammer *et al.* [81]. The parameter $r = G_N/G_B$ where G_N is the conductance of the normal region and G_B is the conductance of the barrier with $r = 0$ for an ideal interface. A value of $r \sim 7$ best fits the data, which suggests that the interface resistance is seven times that of the graphene sheet resistance.

While interface transparency issues account for a large amount of the suppression of I_c it cannot explain the additional suppression of I_c close to the CNP. The mechanism proposed by Komatsu *et al.* [42] to explain this expression is specular Andreev reflection of Andreev pairs at the interface of charge puddles in the graphene chan-
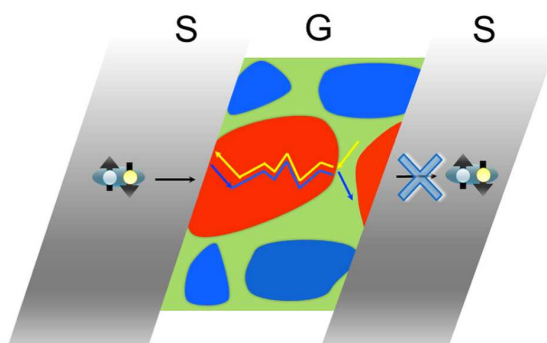
Figure 2.29: Schematic showing specular reflection of an Andreev pair at an n/0 junction leading to loss of counter propagation and large phase accumulation within an Andreev pair. The red region is electron doped, the blue region hole doped and the green region has zero doping. [42]

nel (see Figures 2.29 and 2.30). The puddles correspond to electron-rich (n-type) and hole-rich (p-type) regions with a spatial extent typically greater than 50 nm. Between n-type and p-type puddles are regions of zero doping which can be termed the 0 region. When V_G is close to the CNP, Andreev pairs (which are responsible for carrying the supercurrent across the junction) have a high likelihood of meeting an n/0 or p/0 boundary. At the boundary, a pair will undergo a specular reflection-like event, which acts to destroy the counter propagation of the Andreev pair, as the two electrons diffusing across the graphene undergo uncorrelated scattering events, which increase their relative phase difference. This results in a loss of phase coherence across the junction which acts to suppress the critical current. Charged puddles in graphene sheets have been observed directly by Martin *et al.* [82] via scanning single-electron transistor spectroscopy. An example of such a measurement for a graphene device is shown in Figure 2.31 which shows the spatial extent of the n- and p-type regions as well as the effective variation in charge density, which is approximately $\pm 10^{11}$ carriers cm^{-2}. As such, when the average carrier density in the graphene exceeds 10^{11} carriers cm^{-2} the puddles will be washed out resulting in an increase in the magnitude of I_c. Furthermore, the suppression of the supercurrent is expected to be largest in samples that are long because of the increased probability of an Andreev pair meeting a puddle interface. The supercurrent will also be suppressed when superconducting electrodes with large Δ are used because of the reduction in the superconducting coherence length, ξ.
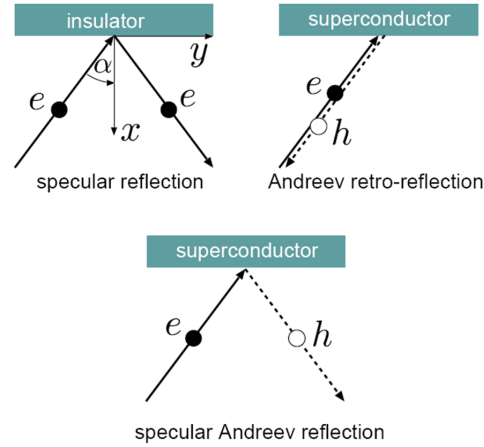
Figure 2.30: The panels at the top of the figure show the reflection processes that occur in a normal metal. These processes are specular reflection at a metal-insulator interface (left) and Andreev retro-reflection at the metal-superconductor interface (right). The panel at the bottom of the figure shows the counter-intuitive process known as specular Andreev reflection that can occur at a graphene-superconductor interface. Arrows indicate the direction of propagation of the charge carriers, electrons (*e*) and holes (*h*).[26]
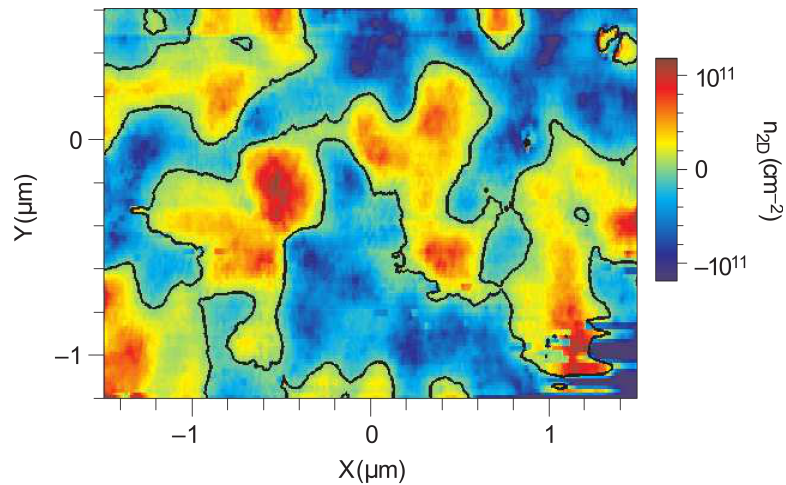
Figure 2.31: Colour map of the spatial density variations in the graphene flake extracted from surface potential measurements at high density and when the average carrier density is zero. The blue regions correspond to holes and the red regions to electrons. The black contour lines mark the zero density regions.[82]

CHAPTER 3

Experimental Methods

A wide array of experimental techniques have been utilised throughout this project, in both the fabrication of graphene devices and their subsequent characterisation. This chapter first outlines the fabrication methods used, starting with the production of graphene through mechanical exfoliation. This is followed by a description of the cleanroom based lithography techniques used to pattern exfoliated graphene flakes, as well as a discussion of the metal deposition methods used, which are thermal evaporation and DC magnetron sputtering. Further discussion of oxygen plasma etching, used to define graphene flakes into specific geometries, is discussed as well as the wire bonding and back gating of completed devices ready for measurement.

Device characterisation is then discussed outlining a typical electrical measurement set-up used in transport measurements. With a significant number of measurements being performed at low temperature, the use of a He flow cryostat is discussed with attention to the graphene specific procedures used. An outline of the Raman spectroscopy technique, which was used to gain further insight into the properties of the graphene samples produced, then follows.

3.1 Device Fabrication

3.1.1 Graphene Production

A wide array of graphene fabrication methods are now available to produce graphene ranging from bottom-up methods such as decomposition of SiC[83] or carbon[84], large area CVD[85] and chemical processing of graphite oxide[86] to top down methods such as unzipping carbon nanotubes[87]. The first true isolation of single layer graphene flakes however was achieved via the mechanical exfoliation (Scotch tape) method by Novoselov *et al.* [1; 61] and it is this method of production that is employed in this thesis. While unsuitable for commercial exploitation because of a low production yield and relatively small flake sizes few methods can rival the quality of graphene produced and so it is still ideal for studies into the fundamental properties of graphene.

The exfoliation method employed is as follows. A single large high quality graphite

flake[1] is placed in the centre of a 10×10 cm square of tape[2]. The tape is then folded on itself repeatedly ($\sim$15 times), each time separating the graphene flake until the entire tape is covered in graphite. Because of the weak van der Waals bonding between the constituent graphene layers in graphite[88] the graphene preferentially bonds to the tape allowing for the separation of individual layers. Following this the graphene is transferred to the substrate by placing the graphite covered side face down on top of the upper surface of the substrate, followed by lightly rubbing of the tape for 1 minute to ensure good adhesion. The tape is then very slowly removed from the substrate over the course of a minute to ensure the graphene flakes are not damaged during the procedure.

The substrates used in this study consist of highly doped silicon with a 300 nm oxide layer[3]. The highly doped silicon enables the substrate to be used as a global back gate for the device for use in EFE measurements. The 300 nm oxide performs two functions, acting as a gate dielectric and giving the graphene flakes sufficient contrast (through interference effects) that they can be observed using an optical microscope[18]. While a 100 nm oxide layer gives similar optical contrast and provides a greater change in carrier density for a given gate voltage, it was found to be easily damaged during wire bonding. This resulted in inoperable devices because of gate leakage. An array of optical alignment marks were also patterned on the substrates before graphene deposition to enable further patterning of devices as outlined in Section 3.1.2.

Following deposition, graphene flakes were identified by scanning across the entire sample surface with an optical microscope with a 20$\times$ objective lens. Upon identification of a possible graphene flake an optical image was taken so that the flake could be aligned in the CAD software. Differentiation of MLG, BLG and FLG was achieved using Raman spectroscopy as outlined in Section 3.2.3.

3.1.2 Lithographic Processing

Lithography utilises polymer resists which can have their solubility altered through bond breaking (or formation) by exposure to photons, known as optical lithography

---

[1]1.8−5.0 mm "Graphenium" flakes supplied by NGS Naturgraphit
[2]Blue surface protection tape supplied by Nitto
[3]N<100>As doped silicon ($\rho = 0.001$-0.005 Ωcm) supplied by IDB Technologies

(OL), or electrons, known as electron beam lithography (EBL). Through careful exposure of specific lateral regions of the resist, it can be selectively removed leaving resist free regions ready for metal deposition. An outline of a generic lithography procedure is shown in Figure 3.1.

In OL the resist is exposed to UV light through a pre-patterned chrome-on-glass (COG) mask using an optical mask aligner. This allows patterning of large areas in a short space of time, often tens of seconds once aligned, with a resolution of ~ 1 μm using our equipment. EBL affords the bespoke patterning of nanoscale features by controlling the path of a beam of electrons incident on the sample with an applied magnetic field. The trade-off is that EBL is time consuming, with the patterning of very large scale features requiring several hours of writing, as well as being considerably more expensive to perform.

A bilayer resist recipe is used in both OL and EBL steps to create an undercut in the resist profile as shown in Figure 3.1(d). The purpose of this is to ensure that there is good separation between the resist and the deposited metal. This aids lift-off procedure in which acetone is used to remove the resist and unwanted metal leaving the patterned features intact.

A false colour optical image showing a complete graphene device is shown in Figure 3.2. First the alignment marks (yellow) are patterned using optical lithography and thermal evaporation. The graphene flakes (magenta) are then deposited using mechanical exfoliation and located using an optical microscope. Next the bond pads and tracks (green) are patterned using EBL, as well as some additional alignment marks (red), which enable subsequent EBL steps to be performed with greater accuracy. Finally the graphene flakes are contacted with sputtered contacts (blue) also patterned using EBL. The specific recipes used during these procedures will now be discussed.

3.1.2.1 Optical Lithography

OL was used to pattern an array of optical markers onto the SiO_2 substrate before graphene deposition. These were used to identify the location of the flake and to align the first step EBL pattern on the device with an accuracy of a few micrometers. The optical markers had a spacing of 200 μm with every 5 markers in the x and y direction also featuring numbers corresponding to the co-ordinate of that marker. An optical
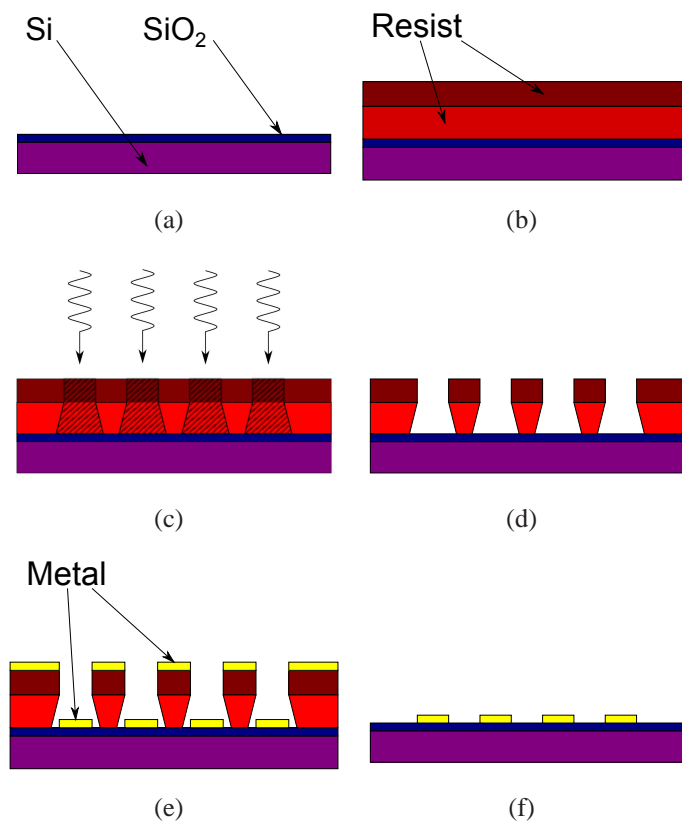
Figure 3.1: Schematic showing a typical lithography procedure. a) A clean substrate is prepared. b) Resist is then spun onto the substrate to obtain the required thickness and baked either on a hotplate or in a convection oven. c) The resist is then selectively exposed (shaded region) to either photons (OL) or electrons (EBL) followed by d) development in a solvent which removes exposed resist. e) Metal is deposited onto the sample and f) lift-off is performed in acetone which removes the resist and unwanted metal leaving the patterned metal features intact.
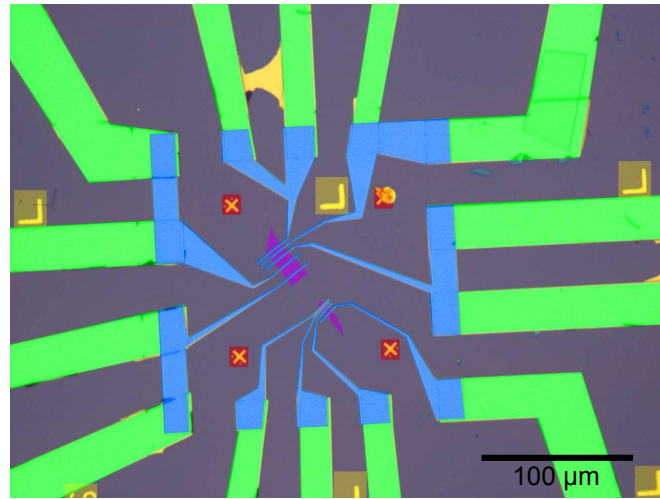
Figure 3.2: Optical image of a finished graphene device. Features are shown in false colour to aid discussion of the fabrication procedure (see main text).

image taken of one the numbered optical markers after graphene deposition is shown in Figure 3.3(a).

The OL procedure was as follows; the substrate was cleaned via sonication for 5 minutes first in acetone and then in isopropanol (IPA) followed by drying with N_2. The bottom resist layer (8% PMMA in anisole) was then deposited on the substrate and spun at 4000 RPM for 30 seconds before baking at 170 °C for 15 mins. The top resist (Shipley S1813) was then spun at 5000 RPM for 30 seconds and placed on a hot plate at 120 °C for 2 minutes.

A Karl Suss MJB3 photomask aligner was used to align the substrate beneath the COG mask before UV exposure for 8.7 seconds at a power of 3 mW/cm^2. The sample was then developed in Microposit MF-319 for 40 seconds, removing the exposed S1813, rinsed in de-ionised H_2O and dried in N_2. To remove the PMMA underlayer the sample was placed into a UV ozone cleaner for 15 minutes, developed in a 1:3 MIBK:IPA solution for 30 seconds, rinsed in IPA and dried in N_2. The sample was then ready for metal deposition which for the optical markers was 20 nm of Ti and 40 nm of Au deposited via thermal evaporation. The Ti was used as an adhesion layer with Au deposited as it gives good image contrast in the SEM during the EBL step.

Following this, lift-off was performed by placing the sample in acetone for several hours. As this step was performed before graphene deposition the sample was sub-

(a)   (b)
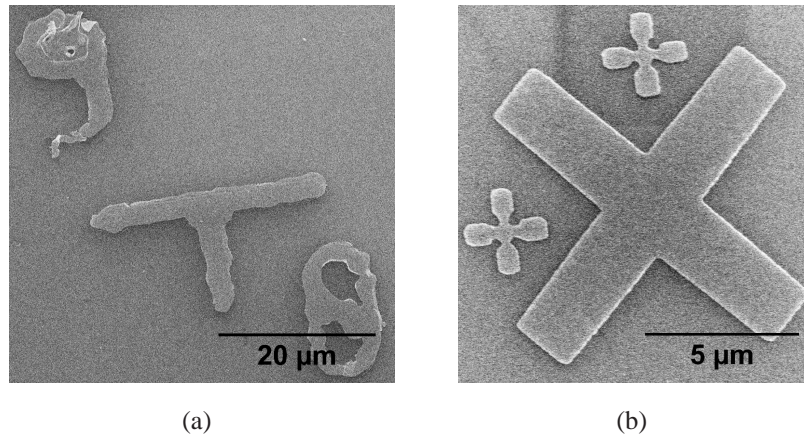
Figure 3.3: SEM images of a) an optical alignment marker and b) an electron beam lithography marker.

sequently cleaned using an O_2 plasma asher at 50 W for 2 minutes as this improved graphene adhesion manifesting as an increased yield of deposited flakes. Because of the low yield of graphene flakes produced via micromechanical cleavage large batches of $20-30$ 15 mm $\times$ 15 mm chips with optical alignment marks were produced at a time to improve the chance of finding suitable flakes in a given run.

3.1.2.2 Electron Beam Lithography

EBL was performed after graphene deposition, see Section 3.1.1, and so it was necessary to first remove tape residues from the sample by soaking in acetone for 5 minutes before repeating the procedure in IPA. Sonication was avoided as it can damage the graphene. 3% PMMA 495k in anisole was then spun on the sample at 2000 RPM for 20 seconds and 3000 RPM for 40 seconds. The sample was then baked at 170°C for 15 minutes. Originally a 45 minute bake time was used[89] but this was suspected to overbake the resist making removal difficult. 2% PMMA 950k in anisole was then spun on at 3000 RPM for 20 seconds and 5000 RPM for 40 seconds and again baked at 170°C for 15 minutes. The sample was then loaded into a Raith 50 system for EBL patterning.

EBL designs were produced using the AutoCAD software package. A schematic of a standard first step EBL design is shown in Figure 3.4. The design consisted of 16 bond pads (shown in red) with thick tracks heading towards the centre of the design

where the graphene flake is situated. Alignment of the EBL design to the optical alignment marker array is performed by aligning an optical image of the flake and alignment marks to a CAD design of the optical alignment markers[1]. The bond pads are 200×200 μm in size which is sufficient for wire bonding purposes. The large number of bond pads ensures that a sufficient number of contacts can be made on the graphene flake, despite the graphitic debris that is on the sample which can cause breaks in some of the tracks. Additional alignment marks are also patterned during the first EBL step, shown in magenta in the magnified region of Figure 3.4, which enable subsequent EBL patterns to be aligned on top of the sample with an accuracy of 10's of nanometres. A scanning electron microscope (SEM) image of an EBL alignment mark is shown in Figure 3.3(b) for clarity and consists of a large cross used for locating the features and smaller features which are used for the actual alignment. Typically the large bond pads were patterned first using a large beam current of 5 nA at 30 keV to shorten the necessary exposure time to ~ 20 minutes. The beam current was then reduced for the smaller features to 50 pA at 30 keV which gave sufficient resolution. A dose of 346 μA/cm^2 was used for patterning all features.

Following patterning the sample was developed in a solution of MIBK:IPA (1:3 concentration) for 90 seconds, before rinsing in IPA for 30 seconds and drying with N_2. It was then transported from the cleanroom to the sputter lab in a Desi-Vac^{TM} hand-pumped desiccator at a pressure of 0.5 atmospheres to avoid contamination. After sputtering the sample it was returned to the cleanroom for lift-off in acetone for several hours before rinsing with IPA and drying with N_2.

3.1.3 Metal Deposition Techniques

3.1.3.1 Thermal Evaporation

In thermal evaporation the metal to be deposited is placed in a resistive boat (usually made of tungsten), through which a large current is applied. Through Joule heating the boat reaches a sufficiently high temperature to melt the metal. The procedure is performed under vacuum to reduce the vapour pressure, allowing the metal to evaporate for re-deposition on a substrate, which is in line-of-sight of the boat.

---

[1]2 point align procedure using ALIGN command in AutoCAD
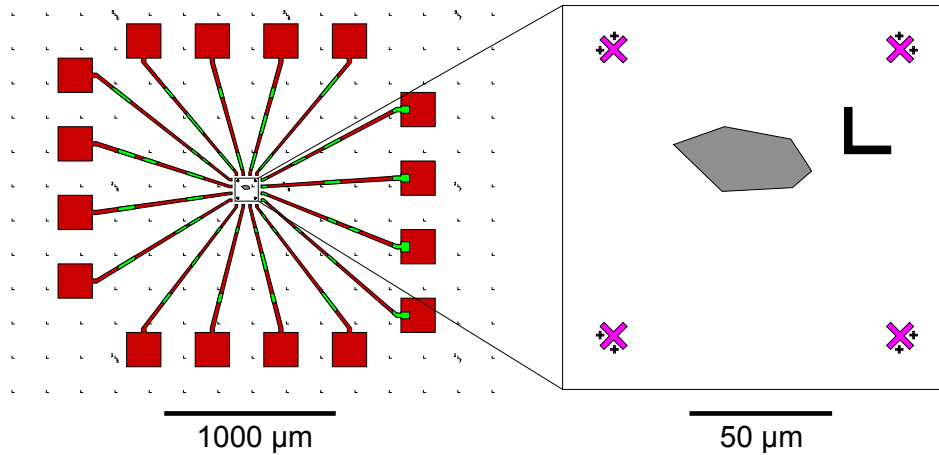
Figure 3.4: Schematic showing the first step EBL procedure in red and green. The magnified region (right) shows the EBL alignment marks patterned next to a graphene flake (shown in grey).

Thermal evaporation of Ti and Au was performed in an Edwards 306 evaporator, fitted with a turbo pump, enabling evaporation to be performed at a pressure of less than 10^{-6} mbar. Ti and Au were placed into separate boats allowing the growth of both materials without breaking vacuum. A current of approximately 30 A for Au and 40 A for Ti was passed through the boat, resulting in a growth rate of 0.1 nm/s which was measured with a crystal monitor.

An advantage of the thermal evaporation procedure was that greater than 10 samples could be evaporated at once, with the deposition completed in approximately 1 hour. The disadvantage was that the procedure often baked the resist making the subsequent lift-off procedure difficult. As a result thermal evaporation was generally used only for depositing optical alignment markers as, at this stage, the sample could be sonicated if necessary without damaging the graphene. Thermal evaporation is also only suitable for metals with a low melting temperature and so is not suitable for Nb.

3.1.3.2 Magnetron Sputtering

Magnetron sputtering has been used extensively in this work to deposit contact materials on graphene. A schematic of a typical magnetron set-up is shown in Figure

3.5. Sputtering was performed in an evacuated chamber in which a working gas is introduced. Argon (Ar) is frequently used as a result of its inert nature which ensures it will not react with the target material. In DC sputtering a large DC voltage is applied between the anode and the cathode which causes electrons at the cathode to be accelerated toward the anode because of the electric field. Once an electron has gained sufficient kinetic energy it can convert a neutral Ar atom into a positively charged ion, Ar^+, through collision via Townsend discharge[90]:

$$e^- + Ar \rightarrow 2e^- + Ar^+. \tag{3.1}$$

For charge conservation an additional electron is released, which can cause additional ionization. Concurrently, the Ar^+ ions are accelerated toward the cathode, which upon collision can eject secondary electrons, which also contribute to the process. This cascade of electron generation results in the breakdown of the gas and the measurement of a current between the cathode and the anode. Simultaneously, atoms from a target situated on the cathode are also ejected (sputtered) towards the substrate, because of the transfer of momentum that occurs from the impinging Ar^+ ions to the target material. As the process occurs in gas, the path of the ejected material is more diffusive than in vacuum (as in thermal evaporation). This necessitates the use of bilayer resist recipes when patterning, to avoid build up of material on the walls of the resist, which can make lift-off difficult.

By increasing the electrical potential between the cathode and the anode, as well as increasing the gas pressure, the rate of deposition during sputtering can be increased. Further enhancement can be achieved via housing a ring of powerful NdFeB bar magnets behind the target. Consequently the resultant stray field confines generated electrons to a circular "racetrack" above the target. The increased negative charge density in this region attracts the Ar^+ ions, increasing the plasma density, and hence the sputter rate.

Sputtering was performed in the Mjolnir sputter system, which consists of a vacuum chamber, 4 independent magnetron sources (2 magnetic targets, 2 non-magnetic) about 8 cm from the surface of a rotatable sample wheel capable of carrying 6 substrates. A turbo pumped load lock is used to place samples into the chamber, which enables a greater number of samples to be patterned in-between changing targets. The base pressure of the system measured with a mass-spectrometer is 10^{-9} Torr (with a

59
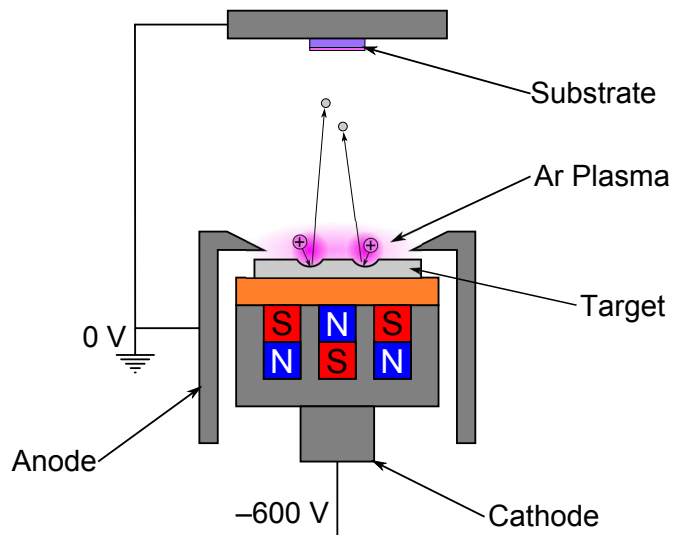
Figure 3.5: Schematic showing principle of DC magnetron sputtering.

Material	Current (mA)	Power (W)	Rate (Å/s)
Niobium (Nb)	300	22	1.2
Palladium (Pd)	70	92	1.4
Titanium (Ti)	100	31	0.4
Gold (Au)	70	27	2.7

Table 3.1: Table of sputtering parameters for grown materials.

partial pressure of water of 10^{-10} Torr), which is achieved through several stages of pumping. Firstly the chamber is pumped from atmosphere to a rough vacuum using a rotary pump, secondly the chamber is pumped using a cryopump which consists of a cold surface at $T \sim 10$ K upon which gases can condense. Further removal of water is achieved by using a Meissner trap, which consists of a coil of copper tubing through which liquid Nitrogen at $T = 77$ K is passed, condensing the water vapour away from the sample. The removal of water is particularly important to reduce the possibility of oxidising any deposited metals, which can adversely affect their properties. Optionally, gettering can be performed, whereby a reactive metal such as Fe or Ti is pre-sputtered to remove remnant oxygen in the system.

Sputtering was performed at an Ar pressure of 2.6 mTorr. The sputter parameters for the main materials deposited in this thesis are shown in Table 3.1. The sputter rates were calibrated by growing thin films for a given time and measuring the thickness of the films with x-ray scattering.

3.1.4 Oxygen Plasma Etching

Some of the devices produced required the shape of the graphene to be controlled. This was achieved by using an oxygen plasma to etch the graphene exposed through an etch mask. In this case the etch mask consisted of the standard bilayer PMMA recipe which was exposed using EBL in the regions in which the graphene was to be removed. An example of a PMMA etch mask on graphene prior to etching is shown in Figure 3.6(a). After depositing the etch mask, the sample was placed in an Emitech K1050X oxygen plasma asher and etched for 2 minutes at a power of 50 W, which was found to be sufficient to remove a single layer of graphene without removing all of the resist. Following etching, the resist is removed by soaking the sample in acetone for 5 minutes, followed by rinsing it with IPA. The result of an etch step is shown in Figure 3.6(b). A similar procedure was attempted on a bilayer sample, however it was found that the time to etch 2 layers of graphene was more than the time to remove the resist. As such, an alternative method would have to be employed for etching bilayers.
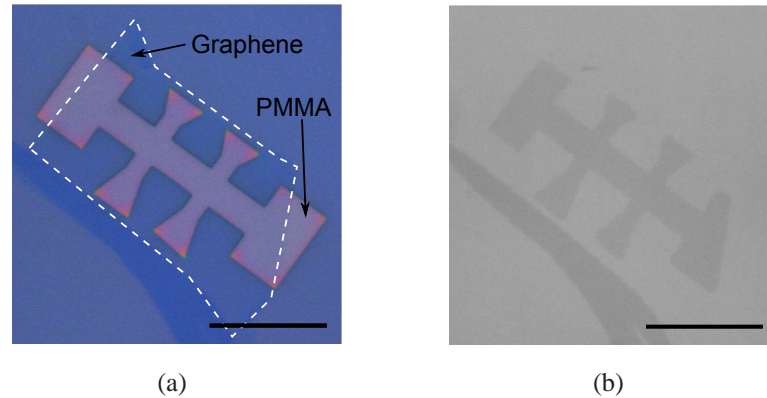
Figure 3.6: Optical images of graphene flake a) before and b) after an oxygen plasma etch. For clarity the graphene flake is outlined in a). Colour differences between a) and b) are an artifact of the microscope cameras used. Scale bar is 50 μm.

3.1.5 Wire Bonding and Back Gating

Upon completion of the lithography steps, the substrate is cut to fit a ceramic chip holder using a mechanical diamond scribe. An optical image of a completed device is shown in Figure 3.7. The device is secured to the chip carrier with conducting silver paint. For the substrate to be used as a global back gate, good electrical contact must be made to it. Initial attempts to form a good contact to the back gate involved removing the thermal oxide on the silicon with a diamond scribe, applying a small amount of indium and baking the sample on a hot plate in air at 200° C until the indium melted. Unfortunately, this procedure resulted in graphene devices with uncharacteristic gate responses. Instead the oxide was removed and a thin layer of silver paint applied to the etched area, which produced devices with satisfactory performance.

Contact between the bond pads on the device and the electrical contacts on the chip carrier was made using a Kulicke and Soffa Industries Model 4526 wire bonder. The wire bonder uses aluminium wire and makes a bond by applying an ultrasonic pulse via a metal wedge to the wire, causing it to melt and form an alloy with the material it is adhering to. The force applied to the wire, as well as the time and amplitude of the ultrasonic pulse, had to be minimised to avoid penetrating the oxide layer during bonding, as this caused the gate to leak during measurements. Moving from substrates with a 100 nm oxide layer to a 300 nm one also reduced the occurrence of gate leaks.
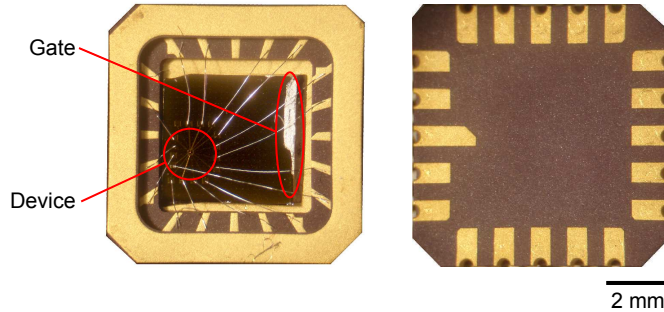
Figure 3.7: Optical image of device housed in a ceramic chip carrier. Contact is made to the chip carrier via pogo pins which push against the contacts on the back of the chip.

3.2   Device Characterisation

3.2.1   Electrical Measurements Set-up

A schematic of the electrical measurement set-up is shown in Figure 3.8. A 16 bit digital to analogue converter (DAC) supplied by National Instruments (NI-DAQ 6221) is fitted to a desktop computer and used to output a voltage to the device. The maximum input and output of the DAC is ± 10 V with a resolution of 320 µV. To improve the resolution of the output, a potential divider with a variable resistor is utilised to step down this voltage by 1000 times, giving a maximum output of ± 10 mV with a resolution of 320 nV which is sufficient for our measurements.

The drain current of the device is measured using a low noise current pre-amplifier (SR570), which converts the measured current to a voltage which is read back by the DAC. The amount of volts output per ampere measured can be set to accommodate the maximum range and measurement resolution of the DAC, mostly this was set to output 1 V for every 1 µA measured. Similarly the voltage across the device was measured using a low noise voltage current pre-amplifier (SR560). In the configuration shown, the SR560 outputs a voltage based on the difference of the two input voltages ($V_A - V_B$). This output can again be amplified up to 5×10^4 times before readback, although given the mV range voltages applied, amplification of 10^3 times was sufficient. Both amplifiers also provide internal RC filters to remove unwanted noise from the input signal before amplification; in this case a 1 kHz low-pass filter was selected to eliminate any high frequency noise. For QHE measurements an additional
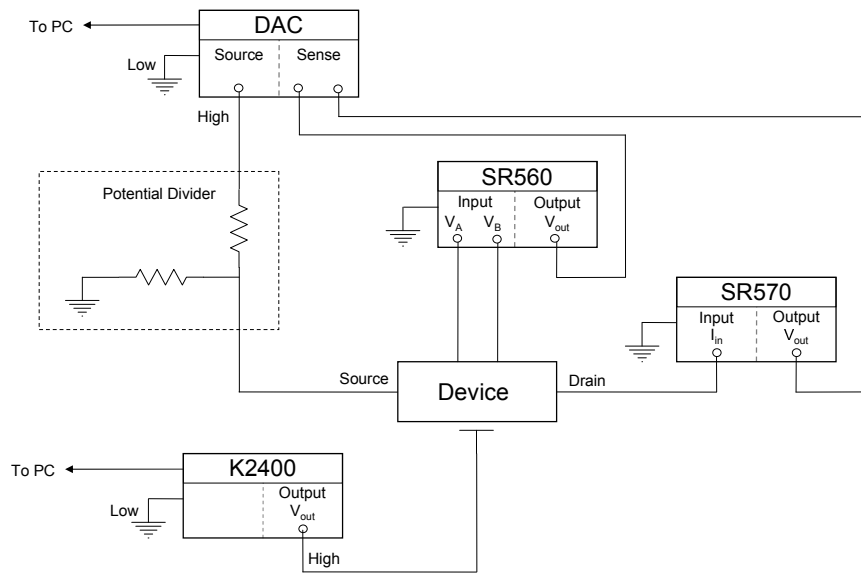
Figure 3.8: Schematic of electrical measurement set-up.

SR560 was connected to the device to measure the Hall voltage at the same time as the longitudinal voltage.

Previous efforts to back-gate bias carbon nanotubes in Leeds for EFE measurements used the DAC to bias the back gate[89]. For graphene measurements the maximum output of the DAC is insufficient as voltages up to ~ 70 V are required. As it has a maximum output of ± 200 V the Keithley 2400 Source Meter (K2400) was employed to bias the back gate. The high output was connected to the highly doped substrate of the device, while the low output was connected to the ground of the DAC card to ensure a common voltage reference point with the device. Communication between the desktop computer and the K2400 was performed using a GPIB interface card.

To reduce electrical noise, cabling between instruments consisted of shielded coaxial cable, terminated with BNC connectors. Connections to the device were made via a breakout box which allowed each line to the device to be independently grounded. This is necessary when changing contacts to avoid damaging the device. A cable from the DAC to the breakout box was connected at all times to ensure that it was not floating when connected to the device. Both pre-amplifiers were grounded to the DAC card through the outer shield of the coaxial cable, which in turn was grounded via the earth of the desktop computer.

Measurements to determine the resistance of the device consisted of taking multiple IV measurements as a function of gate voltage. In each case the source-drain voltage, V_{sd}, was commonly swept over a range of $\pm$ 1 mV, followed by stepping the back-gate voltage, V_{G}, by a set amount and repeating. Resistance was subsequently determined by fitting the multiple IV measurements to a linear function. All measurements were performed using custom LabVIEW^{TM} software[1] which controlled the DAC, K2400, temperature controller and the magnet power supply.

3.2.2 Cryogenic Measurements

Low temperature measurements were performed in an Oxford Instruments continuous flow He cryostat as depicted in Figure 3.9. A variable temperature insert (VTI) is housed inside the cryostat within which a sample can be placed. The VTI sits in a reservoir of He at 4.2 K, which is used both as a sample coolant source, as well

---

[1]Written by Dr Gavin Burnell
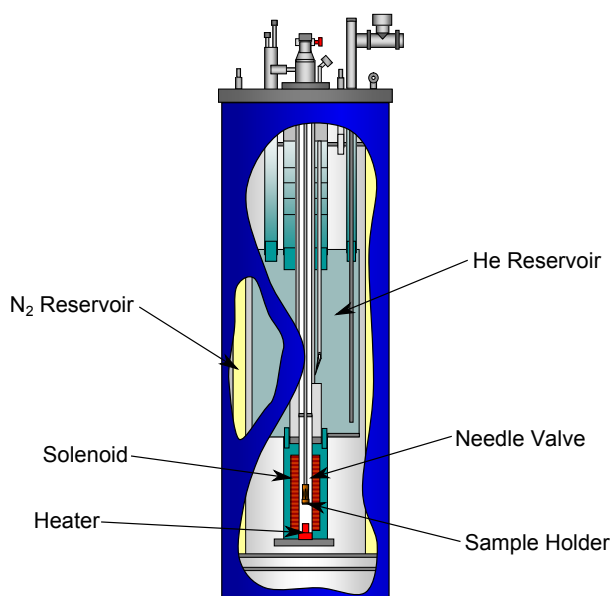
Figure 3.9: Schematic showing He flow cryostat apparatus. Modified with permission from Ref. [91].

as cooling the superconducting solenoid below its critical temperature. The solenoid can run in both variable and persistent modes up to fields of 8 T, controlled via the power supply. The entire outer jacket of the cryostat is filled with liquid nitrogen to thermally shield the He bath and experiment, from the ambient temperature of the laboratory. The VTI provides temperature control over the range 1.2 to 300 K by releasing gaseous helium into the VTI from the He reservoir via a needle valve and heating the inner chamber using a heater. The VTI is continuously pumped to below atmospheric pressure by an oil free scroll pump, lowering the vapour pressure inside, allowing for temperatures below 4.2 K to be achieved. Graphene devices have been shown to have extreme sensitivity to gaseous species in the experimental environment[12] and so an oil free pump is preferred to avoid contaminating the sample.

Temperature control is achieved through the use of an Oxford Instruments Intelligent Temperature Controller (ITC) which controls the heater power and He flow rate using a proportional integral derivative (PID) control loop for stability. Normally the ITC only controls the heater power to avoid flooding the chamber with too much He (which then has to be pumped away). The chamber temperature is monitored using a thermometer which is also connected to the ITC. During high field measurements

the temperature is controlled manually, as the measured chamber temperature can be incorrect as the thermometer has a magneto-response.

The sample is loaded into a custom built sample holder which sits at the bottom of the sample stick. The stick has a sliding seal at the top of the cryostat and allows the sample to be slowly lowered into the bottom of the cryostat. Lowering the sample too quickly into the base of the cryostat results in condensation forming on the device and so to avoid this the sample was pumped for several minutes at the top of the cryostat before slowly being moved down into the bore of the magnet. The temperature of the sample head is monitored using a Cernox thermometer connected to a Lakeshore 340 temperature controller. Cooling of the sample to its desired temperature was performed at a rate of less than 3 K per minute to ensure no damage was caused to the graphene as its thermal expansion coefficient is of opposite sign to that of the Si substrate[92].

Samples were warmed, where possible, to above 273 K before removal from the cryostat to avoid condensation of atmospheric water on the sample. This is of particular importance in graphene devices because of their exposed surfaces and sensitivity to surface species. This was achieved by closing off the pumping line and flooding the VTI with He gas followed by heating the chamber to above 273 K. This procedure was particularly time consuming and only performed on samples which showed good transport properties and thus warranting further measurement.

3.2.3 Raman Spectroscopy

Two Raman spectrometers were used during the course of this research, one a Renishaw 2000 equipped with a HeNe 633 nm laser, the other a Horiba-Jobin-Yvon LabRAM HR system which has a 532 nm Nd:YAG laser in addition to a HeNe laser. The operating principles of both system are similar yet the Horiba system has the capacity to control the sample temperature, map across the sample and bias the sample as well as having an additional excitation wavelength to use. For this reason the following discussion shall be limited to this system.

A schematic of the Raman apparatus is shown in Figure 3.10. Monochromatic light is emitted from the laser and passes through a line filter (LF), which lets only the primary laser wavelength through. The light then passes through an adjustable intensity filter (IF), which controls the intensity of the light that is incident on the sample, before
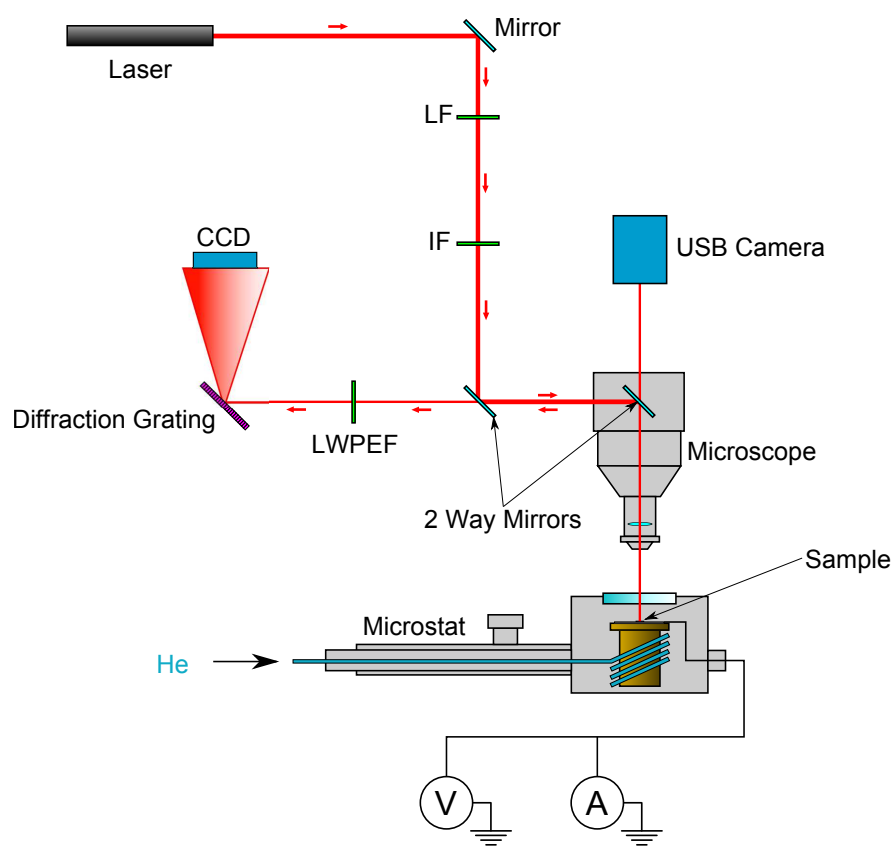
Figure 3.10: Schematic of the Raman spectrometry apparatus with line filter (LF), intensity filter (IF) and long wave pass edge filter (LWPEF) labelled.

reflecting off a 2 way mirror and entering the microscope. The microscope is used to focus on the sample, observed through a USB Camera using a white light source, and to ensure the laser spot is incident on the sample and is fitted with both $50\times$ and $20\times$ objective lenses. Most of the laser light elastically scatters (Rayleigh) off the sample, while some of the light is inelastically scattered as discussed previously. This reflected light then travels back through the microscope, reflects off the first mirror and through the second mirror. It then passes through a long wave pass edge filter, which blocks the Rayleigh scattered light, leaving only the inelastically scattered light. This light then diffracts off a diffraction grating, revealing the spectra which is detected using a charge coupled device (CCD). Observation of a wide range of scattered wavelengths can be achieved by rotating the diffraction grating and the fidelity of the measurement improved by using a finer diffraction grating (although this will increase the required measurement time).

The sample is housed in an Oxford Instruments Microstat-HiRes II continuous flow liquid helium cryostat. The sample sits on top of a copper sample stage which can be cooled to 4.2 K by flowing liquid helium through the coils that surround it. The sample chamber is sealed and pumped using a diffusion pump before cooling, which ensures condensation does not form on the observation window. The cryostat also has 10 electrical connections which enable the sample to be connected to the standard transport measurement apparatus. Coarse movement of the sample is achieved through the use of a manually controlled XY stage which moves the entire cryostat. Fine movement (step size ~ 0.05 μm) is achieved through the use of an automated motorised mirror, which deflects the beam prior to passing through the objective lens.

Simultaneous Raman and transport measurements are aided by a custom TCP/IP[1] server application that runs on the Raman PC. This application enables remote control of the diffraction grating, laser intensity and laser spot lateral position as well as the taking of Raman spectra.

---

[1] Transmission Control Protocol (TCP) and Internet Protocol (IP)

CHAPTER 4

Optimisation of Graphene Devices

It has been demonstrated extensively in the literature that graphene samples produced in the lab have a large degree of variability in their properties as a result of the presence of disorder. This disorder primarily consists of defects in the graphene sheet[93], interactions with the substrate (typically SiO_2)[19; 94] and unintentional doping of the graphene by surface adsorbents[95]. These sources of disorder manifest in transport measurements mainly as a shift in the position of the charge neutrality point in gate voltage and a sub optimal carrier mobility that is several orders of magnitude lower than theoretically predicted.

There have been a number of methodologies employed to overcome these issues. Trapped charges in SiO_2 [19] - and the rippling of graphene that occurs upon it[94] - when it is used as a substrate, have been shown to limit carrier mobility and induce hysteresis in electric field effect measurements. This has been overcome through either suspending the graphene over a channel[10; 24] or by placing it on single crystal h-BN[22; 96] which is defect free and well latticed matched to graphene while still acting as a dielectric, negating the difficulties associated with working on SiO_2. Unfortunately, the extremely challenging nature of these techniques renders them beyond the scope of this work.

Another major source of disorder that is universally observed in graphene devices produced in the lab, is the presence of unwanted contaminants on the surface of the graphene. As the surface of the graphene sheets are exposed to atmospheric conditions during processing species such as atmospheric water can be adsorbed onto the graphene surface. Remnant polymer resist remaining on the graphene device after lithographic processing can also prove to be particularly impervious to any removal attempts[97]. Whilst graphene devices prove surprisingly resilient to processing - despite being only one atom thick - many of the techniques that would be used to remove organic residues, such as UV ozone cleaning, oxygen plasma or chemical solvents, also act to destroy the graphene. One method that has been found to improve sample properties, without causing significant damage to the graphene, is high temperature annealing. A common method that has been employed, is annealing the device in a reactive Ar/H_2 atmosphere for 1 hour at 400 °C[98]. While this has been shown to remove PMMA residues, it is difficult to incorporate such a technique into a cryostat system and so exposure of the cleaned sample to ambient conditions before measuring cannot be avoided. An alternative method that has been explored that allows for *in-situ*

cleaning of the sample is current annealing[79], which is one of the methods that is explored in this chapter.

In this chapter two methods of annealing samples via Joule heating are employed. Firstly the use of a resistive platinum (Pt) heater lithographically patterned in close proximity to the graphene sheet is explored. By passing a large current through the heater a rise in temperature, monitored through a calibrated platinum strip thermometer which is patterned alongside the heater, is observed acting to remove dopants. In a second independent experiment current annealing is performed on a device following the methodology of Moser *et al.* [79]. In this method the graphene sheet itself is used as a resistive heater to remove any contaminants that might be present. Finally, to try and gain further insight into the current annealing procedure, time-resolved Raman spectroscopy is performed *in-situ* while current annealing a graphene device in vacuum.

4.1 On-chip Heaters

4.1.1 Heater Design and Thermometry Calibration

A technique to anneal graphene devices was developed using a resistive element, a schematic of which is shown in Figure 4.1, patterned in close proximity to the device (50 μm- 100 μm device-heater separation). The element consisted of a 1.3 mm long 3 μm wide track with 24 turns defined by EBL, into which 50 nm of Pt was deposited via sputtering. Pt was used as it has a relatively high electrical resistivity and melting point, $\rho = 1.1 \times 10^{-7}$ Ωm (at room temperature) and $T = 2041.5$ K, which is beneficial, given that the power output of the heater is proportional to its resistance and that it must operate at high temperature. Also Pt has a highly linear resistance versus temperature response, which makes it ideal for use as a thermometer[99], which allows us to also pattern a strip of Pt adjacent to the heater which enables more accurate monitoring of the local temperature. The heater was designed such that the meandering element was of higher resistance than the connecting leads, to ensure the majority of the heating occurred near the graphene sample rather than lost in the leads.

Before heating the device, the Pt strip thermometer was calibrated by measuring the resistance of the strip as a function of temperature as determined by a Cernox ther-
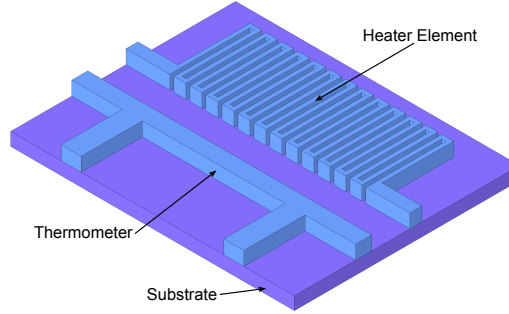
Figure 4.1: Schematic showing the design of a Pt resistive element heater and accompanying Pt thermometer on an Si/SiO$_2$ substrate. Pt thickness is 50 nm.

mometer situated in the sample holder. The sample was cooled in a He flow cryostat and the resistance of the Pt strip measured using a 4 terminal geometry so that the resistance of the leads could be ignored. In addition the Pt strip thermometer was biased using a 1 mV square wave to avoid self heating effects.

The change in resistance for a given material can be quantified in terms of its temperature coefficient of resistance α which is given by Equation 4.1:

$$R(T) = R(T_0)\left(1 + \alpha\Delta T\right),\tag{4.1}$$

where R is the resistance, T is temperature of the material, T_0 a reference temperature and $\Delta T = T - T_0$. The temperature coefficient of resistance for the Pt strip was found to be $\alpha = (3.46 \pm 0.01) \times 10^{-3}$ K^{-1} which is comparable to that found in the literature for bulk Pt, $\alpha_{\text{bulk}} = 3.8 \times 10^{-3}$ K^{-1} [100]. The positive value of α indicates that as the resistive heater gets hotter its resistance will also increase. Given that the resistive heater should conform to Joule's law, namely that the rate of heat dissipation is given by the power output of the heater $P = I^2R = V^2/R$, it was necessary to voltage bias the resistive heater to avoid increasing heat dissipation as the temperature of the heater element increases. A K2400 was used to bias the heater element as it enables large voltages (±210 V at ±105 mA) to be applied and so can provide appreciable heating power.
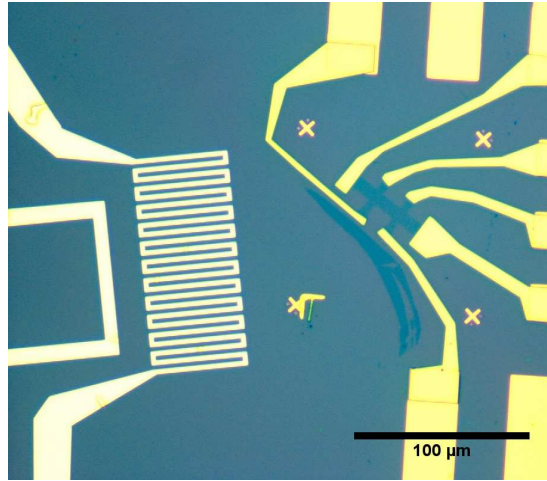
Figure 4.2: Optical image showing the Pt heater and thermometer in proximity to an etched graphene device.

4.1.2 Experimental Data

A preliminary effort to measure the QHE in a graphene sample was performed on the sample shown in Figure 4.2. The comparatively large graphene flake (~ 50 µm) was etched into a Hall bar and contacted with Pd(3nm)/Nb(90nm) contacts deposited via sputtering. A schematic of this sample is shown in Figure 4.3 with the contacts labelled to aid further discussion. The sample was cooled in a He flow cryostat to 1.4 K and measurements were made in a field of 8 T to try and observe the characteristic half integer anomalous Hall effect that has been uniquely observed in graphene. This was not observed and so the on-chip heater was utilised to try and improve the sample.

The EFE was measured between every permutation of contact pairs to determine the inhomogeneity across the device. The sample was then annealed using the on-chip heater before being cooled again and the EFE measurements repeated. This procedure was performed several times with different annealing profiles. The electrical measurement data taken before and after annealing between pairs of contacts is shown in Figures 4.5 and 4.6 with the thermometry data and corresponding applied heater powers recorded during annealing shown in Figure 4.4.

The individual EFE curves of the sample prior to annealing show significant differences to one another indicating that the sample is highly inhomogeneous. The curves mainly fall into one of three categories:
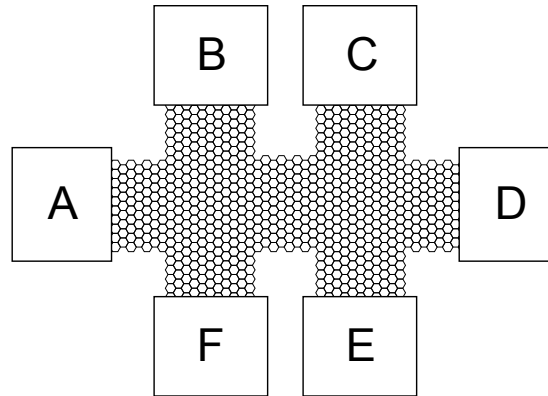
Figure 4.3: Contact layout of sample SG075.

- A highly symmetric curve with V_{Dirac} close to 0 V, for example between contacts A and B as shown in Figure 4.5(a).

- A curve with V_{Dirac} close to 0 V with lower conduction in the electron carrier regime, for example between contacts A-C , A-D and B-E as shown in Figures 4.5(b), 4.5(c) and 4.5(h) respectively.

- A highly anomalous response showing a very broad peak centred at a high V_{G} of around 40 V, for example between contacts C-E and D-E as shown in Figures 4.6(c) and 4.6(e) respectively.

The first instance shows the desired case as the un-shifted position of V_{Dirac} and equal mobilities of electrons and holes represent a sample free from contaminants that dope the sample and contribute to scattering. The second instance deviates from this ideal with asymmetry between electron and hole conduction. The likely cause for this is the unwanted presence of dopants on (or under) the graphene flake. Given that the peak is still close to 0 V it is likely that the current path between these contacts is primarily through regions consisting predominantly of clean graphene but there is an additional contribution from highly doped regions. The final case represents highly disordered graphene with a range of magnitudes of doping present resulting in a broad feature. As such the sample seems to generally be undoped closer to contact A with more doping induced disorder towards contact D. An additional point of note is that the measurements featuring contact F show a resistance which is an order of magnitude

(a) 1st Anneal

(b) 2nd Anneal

(c) 3rd Anneal

(d) 4th Anneal
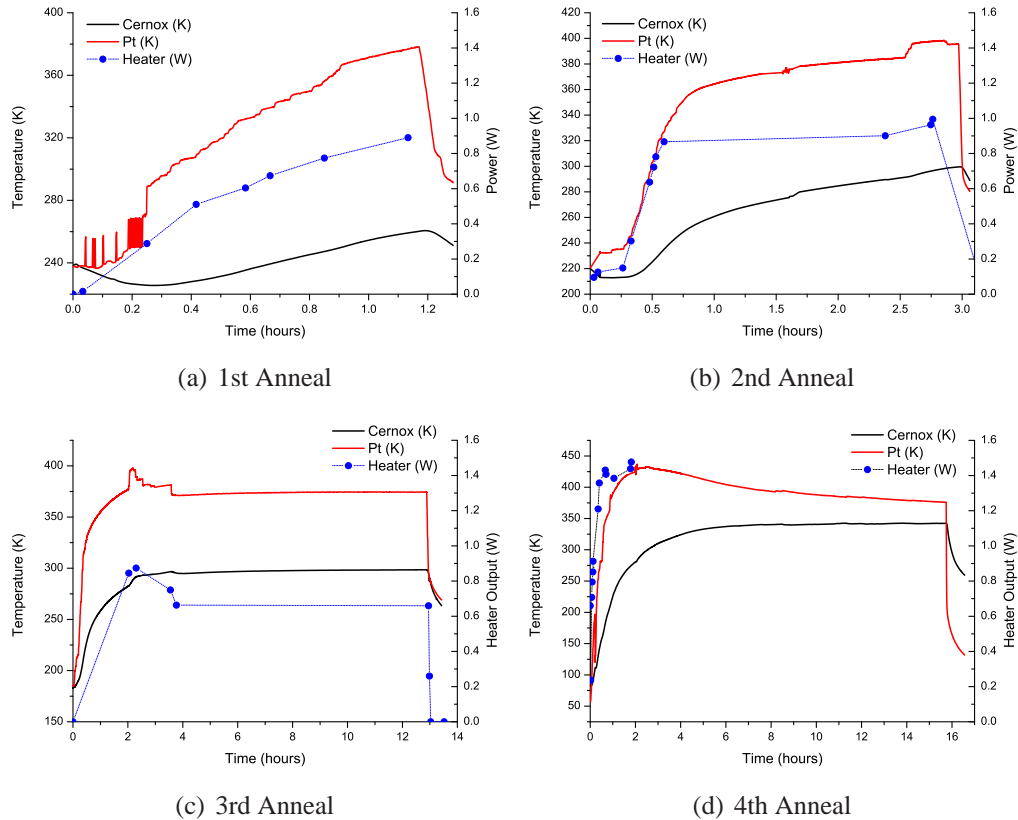
Figure 4.4: Thermometry readings from on-chip Pt strip (red) and sample holder Cernox (black) as a function of time during the sequential anneal procedures performed on sample SG075. The manually recorded power output of the Pt heater is also shown.

larger than other measurements; this is likely to be caused by a high contact resistance between contact F and the graphene sheet.

The annealing procedures performed after these measurements are shown in Figure 4.4. During the first anneal, shown in Figure 4.4(a), the heater output power was increased manually at irregular time intervals, while the temperature of both the on-chip Pt strip and the sample head Cernox was monitored. An output power of around 0.3 W was sufficient to cause an appreciable change in the temperature of the Pt strip (which should be indicative of the sample temperature), while the change in temperature of the Cernox was less pronounced. As such, it seems the on-chip heater provides highly localised heating (as was expected). This first annealing procedure lasted approximately 1.2 hours with a maximum heater output of 0.9 W reached during this time,

corresponding to a heater bias voltage of 44.5 V ($I = 20$ mA, $J = 1.3 \times 10^7$ A/cm^2). The maximum sample temperature reached was $T_{max} = 370$ K which is a temperature change of $\Delta T = 130$ K from the initial sample temperature. The maximum temperature the sample holder reached was $T_{max} = 260K (\Delta T = 20K)$. Upon removal of the heater bias voltage after 1.2 hours the temperature of the Pt strip is observed to rapidly decrease (> 80 K in 6 minutes). The temperature of the Cernox also decreases at this point although at a slower rate owing to it having more thermal mass. The additional annealing procedures performed can be summarised as follows:

- 2nd anneal - 3 hour anneal with a maximum sample temperature of 400 K reached, see Figure 4.4(b).

- 3rd anneal - 13 hour anneal with the sample at 370 K for 9 hours, see Figure 4.4(c).

- 4th anneal - 15 hour anneal with a maximum temperature of 430 K that decays to 375 K over 13 hours, see Figure 4.4(d).

During the fourth anneal at 15 hours the heater element was observed to fail. Between 2 and 15 hours the Pt strip temperature decreased slowly, corresponding to a reduction in the power output of the heater element. As the heater was voltage biased and the power output, $P = V^2/R$ it is likely that during this time the resistance of the heater was increasing as a result of gradual breakdown caused by the high current density, $J = 1.6 \times 10^7$ A/cm^2. Breakdown in Pt micro-heater elements used for gas sensing has been ascribed to stress caused by electromigration, as a result of using high current densities ($J \sim 10^5$ A/cm^2) [101–103]. While this may have contributed to the failure of the element, inspection of the damaged heater as shown in Figure 4.7 indicates that damage mainly occurred at the connecting points between the high resistance thin wire meander and the wider connecting leads. The changes in track width at these points will result in a non-uniform current density along the wire and generate a substantial thermal gradient. This could cause the wire to be strained and increases the chance of breakdown. It should also be noted that the heater temperature is likely to be much higher than the Pt thermometer indicates as they are in poor thermal contact via SiO$_2$ which has a low thermal conductivity ($\lambda \sim 1.3$ Wm $^{-1}$K $^{-1}$ for a 300 nm

film)[104], while the Pt contacts connected to the thermometer act as a heat sink, with the thermal conductivity of Pt $\lambda \sim 70$ Wm^{-1}K^{-1}.

Only a few permutations of contact pairs had EFE measurements taken between them after the first annealing step because of minimal observed shifts in V_{Dirac} or appreciable changes in other features. The contact pairs tested were A-B, A-D and C-D shown in Figures 4.5(a), 4.5(c) and 4.6(b). All measurements show a positive shift in position of the resistance maxima which would correlate with an increase (decrease) in p-type (n-type) dopant concentrations. The longer second anneal showed more pronounced feature changes and so all permutations of contact pairs were investigated. The broad EFE peak observed between C-D, C-E and D-E in Figures 4.6(b), 4.6(c) and 4.6(e) is replaced by a narrower peak around $V_{\text{G}} = 22$ V. This suggests that a significant change in the sample in this region has occurred, most likely the removal of a significant quantity of p-type dopant. The anneal has also impacted the EFE measurements that demonstrated an apparent low carrier mobility in the $V_{\text{G}} > V_{\text{Dirac}}$ electron conduction regime such as between contacts B and C in Figure 4.5(f). In this case the accompanying wide shoulder feature between $V_{\text{G}} = 20$ and 60 V has been replaced by an additional peak at $V_{\text{G}} = 30$ V. This double peak response is indicative of a p-p, p-n or n-n structure depending on the position of E_F (such structures have been observed extensively in the literature [105–111]). As such, the previously mentioned EFE shoulder erroneously attributed to low electron mobility was, in actuality, from a broad peak caused by a highly doped region of graphene on the device.

The shift in E_F from the applied gate voltage V_{G} in the undoped graphene case can be found using the following relation[112]:

$$E_F^{SLG} = \text{sign}(\Delta V_G)\hbar v_F \sqrt{\alpha\pi|\Delta V_G|}, \tag{4.2}$$

where ΔV_G is the applied gate voltage, v_F is the Fermi velocity in graphene and $\alpha = 7.2\times 10^{10}$ cm^{-2} V^{-1} is the gate capacitance for a 300 nm silicon oxide layer. If the sample is doped then E_F must be adjusted by a corresponding amount to coincide with the Dirac point. As the two peaks in Figure 4.5(f) occur at $V_{\text{G}} = +10$ V and $+30$ V this corresponds to a shift in E_F of -98 meV and -170 meV respectively.

The prolonged third anneal caused a further shift in all peak positions towards $V_{\text{G}} = 0$ V as a result of dopant removal. The other notable feature is a pronounced increase in the resistance in measurements involving contact F, see Figures 4.5(e), 4.6(a), 4.6(d),

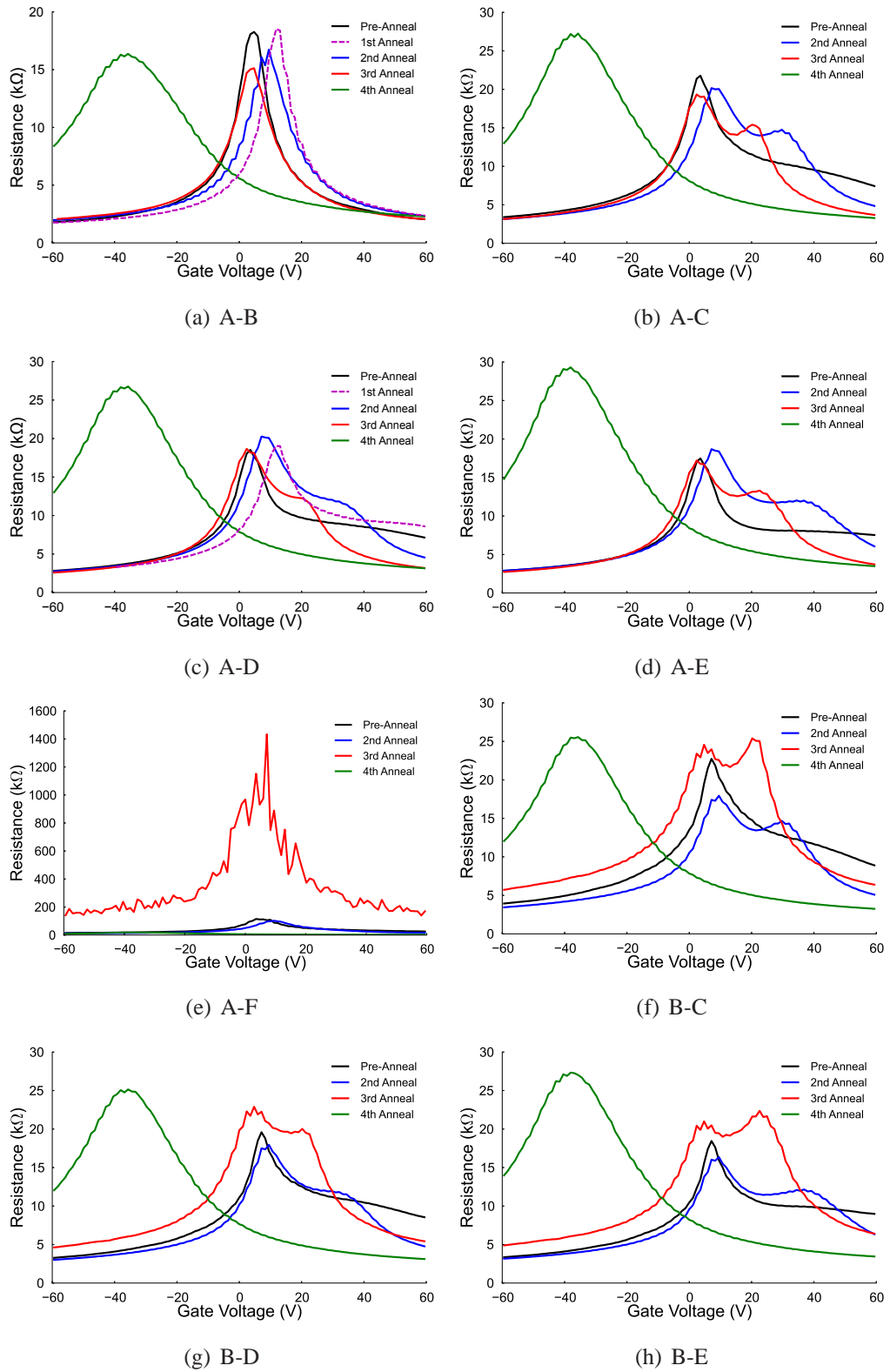**Figure 4.5:** SG075 Gate response before and after annealing

(a) B-F

(b) C-D
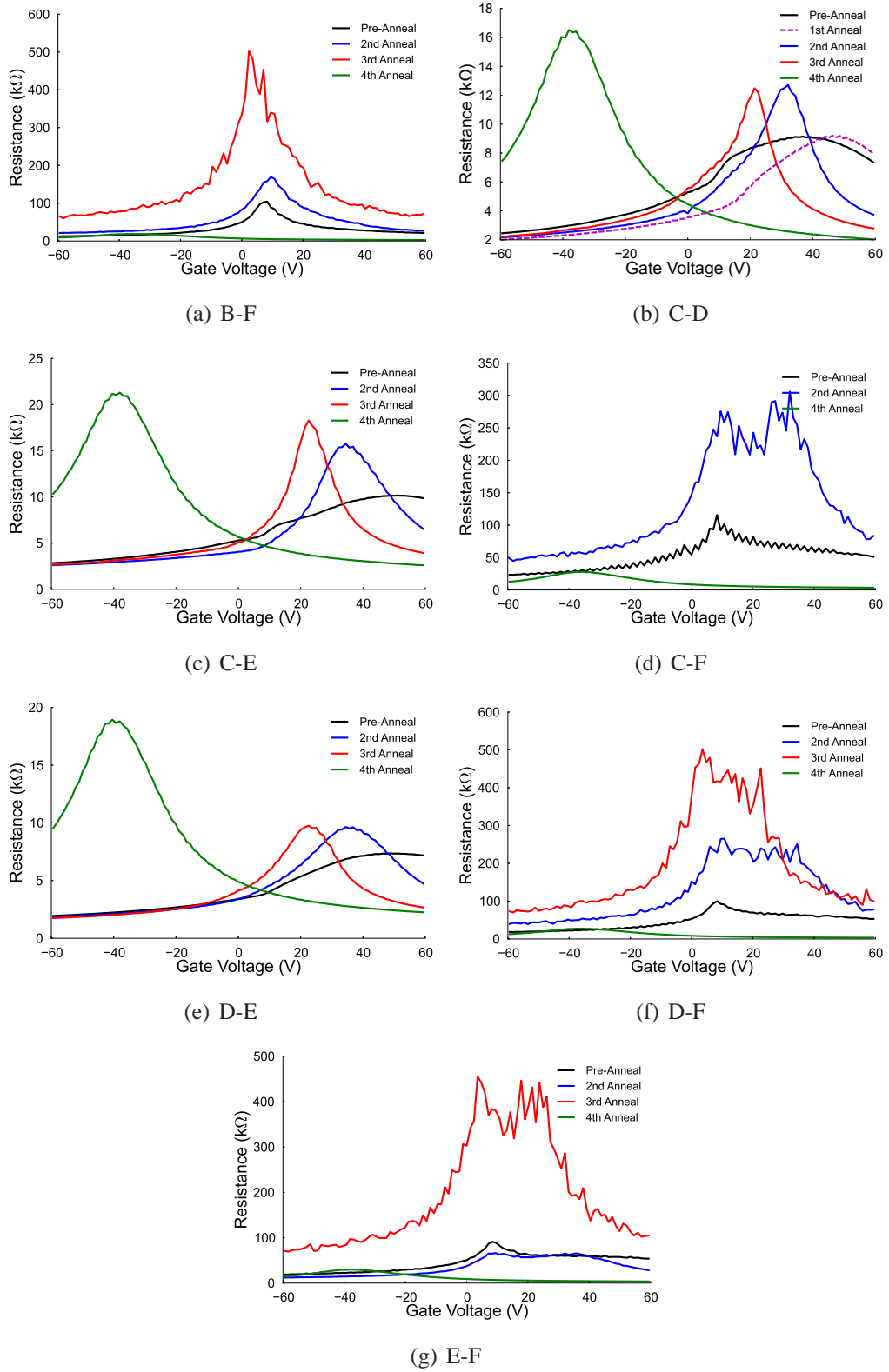
(c) C-E

(d) C-F

(e) D-E

(f) D-F

(g) E-F

Figure 4.6: SG075 Gate response before and after annealing (continued).

80

4.6(f) and 4.6(g), which could be caused either by damage to the graphene located near contact F or an increase in contact resistance as a result of annealing. From the optical image in Figure 4.2 it is apparent that the metallic electrode for contact F is ~ 10 µm from the heater at its nearest point and so it is possible that the heated electrode has caused preferential heating and damage of the graphene near contact F.

Following the fourth anneal procedure, in which the heater element was observed to fail, all EFE measurements between contact pairs show a single broad feature at V_G ~ -40 V. A possible cause for this is re-deposition of Pt from the destroyed heater onto the surface of the graphene device. A negative shift in V_{Dirac} of 40 V is equivalent to a positive shift in E_F of 0.2 eV based on Equation 4.2. This is theoretically plausible based on the interfacial dipole model proposed by Giovenetti *et al.* [113], which gives a similar shift for Pt when the distance between the dopant metal adatoms and graphene is less than 3 Å(refer to Figure 6.10). Furthermore, this result is in very good agreement with graphene samples covered by Pt deposited by MBE as produced by Pi *et al.* [114]. They observed a shift in V_{Dirac} proportional to the number of monolayers (ML) of transition metal covering the graphene. For Pt they found that 0.075 ML of Pt caused a shift in V_{Dirac} of -40 V, where 1 ML $\equiv 1.908 \times 10^{15}$ atoms/cm^2 (the areal density of primitive unit cells in graphene)[114], which would suggest a similar distribution of adatoms has been achieved via heater damage. The fractional change in carrier mobility after Pt deposition, $\mu/\mu_0 = 0.3$,where μ_0 and μ are the carrier mobilities before and after deposition, extracted using the Drude model from data in Figure 4.5(a), is also comparable to that observed by Pi *et al.* further supporting the premise of Pt adatom deposition via thermal evaporation.

4.2 Current Annealing

It was established by Moser *et al.* [79] that a graphene device could effectively be cleaned through the application of a large current density, $J \sim 10^8$ A cm^{-2}. The procedure consists of gradually increasing the voltage applied across two contacts on a graphene device and monitoring the change in current. When a sufficient voltage is reached, the current is seen to decrease, indicating an increase in the resistance of the device. This increase in resistance corresponds to a shifting of the Dirac point - and subsequently the resistance maximum, R_{max} - towards $V_G = 0$ as dopants (such as
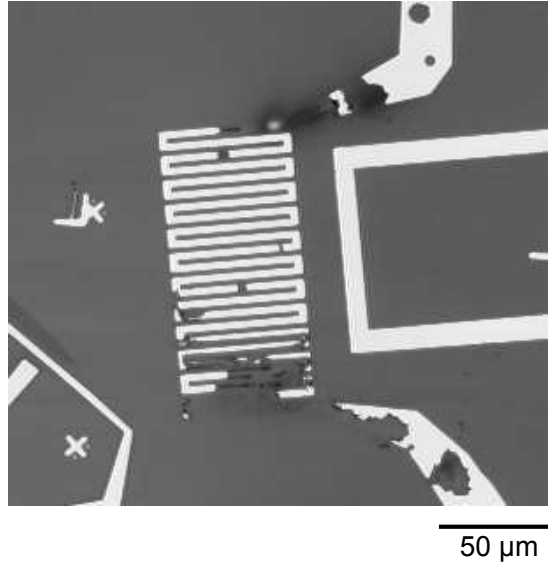
50 μm

Figure 4.7: Optical image of heater destroyed during annealing process.

PMMA residues) are removed through Joule heating. A lower limit on the temperature reached on the surface of the graphene during this process was established by Moser *et al.* [79] through the observation of the removal of CdSe nanoparticles with a melting temperature of 600°C from the surface of a graphene flake during this process.

The gate voltage dependence of resistance (gate voltage sweep) for a two terminal graphene device before and after a current annealing procedure is shown in Figure 4.8. The measurements were performed using the method outlined in Section 3.2.1 with 21 point IV measurements, with a maximum source-drain voltage of ± 10 mV, being taken at each applied gate voltage. The resistance values shown were calculated by performing linear fits to each individual IV measurement.

Current annealing was performed in a helium cryostat at $T = 292$ K with no gate voltage bias and $V_{\text{s-d}}$ supplied by a K2400 as it enables the application of voltages greater than the limit of the DAC (10 V). Over the course of 30 minutes $V_{\text{s-d}}$ was gradually increased from $0 \rightarrow 14$ V at which point the current through the device reached 4.1 mA and was observed to be decreasing with time. This equates to a current density $J = 1.6 \times 10^8$ A cm^{-2}, assuming a sheet width of 7.5 μm (as determined by optical measurements) and a graphene thickness of 0.35 nm [79], which is of similar order of magnitude required to anneal a graphene sample as stated by Moser *et al.* [79].
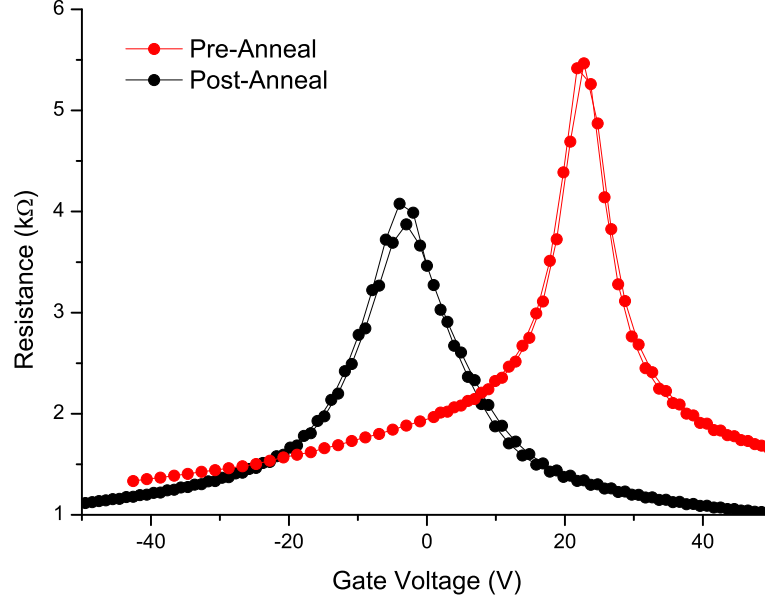
Figure 4.8: Resistance as a function of gate voltage before (red) and after (black) current annealing graphene sample SG084.

The reduction in current indicated that the resistance of the device was increasing with time and thus it was likely that the CNP was shifting towards $V_G = 0$ V because of the removal of dopants. A bias voltage of 14 V was maintained for 10 minutes, at which point the current was observed to be stable at 3.8 mA, indicating no further removal of dopants was occurring. A post-anneal gate voltage sweep was then performed using the aforementioned electrical measurement set-up.

To quantify the changes that occurred to the device after the current annealing procedure, the gate sweep curves shown in Figure 4.8 have been fitted using equation 4.3 taken from Ref. [115]:

$$\sigma(V_G) = \left\{ \begin{array}{ll} \mu_e c_g(V_G - V_{\mathrm{Dirac}}) + \sigma_{res} & V_G > V_{\mathrm{Dirac}} \\ -\mu_h c_g(V_G - V_{\mathrm{Dirac}}) + \sigma_{res} & V_G < V_{\mathrm{Dirac}} \end{array} \right\} \tag{4.3}$$

Where μ_e (μ_h) is the electron (hole) field-effect mobility, c_g is the gate capacitance per unit area, 1.15×10^{-4} F m^{-2}, V_G is the gate voltage, V_{Dirac} is the gate voltage at which the conductance minima is observed and σ_{res} is the residual conductivity associated with a given fit. This procedure gave $\mu_e = 0.24$ m^2 V^{-1}s^{-1} , $\mu_h = 0.21$ m^2 V^{-1}s^{-1}, $V_{\mathrm{Dirac}} = 22$ V, $\sigma_{res} = 1.6 \times 10^{-4}$ Ω^{-1}, $\mu_e/\mu_h = 1.1$, for the sample pre-anneal and $\mu_e =$

0.18 m^2 V^{-1} s^{-1} , $\mu_h = 0.22$ m^2 V^{-1} s^{-1}, $V_{\text{Dirac}} = -3.7$ V, $\sigma_{res} = 2.1 \times 10^{-4}$ Ω^{-1} and $\mu_e/\mu_h = 0.82$, post-anneal.

The pre-annealed sample clearly shows unintentional doping, as evident by the shifting of the CNP away from $V_G = 0$ V, as would be true in an intrinsic (undoped) graphene sample. The positive value of this shift indicates that there is a p-type (hole donor) dopant, which has reduced E_F in the graphene sample away from the Dirac point, which can subsequently only be recovered by filling states via the application of a positive gate voltage. The annealing procedure has shifted the CNP closer to 0 V which is most likely caused by the removal of the p-type dopant. The fact that the CNP is at -3.67 V rather than 0 V could result from the presence of an n-type dopant or electrostatic effects because of the high current densities achieved during the annealing process, as shown by Chui *et al.* [105]. A change in the field-effect mobility is also observed with a slight increase in μ_h compared to a moderate decrease in μ_e. A carrier dependent change in mobility has been observed caused by ionic dopants acting as long range scatterers [116], and so, such dopants are likely cause for the shift in the CNP in this sample.

A final characteristic of note is the reduction in R_{max} after current annealing. This could be caused by a reduction in the homogeneity of the surface doping of the graphene sheet, resulting in different areas of the device having different CNPs [117]. As this is a two terminal measurement, the observed reduction in resistance could also be from a reduction in the contact resistance.

4.3   *In-situ* Raman while Current Annealing

To gain further insight into the current annealing process, *in-situ* time resolved Raman spectroscopy was performed. This consisted of taking repeated Raman spectra over the $1250 - 2750$ cm^{-1} wavenumber range ,while increasing the current density passing through a 7.5 μm × 7.5 μm graphene sheet between two electrodes. The sample was housed in an Oxford Instruments microstat and pumped to below atmospheric pressure using the combination of a rotary pump and diffusion pump with the measurement performed at room temperature. The sample was held under vacuum for two reasons, firstly to stop oxidisation of the sample from heating in an oxygen rich atmosphere and

secondly to reduce the amount of water vapour which can cause hysteresis in the EFE measurements of graphene devices.

4.3.1 Hysteresis in EFE Measurements Performed in the Microstat

An example of such hysteresis in a different graphene sample is shown in Figure 4.9. In both cases V_G was first swept forward from an initial gate voltage of 0 V. Prior to placing the device under vacuum the device shows marked hysteresis, with a reduction in the resistance maximum at the CNP at $V_G \sim 17$ V on the back sweep compared to the forward sweep. Similar responses have been observed in graphene field effect transistors and have been attributed to both charged dopants on the surface of the graphene and trapped charges beneath the graphene[118; 119]. Following placing the sample under vacuum the hysteresis is almost completely eliminated as well as an observed shift of the CNP to a more negative value. The negative shift would imply the removal of a p-type dopant such as water vapour via the pumping process. This result suggests that all transport measurements should be performed under vacuum to avoid the effects of water vapour on the sample. A complimentary technique to avoid water contamination is to place the graphene flake on a hydrophobic substrate. This can be achieved with the standard Si/SiO$_2$ substrates by treating them with Hexamethyldisilazane (HMDS) prior to graphene deposition. This technique was pioneered by Lafkioti *et al.* [120], who observed an increase in carrier mobility and reduced shift of the CNP in devices treated with HMDS prior to graphene deposition. An attempt to replicate this result here at Leeds was unsuccessful, owing to difficulties in getting both photoresist and PMMA to adhere to the substrate following treatment.

4.3.2 Modification of the Graphene via Laser Irradiation

A He-Ne laser ($\lambda = 532$ nm) was used to illuminate the sample with a circular spot size of 9 μm^2. The maximum laser power at the sample is 30 mW, which was reduced to 0.3 mW through the use of an intensity filter, giving a laser power per unit area of 33 μW/μm^2. The intensity of the laser was reduced in order to minimize the possibility of laser induced damage to the graphene, as well as any laser induced heating. A nominal laser power was still required however, to ensure sufficient scattered light reaches the spectrometer during the individual spectra acquisition time, which was 30 seconds.
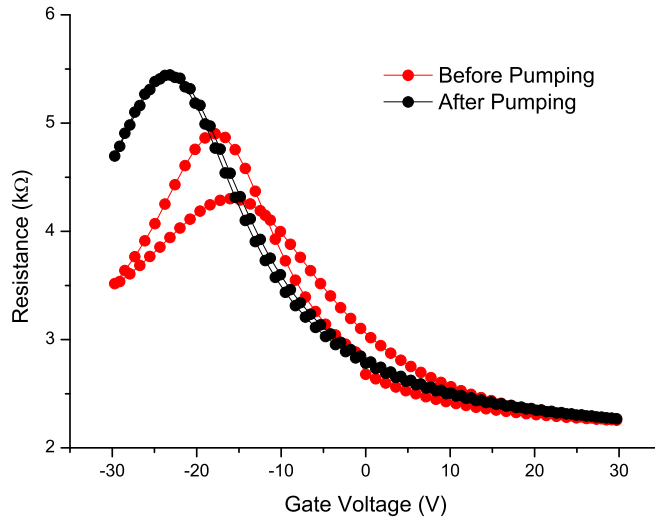
Figure 4.9: Room temperature gate sweeps taken on graphene sample (SG100) before and after pumping down the optical microstat showing signs of hysteresis because of ambient conditions.
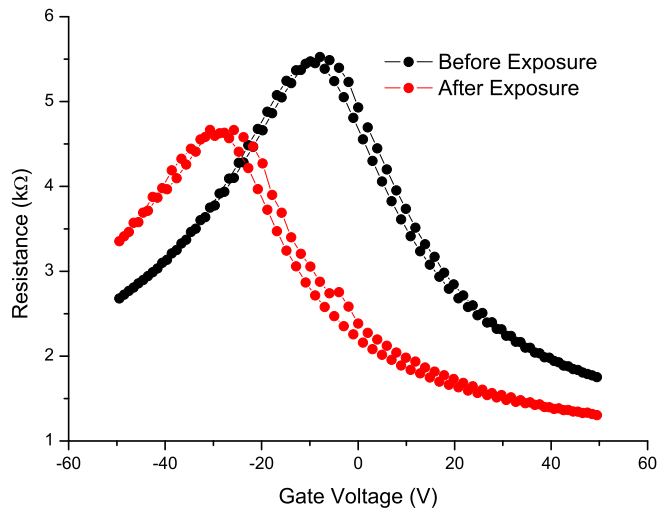

Figure 4.10: Room temperature gate sweeps taken on graphene sample (SG103) before and after raster scanning the sample with the laser over 8 hours.

Even at this reduced laser power there is evidence of appreciable modification to the graphene following prolonged laser exposure. An EFE measurement made on a graphene device before and after prolonged exposure to laser radiation is shown in Figure 4.10. The prolonged laser exposure was performed as part of a measurement of the photocurrent response of the device, which involved raster scanning the laser spot across the entire surface of the device over the course of 8 hours. The laser spot was directly on the graphene sheet for approximately a quarter of this time. The EFE measurement following this procedure shows a pronounced shift in the position of the CNP with V_{Dirac} moving from approximately -9 V to -29 V.

The prospect of modification of graphene through prolonged laser exposure was explored in detail by Krauss *et al.* [121]. In this case a laser with $\lambda = 488$ nm with a power of 1 mW was focussed on a graphene sample to a 500 nm diameter spot. This equates to a power per unit area of 5000 μW/μm^2, which is several order of magnitudes larger than the sample in Figure 4.10 was subjected to. The authors studied the change in Raman features, EFE measurements and the topography of their devices (using AFM) as a function of laser exposure time. In their EFE measurements they observed a gradual large shift in the position of the CNP, greater than 80 V after 8 hours exposure, with an accompanying reduction in carrier mobility. This was attributed to several phenomena inferred from Raman and AFM measurements.

At first the laser anneals the sample which acts to remove adsorbed dopants from the surface of the graphene. This manifested as a reduction in the height profile of the graphene measured using AFM after 5 minutes of laser exposure. Following this the measured height of the graphene rapidly increases to 2 nm after 30 minutes exposure. This was attributed to the cracking of sp^2 bonds by the laser, forming nano-crystalline graphene, which provide sites for molecular adsorbents to adhere to, increasing the observed height of the graphene. The formation of nano-crystalline graphene is supported by the evolution of the ratio of intensities in the Raman spectra, which follow the disorder trajectory for graphene $\rightarrow$ nano-crystalline graphene which was established by Ferrari *et al.* [63] (this is discussed in more detail in Section 6.4). Despite the reduced laser intensity and excitation energy used in our study, it is possible that bond breaking is occurring as a result of the long duration of scans, along with a poor vacuum, providing an abundance of possible adsorbates which are the source of the observed shift of the CNP in Figure 4.10.
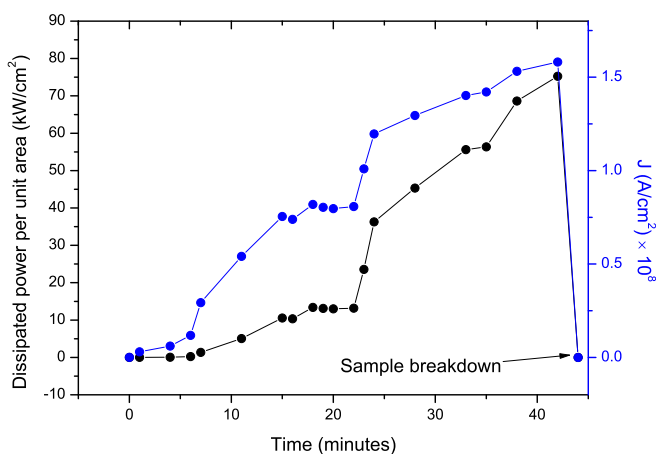
Figure 4.11: Graph showing the applied power and current density applied to the graphene sample as a function of time. The lines are guides for the eyes.

4.3.3   Annealing Procedure

The applied power to the device and subsequent current density across the device, J, during the current anneal procedure is shown as a function of time, t, in Figure 4.11. The current density was calculated using a graphene sheet cross sectional area of 7.5 μm × 0.35 nm. The sample was current biased and the power calculated using $P = I^2 R$, with R being the resistance of the device measured the instant the current had been increased. The current was increased manually until an appreciable increase in R was observed, which should correspond to a shifting of the position of the CNP towards $V_G = 0$ V because of the removal of dopants. At $t \sim 20$ minutes J is increased from $0.75 \rightarrow 1.25 \times 10^8$ A/cm^2 because of a minimal change in resistance being observed at the lower current density, coupled to no apparent change in the observed Raman spectra being continually taken during the procedure. After $t = 40$ minutes ($J \sim 1.5 \times 10^8$ A/cm^2) the device was observed to fail and no further current flow was possible through the device.

4.3.4   Discussion of Raman Measurements

A selection of Raman spectra during the anneal procedure are shown in Figure 4.12, each of which clearly shows a G and 2D peak, at around 1600 cm^{-1} and 2680 cm^{-1} respectively, characteristic of a graphene device. The individual spectra have been
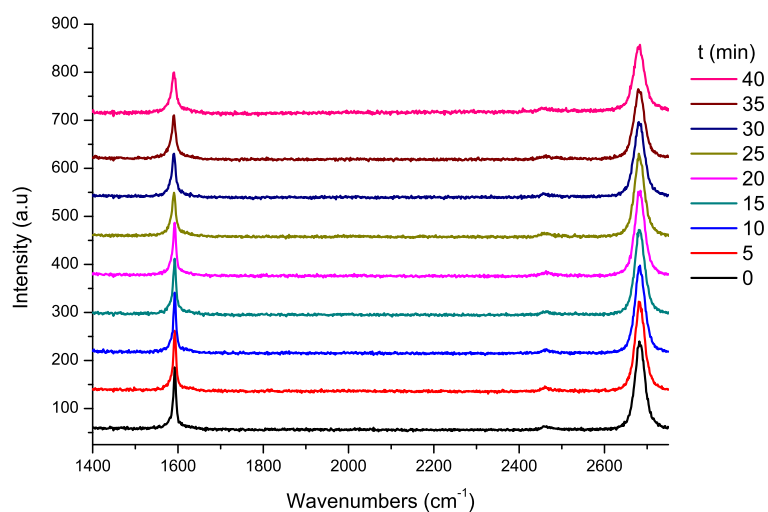
Figure 4.12: Individual Raman spectra taken at different times during the current annealing procedure. Curves have been shifted vertically 80 units from one another.

offset from one another in the y-axis for clarity. Some subtle changes are apparent, such as a reduction in the intensity of the G and 2D peak with time, as well as a clear broadening of the G peak. An additional observation is that the background signal also increases. This is expected as the heated graphene system should radiate energy, in accordance with Planck's law for a grey body[122]. To gain further insight into the change in the spectra during the anneal, it is necessary to fit the peaks and extract the fitting parameters.

The results of fitting the data to a Lorentzian, as given by Equation 2.31, using a least squares method, are shown for both the 2D peak and G peak in Figures 4.13(a) and 4.13(b) respectively. The band width of both peaks is observed to increase with time (and subsequently the current density), while the band energy (i.e. the position of the peak) is shown to decrease. Notably in the first 10 minutes of the measurement, when $J < 0.5 \times 10^8$ A/cm^2, there is no significant change to neither the width nor the position of the peaks. This not only suggests that J is too low to cause any appreciable change, it also indicates that heating from the laser is not a major contributor to any change in the Raman features in this study. A significant broadening of the Raman peaks and red shifting of their positions is observed after 20 minutes, when the current density was increased from $0.75 \rightarrow 1.25 \times 10^8$ A/cm^2.

Beyond 20 minutes the data for the G peak has a significant amount of error, both
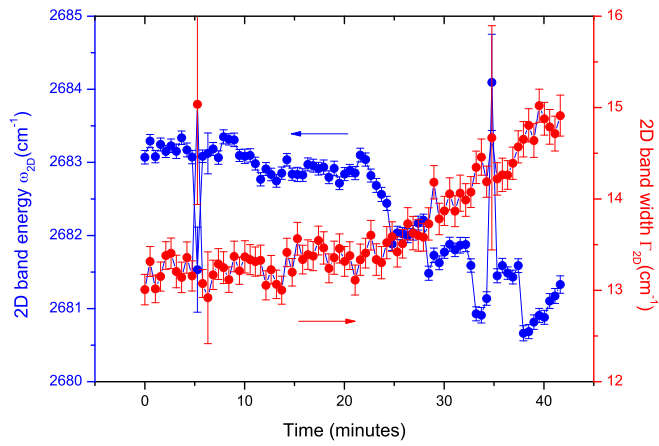
(a)
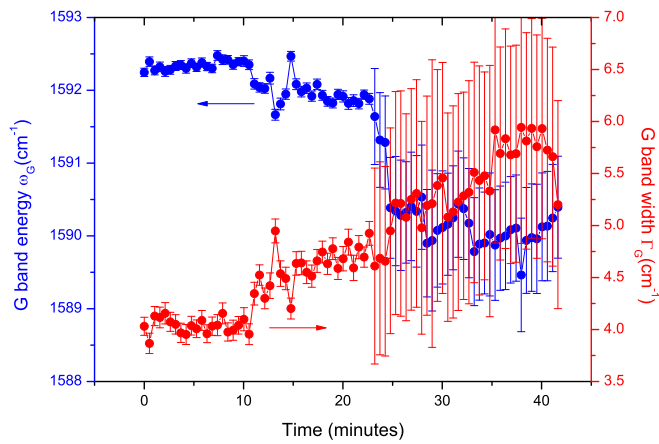
(b)

Figure 4.13: Raman band energy and width as a function of current anneal time. The 2D peak and G peak fitting parameters are shown in a) and b) respectively.

in position and width. This is caused by a reduction in peak intensity, coupled to the already narrow peak, making fitting difficult. To improve this measurement, either the integration time (the time taken to capture the spectra) would have to be increased or the diffraction grating constant (number of lines per unit length) increased, to ensure more points were sampled in the wave-number range $1589 \rightarrow 1593$ cm^{-1}. An increase in the integration time would result in a loss of resolution in time, although this would be acceptable given the time taken between changes in J. The use of a larger grating constant would be acceptable if only one peak was of interest as the wave-number range that can be sampled by the Raman's CCD at any given time would be reduced. Despite the large errors it is still clear that with increasing J an increase in G band width has been measured alongside a reduction in the band energy. There are a number of possible mechanisms that the observed changes could be attributed to and these will now be discussed.

There is the possibility that the high current density employed is damaging the graphene. A comprehensive study into how disorder influences the characteristic peaks of graphene was performed by Martins Ferreira *et al.* [123]. The authors studied how the band energy, ω, and band width, Γ, were dependent on the average distance between defects, L_D. It was observed that as disorder increased and $L_D \rightarrow 0$ that ω_G, Γ_G and Γ_{2D} increased while ω_{2D} decreased. The asymmetry of the responses of ω_G and ω_{2D} is counter to that observed in Figure 4.13, which suggests that an increase in disorder is not the main mechanism behind the evolution of the features with annealing time.

There have been several studies on Raman spectroscopy of graphene flakes at different temperatures, mainly focusing on the response of the G peak[122; 124; 125]. Calizo *et al.* [124; 125] performed Raman measurements not only on graphene flakes with varying number of layers, but also as a function of temperature. The temperature of the graphene was controlled by thermally anchoring the sample to a hot-cold source and Raman measurements were made with an excitation laser with $\lambda = 488$ nm. They observed that ω_G roughly decreased linearly with increasing temperature over the measured temperature range of $73 - 373$ K, stating that the following relation holds:

$$\omega_G = \omega_{G,0} + \chi T, \tag{4.4}$$

where $\omega_{G,0}$ is the frequency of the G mode when the temperature T is extrapolated to 0 K and χ is the first-order temperature coefficient. The applicability of this relationship to the current annealed sample is limited, as at high temperature a second-order term appears which the authors did not extract from their data. Despite this, it is possible to determine a lower bound estimate for the change in temperature of the annealed sample. From Figure 4.13(b) an overall change of $\Delta\omega_G \approx 2.3$ cm^{-1} is observed during the course of the anneal. Calizo *et al.* measured $\chi_G = (-0.016\pm0.002)$ cm^{-1}/K which according to Equation 4.4, gives a maximum temperature reached of 450 ± 20 K. Again this is a lower bound, as it does not include the second-order temperature coefficient and the error has been greatly underestimated, as a result of ignoring the large error in ω_G.

Another comparable study to this work is that of Berciaud *et al.* [122], in which they investigated the electron and optical phonon temperatures, T_{el} and T_{op} respectively, in electrically biased graphene. T_{el} was determined by measuring the spectral radiance of a graphene sample as a function of photon energy, which was then fitted to Planck's law for a grey body[122]. Owing to the nature of this measurement, it was only applicable to $T_{el} > 1100$ K. T_{op} was determined by comparing the relative intensities of the Stokes and anti-Stokes peaks which for the G peak can be written as:

$$\frac{I_{as}}{I} = C \exp\left(\frac{-\hbar\omega_G}{k_B T_{op}}\right), \tag{4.5}$$

where I_{as} and I are the intensities of the anti-Stokes and Stokes peaks respectively, $\hbar\omega_G$ is the G phonon energy (≈ 195 meV), k_B is the Boltzmann constant and C is a numerical factor.

The fact that such a relationship holds is intuitive, as the greater the temperature the higher the probability of an electron being in an excited state which leads to a greater chance of anti-Stokes scattering occurring. As a result, this mechanism is the likely source of the reduced intensity of the peaks observed with time/current density which was shown in Figure 4.12. Berciaud *et al.* also showed that at high temperature T_{el} and T_{op} are approximately equal and that overall the sample temperature is roughly proportional to $\sqrt{P}$. The maximum dissipated power during the current anneal we performed was ~ 80 kW/cm^2, which when compared to the data acquired by Berciaud *et al.* corresponds to a temperature $T = 640 \pm 120$ K, assuming similar sample conditions.

Berciaud *et al.* also measured ω_G and Γ_G as a function of calculated temperature, observing a general trend of a reduction in ω_G and an increase in Γ_G with temperature. This is in agreement with our data assuming the sample is getting hotter with anneal time. The increase in Γ_G indicates a reduced phonon lifetime, which is expected at higher temperatures. The maximum change in fitting parameters from the initial state at $T = 300$ K in our measurements are $\Delta\omega_G \approx -2.3$ and $\Delta\Gamma_G \approx 1.8$. Again these correspond to a similar change in T according to the data presented by Berciaud *et al.* although an accurate comparison is difficult because of the large error bars in their data and poor fit to the theoretical model. A final point of merit is that much higher values of P were achieved in their samples compared to ours. One possible explanation is that their vacuum is much better and so their samples are less susceptible to oxidation. This is likely as our chamber was not continuously pumped during the course of the experiment. Another possible explanation is a high contact resistance at the graphene-metal interface, which would increase the amount of power dissipated at the contact. Having this interface as the point of failure seems likely as a Raman signal is still observed, even after electrical contact has been lost. Furthermore, under inspection of the sample after the anneal with an optical microscope, there was no evidence of damage to the graphene sheet within the channel between the contacts.

Another possible contributor to the change in ω_G and Γ_G is a change in doping during the anneal. Figures 4.14(a) and 4.14(b) show why Γ_G and ω_G respectively vary with the position of E_F. Γ_G is dependent on the G phonon lifetime and so if another decay pathway is available to the phonon, its lifetime will be reduced, which will result in a broadening of the peak. When E_F is close to the Dirac point, a G phonon can decay into an electron-hole pair as shown in the Feynmann diagram in Figure 4.14(a). However, when the magnitude of the E_F is greater than the phonon energy $\hbar\omega_G$, this decay pathway is forbidden as a result of the Pauli exclusion principle. This results in an longer phonon lifetime and a reduction in Γ_G. In the process shown in Figure 4.14(b), G phonons with energy greater than $|E_F|$ can undergo a renormalization process, where an electron-hole pair is generated and then recombined to form another G phonon, which alters the frequency of the phonon. Again, as the carrier density increases this process is available only to the higher energy G phonons.

The effect of doping was investigated prior to annealing the sample by measuring ω_G and Γ_G as a function of V_G. The results of this measurement are shown in Figure

(a)

(b)
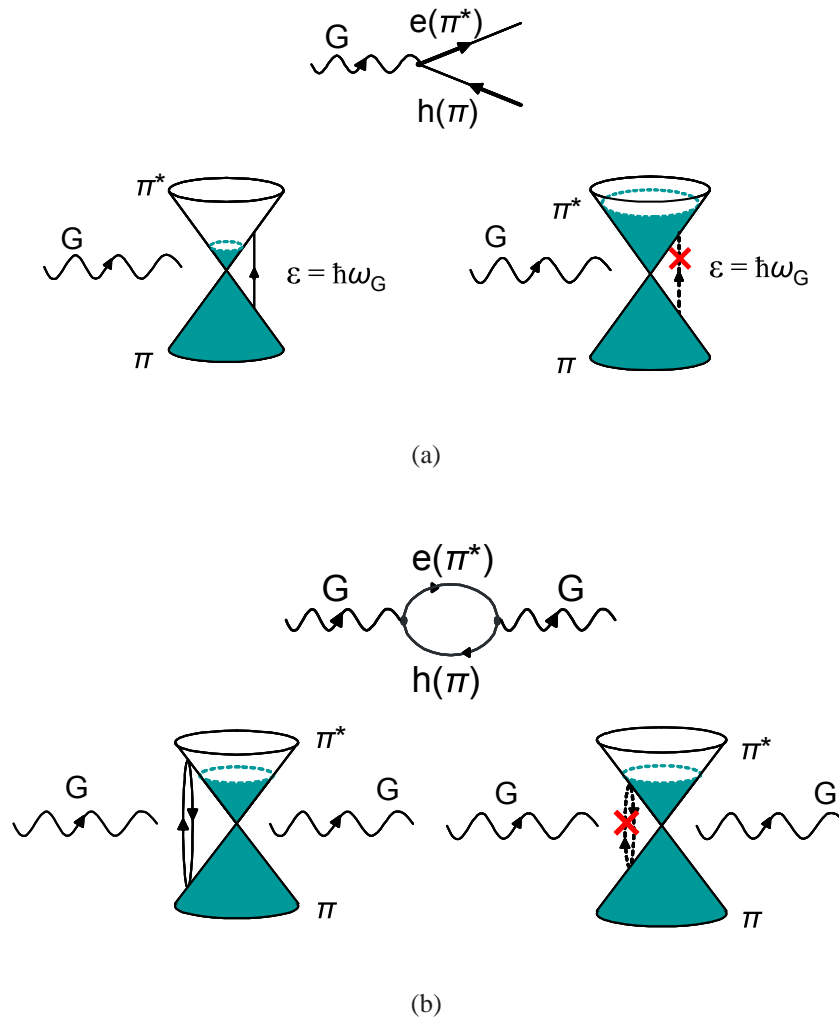
Figure 4.14: a) G band damping and b) G band renormalisation processes in n-type graphene. In a) a Feynmann diagram is shown for the electron-phonon coupling applicable to the G phonon. When E_F is close to the Dirac point the G phonon is broadened from an electron-hole pair decay process. At high carrier densities this process is forbidden by the Pauli exclusion principle. In b) the Feynmann diagram shows the renormalisation process that is mediated by the G-phonon interacting with virtual electron-hole pairs. Only electron-hole pairs with energy greater than $2|E_F|$ are allowed. Taken from Ref. [65].
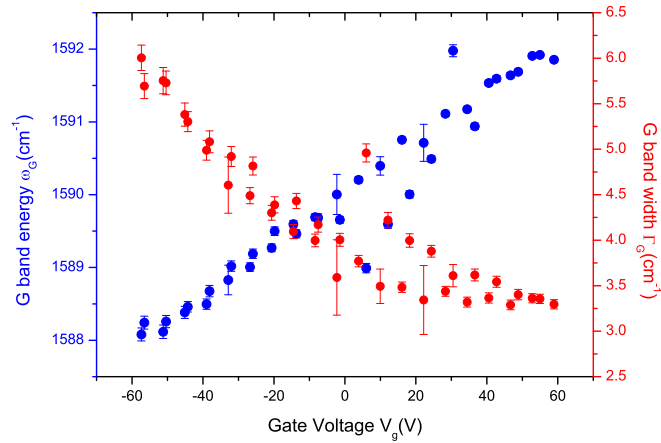
(a)
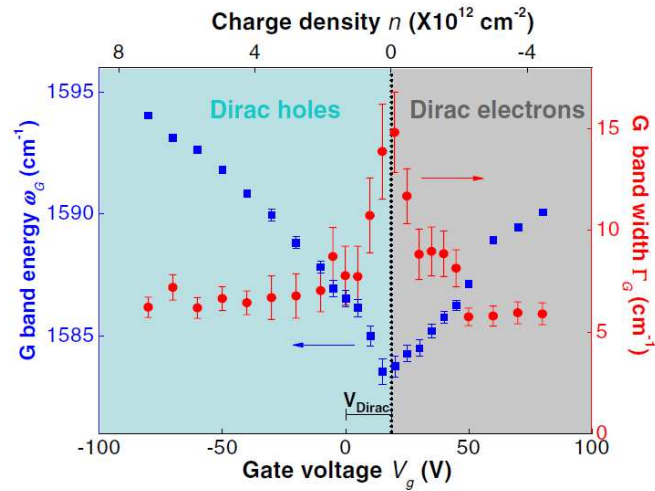
(b)

Figure 4.15: G band energy and G band width extracted from the Raman spectra of SLG devices as a function of applied gate voltage. a) Measurement performed on sample SG103 at a laser wavelength of 532 nm at $T = 4$ K. b) Measurement performed by Yan *et al.* at a laser wavelength of 488 nm at $T = 10$ K with the Dirac point indicated by a dotted line[65].

4.15(a) alongside a similar measurement performed by Yan *et al.* [65] in Figure 4.15(b) for comparison. In the work of Yan *et al.* V_{G} was varied from -100 V to $+100$ V with ω_G and Γ_G extracted from the Raman data at each value of V_{G}. A central peak in the value of Γ_G coincided with a dip in the value of ω_G. From the symmetry of the data, this point was identified as the CNP with $V_{\mathrm{Dirac}} = 18 \pm 2$ V. Away from this point, as the carrier density increases, an increase (decrease) in values of ω_G (Γ_G) are measured. Raman measurements were performed on our device and V_{G} was varied from -60 to $+60$ V. No peak or corresponding dip was observed in either parameter, which indicates that V_{Dirac} lies outside the measured range of V_{G}. Given that ω_G (Γ_G) increases (decreases) for more positive values of V_{G} it is clear that $V_{\mathrm{Dirac}} < -60$ V because of a large amount of n-type doping. In this case the result of dopant removal during annealing would be a decrease in ω_G and increase in Γ_G as the $V_{\mathrm{Dirac}} \rightarrow 0$ V. Given the same trend is observed because of an increase in temperature, the two effects are indistinguishable during the annealing procedure.

4.4   Conclusion

It has been demonstrated that a Pt heater which is capable of sustaining temperatures of around 400 K, can be patterned using EBL and sputter deposition. Furthermore, the temperature can be successfully monitored using an accompanying thermometer patterned in proximity to the heater. While the heater was shown to fail when dissipating a power of 1.4 W, 1 W would have been sufficient to reach a comparable temperature of 400 K without causing damage to the heater. The annealing performed using the heater removed a p-type dopant from a large etched graphene flake, which had an otherwise inhomogeneous doping profile across its surface. Despite this it was not possible to remove all dopants resulting in a graphene n-n, p-n or p-p junction type EFE response, as a consequence of having two regions with different doping. While metallic strips have been previously used to apply a thermal gradient to a graphene device[126], this is the first time such a heater has been used to remove dopants. Large graphene devices, as investigated here, often have inhomogeneous doping and so further efforts to measure phenomena such as the quantum Hall effect (as presented in Chapter 5) concentrated on devices with smaller dimensions.

An unintended consequence of the destruction of a heater element during an anneal procedure was the *in-situ* deposition of Pt adatoms on a graphene flake. This has been demonstrated to give comparable results to adatoms deposited using MBE. The deposition of transition metal clusters on graphene has been utilised by others to investigate scattering mechanisms in graphene [85; 127; 128], as well as other phenomena such as induced superconductivity[28]. The method to deposit such clusters as presented here, could prove beneficial when undertaking *in-situ* measurements in instruments where placing a metal deposition source is not possible. Additional investigation would have to be undertaken to understand how reproducible the deposition is and what sort of control can be gained over the areal density of the transition metal deposited.

Modification of the properties of graphene samples has also been achieved through the application of high current densities with $J \sim 10^8$ A/cm^2. A shift in the position of the CNP towards $V_G = 0$ V indicated a removal of dopant adsorbents, while a reduction in resistance was attributed to a possible improvement in the transparency of the contact interface. While current annealing does show promise in terms of removing dopants from the surface of the sample, it does have its limitations, such as an apparent reduction in the electron mobility. The technique is also likely to only remove dopants on the upper surface of the graphene sheet, as those trapped between the graphene and the substrate cannot escape because of the impermeability of graphene [129]. Current annealing is also high risk, as the graphene sample can easily be ruptured if too large a voltage is applied.

To gain further insight into the current annealing process, another device was simultaneously probed, using a developed time-resolved Raman spectroscopy technique. During a current anneal procedure an increase in bandwidth and decrease in band energy of both the 2D and G Raman modes was observed with increasing anneal time / current density. This was understood to be resulting from an increase in temperature of the graphene sheet of several 100 K, as well as a possible contribution from the removal of dopants. This dopant level dependency of Raman features was also investigated through varying the doping in the graphene via the electric field effect.

CHAPTER 5

Characterisation of Graphene via Transport Measurements

While many experimental techniques have been utilised to probe the properties of graphene, it was through transport measurements that the initial excitement about the material was generated. The demonstration of the QHE showed directly that the material was truly two dimensional. Furthermore, by showing a unique half integer quantisation of the Hall conductivity, it was identified that the low energy excitations in graphene, are in fact massless Dirac fermions, analogous to those in high energy physics only in a condensed matter system.

In this chapter the results of EFE measurements made on single layer graphene samples are shown. The mobility and minimum conductance are extracted and compared to similar devices on SiO_2 substrates presented in the literature indicating their high quality. Following this, the results of QHE measurements on both etched and unetched devices performed at low temperature are shown confirming the single layered nature of the samples. Finally, an extensive QHE measurement is performed on an unetched device at a range of field values in which Shubnikov de-Haas oscillations (SdHOs) are observed. From these oscillations a direct measurement of the carrier density is achieved, comparing favourably to that determined by the parallel plate capacitor model. The Berry's phase is also extracted, confirming that monolayer graphene has a geometric phase of π. These measurements confirm that monolayer graphene samples of sufficient quality have been successfully produced at Leeds.

5.1 Mobility and Conductance Minima in a High Quality Sample

Figure 5.1 shows a field effect measurement performed on a typical graphene device, using a four point probe geometry performed at $T = 1.4$ K, in a continuous flow He cryostat with no applied field. The data has been plotted in terms of resistance and conductance in Figures 5.1(a) and 5.1(b) respectively. The resistance in this case is in fact the square resistance given by:

$$R_\square = \frac{W}{L}R, \tag{5.1}$$

where R is the measured resistance and W and L are the width and length respectively, of the graphene sheet between the electrodes. Similarly the conductance is given by

the inverse of $R_\square$ and hence incorporates the same geometrical pre-factor.

The maximum in resistance equating to the position of the CNP occurs at $V_\mathrm{G} = 0.5 \pm 0.5$ V, which according to Equation 2.8, corresponds to a very low p-type impurity contribution of $4 \pm 4 \times 10^{10}$ carriers cm^{-2}. Many prepared samples had CNPs at $V_\mathrm{G} \approx 20$ V because of a large contribution from a p-type dopant. It is believed that the reduced dopant concentration in this sample resulted from the particular care taken during the fabrication procedure to avoid contaminating the surface of the device. The time for which the lithography resists were baked was reduced - from 45 minutes to 15 minutes - in order to facilitate their removal following lithography. Effort was also made to reduce the duration for which the sample was exposed to atmosphere, by keeping the sample in a pumped container, at a pressure of 0.5 atmospheres with a desiccant to remove any excess water.

Figure 5.2 shows the carrier mobility, μ, as extracted from the data using Equation 2.10. The carrier density is also shown, determined using Equation 2.8. The divergent nature of μ close to the Dirac point was confirmed by Zhang *et al.* [7] via QHE measurements, although in those measurements $\mu \approx 10,000$ cm^2/Vs in the high carrier density regime, whereas this sample has $\mu \approx 5,000$ cm^2/Vs. A small amount of asymmetry in the mobility of the p-type and n-type regions is observed and expected, given the low dopant concentration. The minimum in conductance, σ_{min} occurs at $1.0 \pm 0.2 \times (4e^2/h)$. The magnitude of σ_{min} and μ are in very good agreement with a plethora of measurements performed on similar devices in the literature as shown in Figure 5.3.

While there were initially some indications that $\sigma_{min} = 4e^2/h$ was a universal value for graphene devices, this has now been understood not to be the case. In fact σ has been shown to be a function of temperature, frequency, Fermi energy, impurity scattering strength, intervalley scattering strength and system size[4]. For example a finite temperature always results in there being some thermally excited carriers, as there is no gap between the conduction and valence bands. Independently, the highly inhomogeneous landscape of experimentally realised graphene - from the formation of electron-hole puddles - results in the Fermi level never being exactly at the Dirac point across the entire surface of the graphene sample. This also results in the observation of a non-zero conductance minimum. Nevertheless the measured value of σ_{min} is in good agreement with similar devices produced by other groups, suggesting the sample quality is reaching the limits of exfoliated graphene on SiO$_2$ substrates.
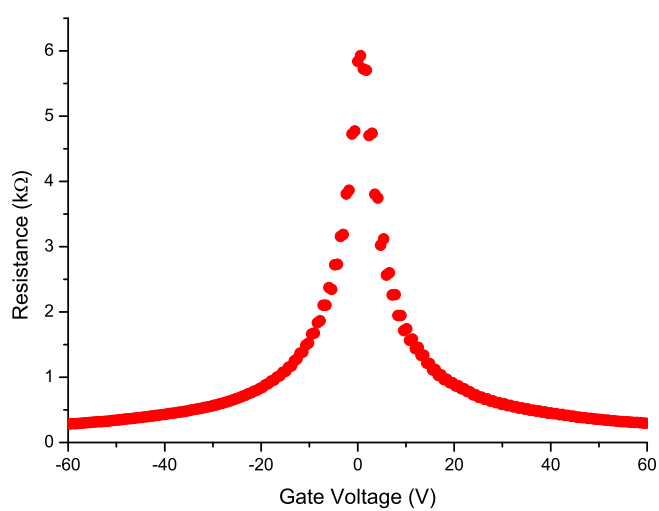
(a)
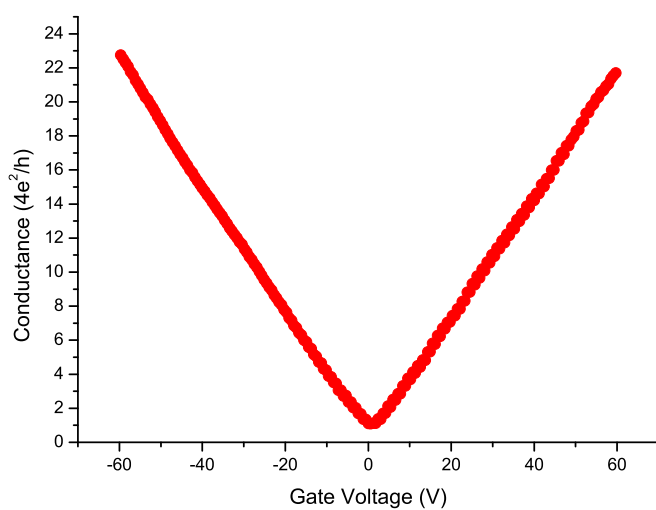
(b)

Figure 5.1: Electric field effect measurements of sample SG071 showing the gate response of a) resistance and b) conductance. Measurement performed at T = 1.4 K with no applied external field.

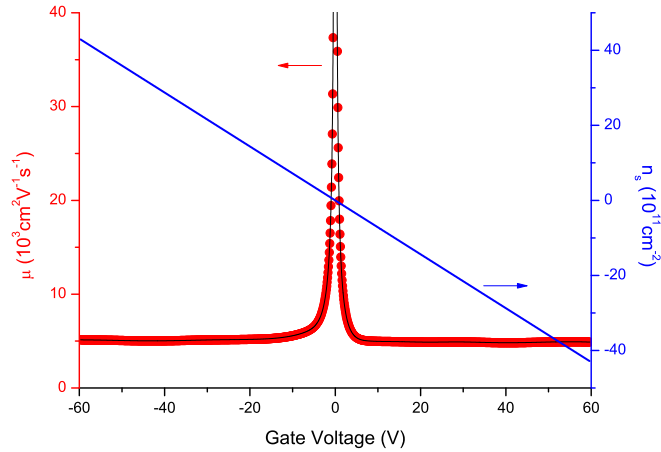**Figure 5.2:** Calculated carrier mobility (red) and carrier density (blue) as a function of gate voltage for sample SG071.
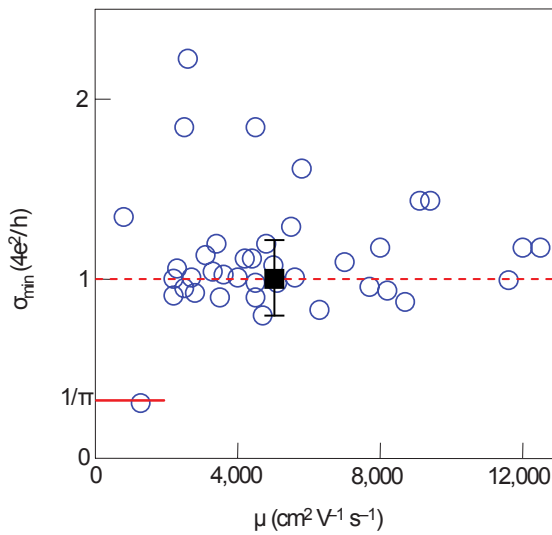

Figure 5.3: Measured minimum conductance values as a function of carrier mobility for a variety of graphene devices on SiO_2 substrates. Circles (unfilled) represent data taken by other groups while the square (filled) shows the values extracted from sample SG071. Adapted from Ref. [9].

Despite a low dopant impurity concentration, an appreciable effect in the form of a linear dependence of σ with carrier concentration, n, is observed. The weakly interacting nature of charge carriers in graphene enable the conductivity to be described by Boltzmann theory, which in the $T = 0$ K limit gives:

$$\sigma = \frac{e^2 v_F^2}{2} D(E_F)\tau(E_F) = \frac{e^2}{h}\frac{2E_F}{\hbar}\tau(E_F), \qquad (5.2)$$

where v_F is the carrier velocity at E_F, $D(E_F)$ is the density of states and $\tau(E_F)$ is the scattering time[4]. The two main contributors to scattering are neutral impurities and charged impurities that are responsible for short range and long range scattering respectively. It has been shown that for short range scatterers:

$$\tau \propto \frac{1}{\sqrt{n}} \implies \sigma(n) \propto n^0, \qquad (5.3)$$

while for long range scattering charged impurities:

$$\tau \propto \sqrt{n} \implies \sigma(n) \propto n. \qquad (5.4)$$

As a result, charge impurities are expected to dominate conduction at low carrier densities, while at higher densities shorter range scattering plays a larger role. In very high mobility samples a sub-linear $\sigma(n)$ is observed. This is because of a reduction in charged impurities (which dominate the conduction of lower mobility samples), resulting in a greater relative contribution to the conductivity from short range scatterers. From the highly linear dependence of $\sigma(n)$ shown in Figure 5.1(b) it can be concluded that charged impurities are the dominant scattering mechanism in the measured sample.

5.2   Sample Geometry for QHE Measurements

Two sample geometries were considered for QHE measurements as shown in Figure 5.4. The first geometry consists of an unetched graphene flake with source and drain contacts patterned at either end. The voltage probes through which the longitudinal voltage, V_{xx}, and transverse (Hall) voltage, V_{xy}, are measured, are patterned as close to the sample edge as possible. The sample is then measured with the applied external field perpendicular to the xy plane of the sample. The second geometry consists of

a graphene flake that has been etched into a Hall bar geometry, before patterning and depositing the contacts using the method outlined in Section 3.1.4. A false colour SEM image of an etched graphene flake (yellow), that is contacted with a Pd/Nb bilayer (blue) is shown in Figure 5.5. The device was designed to have a central channel width of 1 μm, however the final width as measured using the SEM image is 0.7 μm. The discrepancy is attributable to the undercut in the bi-layer resist profile used to define the etch area, which results in more graphene being etched than designed. Contacts 4 and 1 are the source and drain contacts, respectively with V_{xx} and V_{xy} measured between contacts $5 - 6$ and $5 - 3$ respectively. Contacts $2 - 3$ are bridged by some material, likely graphite debris remnant from the graphene deposition procedure, although this seemed to have minimal impact on the QHE measurements made on this device.

5.3 Measurement of the Quantum Hall Effect in an Etched Hall Bar Sample

To measure the QHE the etched sample was cooled to T = 1.5 K in a He flow cryostat and a magnetic field of 8 T perpendicular to the plane of the sample was applied. Individual IV measurements (maximum source-drain bias = 1 mV) were then performed, measuring both voltage geometries simultaneously over a range of applied gate voltages (-50 V $< V_\mathrm{G} < 50$ V). The results from this measurement are plotted in Figure 5.6 with the longitudinal resistance, R_{xx}, and Hall conductance, σ_{xy}, extracted from the IV measurement shown in red and blue respectively. σ_{xy} is plotted in units of 4 e^2/h which corresponds to a single quantum of conductance for carriers with fourfold degeneracy (two from spin and two from pseudospin). The largest peak in R_{xx}, coinciding with the $n = 0$ Landau level (LL) and V_Dirac, occurs at $V_\mathrm{G} \sim 12$ V. This is shifted from $V_\mathrm{G} = 0$ because of an extrinsic p-type dopant source contributing 8.6×10^{11} carriers cm^{-2}, according to the parallel plate capacitor model, see Equation 2.8. At this point σ_{xy} is observed to change sign, which confirms a change of carrier type from holes to electrons as E_F moves through the Dirac point. The existence of an $n = 0$ LL and plateaus in the Hall conductance at $\sigma_{xy} = (n + \frac{1}{2})4e^2/h$ confirms unequivocally that this sample is a monolayer of graphene.

(a) unetched

(b) etched

Figure 5.4: Geometry for measuring the QHE in a) unetched and b) etched samples.

Figure 5.5: False colour SEM image of sample SG091 showing Pd/Nb contacts (blue) and the etched graphene Hall bar (yellow). The contacts have been numbered to aid discussion. The scale bar is 2 μm.
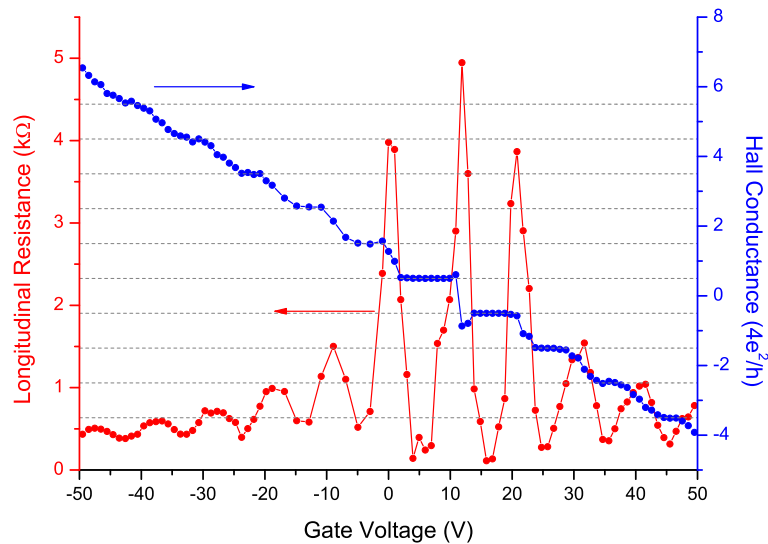
Figure 5.6: Gate response of an etched graphene Hall-bar (sample SG091A) at T = 1.5 K and H = 8 T. Dashed lines indicate expected level of half-integer quantum plateaus $\sigma_{xy} = (n + 1/2)4e^2/h$ for monolayer graphene.
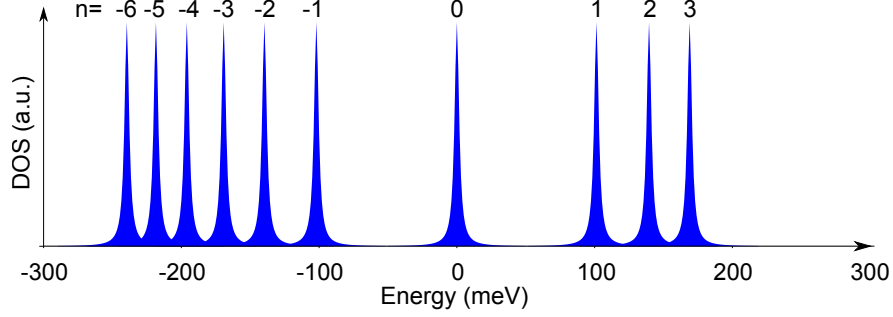
Figure 5.7: Schematic showing the observable LLs in an etched monolayer graphene sample using parameters extracted from QHE measurements. The LLs are labelled with their respective indices. The shape of the LLs are given by Lorentzian curves, broadened by scattering, with $\Gamma = 2$ meV.

5.3.1 Extraction of Landau Level Separation from QHE

To further illustrate the point, a schematic of the LL energy separation as taken from this data is shown in Figure 5.7 calculated using:

$$E = \pm\hbar v_F k = \pm\hbar v_F \sqrt{\pi n_s} = \pm\hbar v_F \sqrt{\pi \frac{\epsilon_0 \epsilon}{te}|V_G - V_{\text{Dirac}}|} \qquad (5.5)$$

where n_s is the carrier density, v_F the Fermi velocity, ϵ_0 the permittivity of free space, ϵ the permittivity of SiO$_2$, V_G the gate voltage, V_{Dirac} the voltage coinciding with the Dirac point, t the thickness of the substrate oxide and e the charge of the electron. The sign of the energy is given by the sign of $(V_G - V_{\text{Dirac}})$.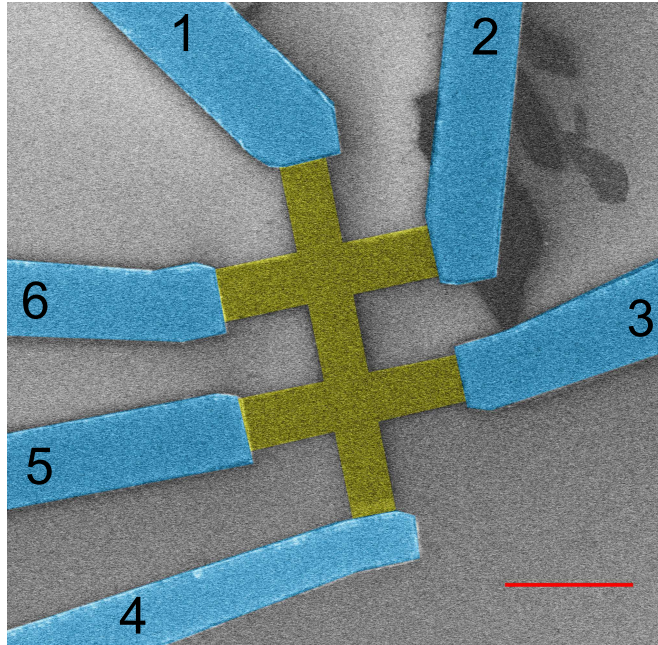 The large energy separation of the $n = 0$ and $n \pm 1$ levels results in clear resolution of the central peaks in R_{xx} and a sharp transition between plateaus in σ_{xy} close to V_{Dirac}. The shape of the LLs is approximated to a Lorentzian distribution as observed in infra-red absorption spectroscopy measurements[130]. The half width at half maximum of the Lorentzian distributions, Γ, is equivalent to the scatter induced broadening of the LLs and is set at a representative value of 2 meV[131].
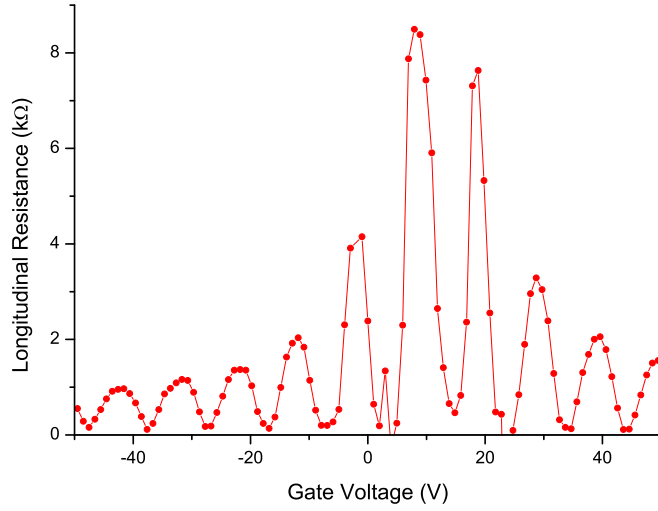
(a) Longitudinal Resistance
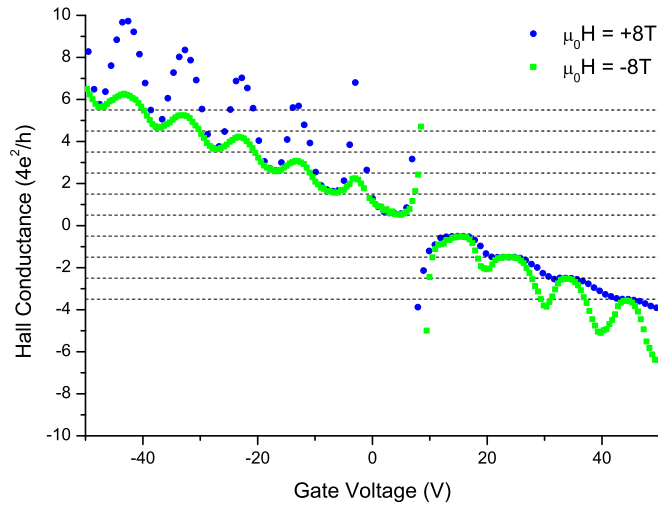
(b) Hall Conductance

Figure 5.8: Quantum Hall effect measurements performed on an unetched sample (SG089) for T = 1.4 K. a) Longitudinal resistance and b) Hall conductance measurements are both shown. The Hall conductance is shown for two different field directions with dashed lines indicating expected level of half-integer quantum plateaus $\sigma_{xy} = (n + 1/2)4e^2/h$ for monolayer graphene.

## 5.4 Measurement of the Quantum Hall Effect in an Unetched Graphene Device

Further probing of the QHE in graphene can be achieved by varying the applied magnetic field. Because of the failure of the etched device (attributed to electrostatic discharge), an unetched device with the geometry shown in Figure 5.4(a) was employed. R_{xx} as a function of V_G for this device is shown in Figure 5.8(a) with σ_{xy} measured in two magnetic field orientations shown in Figures 5.8(b). The R_{xx} response of the unetched device demonstrates a comparable number of LLs observable over the 100 V gate voltage range, as the etched devices indicating that the samples exhibit similar carrier mobilities. While the etched device showed a relatively symmetric response about V_{Dirac}, the unetched device has an asymmetric response with the peak in R_{xx} corresponding to the $n = 1$ LL being twice as high as the $n = -1$ peak. The cause of the asymmetry is that the contacts used to measure V_{xx}, also measure a component of V_{xy}, and vice-versa, because they are placed within the graphene channel. This is most pronounced in the σ_{xy} measurements, which clearly show oscillations coinciding with the oscillations in R_{xx}. Despite this effect, the quantised values of $\sigma_{xy} = (n + \frac{1}{2})4e^2/h$ (indicated by the dashed lines), are still evident, particularly in the electron conduction regime when $\mu_0 H = +8$ T.

5.4.1 QHE as a Function of Field and Gate Voltage

QHE measurements were performed on the unetched sample varying B as well as V_G. The applied field ranged from $8 \rightarrow 0$ T with a step size of 50 mT and V_G ranged from $50 \rightarrow -50$ V with a step size of 1 V. At each value of B and V_G, a 21 point IV measurement was performed, with a maximum source-drain bias of 1 mV, with V_{xx} and V_{xy} measured simultaneously, using two voltage pre-amplifiers and the DAC. As a result of time constraints, only $B \geq 0$ T was investigated, as the main interest was in R_{xx}, which should depend only on the magnitude of the applied field, not its direction. The temperature remained at T = 1.4 K throughout the measurement for a duration of 16 hours.

The result of these measurements is shown as a colour plot in Figure 5.9 with the magnitude of R_{xx} indicated by the colour bar. The value of each pixel is obtained
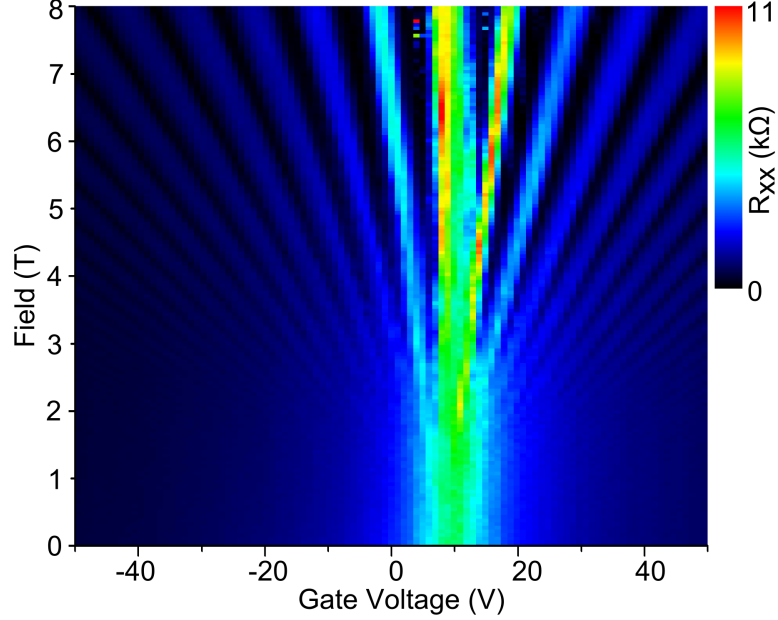
Figure 5.9: Longitudinal resistance of a graphene sample (SG089) as a function of applied gate voltage and external magnetic field.

by performing a linear fit to the IV data, at that respective value of V_G and applied field. The centres of the LLs correspond to peaks in R_{xx}, which in the colour plot are represented by the features coloured blue $\rightarrow$ red. The LL plateaus occur when R_{xx} is at a minimum which are seen as black features in the colour plot. For $B = 0$ T a single peak is observed along the x-axis at $V_{\text{Dirac}} \approx 8$ V. Increasing the field has little effect until $B \sim 2.5$ T at which point oscillations in R_{xx} as a function of V_G are observed because of the formation of LLs, having satisfied the criteria $\omega_c \tau \sim 1$. As $E_n \propto \sqrt{N}$ the LLs separation increases with field and, as a result, fewer LLs are observable within the specified range of V_G. For example at 8 T the LLs with indices in the range $-5 \leq n \leq 4$ are observable compared to $-11 \leq n \leq 7$ at 4 T. The maximum energy separation in the data is observed at 8 T where the relationship between R_{xx} and V_G is equivalent to that measured previously and presented in Figure 5.8(a).
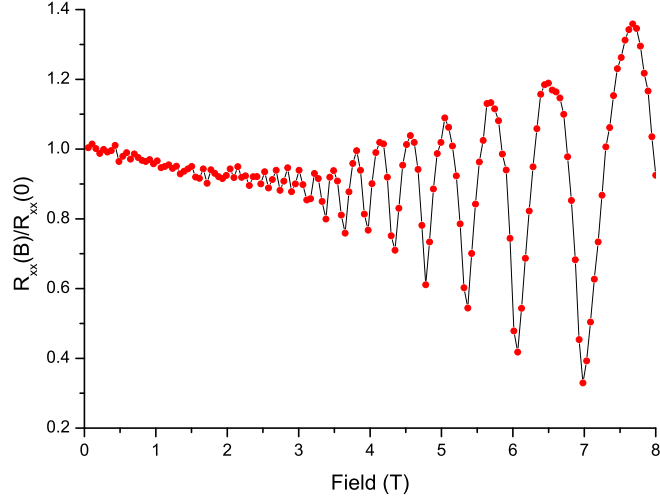
Figure 5.10: Normalised longitudinal resistance as a function of applied field showing SdHOs in sample SG089 at $V_G = -50$ V. The line connecting points is a guide for the eye.

5.4.2 SdHOs and an Estimation of the Landau Level Broadening

Figure 5.9 provides a particularly satisfying explanation of the source of the oscillations in magnetoresistance (MR) with increasing field, known as the SdHOs (refer to Section 2.2.1 for more details). Taking slices of the data in the y-direction is equivalent to performing an MR measurement at a given value of n_s. This makes it clear that as n_s increases additional SdHOs are observable owing to the sampling of LLs with higher indices. $R_{xx}(B)$ (normalised by the zero field resistance) as a function of field at $V_G = -50$ V is extracted from Figure 5.9 and is shown in Figure 5.10.

The field strength at which the SdHOs are first observable, B_{SdH}, can be used to extract some key parameters regarding the quality of the sample, namely the elastic scattering time, τ, LL broadening, Γ, and the mobility, μ. SdHOs correspond to the formation of LLs which can only be resolved once $\omega_c \tau \sim 1$. The effective cyclotron mass, m^*, of graphene is given by $E = m^* v_F^2$ where E is energy[8]. Combining this relation with the standard definition of cyclotron frequency and the dispersion relation for graphene, given by Equations 2.12 and 2.13 respectively, produces the following relation:

$$\omega_c = \frac{e v_F B}{\hbar \sqrt{\pi n_s}},$$ (5.6)
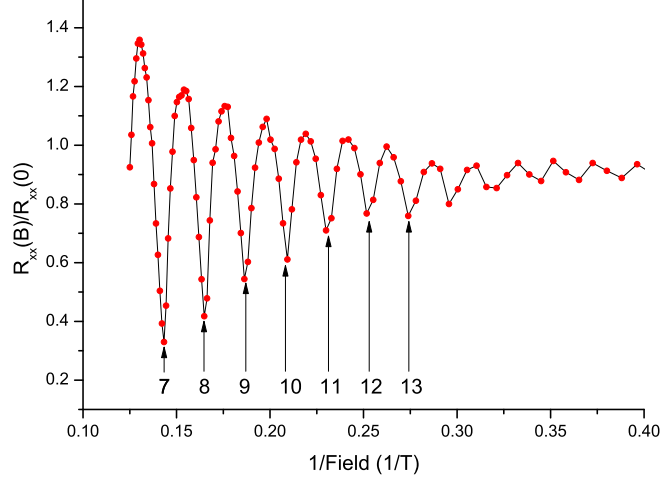
Figure 5.11: Normalised longitudinal resistance as a function of the inverse of the applied field from sample SG089 at $V_G = -50$ V. The labels indicate the respective Landau level indices n associated with each minima in MR. The line connecting the data points is a guide for the eye only.

and hence the elastic scattering time is given by:

$$\tau \sim \frac{\hbar\sqrt{\pi n_s}}{e v_F B_{\text{SdH}}}. \tag{5.7}$$

In the high carrier density regime at $V_G = -50$ V, $n_s \sim 4.5 \times 10^{13}$ carriers cm^{-2} and the first SdHO is observed at $B_{\text{SdH}} \sim 2.5$ T, which gives $\tau \sim 300$ fs. The uncertainty principle gives the broadening of a LL by defect scattering as $\Gamma \approx \hbar/\tau \sim 2$ meV, which is comparable to the broadening reported by other authors for graphene on SiO$_2$ substrates[131]. Given that $\mu = e\tau/m^*$ the criteria for LL generation in terms of mobility and field is $\mu B_{\text{SdH}} \sim 1$, giving a lower bound mobility of $\mu \sim 4{,}000$ cm^2 V^{-1} s^{-1}, which is in good agreement with values obtained from electric field effect measurements. Based on these considerations our samples are of similar quality to those presented in the literature[9].

5.4.3 Extraction of Berry's Phase and Carrier Density from Sd-HOs

Several fundamental quantities can be extracted from the SdHOs, namely the carrier density, Berry's phase β and the cyclotron mass. As the determination of m^* requires

a measurement of the SdHO amplitude as a function of T, which was not a variable in this measurement, only the former two quantities are measured in this section. The change in R_{xx} because of the SdHOs is given by the following relation[131–133]:

$$\Delta R_{xx} = R(B,T)\cos\left[2\pi\left(\frac{B_F}{B} + \frac{1}{2} + \beta\right)\right],\tag{5.8}$$

where $R(B,T)$ is the SdHO amplitude and β is the Berry's phase. The frequency of the SdHO in $1/B$ is given by B_F:

$$B_F = \frac{E_F^2}{2ev_F^2\hbar} = \frac{\hbar k_F^2}{2e} = \frac{\hbar\pi n_s}{2e},\tag{5.9}$$

and so is only dependent on the carrier density, n_s. R_{xx} is a minimum when an integer number of LLs is filled and the following relation is satisfied:

$$2\pi(B_F/B + 1/2 + \beta) = 2\pi(n + 1/2),\tag{5.10}$$

where n is the Landau index of the highest filled level which takes integer values. Rearranging this relation gives the following expression for n in terms of B:

$$n = \frac{B_F}{B} + \beta.\tag{5.11}$$

By producing a plot of n as a function of $1/B$ (otherwise known as a fan diagram), both B_F (and hence n_s) and β can be extracted from the gradient and y-intercept of the linear fit respectively. Figure 5.11 shows a plot of normalised R_{xx} as a function of $1/B$ for $V_G = -50$ V. The minima in R_{xx} are spaced equally in $1/B$ in agreement with theory and have been assigned Landau indices representing the highest filled LL through comparison with the complete data set (shown in Figure 5.9). As the spacing of the data points in Figure 5.11 increase with $1/B$ it is more difficult to assign an accurate value of the minima for higher LLs and so only the first 7 observable levels are selected in this case. This process was repeated for all carrier densities with the result plotted for a selection of gate voltages in a fan diagram as shown in Figure 5.12. The dashed lines correspond to fits to Equation 5.11 with lines of positive and negative gradient corresponding to values of V_G above and below V_{Dirac} respectively, which in turn corresponds to electron-like and hole-like charge carriers.
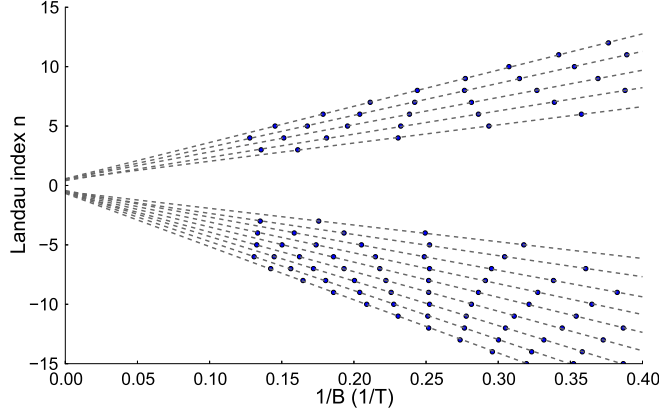
Figure 5.12: Fan diagram for sample SG089 showing SdHO minima positions for a selection of values of gate voltage for clarity.

A plot of n_s versus V_G is shown in Figure 5.13. The points represent the carrier density as determined from the fan diagram using:

$$n_s = \frac{4eB_F}{h},$$ (5.12)

where B_F is the gradient of the individual Landau plot fits. The line shows the result of using the parallel plate capacitor model as given by Equation 2.8. The response is symmetric about $V_{\text{Dirac}} \approx 8$ V and the lowest experimentally determined value of n_s is $1.2 \pm 0.2 \times 10^{11}$ carriers cm^{-2}. The validity of the parallel plate capacitor model is confirmed via its good agreement with the extracted values of carrier density.

The intercept values of the linear fits on the fan diagram are equal to β. The magnitude of β is plotted as a function of V_G in Figure 5.14. From the plot a value of $\beta = 0.48 \pm 0.01$ is found. The expected value for β is 0.5, which suggests there is a systematic error. A likely source of this error is the limited resolution of the measurements in B. Despite this discrepancy it is clear that β is close to 0.5 and does not take an integer value as is observed in 2DEGs. The extracted value of β directly supports the conclusion that the charge carriers are spin $1/2$ Dirac fermions.

5.5 Conclusion

Graphene samples of comparable quality to those in the literature have been produced as confirmed by EFE measurements. A sample with V_{Dirac} close to 0 V was measured,
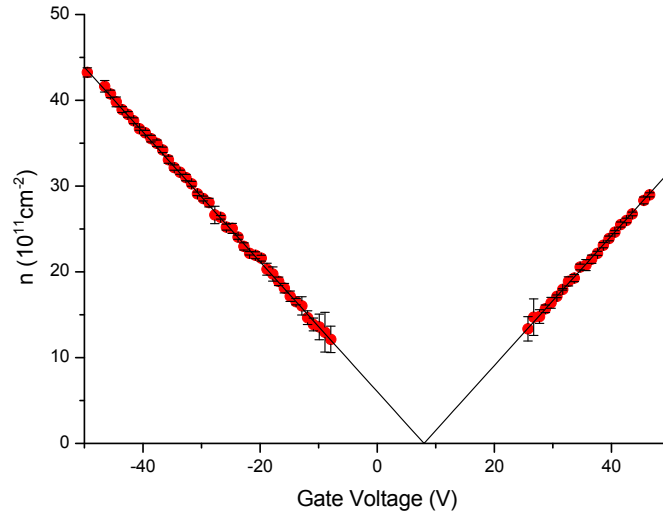
Figure 5.13: Carrier density as a function of gate voltage. The red points indicate the carrier density as determined from the landau plot in Figure 5.12. The solid black line is the predicted carrier density based on a simple gate capacitance model.
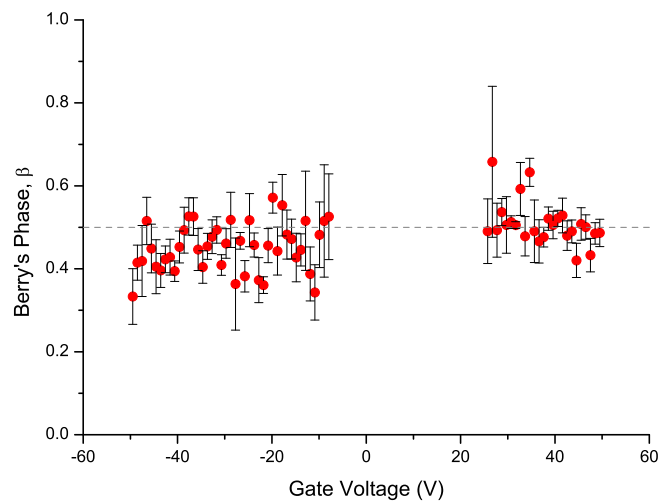
Figure 5.14: Magnitude of Berry's phase as a function of gate voltage for sample SG089.

115

indicating a very low charged impurity concentration. The mobility and minimum conductance of this sample were found to be 5,000 cm^2/Vs and $4e^2/h$ respectively, which is in good agreement with samples produced by other groups on SiO$_2$, using mechanical exfoliation and lithography. A highly linear dependence of conductance on gate voltage was observed, which is understood in terms of the dominance of long range scattering by charged impurities over the short range scattering by neutral impurities.

Following this study, QHE measurements have been performed on two types of graphene sample. One type consisted of a graphene sheet with undefined shape with invasive contacts; the other was etched into a Hall bar using electron beam and oxygen plasma ashing. The QHE was measured at low temperature in both devices with plateaus in the Hall conductance observed at values of $(n+1/2)4e^2/h$, confirming that the samples consisted of single layer graphene sheets. The plateaus in conductance of the unetched device were not very well defined, which was attributed to the use of invasive voltage probes. The unique energy spacing of the LLs in graphene was also extracted directly from this QHE data.

Finally an extensive study of the QHE in an unetched sample was performed as a function of applied field strength. The onset of the Landau level separation was observed at $B \sim 2.5$ T at $T = 1.4$ K. From this the elastic scattering time and the Landau level broadening were estimated to be $\tau \sim 300$ fs and $\Gamma \sim 2$ meV respectively. Additionally, oscillations in longitudinal resistance with field were observed and identified as SdHOs. The minima of these oscillations were spaced by a constant value in $1/B$ as expected for a monolayer graphene sample. By assigning the resistance minima to specific LLs, the carrier density and Berry's phase were determined directly. The dependence of carrier density on gate voltage was shown to conform to the proposed parallel plate capacitor model. The Berry's phase was found to by $\beta = 0.48 \pm 0.01$ which indicates a phase change of the wavefunction of π when rotated by 2π in k-space, which is consistent with having spin $1/2$ Dirac fermions as charge carriers.

The single layer nature of the samples has been unambiguously shown via a demonstration of the rich and fundamentally new physics predicted in graphene by theory. Furthermore, the quality of the graphene produced here has been shown to be of comparable quality to some of the best graphene on SiO$_2$ devices made. As a result, it is likely that the performance of our graphene devices is not limited by the quality of the

graphene but by the contact made to it. The following chapter explores the contacting of graphene in more detail.

CHAPTER 6

Contacting Graphene

It is well understood that the discontinuity between the properties of bulk materials and those with restricted dimensionality makes contacting nanoscale devices with metallic contacts a non-trivial problem[134]. Graphene is no exception, with many factors playing a role in the quality of contact that can be made, from the fabrication techniques used, to the choice of contact material[135–139]. The contact resistance has also been shown to be highly dependent on carrier concentration and temperature in graphene devices, with an additional degree of variability between otherwise identical devices. Given that the ability to form highly transparent (i.e. low resistance) contacts is particularly important when producing devices where maintaining phase coherence across the contact and graphene is necessary (such as in a SGS junction) it seems wise to measure the contact resistance, to assess the viability of observing phase coherent phenomenon. This is of additional interest given that the majority of devices presented in the literature are fabricated using contacts deposited with electron beam evaporation, whereas the devices presented within this thesis are deposited by means of sputter deposition.

This chapter presents the results of investigating the contacting of graphene with metals. Contact resistances are measured on both etched and unetched graphene devices. Asymmetry observed in the transport measurements of these graphene devices is then discussed in terms of contact induced doping, resulting from the formation of a dipole at the graphene-metal interface, and a model is presented to explain the effect this has on the transport properties. The impact of sputtering contacts on graphene is then investigated using Raman spectroscopy, followed by a review of contact resistance measurements made on devices in the literature and how this compares to our samples.

6.1   Measuring Contact Resistances

6.1.1   Transmission Line Model

One of the main considerations when determining the contact resistance of devices with planar geometries is that current is not necessarily injected uniformly over the full area of the contact. This can be understood in terms of the transmission line model first proposed by Murrmann and Widmann and later refined by Berger[141]. A schematic
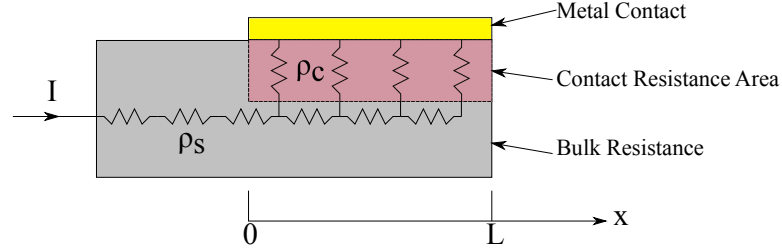
Figure 6.1: Schematic of a planar device with electrical resistance represented by a model circuit as assumed in the transmission line model[140].

of this model is shown in Figure 6.1, which shows that the area under the contact can be described by a network of resistors in parallel. Therefore, current injection from the bulk material to the contact primarily occurs at the $x = 0$ contact edge as this proves the path of least resistance. By considering this network of resistors the spatial change in potential under the contact is found to be:

$$V(x) = I \frac{\sqrt{\rho_s \rho_c} \cosh\left[(L-x)/L_T\right]}{Z \sinh\left(L/L_T\right)}, \tag{6.1}$$

where L is the contact length, I is the current flowing and Z is the width of the conducting channel. The distance over which most of the current transfer occurs is given by:

$$L_T = \sqrt{\rho_c/\rho_s}, \tag{6.2}$$

where ρ_s and ρ_c are the sheet resistance and specific contact resistance respectively. Despite this model being originally proposed for bulk semiconductor-metal interfaces, conceptually the situation in planar graphene devices should be similar. The main discrepancy will likely be the assumption that the sheet resistance is the same in the channel and under the contact, which may not be the case if the graphene is damaged by the metal deposition procedure.

6.1.2 Transfer Length Method

A common method used for determining the contact resistance, and transfer length is through the use of a technique called the transfer length method (TLM). The technique utilises a test structure as shown in Figure 6.2(a), in which a channel of uniform width

(a)

(b)
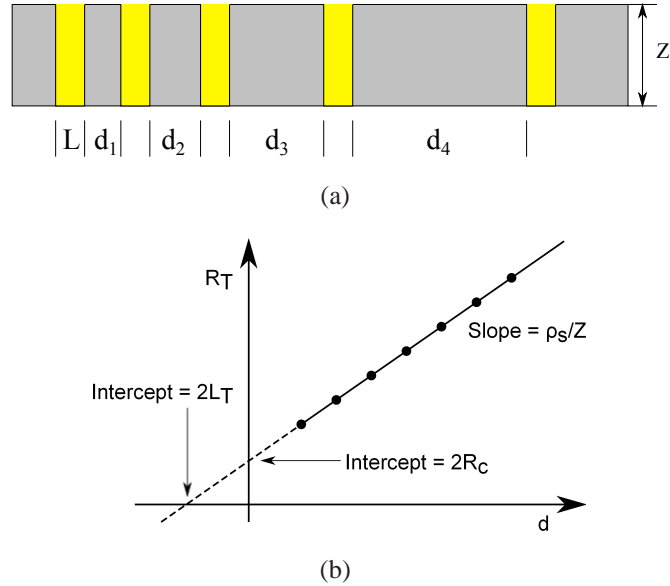
Figure 6.2: a) A transfer length method test structure and b) an example plot of total resistance as a function of contact spacing. Adapted from [140].

Z is contacted by identical contacts with unequal spacing d. When measuring the resistance between adjacent contacts the total resistance, R_T, is given by:

$$R_T = \frac{\rho_s}{Z}d + 2R_c,\tag{6.3}$$

where R_c is the contact resistance in Ohms. By plotting R_T as a function of d (keeping Z constant) it is possible to extract both the R_c and L_T as shown in Figure 6.2(b).

An alternative form of the equation was proposed by Venugopal *et al.* [136] for a non-uniform channel. Considering an irregularly shaped channel as shown in Figure
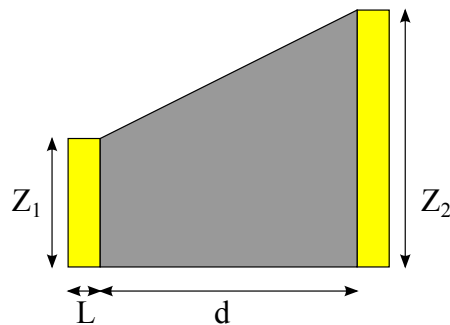
Figure 6.3: Irregularly shaped graphene device geometry [136].

121

6.3, it can be shown that the total resistance is of the form:

$$R_T = \rho_s \frac{d}{Z_{\text{eff} 1}} + \frac{2\rho_c}{L Z_{\text{eff} 2}}, \tag{6.4}$$

where,

$$Z_2 > Z_1,$$

$$Z_{\text{eff} 1} = (Z_2 - Z_1)/\ln(Z_2/Z_1),$$

$$Z_{\text{eff} 2} = 2Z_1 Z_2/(Z_1 + Z_2),$$

and Z_1 and Z_2 are the width of the graphene at either end of each respective channel between two adjacent contacts. In this case ρ_c is the specific contact resistance in $\Omega\,\text{m}^2$ as Venugopal *et al.* assumed current flow occurred along the full length of the contact. Samples consisting of both irregularly shaped graphene and uniform width graphene have been investigated, the results of which are presented in the following section.

6.2 Experimental Data

In the following section the contact resistance measurements taken on graphene samples with sputter deposited Pd/Nb (3 nm/90 nm) contacts are presented. Measurements are first shown for an irregularly shaped sample (SG085), followed by a device with uniform width (SG098).

6.2.1 Irregularly Shaped Device

EFE measurements were taken between pairs of adjacent contacts on the unetched graphene flake shown in Figure 6.4, with channel length, $d = 0.8$, 1.3, 2.5, 4.4 and 6.3 μm and contact length, $L = 1$ μm. The two terminal resistance as a function of V_G for each pair of contacts is shown in Figure 6.5(a), with the channel length given in the legend. As the channel length reduces, the total resistance, R_T, is observed to reduce over the total gate voltage range investigated, although comparing curves visually is problematic given the varying channel widths. The smallest channel ($d = 0.8$ μm) shows an anomalous response, as the resistance at $V_G = -60$ V is comparable to that of the largest channel ($d = 6.3$ μm). This is despite the narrower junction having a significantly smaller area of graphene between the contacts. The cause of this

Figure 6.4: False colour SEM image of TLM sample SG085 showing Pd/Nb contacts (blue) and the unetched graphene flake (yellow). The scale bar is 10 µm.

anomalous resistance is not clear, although it is possible that there is debris under the outermost contact, which having a particularly small contact area, would be heavily impacted even by small obstructions.

In order to extract the sheet and contact resistances, ρ_s and ρ_c respectively, as a function of V_G, the data was fitted using the TLM equation for an irregular sample, Equation 6.4. As the channel width at either end of the channel (Z_1 and Z_2) vary for each pair of contacts, the data was fitted using a least squares method, minimising the difference between R_T as measured and calculated using ρ_s and ρ_c as the only fitting parameters. This procedure was repeated for data taken at each value of V_G and the results of these fits are shown in Figures 6.5(b) and 6.5(c).

The sheet resistance extrapolated from the TLM measurements is shown in Figure 6.5(b) and displays a field effect typical of a graphene device. The field effect mobilities as extracted using the Drude model (Equation 4.3) are $\mu_e = 4{,}200$ cm^{2}V^{-1}s^{-1} and $\mu_h = 4{,}900$ cm^{2}V^{-1}s^{-1} and are comparable to those measured by other groups for non-suspended graphene on SiO$_2$ substrates[9].

Venugopal *et al.* [136] reported a current transfer length greater than the contact length based on the transmission line model and concluded that this indicated that charge transfer occurred over the entire contact. This was countered by Xia *et al.* [138], who stated that this reasoning was not applicable to graphene for two main reasons. Firstly, the model assumes the metal-semiconductor contact is diffusive, which

(a)

(b)   (c)
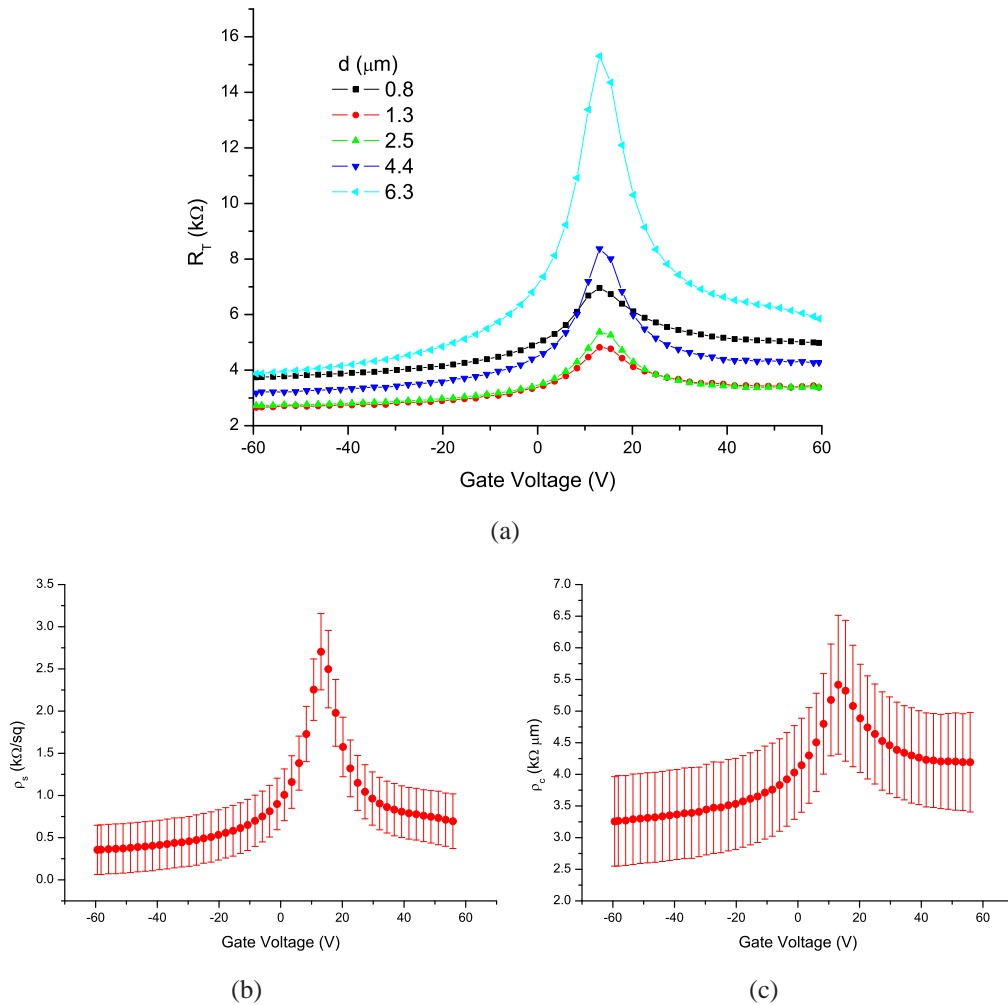
Figure 6.5: TLM measurements taken on an unetched graphene flake. EFE measurements taken between pairs of adjacent contacts are shown in a) with the sheet resistance and contact resistance as a function of gate voltage shown in b) and c) respectively.

does not apply to graphene, as the mean free path is significantly larger than a typical semiconductor structure, around 1,000 nm for graphene[3] compared to $10 - 100$ nm for Si (depending on dopant concentration and temperature)[142]. Secondly, the model assumes that the sheet resistance under the contact and in the channel is the same. This is unlikely to be the case in a graphene device, as the graphene can be damaged by the deposition technique (expected for sputtered samples[143]), doped by the contacting metal[113] or have its band structure altered by interaction between the carbon and metal atoms[144; 145].

It is now generally accepted that carrier injection occurs over a short distance at the contact edge[135; 138; 139] and so ρ_c has been plotted in units of $\Omega\mu$m to be comparable with values quoted in the literature. The specific contact resistance shown in Figure 6.5(c), shows a clear dependence on gate voltage with a peak in ρ_c at V_{Dirac}, which decreases away from the Dirac point, saturating at high gate voltages. The specific contact resistance in the p-type ($V_{\mathrm{G}} - V_{\mathrm{Dirac}} < 0$) and n-type ($V_{\mathrm{G}} - V_{\mathrm{Dirac}} > 0$) branches display asymmetry, saturating at 3.3 ± 0.7 k$\Omega\mu$m and 4.2 ± 0.8 k$\Omega\mu$m respectively. Such asymmetry, with higher contact resistances when n-type doping, was also observed by Xia *et al.* [138] in all their samples contacted with Pd. For Ti doped samples they observed the opposite asymmetry and so attributed this effect to doping of the graphene by the metal contact, with the type of doping depending on the work-function of the metal (see Section 6.3.1).

The large error bars on both Figure 6.5(b) and Figure 6.5(c) are primarily from the difficulty in assigning an appropriate value of channel widths Z_1 and Z_2. The model assumes that the overall channel width decreases linearly between both contacts which is not the case for at least one of the channels. Shaping the graphene flake so it has a uniform width eliminates this source of error and makes interpretation of the data simpler. This is because of the simple relationship between R$_T$ and d, based on Equation 6.3 can be employed for a uniform width device rather than using a width dependent least squares fit, based on Equation 6.4, as required for a non-uniform device.

6.2.2 Uniform Width Device

Uniform width graphene samples were produced by isolating exfoliated flakes of sufficient size to accommodate a test structure, typically requiring a flake with a length
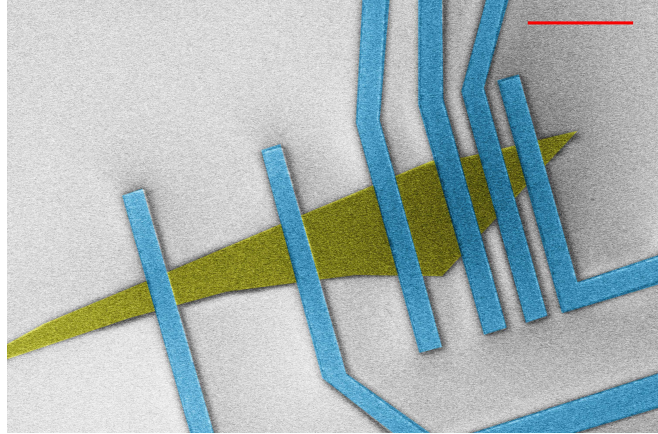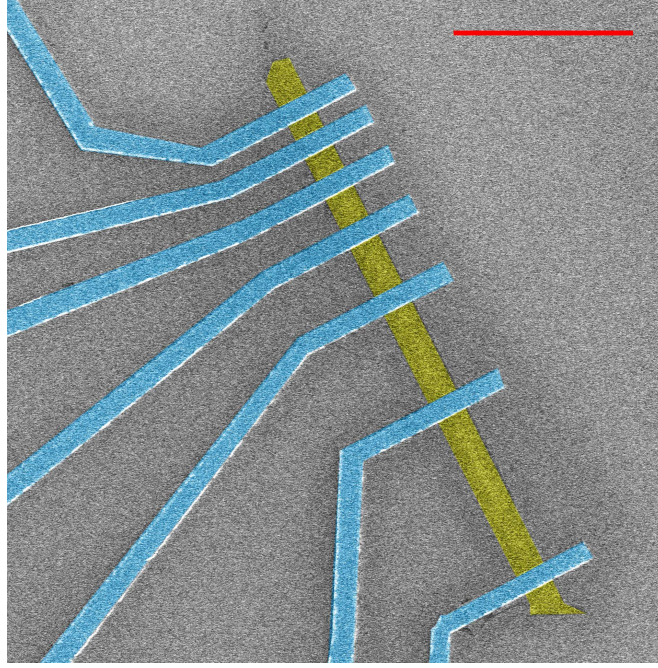
Figure 6.6: False colour SEM image of TLM sample SG098 showing Pd/Nb contacts (blue) and the etched graphene flake (yellow). The scale bar is 10 μm.

greater than 20 μm. It was necessary to then etch the flakes using electron beam lithography and oxygen plasma, as outlined in Section 3.1.4 to ensure Z was constant. This was then followed by depositing contacts using the standard EBL and sputtering techniques. One such device, SG098, was produced in this manner with contacts of width, $L = 1$ μm, $Z = 2.0$ μm and channel lengths, $d = 1.0$, 1.5, 2.0, 3.0, 5.5 and 9.0 μm respectively, see Figure 6.6. Measurements were made under vacuum in a He flow cryostat, to avoid any hysteresis in the EFE measurements caused by ambient conditions.

The two terminal EFE measurements for each of the pairs of contacts separated by a uniform graphene channel of length d are shown in Figure 6.7. The device with a 9 μm channel shows the most typical graphene-like response, with a resistance maxima corresponding to the CNP occurring at $V_G = 15$ V. At this value of V_G we see that the values of R_T decrease as the channel length is reduced, which is to be expected because of the contribution to R_T from ρ_s being proportional to d as stated in Equation 6.3. The more striking feature in these measurements is the increasing asymmetry in the curves
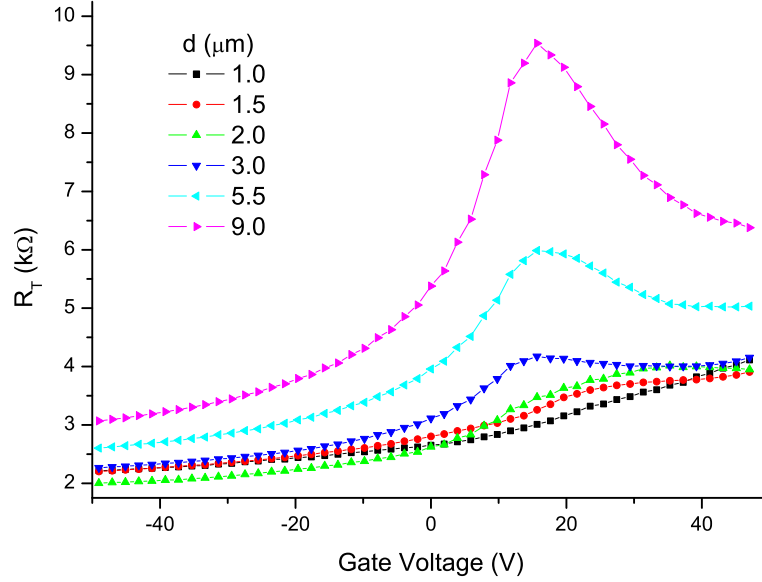
Figure 6.7: EFE measurements taken on a TLM structure with uniform width.

about V_{Dirac} as d decreases. As the carrier mobility $\mu \propto \text{d}R/\text{d}V_G$ the naive assumption would be that the ratio of μ_e to μ_h changes significantly with d. By extracting the sheet and contact resistances independently from the data it is evident that this is not the case.

Figure 6.8(a) shows the total resistance versus channel length extracted from the EFE measurements and the linear fits from which the specific contact resistance and sheet resistance can be extracted based on Equation 6.3 for several values of V_{G}. It is clear from this plot that for $V_{\text{G}} < V_{\text{Dirac}}$ the intercept of the fit, and hence the contact resistance, is relatively constant, despite the changing sheet resistance (indicated by the varying fit gradients). It is also clear that the fits will intercept the x axis at a value much more negative than $-2\,\mu$m. As the value of this intercept is equivalent to $2L_T$ this would indicate that charge injection is occurring over the entirety of the contact, which was the conclusion of Venugopal *et al.* [136]. Several other groups have found similar results for L_T from TLM measurements, yet complementary transport measurements have indicated that the charge injection occurs only at the contact edge.

The extracted value of ρ_s and ρ_c are shown as a function of V_{G} in Figure 6.8(b) and Figure 6.8(c) respectively. It is clear that when ρ_s is considered independently from the contact resistance, the characteristic symmetric shape in the gate voltage response

127

(a)

(b)   (c)
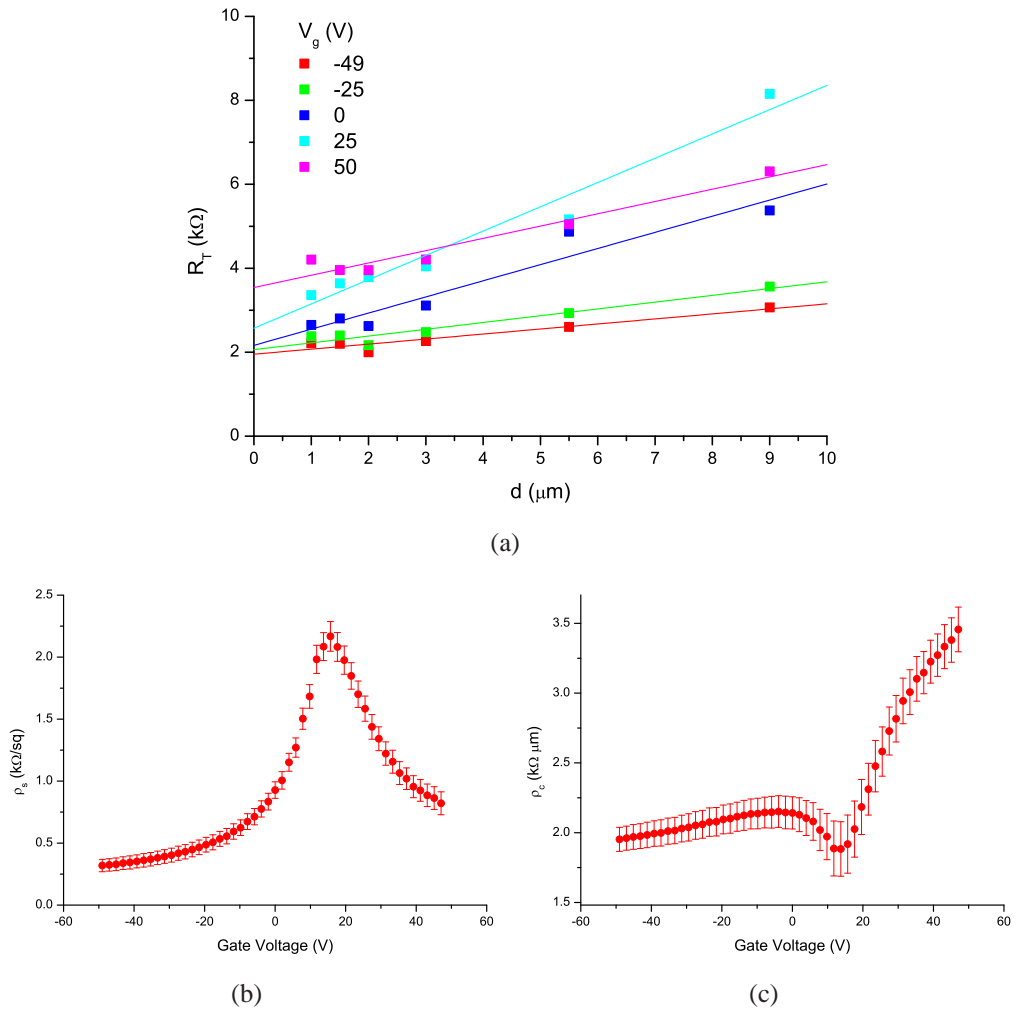
Figure 6.8: TLM measurements taken on an etched graphene flake with uniform width. Total resistance versus channel length for a range of gate voltages is plotted in a) with the extracted sheet resistance and specific contact resistivity plotted in b) and c) respectively.

is recovered, indicating that μ_e and μ_h are comparable and independent of the channel length and that the asymmetry in the resistance curves is because of a gate dependent contact resistance. Figure 6.8(c) shows that this gate dependence is significantly different when in the hole ($V_G < V_{Dirac}$) or electron ($V_G > V_{Dirac}$) conduction regime, with ρ_c(holes) remaining relatively constant at approximately 1.9 ± 0.3 kΩµm, even as the carrier density increases. In the electron regime ρ_c(electrons) is highly dependent on carrier density, increasing by a factor of 2 over a 20 V range in V_G.

Huard *et al.* [146] investigated electron-hole asymmetry in the resistance curves of graphene by producing devices with both invasive contacts (those that covered the entire width of a graphene channel) and external contacts (those connected to the channel via etched graphene arms). They observed that the devices with invasive contacts showed strong electron-hole asymmetry (in addition to sub-linear conductance), which the external contacts did not. This phenomenon was attributed to the transport properties of the metal-graphene interface and moreover to the formation of p-p or p-n junctions at the interface, through charge transfer from the metal to the graphene. The mechanism by which the charge transfer occurs is discussed in Section 6.3, followed by a model explaining the electron-hole asymmetry in the contact resistance measurements.

6.3 Modelling Charge Transfer from Metal Contacts to Graphene

6.3.1 Model of Doping Graphene Through Metal Contacts

Based on density functional theory (DFT) calculations of graphene on different metal substrates, Giovannetti *et al.* [113] developed a phenomenological model that predicts the shift in E_F of graphene when in contact with a metal. This section outlines this model and the results that can be obtained from it for several different metallic species, including those used to contact graphene in this thesis.

When graphene is contacted with a metal, a transfer of electrons occurs to bring the Fermi levels into equilibrium which is dependent on the relative work-functions of the graphene, W_G and metal surface, W_M. The density of states of graphene is given

Figure 6.9: Schematic illustration indicating the parameters used in the modelling of a dipole forming at the interface between the graphene and contact metal. Reproduced from Ref. [113].

by the following relation:

$$D(E) = \frac{2E_F}{\pi(v_F\hbar)^2} = D_0 E_F, \tag{6.5}$$

giving $D_0 \approx 1.6 \times 10^{17}$ m^{-2}eV^{-1} for E within 1 eV of the Dirac points. This is much lower than for a normal metal, and so equilibrium is achieved by the movement of E_F in the graphene, as even a small electron contribution can make a significant change in E_F. The result is the formation of an interface dipole between the graphene and the metal as illustrated in Figure 6.9, where d is the metal-graphene separation, z_d is the effective distance between the charge sheets and ΔV is the potential change generated by the metal-graphene interaction. As most of the charge sheets exist within the space between the graphene and the metal, it is modelled as $z_d = d - d_0$ where d_0 is a constant.

The potential change is given by:

$$V(d) = \Delta_{tr}(d) + \Delta_c(d), \tag{6.6}$$

where Δ_{tr} is the contribution from charge transfer because of the difference in work-functions in the metal and Δ_c is the contribution from the chemical interaction between the graphene. Both components are dependent on the metal-graphene separation d. The chemical interaction is necessary to explain why the graphene doping is not simply

electron (hole) doped when $W_G > W_M$ ($W_G < W_M$) but instead the crossover from n-type to p-type doping is at $W_M - W_G = 0.9$ eV for an equilibrium separation $d \sim 3.3$ Å. The work-function of the metal covered graphene is thus given by:

$$W(d) = W_M - \Delta V(d), \tag{6.7}$$

with the shift in Fermi level:

$$\Delta E_F(d) = W(d) - W_G. \tag{6.8}$$

The charge transfer component is modelled using a parallel plate capacitor model:

$$\Delta_{tr}(d) = \alpha N(d) z_d, \tag{6.9}$$

where $\alpha = e^2/\epsilon_0 A = 34.93$ eV/Å where $A = 5.18$ Å^2 is the area of the graphene unit cell. $N(d)$ is the number of electrons per unit cell transferred to the graphene and is found by integrating Equation 6.5:

$$N(d) = \int D(E)\, \mathrm{d}E = D_0 \frac{\Delta E_F(d)^2}{2}. \tag{6.10}$$

Combining Equations 6.6, 6.7, 6.8 and 6.9 and solving the resultant quadratic equation gives the following expression for the shift in the graphene Fermi level:

$$\Delta E_F(d) = \pm \frac{\sqrt{1 + 2\alpha D_0 (d - d_0)|W_M - W_G - \Delta_c(d)|} - 1}{\alpha D_0 (d - d_0)}. \tag{6.11}$$

Assuming that the parameters d_0 and $\Delta_c(d)$ depend very weakly on the choice of metal, the model is found to be dependent only on W_M, W_G and d. The values of d_0 and $\Delta_c(d)$ were found by fitting Equation 6.11 to their DFT results for Cu (111). This was achieved using a parameterised form of $\Delta_c(d) = e^{-\kappa d}(a_0 + a_1 d + a_2 d^2)$, finding $d_0 = 2.4$ Å , $\kappa = 1.6443$ Å^{-1}, $a_0 = -2048.56$ eV, $a_1 = 1363.87$ eV/Å and $a_2 = -205.737$ eV / Å^2 for $d \gtrsim 3.0$ Å. The resultant ΔE_F dependencies for various metals on graphene, based on their respective work-functions and Equation 6.11, are shown in Figure 6.10.

Giovannetti *et al.* only presented results based on Al, Cu, Ag, Au and Pt, as these metals were found to be weakly interacting with the graphene and so $\Delta_c(d)$ was only dependent on exchange repulsion. The chemisorption of Pd on the other hand is particularly strong because of hybridisation between the graphene p$_z$ orbitals and the metal d
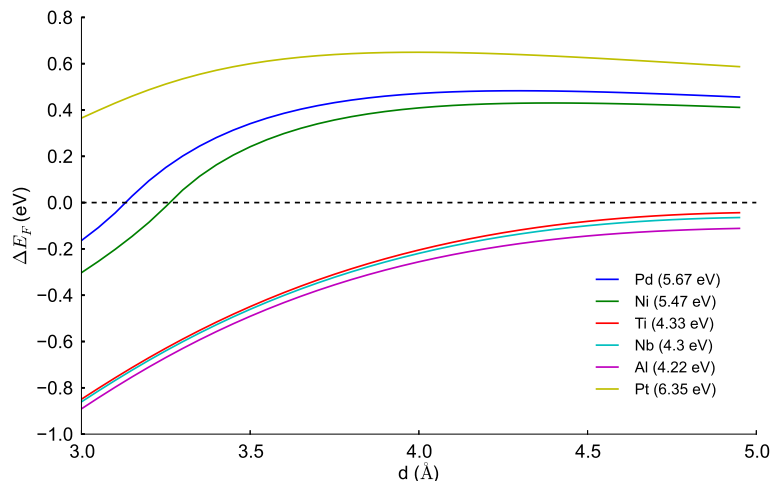
Figure 6.10: Calculated shift in E_F as a function of graphene-metal surface distance for various metals using the model developed by Giovannetti *et al.* [113].

orbitals (Pd orbital configuration is ([Kr] $4d^{10}$)), heavily distorting the graphene bands in addition to having reduced separation of d_{eq} = 2.30 Å[113]. Hence, the calculated ΔE_F for Pd contact is not accurate as it changes $D(E)$ for the graphene, has a greater dependence of ΔV on Δ_c as well as predicting $d_{eq} < d_0$ which is un-physical. Instead ΔE_F for Pd can be found via DFT calculations[147].

Interestingly, another species that undergoes chemisorption on graphene is Ti (d_{eq} = 2.1 Å)[147], which has an orbital configuration of [Ar] $4s^2$ $3d^2$ with outer d orbitals that can undergo hybridisation. This orbital hybridisation explains the prevalence of adhesion layers consisting of Pd and Ti when contacting carbon structures. Conversely a metal such as Nb has an orbital configuration of [Kr] $4d^4$ $5s^1$, and so the d orbitals cannot undergo hybridisation with the graphene p$_z$ orbitals, resulting in poor adhesion. IV measurements performed on graphene samples contacted with Nb with and without a 3nm Pd adhesion layer are shown in Figure 6.11. The sample without Pd clearly has a non-linear IV characteristic of tunnelling because of poor metal-graphene adhesion whereas the sample with a Pd adhesion layer has an Ohmic response indicative of a good contact.

Given the planar geometry of the devices presented in this thesis, the influence of the metal covered graphene on the uncovered graphene must be considered. A schematic of this situation is shown in Figure 6.12 for a metal which induces $W < W_G$.
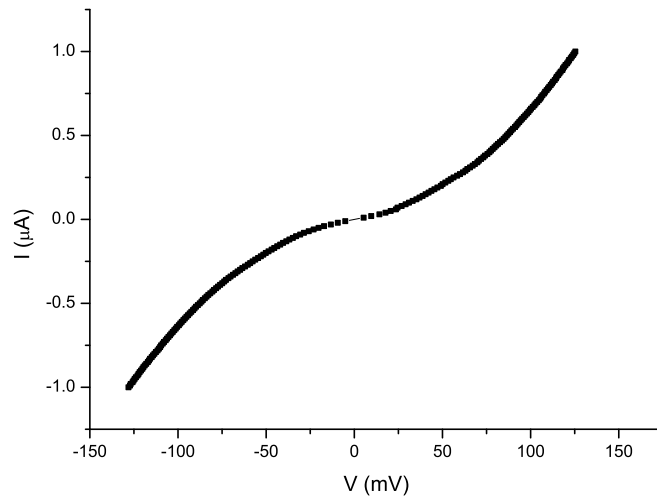
(a) Nb (100 nm)
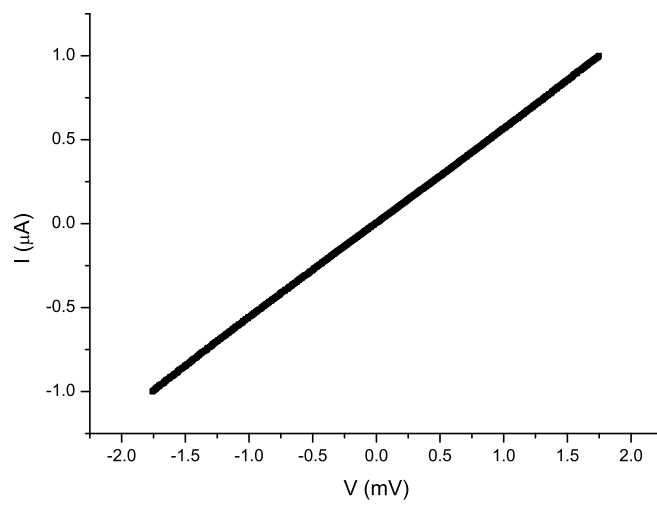
(b) Pd (3 nm) Nb (90 nm)

Figure 6.11: *IV* measurements performed on graphene contacted a) with and b) without a 3 nm Pd adhesion layer between the graphene and the Nb. Measurements were performed at 3 K and 2.2 K respectively.
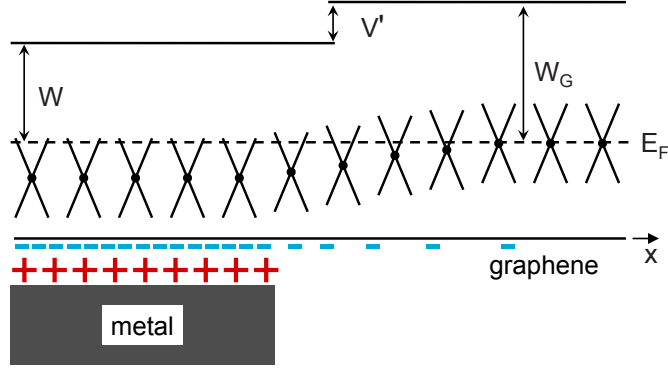
Figure 6.12: Effective Fermi shift as a function of distance for a current in-plane graphene device with a metallic contact. Reproduced from Ref. [147].

As there is a discontinuity between the work-functions of the covered and free standing graphene, electrons move from the low to the high work-function area to equilibrate E_F across the sample. The result of this band bending is a perceived doping of the graphene into the uncovered channel, whose magnitude depends on the distance away from the metal contact. The manifestation of this effect in EFE transport measurements is considered in the following section.

6.3.2 Applying the Charge-transfer Model to EFE Measurements in Graphene Devices

Nouchi *et al.* [148] proposed a simple model that accounts for the electron-hole asymmetry, observed in graphene devices with invasive contacts. They attributed the asymmetry to an effective non-uniform doping profile across the graphene channel because of doping by the metal contacts, a concept supported by scanning photocurrent microscopy measurements. The device geometry they considered was a uniform width graphene channel of length L contacted directly with metallic electrodes that dope the graphene over a length L_d away from the contacts, see Figure 6.13.

Assuming that the graphene is homogeneous parallel to the contact edge, then the total resistance, R, of the graphene channel between the source and drain contacts can be determined by integrating the resistivity over the full length of the channel L:

$$R = \frac{1}{Z} \int_0^L \rho(x)\, \mathrm{d}x = \frac{1}{Z} \int_0^L \frac{1}{\sigma(x)}\, \mathrm{d}x. \tag{6.12}$$
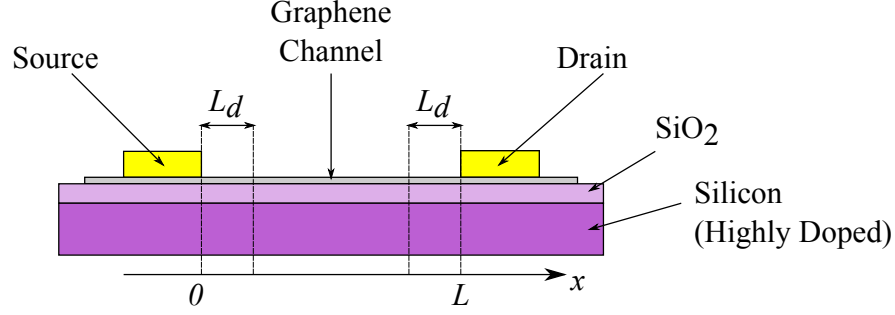
Figure 6.13: Schematic diagram of a graphene FET indicating the geometry used in the charge transfer model.

where Z is the channel width and $\rho(x)$ and $\sigma(x)$ are the local resistivity and conductivity at a distance x from the source edge respectively. Using the Drude model and assuming that the carrier density dependence on V_G obeys a parallel-plate capacitor model, the conductivity as a function of distance can be defined as:

$$\sigma(x) = \sqrt{\left\{\mu \frac{\epsilon_0 \epsilon_r}{d} V(x)\right\}^2 + \sigma_{min}^2}. \tag{6.13}$$

The local doping profile is given by $V(x) \equiv V_G - V_D(x)$ where V_G is the applied gate voltage and $V_D(x)$ is the voltage required to reach the Dirac point at a given position. Combining Equations 6.12 and 6.13 results in the following expression for the total resistance across the device:

$$R = \frac{1}{Z} \int_0^L \left(\left\{\mu \frac{\epsilon_0 \epsilon_r}{d} V(x)\right\}^2 + \sigma_{min}^2\right)^{-1/2} dx. \tag{6.14}$$

This equation can be solved easily using numerical integration if the doping profile is known. Two types of doping profile were considered by Nouchi *et al.* for modelling the effects of charge transfer from the contacts, both are shown in Figure 6.14. In the first case, Figure 6.14(a), the doping potential is pinned at the source-graphene interface ($x = 0$), varying linearly over the length L_d until it reaches the gate potential V_G. The doping profile remains at this value until it is a distance L_d from the drain-graphene interface ($x = L$), at which point it once again drops linearly to the pinned value. Varying V_G changes the doping potential within the channel at a distance L_d from the contacts, but the value at $x = 0$ and $x = L$ does not change. The second case is shown in Figure 6.14(b), whereby the potential is not pinned at the interface and V_G is free to
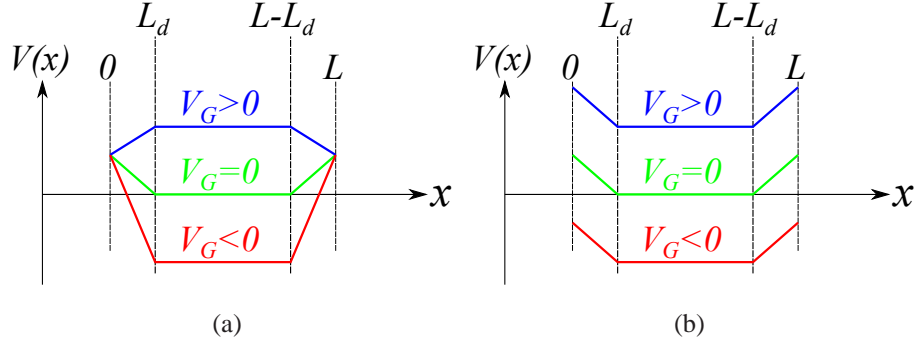
Figure 6.14: Contact induced doping across a graphene channel in which the carrier density beneath the contact is a) pinned and b) not pinned. Reproduced from Ref. [148].

Type	Function
Linear(x)	$V(x) \propto 1 - \frac{x}{L_d}$
1/x:	$V(x) \propto 1/(1 + \frac{2x}{L_d})$
$x^{-1/2}$	$V(x) \propto 1/\sqrt{1 + \frac{6x}{L_d}}$
exponential (e^{-x})	$V(x) \propto \frac{1}{1+e^{(2ln3)(2x/L_d-1)}}$

Table 6.1: Table of considered potential profiles as a function of x. $L_d/2$ is the width over which $V(x)$ drops to half its initial value at the contact edge.

modulate the doping of the entire channel, with a linear offset at the edges because of contact induced doping. From this point on we shall only consider the case where the charge-density is pinned at the interface.

To extend the work of Nouchi *et al.* several additional doping profiles beyond the simple linear case have been consider as proposed by Xia *et al.* [138]. The profiles considered are shown in Table 6.1, with a graphical example given in Figure 6.15. In the graphical example $V(x)$ is pinned at the contact edge at a value of 1.0 V and V_{G} is set to 0 V. In the linear case this results in a linear decrease in $V(x)$ over a distance of L_d at which point it is at a constant value of V_{G}.

Each field effect transistor (FET) consists of 2 contacts at either ends of the graphene channel hence the impact of doping by both contacts simultaneously must be considered. Simulated potential profiles of devices with lengths the same as those on the
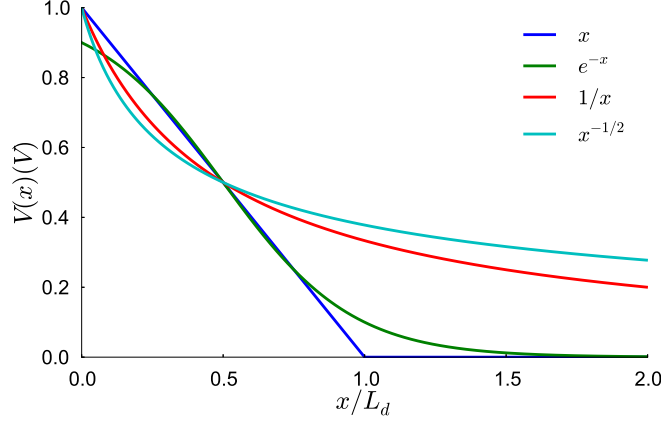
Figure 6.15: Potential steps considered in the charge transfer model.

measured fixed width TLM sample are shown in Figure 6.16. Only the simplest case where the doping varies linearly with x is shown for clarity. In this case the pinned doping level at the contacts because of charge transfer, V_{CT}, is -10 V, $V_G = 0$ V and the length at which the contact induced doping halves $L_d = 0.8$ μm. The sign of V_{CT} was selected to generate resistance curves with the same asymmetry, as seen in the experimental measurements for the etched TLM device. For $L = 9.0$, 5.5, 3.0 and 2.0 μm, $V(x)$ varies linearly from V_{CT} to V_G, with an increasing proportion of the channel affected by the contact induced doping as the channel length reduces. When $L < 2L_d$, as in the profiles for channels with $L = 1.5$ and 1.0 μm, the doping profile is a superposition of the contributions from both contacts. As a result the effective gate potential of the device does not reach V_G. Consequently, the observed position of V_{Dirac} will be shifted positively in the EFE measurements, as a result of an additional gate voltage having to be applied, to compensate for the contact induced doping.

The simulated EFE measurements based on this model for a TLM sample with $\mu = 4{,}000$ cm^2/Vs, $\sigma_{min} = 3 \times 4e^2/h$, $V_{CT} = -60$ V and $L_d = 1.2$ μm are shown in Figure 6.17, from calculations based on Equation 6.14, using the potential profiles discussed previously. The parameters are selected to generate curves in qualitative agreement with the measured TLM device and are reasonable for a graphene device on SiO$_2$ [9]. Only doping induced by an applied gate voltage or via the contacts is considered, while in actual measurements an additional doping caused by contaminants is also present, as evident by a shift in V_{Dirac} away from 0 V. Figure 6.17 shows the modelled total
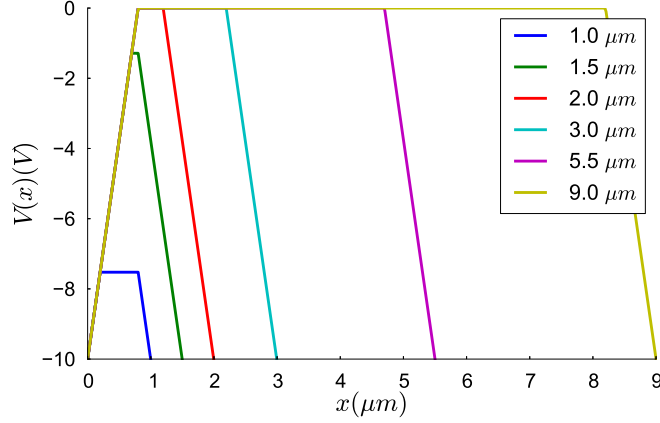
Figure 6.16: Effective gate potentials across graphene channels of varying width for $L_d = 0.8$ μm, $V_\mathrm{G} = 0$ V and $V_{CT} = -10$ V.

resistance as a function of V_G. Only the simulations for the linear doping profile are plotted for clarity.

In comparison to the measured TLM device in Figure 6.7 the model agrees qualitatively in several respects. The experimentally observed electron-hole asymmetry is successfully replicated with higher values of R$_T$ in the electron conduction regime ($V_\mathrm{G} > V_\mathrm{Dirac}$), compared to the hole conduction regime ($V_\mathrm{G} < V_\mathrm{Dirac}$). The model also predicts that very short junctions, such as in the $L = 1.0$ μm case, display a positively shifted V_Dirac and with R$_T$ remaining close to the maximum value at high gate voltages.

Fitting the modelled EFE measurements to the TLM Equation 6.3 enables equivalent plots for sheet resistance, ρ_s, and contact resistance, R_c, to be generated. These are shown in Figure 6.17 for the 4 possible doping profile functions considered. The sheet resistance for the x and e^{-x} doping profiles are symmetric about $V_\mathrm{G} = 0$ V, whereas $1/x$ and $x^{-1/2}$ show a positive shift in V_Dirac from $V_\mathrm{G} = 0$ V. In the case of $1/x$ and $x^{-1/2}$, both functions decay over a longer length scale hence doping of the graphene channel in these regimes is more pronounced. This occurs to such a degree that the carrier density in the channel is always pinned to some extent and V_Dirac is observed to shift. This shift is more pronounced for $x^{-1/2}$ than $1/x$, as the decay rate of the former function is less than that of the latter. The electron-hole asymmetry in ρ_s as a function of V_G observed in the experimental data for both etched and unetched devices is also replicated by the model in the $1/x$ and $x^{-1/2}$ doping regimes. This suggests that they

138
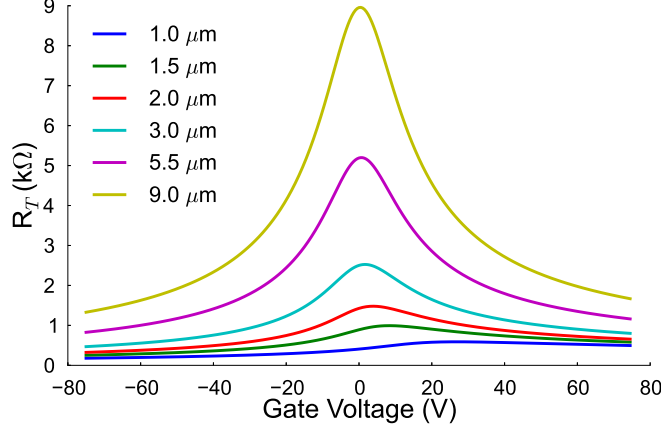
Figure 6.17: Simulated EFE measurements based on charge transfer model with V_{G} plotted as a function of R_T.

are the closest to the physical situation, which is in good agreement with theoretical predictions of the expected contact induced doping profile[149].

The gate dependence of R_c generated by the model, shown in Figure 6.18(b), also replicates key features observed experimentally in the fixed width device, shown in Figure 6.8(c). In particular, a dip in R_c at V_{Dirac} is shown with larger (smaller) values of R_c for $V_{\text{G}} > V_{\text{Dirac}}$ ($V_{\text{G}} < V_{\text{Dirac}}$). Again, the impact of considering a $x^{-1/2}$ or $1/x$ profile is more pronounced than the x and e^{-x} profiles for the same arguments made earlier. Where the model clearly fails is the expectation of a negative R_c close to V_{Dirac} which is clearly not observed experimentally. It must be considered that the calculated R_c from contact induced doping is only one component of the actual measured contact resistance. To model this the following form of specific contact resistance is considered:

$$\rho_c(V_g) = Z \left((A \times f_s(V_g - V_{\text{Dirac}}) + B \times f_c(V_g - V_D) + R_{\text{series}}) \right), \qquad (6.15)$$

where f_s and f_c are the modelled sheet resistance and contact resistance functions respectively, Z is the width of the device, A and B are scaling pre-factors and R_{series} is a series resistance. While the sheet resistance should not contribute to the measured ρ_c, the contact resistance has been observed in Pd contacted devices to be of a similar form[138] and so such a contribution is a reasonable assumption. The pre-factors A and B account for discrepancies between the original parameters (μ, σ_{min}, V_{CT}

139
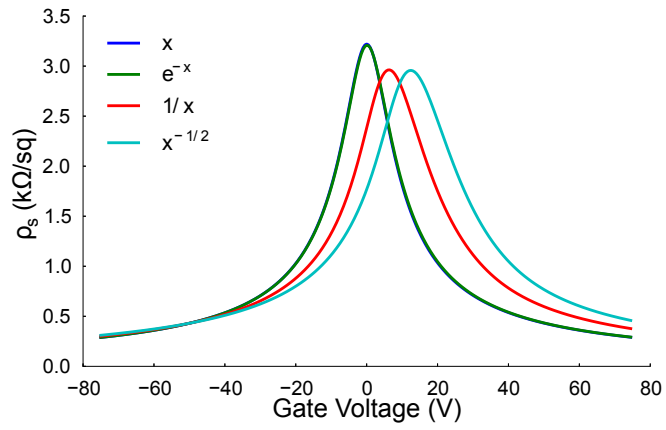
(a)
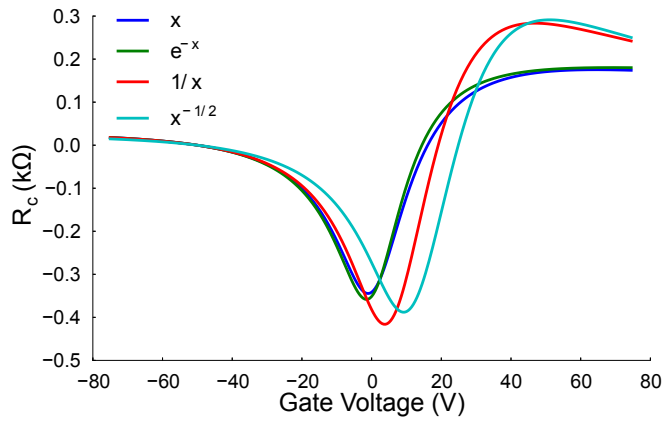
(b)

Figure 6.18: Simulations of a) calculated sheet resistance and b) calculated contact resistance based on charge transfer model.
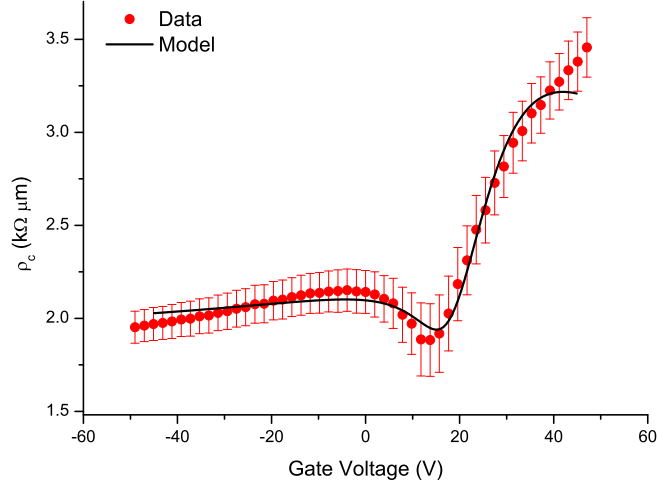
Figure 6.19: Comparison between experimental data and the developed model for specific contact resistance as a function of applied gate voltage.

and L_d) used in the EFE model (from which f_s and f_c were generated) and those in the experimental system. The series resistance accounts for any resistance from the measurement lines or because of any damaged graphene under the contact, which was not included in the original model. Finally, the parameter V_{Dirac} is included, to account for any additional extrinsic doping in the experimental sample from surface contaminants for example. For the fitting procedure, f_s and f_c generated from the $1/x$ doping profile result were used because they produced an asymmetric ρ_s in agreement with the experimental data.

The result of fitting the model in Equation 6.15 to the experimental data obtained from the etched device, via a least squares method, is shown in Figure 6.19 with the fitting parameters used shown in Table 6.2. It is clear that the model is in good agreement with the experimental data and is within the experimental errors. The parameters obtained from the least squares fit are also realistic, with a value of A that suggests that the intrinsic gate dependent contact resistance mirrors the sheet resistance, yet is of a smaller magnitude. The value of B indicates that the initial model has underestimated the magnitude of the contact resistance. The gate independent R_{series} suggests there is an additional series resistance, which is likely to be unassociated with the graphene sheet. Possible sources of this resistance are remnant resist between the contact and the graphene, amorphisation of the graphene beneath the contact or parasitic resistances at

Parameter	Value
Doping Function	$1/x$
μ	4,000 cm^2/Vs
σ_{min}	3×4 e^2/h
V_{CT}	-60 V
L_d	1.2 μm
A	0.44[†]
B	1.7[†]
V_{Dirac}	13.1 V[†]
R_{series}	0.83 kΩ[†]

[†] Fitted using least squares method.

Table 6.2: Table of parameters used in contact resistance model.

the metal-metal interfaces of the device.

While the model provides a good fit there are clearly some discrepancies. This is most likely caused by the way in which the initial modelling parameters were selected. σ_{min} was overestimated to generate a peak in the EFE model that was comparable to the measured values, while not taking into account the series resistance present. Based on the theoretical value for ΔE_F, predicted for Pd(111) on graphene being -0.45 eV[147], the equivalent V_{CT} can be calculated using:

$$V_{CT} = \frac{1}{\pi\alpha}\left(\frac{E_F}{\hbar v_F}\right)^2, \tag{6.16}$$

where $\alpha = 7.2\times 10^{10}$ cm^{-2} V^{-1} for a substrate with 300 nm of SiO$_2$. The calculated value for Pd(111) on graphene is $V_{CT} = -200$ V which is greater than that used in the model, however, this assumes a clean interface between the Pd and graphene and that the graphene beneath the metal is not damaged by the deposition procedure. The contact is also a Pd/Nb bilayer, which could result in an adjustment in the work-function of the Pd and subsequently alter ΔE_F [150], although with a Pd thickness of 3 nm this effect should be minimal[151]. The lower value of V_{CT} used in the model could explain why B > 1, as it needs to compensate for the underestimated contact doping. A reduction in μ would broaden the modelled ρ_c with respect to V_G, which could also give a better fit.

Finally, the discordance between the results for ρ_c between the etched and unetched samples must be considered. While the etched sample clearly shows evidence for charge-density pinning by the contacts, the unetched sample does not. This is possibly because of the etched sample having an additional step of lithography performed upon it or because of damage at the edges of the sample via the plasma etching procedure, promoting charge transfer by an unidentified mechanism. Alternatively, a high contact resistance in the unetched sample is masking any effect from charge transfer, which is worsened by the large amount of error in the measurement because of the fitting procedure used. More devices would have to be fabricated in order to determine whether the difference between etched and unetched samples is universal, or if it is entirely sample dependant.

6.4 Depositing Metals on Graphene

While the carbon-carbon bond in graphene is particularly strong, making graphene a relatively robust material, it comes as no surprise that it is easily damaged given that it is only 1 atom thick. It is thus necessary to consider the possibility of graphene damage during contact deposition and the impact this can have on device performance.

In this section the impact of depositing metals on graphene is discussed. The possibility of damage to the graphene from the sputtering of contacts is investigated, in order to account for the large contact resistances measured. The contact resistance measurements presented in this chapter are then compared to those available in the literature and the impact this may have on superconductor-graphene hybrid devices discussed.

6.4.1 Sputter Induced Disorder

To investigate the impact of sputter deposition on graphene flakes, Raman spectra on several graphene samples were taken before and after sputtering. Furthermore, sputtering was performed at a range of different powers, to investigate the dependence of damage to the graphene on the kinetic energy of the incident atoms.

A total of 8 graphene flake samples were identified and characterised using Raman spectroscopy (laser excitation wavelength $\lambda = 633$ nm) on 5 Si/SiO$_2$ substrates. All samples showed clear graphene signatures before sputtering with prominent features

at around 1565 cm^{-1} and 2650 cm^{-1} corresponding to the characteristic G and 2D peaks respectively. These flakes were then sputtered with 2 nm of Pd in Ar gas (flow = 24 standard cubic centimetres per minute) with powers of 2, 4, 8, 16 and 24 W respectively (background pressure = 2×10^{-8} Torr).

Following sputtering, only 1 flake showed a clear carbon signature, in the form of prominent G and 2D peaks at 1581 cm^{-1} and 2655 cm^{-1} respectively. The normalised Raman spectra taken on this flake before and after sputtering are shown in Figure 6.20. After sputtering the G peak has shifted to 1560 cm^{-1} and the 2D peak is not present. An additional D peak has emerged at 1311 cm^{-1} and a small feature visible at 1591 cm^{-1} (the D' peak) is also present.

An amorphisation trajectory was established by Ferrari *et al.* (summarised in Ref. [63]), in which the evolution of graphite $\rightarrow$ nanocrystalline graphite $\rightarrow$ low sp^3 amorphous carbon $\rightarrow$ high sp^3 amorphous carbon can be identified using Raman spectrometry. The first stage (graphite $\rightarrow$ nanocrystalline graphite) manifests itself in the Raman spectra in the following ways[63]. Firstly the D peak appears and the ratio of intensities of the D and G peak, I$_D$ and I$_G$ respectively, increases in accordance with the Tuinstra-Koenig[152] (TK) relation. The D' peak also appears and the FWHM of all the peaks broaden because of increased disorder.

The TK relation is given by:

$$\frac{I_D}{I_G} = \frac{C(\lambda_L)}{L_a}, \tag{6.17}$$

where L_a is the in-plane correlation length (cluster size) in nm and $C(\lambda_L)$ is a proportionality constant dependent on laser excitation energy. An empirical relationship between C and λ for visible wavelengths was found by Matthews *et al.* [153]:

$$C(\lambda) \approx C_0 + \lambda_L C_1, \tag{6.18}$$

where C_0 and C_1 were found experimentally to be -12.6 nm and 0.033 respectively. A laser wavelength of 633 nm was used during these measurements which corresponds to C ≈ 8.3 nm.

The second amorphisation stage (nanocrystalline graphite $\rightarrow$ low sp^3 amorphous carbon) is characterised by the G peak position decreasing by ~ 90 cm^{-1} because of the softening of the phonon modes as a result of increasing disorder. The TK relation
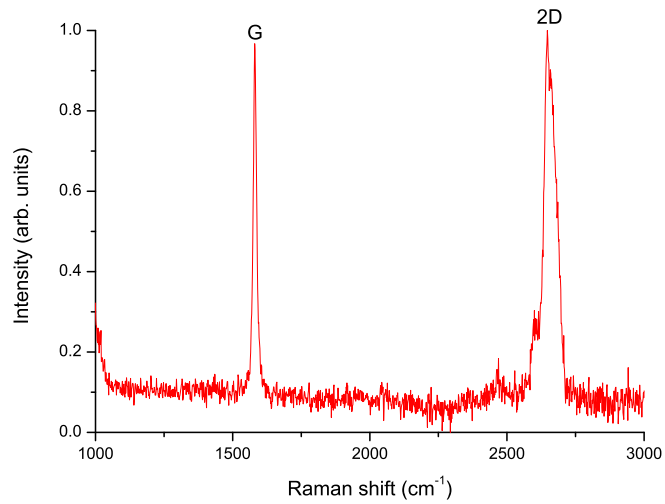
(a) Before sputtering
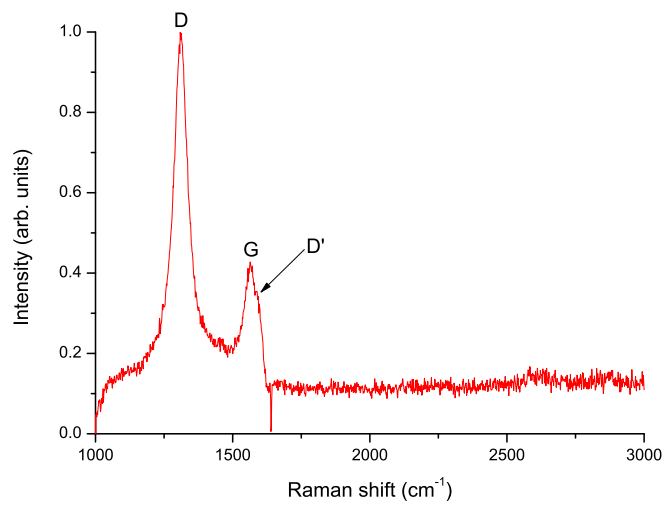
(b) After sputtering

Figure 6.20: Raman spectra for a graphene sample a) before and b) after sputtering Pd on top.
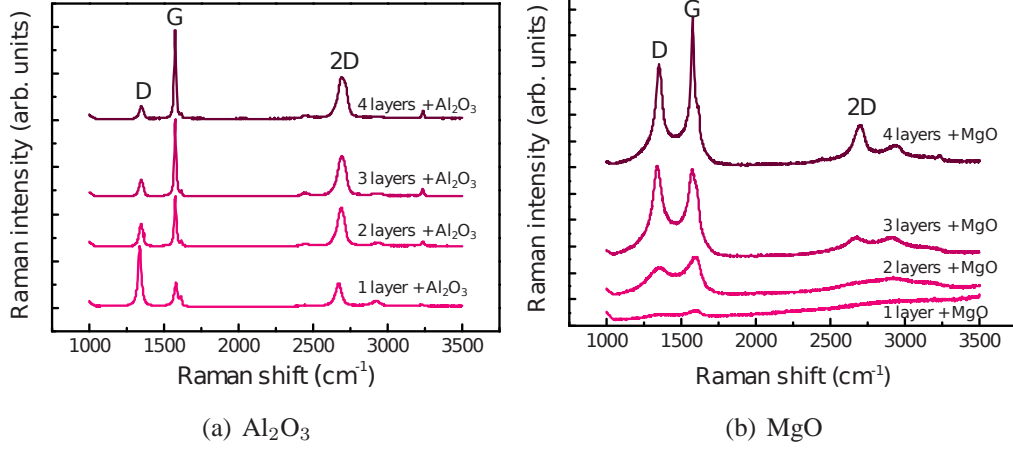
Figure 6.21: Raman spectra taken on graphene flakes of varying thickness after magnetron sputtering of a) Al_2O_3 and b) MgO. Taken from Ref. [155].

is no longer valid and $I_D/I_G \rightarrow 0$ as the amount of amorphous carbon increases. This is coupled with increasing dispersion of the G peak and an absence of the second-order Raman peaks. In the amorphous carbon regime the peak intensity ratio based on the TK relation is replaced by the following relation proposed by Ferrari *et al.* [154]:

$$I_D/I_G = C'(\lambda_L)L_a^2. \tag{6.19}$$

As the transition from nanocrystalline graphite to amorphous carbon occurs at $L_a \sim$ 2.0 nm, C' can be found by solving Equations 6.17 and 6.19 simultaneously. Using this method $C'(633 \text{ nm}) \approx 100 \text{ nm}^{-2}$.

In the Raman spectrum of the graphene sample before sputtering, shown in Figure 6.20(a), there is no D or D' peak, indicating that the sample is highly crystalline and free from disorder. This is in contrast to the spectra of the sample post sputtering as shown in Figure 6.20(b). In this spectra there is a pronounced D peak, broadened G peak and the emergence of the D' peak which would tend to indicate the formation of nanocrystalline graphene. Based on the TK relation, Equation 6.17, the sample consists of graphene islands with $L_a \sim$ 2.9 nm. This conclusion would be valid, if not for the suppression of the 2D peak, which is a key signature of the formation of low sp^3 amorphous carbon. In this regime TK no longer holds and instead L_a must be calculated using Equation 6.19 from which $L_a \sim$ 1.7 nm is found.

Similar results were reported by Dlubak *et al.* [155] in which they deposited Al_2O_3 and MgO via DC and RF magnetron sputtering respectively onto graphene flakes, with varying a number of layers, the results of which are presented in Figure 6.21 for comparison. For the samples where Al_2O_3 was deposited, the amount of disorder decreases with an increasing number of layers, indicated by a reduction in the D' peak intensity, lower D/G peak ratio and a decrease in the 2D peak intensity. They also observed that the number of layers affected by sputtering reduced with increasing total number of graphene layers which they attributed to a reduction in sp^2 bond bending disorder with increasing number of layers. The MgO deposited samples show a more pronounced effect, with a larger suppression of the 2D peak for fewer layers of graphene. The 1 layer graphene + MgO growth result is comparable to that of the 7 other flakes measured in this study.

The sample presented in Figure 6.20 continued to show a graphitic response compared to the other samples for two reasons. Firstly, the sample was grown at 4 W which is the second lowest power in the study. This should result in the impinging metal atoms having less kinetic energy, so fewer carbon atom dislocations should occur. Secondly, the G and 2D peaks before sputtering are of equal height, suggesting that the sample is a bilayer, which should be more robust according to the study of Dlubak *et al.* [155].

These measurements indicate that sputtering Pd onto graphene causes significant damage to the graphene structure, resulting in amorphous carbon beneath the contacts. It is possible that minimising this effect can be achieved through reduction of sputtering power and the use of thicker graphene where applicable. Additionally, the use of higher argon pressures when sputtering could increase the amount of diffusion of deposited metal clusters, reducing their kinetic energy and hence the likelihood of graphene damage. While graphene has been successfully contacted using magnetron sputtering, as shown in the transport measurements presented in this thesis, the amorphisation of graphene under the contacts is likely to have an impact on the transport properties. The contact resistance is likely to be higher in these samples because of a decrease in conductance as graphene becomes more disordered[156]. Moreover it would be difficult to observe interface dependent phenomenon such as Andreev reflection in devices in which the graphene has been amorphised by sputtering. Conse-

quently, an alternative deposition technique such as electron beam evaporation would be more appropriate, when fabricating graphene devices.

6.4.2 Comparison with Literature

A summary of the contact resistance measurements made on graphene devices in the literature is presented in Table 6.3. This list is by no means exhaustive, presenting only studies that were primarily concerned with contact resistance. Some studies erroneously gave the contact resistance in units of $\Omega\mu m^2$, resulting from the belief that charge injection occurred over the entirety of the contact, often through overconfidence in the value of L_T extracted using the TLM method. Where possible ρ_c has been converted from $\Omega\mu m^2$ to $\Omega\mu m$ using the contact length quoted in the literature. Comparison is further complicated by studies being performed on samples prepared using a range of metal deposition techniques, in chambers with different base pressures and contact material choices. Transport measurements were also performed at a range of temperatures and gate voltages, which again can greatly alter the value of ρ_c obtained. Franklin *et al.* also observed an order of magnitude increase in contact resistance as the length of the contact, L_c was reduced from $200 \rightarrow 20$ nm[157]. The values of ρ_c included in the table are thus presented for devices with $L_c > 200$ nm, to avoid discrepancies as a result of having different contact lengths.

The primary reason for choosing Pd as an adhesion layer between the graphene and Nb was because of the prevalence of Pd/Nb bilayers in studies on superconducting carbon nanotubes[48–52]. The contact resistance data presented in Table 6.3 also supports this selection, with some of the lowest values of ρ_c reported with Pd contacts with Xia *et al.* [138] and Watanabe *et al.* [164] reporting $\rho_c \sim 100\,\Omega\mu m$ and $500\,\Omega\mu m$ respectively. From the wide selection of contact materials investigated by Watanabe *et al.* Pd, Ni and Co were found to have the lowest ρ_c closely followed by Ti. Ni and Co are ferromagnetic elements and so would make poor adhesion layer choices for a superconducting device, as magnetism and superconductivity are typically antagonistic phenomenon[165]. Hence Pd is expected to be an ideal candidate for making contact to graphene in superconducting devices.

The gate dependent ρ_c in our devices was $1.7 - 3.6 \times 10^3\,\Omega\mu m$ and $2.5 - 6.5 \times 10^3\,\Omega\mu m$ for the etched and unetched samples respectively. This is greater than the

Author	Material	Thickness (nm)	$\sim \rho_c$ ($\Omega\mu$m)	Metal Deposition	Base Pressure (Torr)	Reference
Danneau	Ti/Au	10/40	$< 4 \times 10^2$	E-beam	2.5×10^{-8}	[158][a]
Franklin	Ti/Pd/Au	0.5/20/30	2×10^2	—	—	[157][b]
Heersche	Ti/Al	10/70	$< 2.5 \times 10^2$	E-beam	8×10^{-9}	[31][a]
Huang	Ti/Pd/Au	0.5/20/30	7.5×10^2	E-beam	—	[159]
	Ni/Au	30/20	2×10^3			
	Ti/Au	5/50	1×10^4			
Liu	Ti/Au	9/80	2×10^3	E-beam	—	[160; 161]
	Ti/Au	9/80	1×10^4	Sputtering		
Malec	Cu	35	6×10^2	Thermal evap.	1×10^{-7}	[162]
Nagashio	Ni	25	5×10^2	Thermal evap.	7.5×10^{-8}	[135; 163]
	Cr/Au	10/20	1×10^3-1×10^6			
	Ti/Au	10/20	1×10^3-1×10^6			
Russo	Ti/Au	10/25	8×10^2	E-beam	8×10^{-7}	[139]
Venugopal	Ni	60	2.5×10^3	E-beam	—	[136]
Watanabe	Ti	100	8×10^2	E-beam	7.5×10^{-8}	[164]
	Ag	100	2×10^3			
	Cr	100	3×10^3			
	Fe	100	2×10^2			
	Co	100	3×10^2			
	Ni	100	3×10^2			
	Pd	100	5×10^2			
Xia	Pd/Au	25/25	1×10^2	—	—	[138]

[a] ρ_c quoted in Ref. [139].
[b] Contacts on CVD graphene.

Table 6.3: Summary of contact resistance measurements presented in the literature.
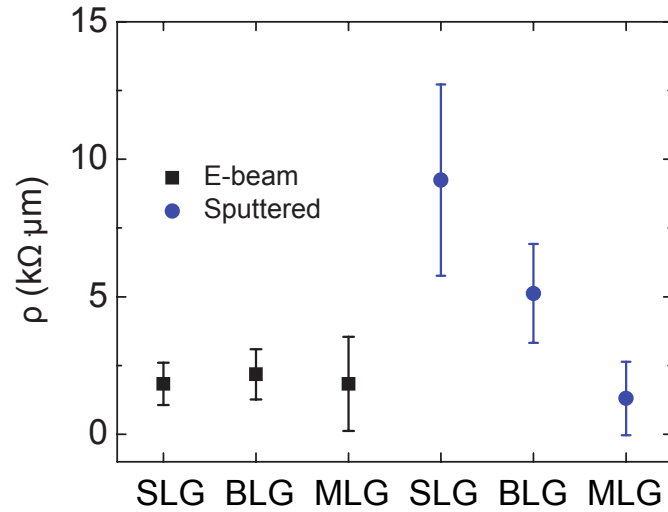
Figure 6.22: Graph of average contact resistance versus number of graphene layers for graphene devices with contacts deposited by electron beam evaporation and sputtering. SLG, BLG and MLG represent single-layer, bi-layer and many-layer graphene respectively. Taken from Ref. [161].

majority of studies presented in the literature, although Nagashio *et al.* [135; 163] did measure ρ_c of similar magnitude for thermally evaporated Cr/Au and Ti/Au contacts, as did Huang *et al.* [159] for Ti/Au contacts deposited by electron beam evaporation. The relatively large values of ρ_c measured in our devices, can be attributed to the use of sputtering to deposit the contacts. Liu *et al.* [160; 161] performed a comparative study of metal deposition on graphene via electron beam evaporation and DC magnetron sputtering, the results of which are shown in Figure 6.22. They observed a fivefold increase in ρ_c for sputtered single layer samples, compared to electron beam evaporated samples. The impact of sputtering was reduced in bi-layer samples and ρ_c for sputtered many-layer samples was comparable to electron beam evaporated samples, suggesting that only the upper few layers are damaged by graphene deposition, consistent with Raman spectroscopy data taken on sputtered samples as discussed in Section 6.4.1. The invariance of ρ_c when electron beam evaporation was used - even when accounting for graphene flakes of varying thickness - suggests that this deposition method leaves the graphene relatively intact. Liu *et al.* [160; 161] also observed an order of magnitude increase in ρ_c for larger sputtering powers, although the powers used were not quantified by the authors. While ρ_c for our devices is lower than
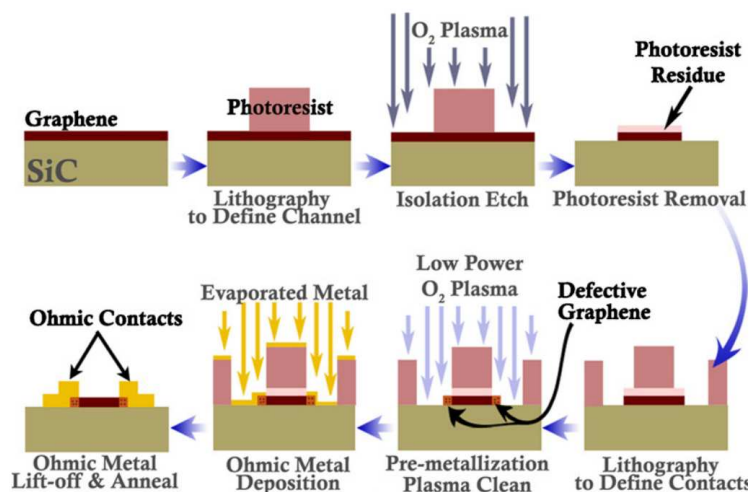
Figure 6.23: Low contact resistance device fabrication procedure performed by Robinson *et al.* using O_2 plasma. Taken from Ref. [137].

measured by Liu *et al.* for single-layer graphene, this could be attributed the benefit of using Pd instead of Ti for the contact.

The fact that sputter deposition induced damage would cause an increase in contact resistance is not immediately apparent. Robinson *et al.* [137] reported a reduction of contact resistance from 10^{-4} to 10^{-7} Ωcm^2 in epitaxially grown graphene samples on SiC, after selectively treating them with O_2 plasma, before metal deposition followed by annealing, see Figure 6.23. They attributed an improvement in ρ_c to the removal of resist residue by the low power O_2 plasma (confirmed by X-ray photoelectron spectroscopy) despite the simultaneous damage to the underlying graphene (confirmed by Raman spectroscopy). It is likely that in this situation the improvement in ρ_c from the removal of resist residue outweighs the increase in ρ_c from the amorphisation of the graphene beneath the contact. Sputtering affords no such benefit, as it only damages the graphene without removing the resist residues.

With regard to superconductor-graphene devices, the only reported contact resistance measurement is on Ti/Al contacted SGS JJs in the seminal experimental work of Heersche *et al.* [31]. They reported a value of $\rho_c < 2.5 \times 10^2$ $\Omega\mu\text{m}$, which is amongst the smallest reported for any graphene device. This is most likely attributable to the UHV base pressure of their electron beam evaporation growth system, as there appears

to be a correlation between base pressure and ρ_c, when comparing the otherwise similar devices of Heersche[31], Danneau[158] and Russo *et al.* [139]. Whether such a low contact resistance is required for SGS devices remains to be determined, however other groups that have successfully observed a supercurrent do explicitly state a need for highly transparent contacts[33].

6.4.3 Discussion of Recent Results on SGS Devices with Sputtered Contacts.

During the course of writing this thesis, results have been published in which a supercurrent was successfully observed in a SGS with Ti (4 nm) Nb (40 nm) contacts sequentially deposited via magnetron sputtering[47]. A schematic of the device geometry as produced by Rickhaus *et al.* is shown in Figure 6.24(a), with false colour SEM images of narrow and wide devices shown in Figures 6.24(b) and 6.24(c) respectively. The contacts were characterised using a 100 μm by 10 μm Ti/Nb test strip, from which the critical temperature, $T_c = 8.5$ K was measured.

The EFE measured on the thin sample is shown in Figure 6.25(a), showing V_{Dirac} very close to 0 V, with a conductance minimum at $G \approx 5e^2/h$ and quoted field effect mobility of $\mu \approx 3,000$ cm^{2}V^{-1}s^{-1}, which is below what we typically measure. IV measurements performed at $T = 20$ mK on the wide sample shown in Figure 6.25(b) indicate the presence of a supercurrent and a critical current, I_c which is gate dependent. $I_c \sim 10$ nA at $V_{\text{G}} = 0$ V for the junction with $W = 30$ μm and $L = 400$ nm. This is a particularly small value for I_c, given the relatively large dimensions of the device. Assuming a similar conductance for this junction as that in Figure 6.25(a) and using $R = L/(GW)$ the $I_c R_n$ product, where R$_n$ is the normal state resistance, is found to be ~ 0.65 μV at $V_{\text{G}} = 0$ V. A survey of the literature as presented in Table 6.4 indicates that this value of $I_c R_n$ is several magnitudes lower than measured in other devices.

The relationship between $I_c R_n$ and T in a Josephson junction was modelled by Likharev[167]. The result of this model is shown in Figure 6.26 for several values of L/$\xi_n(T_c)$ where $\xi_n(T_c)$ is the coherence length in the weak-link between the two superconducting contacts (in this case graphene) when T = T$_c$. In broad terms, $I_c R_n$ is shown to increase as L/$\xi_n(T_c) \rightarrow 0$ and decreases as T $\rightarrow$ T$_c$. ξ_n was measured in a SGS junction to be 260 nm[37], assuming other SGS devices have comparable values

(a)

(b)

(c)
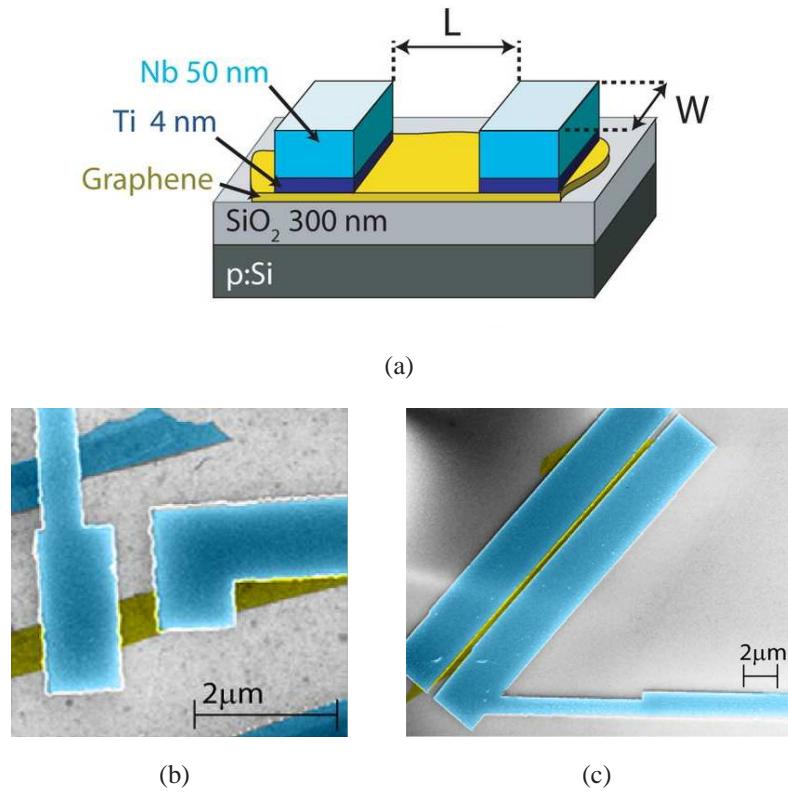
Figure 6.24: A schematic of Rickhaus *et al.*'s Ti/Nb contacted graphene SGS device structure is shown in a). b) and c) show false colour SEM images of two different devices, with the superconducting contacts shown in blue and the contacted monolayer graphene flake in yellow. Taken from Ref. [47].

Author	Material	T_c (K)	Metal Deposition	$\sim I_c R_n (\mu V)$	T (mK)	Reference
Du	Ti/Al	1.0	E-beam	60	200	[32]
Heersche	Ti/Al	1.3	E-beam	60	30	[31]
Jeong	PbIn/Au	4.8	Thermal evap.	150	6	[40]
Ojeda-Aristizabal	Pt/Ta/Pt	2.5	E-beam	50	60	[37]
Rickhaus	Ti/Nb	8.5	Sputtering	0.65	30	[47]

Table 6.4: Summary of $I_c R_n$ for devices in the literature.

(a)   (b)
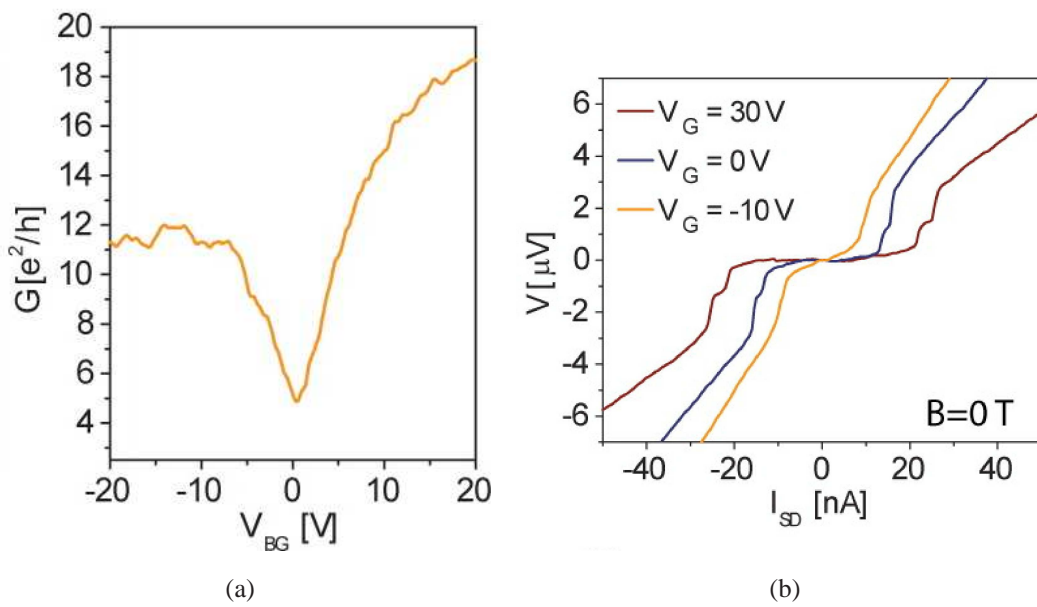
Figure 6.25: Transport measurements performed on Ti/Nb SGS device showing a) conductance as a function of V_G and b) IV curves taken at several values of V_G indicating the presence of a supercurrent. Measurements were performed at T = 20 mK. Taken from Ref. [47].
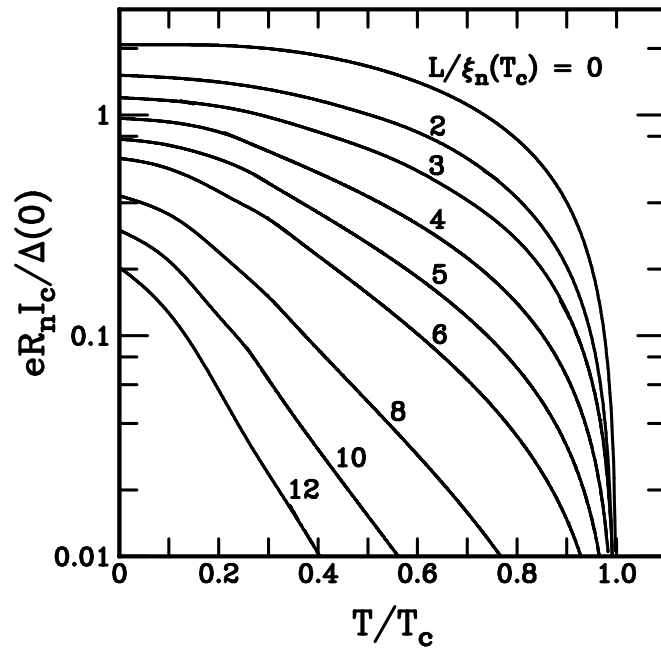
Figure 6.26: Dependence of normalized $I_c R_n$ on temperature based on the microscopic theory developed by Likharev for a superconductor/normal-metal/superconductor Josephson junction. Curves for $L/\xi_n(T_c)$ = 0, 2, 3, 4, 5, 6, 8, 10 and 12 are shown[166].

and knowing L = 400 nm in the Ti/Nb device, it is likely that the device will show an $I_c R_n$ dependence similar to the $L/\xi_n(T_c) = 0$ or 2 curves.

For $0.3 T_c < T < T_c$ a simplified form of the critical current is:

$$I_c \propto \frac{|\Delta(T)|^2 \exp\left(-\frac{L}{\xi_n}\right)}{T_c \xi_n}. \tag{6.20}$$

It is clear that there is a strong dependence on the temperature dependent superconducting band gap, $\Delta(T)$, which, given that $\Delta(0) \propto T_c$, we would expect $I_c R_n$ to increase with T_c. In this respect the Ti/Nb contacted devices clearly underperform with $I_c R_n$ far lower than Ti/Al devices, despite having a higher T_c. The measurement temperature cannot account for this as the devices were measured at $T = 30$ mK, which is well below T_c. A likely cause of the low value of $I_c R_n$ is an increase in damage to the underlying graphene when depositing contacts via sputtering, rather than using electron beam evaporation, which is in agreement with contact resistance measurements as discussed in Section 6.4.2.

The authors also state that a minimum of 4 nm of Ti must be used to observe superconductivity in their samples. It is possible that the Ti is acting as a momentum buffer during sputtering, shielding the graphene from the impact of the Nb atoms during growth. Ti is a relatively light element, and so should damage the graphene less during deposition. This would imply that Ti is preferable to Pd (which is a heavier element) for sputtering on graphene, because of a reduction in transferred momentum.

Ultimately SGS devices with sputtered Ti/Nb contacts show no benefit over evaporated Ti/Al devices, in terms of operating temperature, despite the significantly higher T_c of the contacting metal. The benefit of such a device is the higher critical field of Nb compared to Al, which allows superconducting and high field phenomenon to be observed at the same time, and the interplay between them investigated.

6.5 Conclusion

In this chapter the transfer length method has been used to establish the contact resistance of our graphene devices contacted with Pd/Nb bilayers. The method was applied to both an irregularly shaped sample and a sample with a uniform width achieved

through etching. Both devices demonstrated contact resistances with gate voltage dependencies with a maximum (minimum) in contact resistance observed at V_{Dirac} in the unetched (etched) device. At V_{Dirac} the contact resistance of the unetched and etched devices were found to be 5.5 ± 1.0 kΩμm and 1.9 ± 0.3 kΩμm. The discrepancy between the two devices could be because of the additional fabrication steps required to produce the etched device. Surveying the literature, there is clearly significant variability in contact resistance, depending on factors such as the fabrication method used, choice of contact material and the metal deposition environment. Hence, the contact resistances in the literature span a range from 100 Ωμm to 1 MΩμm.

The use of highly energetic metal deposition techniques, such as magnetron sputtering, is likely to be a key contributor to large contact resistance measurements. Raman measurements performed before and after sputtering of a thin layer of Pd, clearly show that the graphene underneath the contact transformed into amorphous carbon because of sputtering. As a result, sputtered contacts almost universally show higher contact resistance than devices with contacts deposited using a less energetic procedure, such as electron beam evaporation. A low interface transparency has been identified as limiting the magnitude of the critical current in graphene based Josephson junctions (refer to Section 2.6) and so alternatives to direct sputtering of metals in this class of devices should be considered to ensure optimum performance.

Finally, the asymmetry observed in the etched transfer length measurement device, has been understood in terms of the doping of the graphene by the metal contact by the formation of an interface dipole. The model first developed by Nouchi *et al.* [148] considered only a linear decay of the contact induced doping extending into the graphene channel. This has been extended further to explore other possible decay profiles. It was found that a $1/x$ decay gave the best possible fit to the experimental data which is in good agreement with the doping profile predicted by theory.

CHAPTER 7

Opto-electronic Response of Graphene
Devices

While the transport measurements presented in the previous chapters provide a great deal of information about the graphene devices, there is a disadvantage in that they give very little information regarding any spatial variations in the samples' properties. Owing to its marked opto-electronic response, graphene has become a possible candidate for incorporation into photodetectors and photovoltaic devices. Furthermore, there is the possibility of probing the properties of graphene devices by scanning a laser over a device and measuring the generated photocurrent (PC) as a function of laser position, in a technique known as scanning photocurrent microscopy (SPCM). One possibility this opens up is the ability to establish in what manner the position of E_F varies across a given device.

In this chapter, the basic theory behind SPCM is presented, as well as a description of how the Raman system was utilised to perform these measurements. This is then followed by SPCM measurements taken on several devices, which not only show the generation of a photocurrent in our devices, but also confirm the p-type doping of our Pd/Nb contacts, as was suggested by the transfer length measurements presented in Chapter 6.

7.1 Photocurrent Generation in Graphene Devices

There are three main mechanisms that have been established to explain the generation of a PC in graphene devices when stimulated by a laser source. The first mechanism is the photovoltaic effect, whereby photoexcited electron-hole pairs are accelerated in opposite directions by the presence of an electric field. A PC is measured when either these accelerated charge carriers reach the contacts or because of the establishment of a local photovoltage at the laser excitation spot, which acts to drive a PC through the rest of the device[168]. Lee *et al.* [169] were the first to measure an opto-electronic response in a graphene device and they attributed the generated PC entirely to the photovoltaic effect. Several other authors confirmed this mechanism as a source of PC in graphene devices[14; 108; 170] and it provides a particularly convincing explanation of the strong photoresponse measured at graphene-metal interfaces.

Despite the success of the photovoltaic model it proves insufficient to explain the polarity of the PC as a function of V_G in a myriad of graphene based devices, such as top-gated p-n structures[111] or graphene monolayer-bilayer junctions[171]. These

results can be explained by a contribution to the PC from the thermoelectric (Seebeck) effect. When there is a thermal gradient across a metal, electrons at the hotter end have greater velocities than those at the cold end. For this reason, a net diffusion of electrons from the hot end to the cold end occurs, until the generated electric field resulting from the charge imbalance acts to stop any further diffusion of hot electrons. The result of this effect is that a potential difference ΔV is generated across the metal, with the hot end at positive potential. The generation of a potential difference across a sample through this process is known as the Seebeck effect. The magnitude of this potential difference is given by:

$$dV = SdT, \tag{7.1}$$

where S is a material dependent parameter, known as the Seebeck coefficient (or thermoelectric power). When two metals, A and B, with Seebeck coefficients S_A and S_B respectively are joined, a thermo-voltage is measured across the A-B interface. Assuming S_A and S_B are approximately constant over the temperature range investigated, the thermo-voltage can be calculated:

$$V_{AB} = (S_B - S_A)\Delta T, \tag{7.2}$$

where ΔT is the temperature gradient across the junction. This device geometry is otherwise known as a thermocouple and is a common way of measuring temperature. The Seebeck coefficient is related to the electrical resistance, R, through the Mott formula, which in graphene takes the form[110; 126]:

$$S = \frac{\pi^2 k_B T}{3e} \frac{1}{R} \frac{dR}{dV_G} \left. \frac{dV_G}{dE} \right|_{E=E_F}, \tag{7.3}$$

A graphical representation of the variation in S with E_F as predicted by Equation 7.3 for a graphene sample is shown in Figure 7.1. In a graphene sample it is also possible to have spatial variations in E_F (and R) and as a result S can also vary spatially. When irradiating the sample with a laser light source, electrons are excited from the valence band into the conduction band. These electrons then relax back to E_F by phonon emission, to form a distribution of hot fermions, which can be detected as a PC because of this thermoelectric effect. This has been unambiguously demonstrated in top-gated graphene FET devices[109; 110], by showing a PC that depends on the top-gate and back-gate voltage in such a way that can only be explained by the nonmonotonically
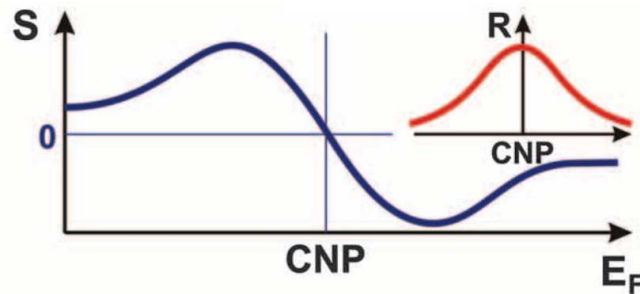
Figure 7.1: Schematic showing the magnitude of the Seebeck coefficient in graphene as a function of E_F with respect to the Dirac point. The inset shows the characteristic resistance response for comparison. Taken from Ref. [110].

varying Seebeck coefficient predicted for graphene, as shown in Figure 7.1, generating a photovoltage in accordance with Equation 7.2.

The third PC generation mechanism that has been suggested is the bolometric effect, where a change in current is measured as a result of the laser heating the device, changing its overall resistance. This mechanism is only applicable to devices under bias and is only of appreciable magnitude at relatively large source-drain biases. Bolometric effects aside, establishing the relative contributions to the PC from the photovoltaic effect and thermoelectric effect is a non-trivial problem, which is only now being addressed[168]. As such, the following work in the remainder of this chapter will be presented in terms of there being an appreciable photovoltaic effect, although there could be a sizeable contribution from the thermoelectric effect.

7.2 Experimental Set-up

A typical set-up used to measure the opto-electronic response of graphene is shown in Figure 7.2. A graphene sample is placed on a Si/SiO$_2$ substrate and contacted with source-drain electrodes forming a FET. The carrier density in the graphene flake is modified via the field effect through the application of a gate voltage to the highly doped Si substrate. The potential between the source-drain contacts is measured with a voltmeter, in this case via a SR560 low noise voltage pre-amplifier coupled to the DAC (see Figure 3.8 for more details).
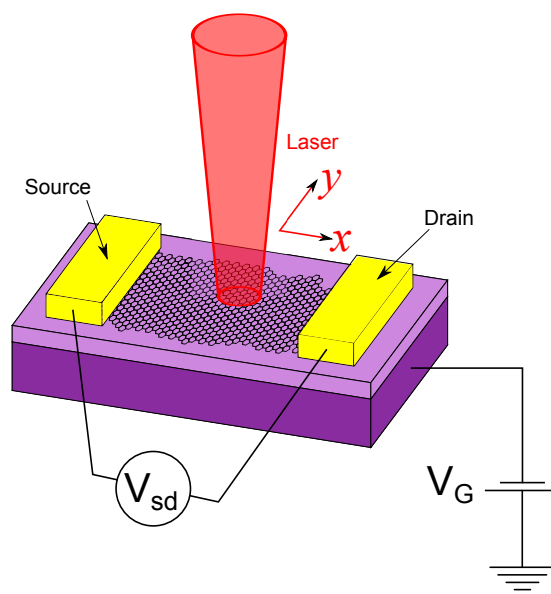
Figure 7.2: Scanning photovoltage microscopy measurement set-up. The laser spot is moved across the sample in the $x - y$ plane while the source-drain voltage is measured. A global back gate enables the measurement to be performed at a variety of current densities.

SPCM is performed by scanning a device with a laser spot and measuring the resultant current (or voltage), between the source-drain contacts. This enables a PC, I_{ph} (or photovoltage, V_{ph}) map to be reconstructed, whereby the source-drain current (voltage) is plotted as a function of laser position. The laser from the Horiba Jobin-Yvon Raman system (refer to Section 3.2.3) was used for this purpose, as the position of the laser spot can be accurately set by reflecting the laser light off a mirror, whose angle can be controlled via piezoelectric motors. The simultaneous positioning of the laser and measurement of the source-drain voltage was achieved via bespoke software, that enabled the transport rig consisting of a PC, DAC and pre-amplifiers to manipulate the laser mirror, via communication with the Raman PC using the TCP/IP network protocol. A circular laser spot with an area of 9 μm^2, power of 0.3 mW and wavelength λ = 532 nm was used to illuminate the graphene sample. The laser spot was then raster scanned over the area encompassing the device. The minimum step size of the laser spot available, based on the use of a 50$\times$ objective lens, was ~ 0.05 μm, however a step size of $\sim 0.2 \rightarrow 1.0$ μm was more typical, depending on sample size and time constraints. After each discrete movement of the laser, either an IV measurement was

performed where V_{sd} was swept over a 1 mV range and the current measured, or V_{sd} was measured at zero bias directly. The advantage of the latter technique was that it was considerably faster, facilitating the use of smaller laser step sizes, so higher resolution V_{ph} maps could be constructed. The disadvantage of this method is that it does not enable the graphene sheet resistance to be monitored, nor the PC to be deduced, without prior knowledge of the graphene sheet resistance.

A common addition to the experimental set-up is a photodiode[108; 109; 169–172], which is used to collect the reflected light from the device. This is useful, as it allows the position of the source of any generated PC to be determined to greater accuracy, with respect to the contacts. Unfortunately, there was insufficient time to fit a photodiode in the Raman system and so an optical image of the device, taken prior to scanning the laser over the device, was used for comparative purposes. The disadvantage of using this technique was that the position of the device would sometimes shift by several micrometers during the course of the measurement, making precise identification of the source of the PC difficult.

7.3 Experimental Results

A preliminary measurement of the opto-electronic response of a graphene sample was performed on sample SG075, the sample that was previously used to investigate the effectiveness of our on-chip heaters (see Chapter 4). An optical image of this device is shown in Figure 7.3, with the Pd/Nb source and drain contacts labelled. The IV response of the device was measured under ambient conditions, using a two terminal geometry, with the DAC used to bias the device, and current and voltage pre-amplifiers used to measure the drain current and source-drain voltage respectively. The laser position was moved in steps of 1 μm over a 40×40 μm area, encompassing the entire device, and at each point an IV measurement was performed using a maximum V_{sd} of 1 mV.

Figure 7.4 shows the IV response of the device for 3 different laser positions, namely when the laser is at the source contact, off the sample (dark current) and at the drain contact. When the laser illuminates either the source or the drain contact, there is an offset in voltage of the IV response, and as a result a PC will be observed to flow, even when there is no source-drain bias. The observed shift in voltage at the source
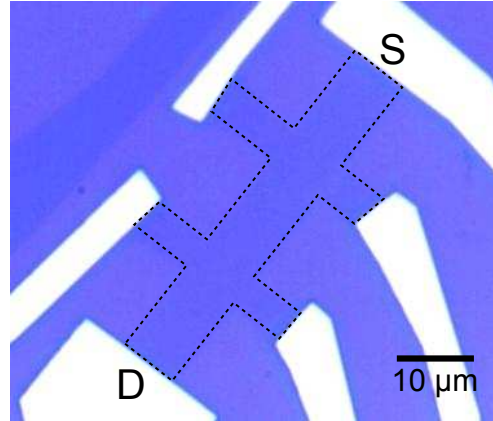
Figure 7.3: Optical image of graphene sample SG075. The source (S) and drain (D) contacts have been labelled in the optical image and the graphene flake outlined.

contact was $\Delta V = -60 \pm 5$ µV, corresponding to a zero-bias PC of $I_{ph} = 32 \pm 2$ nA. At the drain contact $\Delta V = +70 \pm 5$ µV corresponding to a zero-bias PC of $I_{ph} = -45 \pm 2$ nA. The change in polarity of the PC at either contact is a result of the mirroring of the junction geometry, from metal-graphene at one contact, to graphene-metal at the other (see Figure 7.5). The Pd/Nb contacts are expected to dope the graphene p-type, based on the results presented in Chapter 6. The doping profile of SG075 prior to the PC measurements suggested that at $V_G = 0$ V the graphene was doped n-type (refer to Figures 4.5 and 4.6) and as a result the device is expected to consist of a p-n-p junction. The measurement of a positive (negative) I_{ph} at the source-graphene (drain-graphene) interface at $V_G = 0$ V is in good agreement with this conclusion, assuming the PC is generated by the potential profile close to the contacts. The resistance of the device, as determined from the IV measurements, was found to be 1.70 ± 0.02 kΩ for all three measurements, suggesting that there is minimal heating by the laser or that the heating is highly localised.

Figure 7.6 shows the measured I_{ph} as a function of laser spot position. The brightest lobes on the map are situated at the contacts, with the source contact (top right) showing a strong positive PC and the drain contact (bottom left) showing a strong negative PC. $I_{ph} = 0$ nA is measured when the laser is far away from the graphene sheet, which supports the source of the PC is photo-excitation of carriers by the laser. Additional PC features are observed in the graphene channel itself. Peters *et al.* observed
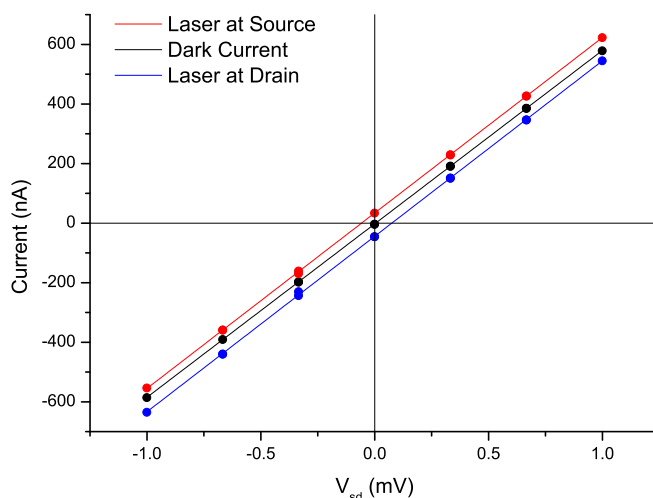
Figure 7.4: IV measurements taken on SG075 with the laser spot in three different positions: at the source contact, off the sample (dark current) and at the drain contact. A positive or negative shift in I is observed depending on the position of the laser. The PC is given by the value of I when $V_{sd} = 0$. Conversely the photovoltage is given by the value of V_{sd} when $I = 0$.

similar features at the boundary between intrinsic graphene and n-doped graphene and attributed the effect to a purely photovoltaic process[108]. Measurements performed by Xu *et al.* also showed features in the centre of the graphene channel at the boundary between monolayer and bilayer graphene, which they attributed entirely to the photo-thermoelectric effect[171]. Given the consistency of the optical contrast of the graphene in the optical image, the presence of charged impurities is a more likely cause of the optically active regions, rather than monolayer-bilayer graphene boundaries.

Further investigation into the opto-electronic effects of graphene necessitates the application of a gate voltage. This was attempted under ambient conditions with sample SG075, however no significant change in PC response was observed. Instead a different sample, SG100, was employed, which was measured under vacuum ($\sim 10^{-5}$ mbar) in a microstat at room temperature. An optical image of this device, consisting of a monolayer graphene flake contacted with Pd/Nb contacts is shown in Figure 7.7(a). A two terminal EFE measurement performed on the same device is shown in Figure 7.7(b), demonstrating a broad peak centred around $V_{Dirac} = -55 \pm 5$ V, suggesting the graphene is significantly n-doped. Photovoltage maps plotted for increasingly more negative values of V_G are shown in Figure 7.8. Each V_{ph} map was taken by mea-
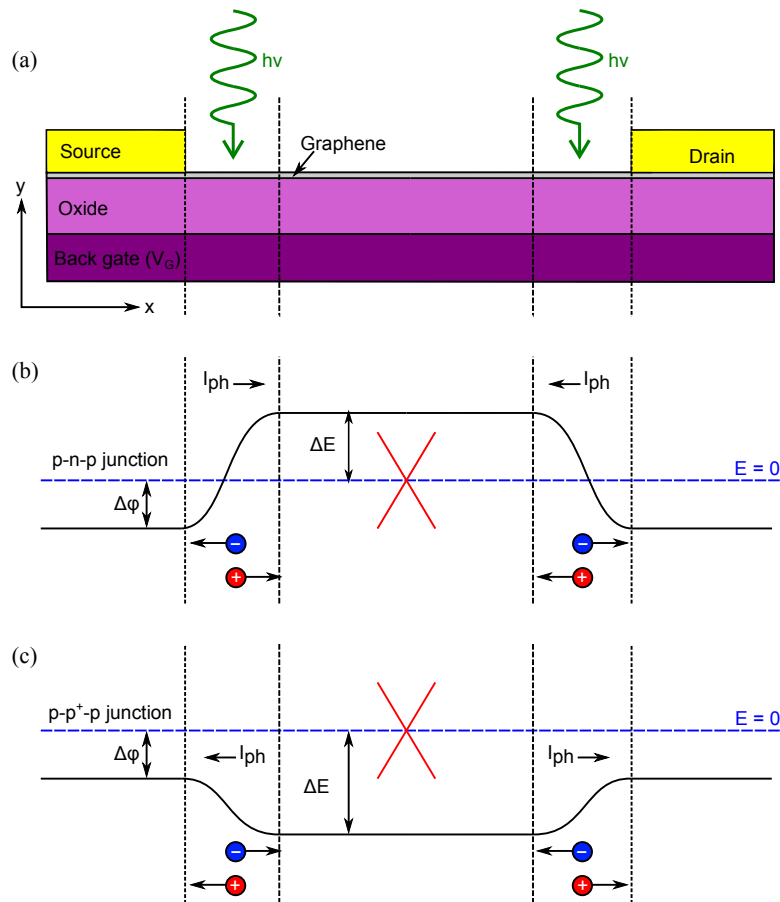
Figure 7.5: Schematic demonstrating the source of the polarity of I_{ph} during a SPCM measurement because of the photovoltaic effect. a) Cross-section of a two terminal graphene device indicating the positions of the source and drain contacts. Laser irradiation of the graphene channel next to the source and drain contacts is considered. b) and c) show the shift in Fermi energy ΔE (solid black line) of the graphene channel as a function of position with respect to the CNP (dashed blue line). Pinning of E_F by the metal contact by an amount $\Delta\phi$ forms a b) p-n-p junction when $\Delta E \gg 0$ and a c) p-p$^+$-p junction when $\Delta E \ll 0$. The direction of travel of photo-excited electrons and holes is indicated by the arrows.
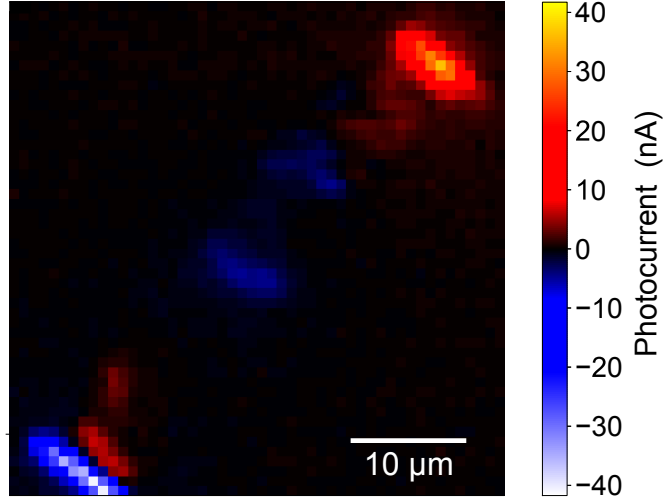
Figure 7.6: Spatially resolved PC map for sample SG075 at $V_G = 0$ V. The bright red and dark blue regions in the upper-right and lower-left regions of the device correspond to the positions of source and drain contacts respectively.

suring the potential across the source-drain contacts, with no applied bias while raster scanning the sample with the laser (step size = 0.5 μm). The source-drain voltage was measured using the DAC card via a voltage pre-amplifier. This method enabled the acquisition of PC data 8.5 times faster than the IV based method, enabling a 30×25 μm area to be sampled with a laser step size of 0.5 μm in 23 minutes for a given value of V_G.

At $V_G = 0$ V a positive (negative) V_{ph} is observed at the drain (source) contact. This is equivalent to the response shown by sample SG075 in Figure 7.6, as the polarity of the V_{ph} is always opposite that of I_{ph}. As $V_G \rightarrow V_{Dirac}$, the magnitude of V_{ph} is observed to increase, which is because of the increasing resistance of the device from a reduction in carrier density. When $V_G > -51$ V, V_{ph} is significantly lower than that near the contacts, while when $V_G < -51$ V the magnitude of V_{ph} is equivalent to that close to the graphene-metal interfaces. The observation of a significant photoresponse in the channel when E_F is close the CNP is in good agreement with measurements made on a similar device by Lee *et al.*, which they attributed to the presence of charged impurities[169]. For values of V_G far from V_{Dirac}, the fluctuations in carrier density across the sheet are insignificant, compared to the overall carrier density and so a reduction in V_{ph} is observed. At $V_G \sim 51$ V, the polarity of V_{ph} at the
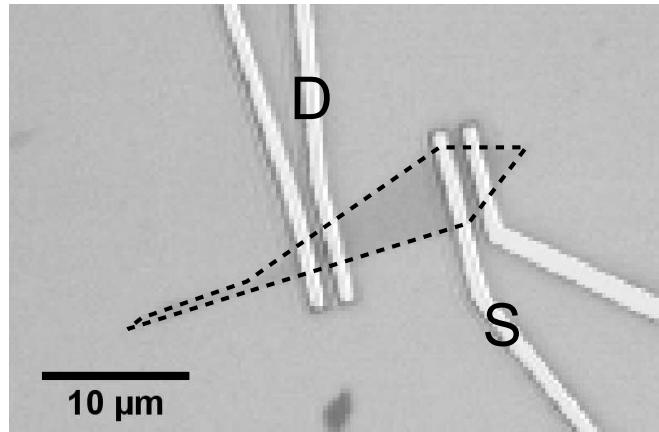
(a)
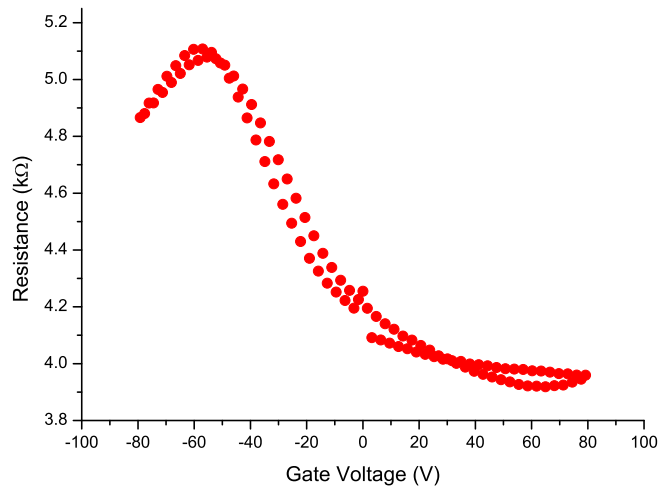
(b)

Figure 7.7: a) Optical image and b) gate response of graphene sample SG100. The source and drain contacts have been labelled in the optical image and the graphene flake outlined. The gate response shows a greatly shifted CNP with $V_{\mathrm{Dirac}} \approx -60$ V.
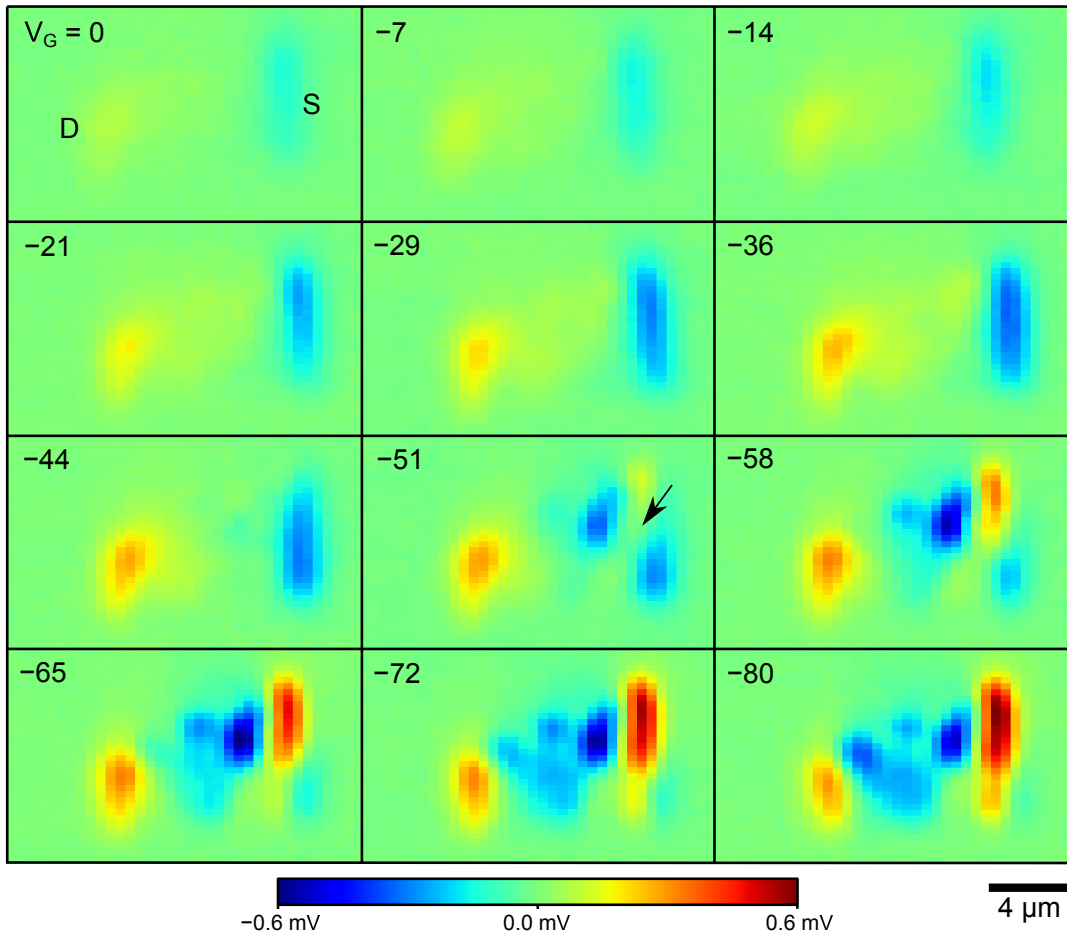
Figure 7.8: Spatially resolved PC maps at various transport regimes of graphene device SG100. The sequence of images display the PC response as V_G is swept from 0 V to -80 V. The approximate positions of the source (S) and drain (D) contacts are indicated. The sign of the V_{ph} response at the drain contact changes at approximately -60 V which corresponds to the position of V_{Dirac}. The arrow shown on the PC map at $V_G = -51$ V is to aid discussion of the results in the main text.
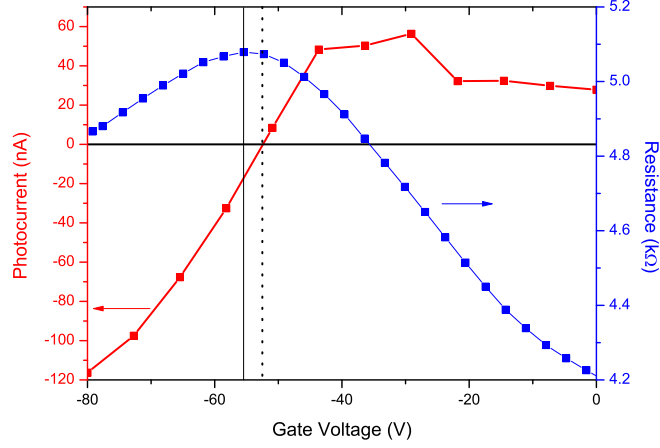
Figure 7.9: PC (red) and resistance (blue) of sample SG100 measured as a function of V_G. PC was measured with the centre of the source contact illuminated with the laser. Resistance was measured without the laser prior to the PC measurement. The peak in resistance occurs at $V_{\mathrm{Dirac}} \sim -56$ V while the sign of PC changes at approximately $V_G \sim -52$ V.

source contact changes from negative when the graphene channel is n-type, to positive when the graphene channel is p-type. The change in polarity is a direct result of the position of E_F, changing to either above or below the pinned Fermi energy, $\Delta\phi$, in the metal contacted graphene. A similar polarity change at the drain contact was expected but not observed. A possible cause of this is charged impurities near the drain contact resulting in E_F in the channel near the drain contact not being the same as that near the source contact. A large amount of inhomogeneity is expected in this device, as a result of the very broad peak in the EFE measurements, in addition to V_{Dirac} being far from $V_G = 0$ V, which is typical for highly doped extrinsic graphene. If V_G had been swept to -100 V or more, it is likely that a reversal of V_{ph} at the drain contact would have also been observed.

The polarity of V_{ph} is first observed to flip at the centre of the source contact as indicated by the arrow in Figure 7.8. A plot of I_{ph} as a function of V_G at this point is shown in Figure 7.9. I_{ph} was calculated using the measured zero-bias V_{ph} and the device resistance, as measured before illuminating the sample with the laser. As there was hysteresis in the gate response, only the down sweep ($V_G = 0$ V $\rightarrow -80$ V) resistance data was used, which coincides with the order in which V_G was varied when taking the maps of photovoltage. The peak in resistance occurs at $V_{\mathrm{Dirac}} \sim -58$ V while the sign

of I_{ph} changes at $V_{\text{G}} \sim -52$ V. A positive offset of the value of V_{G} at which the polarity of I_{ph} changes was observed by Lee *et al.* for Au contacts, while Ti contacts showed a negative offset[169]. This was attributed to Au acting as a p-type dopant while Ti acted as an n-type dopant, as a direct result of the different metal work-functions. As such, the small positive offset observed, further supports that the Pd/Nb contacts act as a p-type dopant when contacting graphene. This agrees with recent measurements performed on Pd contacts performed by several authors[138; 173; 174]. Given that 3 nm of Pd was used in the Pd/Nb contacts, it is expected that the resultant work-function of the bilayer metal will be close to that of pure Pd[151]. It should be noted that the shift in V_{G} away from V_{Dirac} is smaller than expected, based on the results of several authors for Pd contacted graphene[138; 173]. One possible explanation is that scanning the sample with the laser could change the position of the CNP and so the pre-scan R versus V_{G} response is unrepresentative of the state of the sample during the scan. Another possible cause is oxidisation of the contact material or that the Nb cap has a greater impact on the overall properties of the contact. There is also an issue of limited resolution both in x and y, but also in V_{G}. A better method of measuring I_{ph} versus V_{G} would be to position the laser at the contact and then sweep V_{G} with smaller step sizes to determine more accurately when the polarity of I_{ph} switches. Again measuring I_{ph} directly rather than calculating it from V_{ph} would also be beneficial.

7.4   Conclusion

In this chapter the opto-electronic response of several graphene devices has been investigated. This has been achieved by modifying a Horiba Jobin-Yvon Raman system, via the production of custom software enabling the position of the laser on a sample to be correlated to electrical measurements. A laser position dependent PC was measured in all graphene samples tested. A particularly strong PC was observed at the contacts, which is understood to be because of the presence of local electric fields at the graphene-metal interface because of contact induced doping of the graphene. The polarity of the PC at the source and drain contacts suggests that the Pd/Nb electrodes used to contact the graphene act as p-type dopants, which is in good agreement with the model used to fit data taken using the TLM presented in Chapter 6. The PC has also been measured as a function of V_{G}, showing a reversal of the polarity of the PC near

the CNP, which is understandable in terms of the photovoltaic effect. Finally, these measurements establish SPCM as a viable characterisation technique to be used here at Leeds.

CHAPTER 8

Conclusions

In principle, when attempting to produce SGS junctions, there are a number of components that must be optimised, aside from producing contacts which are superconducting. Firstly, graphene of sufficient quality must be produced. While the isolation of individual high quality flakes of graphene by the mechanical exfoliation procedure is relatively trivial, the processes these flakes undergo to produce working devices results in graphene with sub-optimal properties. In particular, surface contaminants such as remnant polymer resists or water from the ambient conditions, act to shift the CNP away from $V_G = 0$ V and broaden the peak in resistance observed in EFE measurements. Consequently, the devices produced have a greater amount of inhomogeneity, with an accompanying reduction in carrier mobility, which acts to prohibit the observation of interesting phenomena such as the QHE.

Chapter 4 presents the data from attempts to remove surface contaminants through *in-situ* annealing techniques. Two techniques were explored, firstly, heating the graphene devices indirectly with a platinum micro-heater patterned in proximity to the graphene device. A second technique involved heating the graphene directly through Joule heating via the application of a large source drain current. The platinum heater was found to successfully sustain temperatures of around 400 K, measured via a calibrated platinum strip. This temperature was sufficient to observe a reduction in p-type dopants which were responsible for a significant positive shift of the CNP in some areas of the device. Upon failure of the heater at higher heating powers, an appreciable shift in the CNP of the graphene to a more negative value was observed. This was attributed to the deposition of platinum adatoms by the destruction of the heater. As such, this method could be used to intentionally dope graphene *in-situ*, when fitting a separate metal deposition system is not possible. The novel use of a platinum micro-heater to improve the homogeneity of graphene devices has thus been proven a viable *in-situ* technique. Through optimisation of the heater design, the heating power and duration could be increased. The use of a local heating technique such as this may also have benefits when incorporated into a temperature sensitive device.

The second annealing method explored was current annealing, a technique pioneered by Moser *et al.* [79], whereby a large source-drain current is applied, which heats the device via Joule heating. By applying a large current density of around 10^8 Acm^{-2}, the CNP of a two terminal graphene device was shifted toward $V_G = 0$ V, which indicated a removal of dopants, while a reduction in the overall resistance was

attributed to a possible improvement in contact transparency. To assess the temperature reached by the graphene during this anneal, time resolved Raman spectroscopy was performed. From the shift in energy and width of the characteristic Raman G and 2D peaks, the increase in temperature was estimated to be of the order of several 100 K. A disadvantage of the current annealing technique was demonstrated, in that it was often highly destructive, with devices regularly losing electronic contact following an anneal. The most likely point of failure is the graphene-metal interface, owing to a high contact resistance, which invariably leads to a disproportionate amount of heating at the contact, in comparison to the graphene sheet.

Ultimately, for the reproducible production of high quality graphene devices with minimal extrinsic dopant contributions, alternative annealing procedures should be explored. An *ex-situ* technique which could remove most of the organic residues is annealing in a reactive atmosphere of argon/hydrogen. This technique is readily available at Leeds using an existing furnace. Despite this, an *in-situ* annealing technique will still need to be employed because of the prevalence of annealed samples to be affected by ambient conditions[175]. A particularly promising avenue is the fitting of an annealing chamber to the top of an existing cryostat, which allows the devices to be annealed and then measured without breaking vacuum in-between. The production of such a chamber is expected to be underway in the near future.

Transport measurements presented in Chapter 5 demonstrate that the quality of the graphene incorporated in our devices after processing is comparable to that achieved by other groups. EFE measurements performed on one sample show a CNP close to $V_G = 0$ V, which indicates minimal doping from extrinsic adsorbates. The carrier mobility and minimum conductance of this sample were measured to be 5,000 cm^2/Vs and $1.0 \pm 0.2(4e^2/h)$ respectively, which is typical for good quality samples produced using lithographic techniques on SiO$_2$ substrates. Despite this, a linear dependence of conductance on carrier density suggests that charged impurities are still the dominant scattering mechanism, even in a sample which otherwise shows minimal doping.

QHE measurements were performed on both etched and un-etched planar devices. A particularly clear anomalous QHE indicative of a monolayer graphene was observed in a device etched into a Hall bar, with sub-micrometer features, using a combination of electron beam lithography and oxygen plasma ashing. Not only does this prove the successful production of a monolayer graphene device, it also shows that the shape

of the flake can be controlled without negatively impacting its properties. The recent acquisition of an EBL system with superior patterning capabilities - combined with this effective etching technique - could open up several experimental avenues.

In addition to the etched device measurements, an extensive study of the V_G and B dependence of longitudinal resistance was performed on an unetched device. This clearly showed the increased splitting of the Landau levels with applied field as well as SdHOs. From the field strength at which the SdHOs were first observable, the elastic scattering time was estimated to be approximately 300 fs, giving an estimated broadening of the Landau levels of 2 meV in line with measurements performed by other authors on devices on SiO_2. A direct measurement of the Berry's phase, β, was also performed, finding $\beta = 0.48 \pm 0.01$, which directly shows that the charge carriers in the device were behaving as spin 1/2 Dirac fermions. These measurements show that producing graphene of sufficient quality for incorporation in devices such as SGS junctions is possible, reaching the limits of device performance on SiO_2. In this respect, significant improvement in device performance from a graphene sheet quality viewpoint will only be possible through the reduction of substrate effects. This could be achieved by moving to suspended devices, or devices on hexagonal boron nitride which - although achieved by several other groups - would prove an appreciable technological hurdle to replicate such devices here at Leeds.

Aside from the properties of the graphene sheet, the other important factor is the requirement to have contacts with a low contact resistance. In Chapter 6 the contact resistance achieved with sputtered Pd/Nb contacts was measured using the transfer length method, in both unetched and etched devices. At the CNP, the contact resistance of the unetched and etched devices were found to be 5.5 ± 1.0 kΩμm and 1.9 ± 0.3 kΩμm respectively, with the variation between the two attributed to differences in fabrication procedure. These values compare unfavourably to those presented in the literature, which for samples with comparable contact materials are a magnitude lower than presented here. This is most likely caused by the use of sputtering to deposit our contacts, which is a highly energetic technique, compared to the more commonly used method of electron beam lithography when depositing contacts on graphene. The impact of sputtering on graphene was investigated directly using Raman spectroscopy, where following deposition of a thin layer of Pd on graphene, a suppression of the 2D peak and pronounced enhancement of the D peak were observed. According to the

work of Ferrari *et al.* [154] this signifies significant amorphisation of the graphene beneath the contact material.

While working SGS junctions produced using sputtering have been demonstrated in the literature, their performance is far lower than those produced using other methods. From our work it is suggested that this is because of a high contact resistance/low interface transparency from the amorphisation of the graphene, which acts to suppress the critical current. To overcome this, contacts should be deposited exclusively using less energetic techniques, such as electron beam evaporation. If this is not possible the method employed by Popincuic *et al.* [43] should be considered, in which the adhesion layer is first deposited using electron beam evaporation, followed by sputtering of the principal superconducting material on top. In this case the adhesion layer acts to preserve the structure of the graphene, which in turn reduces the contact resistance.

The impact of the contacts on the properties of the graphene devices was also investigated. According to the model of Giovannetti *et al.* [113], charge transfer to and from the metal and the graphene (depending on relative work-functions) can lead to the doping of graphene by the contact metal. This contact induced doping is most pronounced at the interface, decaying further in to the graphene channel. Nouchi *et al.* [148; 176] proposed a simple method to model this, based on the pinning of the charge density at the contact, followed by a linear decay of this charge density in the graphene channel. This model was modified to incorporate other possible contact induced doping profiles in the graphene and then used to simulate the results of the etched transfer length method device. It was found that a $1/x$ doping profile, where x is the distance from the contact, gave the best fit to experimental data, which is in good agreement with that expected from theory. The model also successfully reproduced the increasing asymmetry in the electron and hole conduction regimes, as the source-drain contact separation was reduced. Furthermore, the model indicated that the Pd/Nb contacts doped the graphene p-type, which is in good agreement with the literature for Pd contacts, and that this doping extended into the graphene channel. The gate dependence of the measured contact resistance was also extracted from this simulation, although fitting the model to the experimental data required some additional free parameters. This was necessary primarily because of the coarse selection of initial parameters in the model, which could be improved with further refinement. Pinning of the carrier density by the contacts will have a particularly large impact in devices with

177

very narrow graphene channels, such as in Josephson junctions, and is an aspect that should be considered.

Finally, Chapter 7 presented preliminary measurements of the opto-electric response of our graphene devices, measured using SPCM. This was achieved through the modification of the a Horiba Jobin-Yvon Raman spectrometer to allow direct control of the laser position on the sample, coupled with an existing transport measurement rig. The PC generated was measured as a function of laser position on the graphene device and a pronounced response was measured at the contact-graphene interface. This was understood in terms of a local electric field at the interface - caused by charge transfer between the metal and the graphene - resulting in a photovoltaic effect upon laser excitation. Measurements performed as a function of V_G also supported the photovoltaic effect as the source of the PC, with a reversal of the polarity of the photovoltage at the source contact close the CNP. These measurements also indicated that the graphene was doped p-type by the Pd/Nb contacts, in agreement with the model used to explain the previous transfer length measurements.

Close to the CNP a pronounced photovoltage was also observed in the graphene channel itself, which could be attributed to either a photovoltaic or photo-thermoelectric effect. In either case, this suggests a significant amount of inhomogeneity in the carrier density of the graphene as a result of the presence of charged impurities, which is in line with observations of the formation of electron-hole puddles in graphene devices, when close to the Dirac point. Such inhomogeneity has been proposed by Komatsu *et al.* [42], as one contributing factor to the lower than expected critical current in SGS devices. The measurements performed demonstrate the successful implementation of SPCM as a complimentary technique for characterising devices.

The production of high quality graphene devices poses a non-trivial problem owing to the unique nature of the material properties. Its low carrier density results in it being highly susceptible to doping by charged impurities or by interactions with the contacting electrodes themselves, which can have a negative impact on the performance of the devices. Considerations must also be made to the methods used to fabricate graphene devices because of the monolayer nature of graphene, which makes it easily damaged by the use of energetic techniques such as DC magnetron sputtering. In particular, these properties make the production of SGS devices challenging as the standard fabrication techniques result in inherently low transparency contacts and a

highly inhomogeneous carrier density distribution across the graphene channel, which can hinder the transmission of a supercurrent. This thesis provides methods to both characterise and optimise graphene devices to realise the goal of producing working SGS devices.

8.1 Future Work

There is a great deal of scope for future work based on the studies presented in this thesis. Through improvements in the design of the on-chip heaters presented in Chapter 4, the production of a more robust heater with extended mean time of failure should be possible. Recent work on graphene FET based SO_2 gas sensors have shown that these devices have improved performance at higher temperature[177]. Through the incorporation of our on-chip heater technology the sensitivity of such gas sensors could be improved. Furthermore, it was shown that the sensors could be reset, enabling multiple uses, via annealing at 100 °C, which is within the operating range of our heaters.

Regarding the contact resistance measurements, shown in Chapter 6, there is scope for improvement in the charge transfer based model. A more refined model has recently been published which shows reasonable agreement with experimental data[178]. Despite this, there is significant disagreement with the experimental data and the model for some choices of contact material when E_F in the graphene is far from the CNP. The authors only considered a linear doping profile in the graphene away from the contact metal. Based on our investigation of alternative doping profiles, an improved fit may be possible giving a better understanding of the interaction between graphene and metals.

While the Raman measurements performed on sputtered graphene flakes shown in this thesis suggests that significant damage to graphene is caused by the technique, there is scope to reduce this. One such method that could be employed would be to reduce the kinetic energy of the incoming sputtered material by increasing the gas pressure in the chamber. This would act to reduce the kinetic energy of the deposited material by increasing the number of scattering events that the sputtered atoms undergo while travelling from target to substrate. A systematic study of gas pressure versus graphene amorphisation, as determined by Raman spectroscopy, could be performed

in order to improve the operation of graphene devices with sputter deposited contacts. Given the low yield of exfoliated graphene flakes an alternative source of graphene could be employed for this study such as CVD or SiC grown materials.

Finally, the opto-electronic measurements in Chapter 8 are representative of part of a growing body of research into the photoresponse of graphene devices. As such, there are a number of avenues of investigation available to contribute to this growing field. While only Pd/Nb contacts were considered here it is possible that the deposition of contacts with an alternative metal, which results in a greater difference in graphene/metal work-functions, could lead to an increase in the measured photocurrent.

With the recent availability of a higher resolution electron beam lithography system here at Leeds there is also the possibility of producing graphene devices with contact geometries designed to enhance the generated photocurrent via plasmonic oscillations[14]. There is also growing interest in the use of graphene in ultrafast photodetectors[179; 180]. Combining the spatially resolved photocurrent technique established here with a terahertz radiation laser source could enable a greater understanding of the operating principles behind this emergent class of devices.

References

[1] K. S. Novoselov, A. K. Geim, S. V. Morozov, D. Jiang, Y. Zhang, S. V. Dubonos, I. V. Grigorieva, and A. A. Firsov, "Electric field effect in atomically thin carbon films," *Science*, vol. 306, pp. 666 –669, Oct. 2004.

[2] C. Lee, X. Wei, J. W. Kysar, and J. Hone, "Measurement of the elastic properties and intrinsic strength of monolayer graphene," *Science*, vol. 321, pp. 385–388, July 2008.

[3] A. H. Castro Neto, F. Guinea, N. M. R. Peres, K. S. Novoselov, and A. K. Geim, "The electronic properties of graphene," *Reviews of Modern Physics*, vol. 81, pp. 109–162, Jan. 2009.

[4] S. Das Sarma, S. Adam, E. H. Hwang, and E. Rossi, "Electronic transport in two-dimensional graphene," *Reviews of Modern Physics*, vol. 83, pp. 407–470, May 2011.

[5] P. R. Wallace, "The band theory of graphite," *Physical Review*, vol. 71, pp. 622–634, May 1947.

[6] P. A. M. Dirac, "The quantum theory of the electron," *Proceedings of the Royal Society of London. Series A*, vol. 117, pp. 610–624, Feb. 1928.

[7] Y. Zhang, Y.-W. Tan, H. L. Stormer, and P. Kim, "Experimental observation of the quantum Hall effect and Berry's phase in graphene," *Nature*, vol. 438, pp. 201–204, Nov. 2005.

[8] K. S. Novoselov, A. K. Geim, S. V. Morozov, D. Jiang, M. I. Katsnelson, I. V. Grigorieva, S. V. Dubonos, and A. A. Firsov, "Two-dimensional gas of massless Dirac fermions in graphene," *Nature*, vol. 438, pp. 197–200, Nov. 2005.

[9] A. K. Geim and K. S. Novoselov, "The rise of graphene," *Nature Materials*, vol. 6, pp. 183–191, Mar. 2007.

[10] X. Du, I. Skachko, A. Barker, and E. Y. Andrei, "Approaching ballistic transport in suspended graphene," *Nat Nano*, vol. 3, no. 8, pp. 491–495, 2008.

[11] S. Rumyantsev, G. Liu, M. S. Shur, R. A. Potyrailo, and A. A. Balandin, "Selective gas sensing with a single pristine graphene transistor," *Nano Letters*, vol. 12, pp. 2294–2298, May 2012.

[12] F. Schedin, A. K. Geim, S. V. Morozov, E. W. Hill, P. Blake, M. I. Katsnelson, and K. S. Novoselov, "Detection of individual gas molecules adsorbed on graphene," *Nature Materials*, vol. 6, pp. 652–655, July 2007.

[13] S. Bae, H. Kim, Y. Lee, X. Xu, J.-S. Park, Y. Zheng, J. Balakrishnan, T. Lei, H. R. Kim, Y. I. Song, Y.-J. Kim, K. S. Kim, B. Özyilmaz, J.-H. Ahn, B. H. Hong, and S. Iijima, "Roll-to-roll production of 30-inch graphene films for transparent electrodes," *Nature Nanotechnology*, vol. 5, no. 8, pp. 574–578, 2010.

[14] T. J. Echtermeyer, L. Britnell, P. K. Jasnos, A. Lombardo, R. V. Gorbachev, A. N. Grigorenko, A. K. Geim, A. C. Ferrari, and K. S. Novoselov, "Strong plasmonic enhancement of photovoltage in graphene," *Nature Communications*, vol. 2, p. 458, Aug. 2011.

[15] T. Mueller, F. Xia, M. Freitag, J. Tsang, and P. Avouris, "Role of contacts in graphene transistors: A scanning photocurrent study," *Physical Review B*, vol. 79, p. 245430, June 2009.

[16] A. Tzalenchuk, S. Lara-Avila, A. Kalaboukhov, S. Paolillo, M. Syväjärvi, R. Yakimova, O. Kazakova, T. J. B. M. Janssen, V. Fal'ko, and S. Kubatkin, "Towards a quantum resistance standard based on epitaxial graphene," *Nature Nanotechnology*, vol. 5, no. 3, pp. 186–189, 2010.

[17] C. Berger, Z. Song, T. Li, X. Li, A. Y. Ogbazghi, R. Feng, Z. Dai, A. N. Marchenkov, E. H. Conrad, P. N. First, and W. A. de Heer, "Ultrathin epitaxial graphite: 2D electron gas properties and a route toward graphene-based nano-electronics," *The Journal of Physical Chemistry B*, vol. 108, pp. 19912–19916, Dec. 2004.

[18] P. Blake, E. W. Hill, A. H. Castro Neto, K. S. Novoselov, D. Jiang, R. Yang, T. J. Booth, and A. K. Geim, "Making graphene visible," *Applied Physics Letters*, vol. 91, pp. 063124–063124–3, Aug. 2007.

[19] J.-H. Chen, C. Jang, M. Ishigami, S. Xiao, W. Cullen, E. Williams, and M. Fuhrer, "Diffusive charge transport in graphene on SiO_2," *Solid State Communications*, vol. 149, pp. 1080–1086, July 2009.

[20] J.-H. Chen, C. Jang, S. Xiao, M. Ishigami, and M. S. Fuhrer, "Intrinsic and extrinsic performance limits of graphene devices on SiO_2," *Nature Nanotechnology*, vol. 3, no. 4, pp. 206–209, 2008.

[21] C. Hwang, D. A. Siegel, S.-K. Mo, W. Regan, A. Ismach, Y. Zhang, A. Zettl, and A. Lanzara, "Fermi velocity engineering in graphene by substrate modification," *Scientific Reports*, vol. 2, Aug. 2012.

[22] C. R. Dean, A. F. Young, I. Meric, C. Lee, L. Wang, S. Sorgenfrei, K. Watanabe, T. Taniguchi, P. Kim, K. L. Shepard, and J. Hone, "Boron nitride substrates for high-quality graphene electronics," *Nature Nanotechnology*, vol. 5, no. 10, pp. 722–726, 2010.

[23] K. Bolotin, K. Sikes, Z. Jiang, M. Klima, G. Fudenberg, J. Hone, P. Kim, and H. Stormer, "Ultrahigh electron mobility in suspended graphene," *Solid State Communications*, vol. 146, pp. 351–355, June 2008.

[24] J. C. Meyer, A. K. Geim, M. I. Katsnelson, K. S. Novoselov, T. J. Booth, and S. Roth, "The structure of suspended graphene sheets," *Nature*, vol. 446, pp. 60–63, Mar. 2007.

[25] L. N. Cooper, "Bound electron pairs in a degenerate fermi gas," *Physical Review*, vol. 104, pp. 1189–1190, Nov. 1956.

[26] C. W. J. Beenakker, "Specular Andreev reflection in graphene," *Physical Review Letters*, vol. 97, no. 6, p. 067007, 2006.

[27] C. W. J. Beenakker, "Colloquium: Andreev reflection and klein tunneling in graphene," *Reviews of Modern Physics*, vol. 80, pp. 1337–1354, Oct. 2008.

[28] B. M. Kessler, Ç. Ö. Girit, A. Zettl, and V. Bouchiat, "Tunable superconducting phase transition in metal-decorated graphene sheets," *Physical Review Letters*, vol. 104, p. 047001, Jan. 2010.

[29] A. Allain, Z. Han, and V. Bouchiat, "Electrical control of the superconducting-to-insulating transition in graphene–metal hybrids," *Nature Materials*, vol. 11, no. 7, pp. 590–594, 2012.

[30] T. Dirks, T. L. Hughes, S. Lal, B. Uchoa, Y.-F. Chen, C. Chialvo, P. M. Goldbart, and N. Mason, "Transport through Andreev bound states in a graphene quantum dot," *Nature Physics*, vol. 7, no. 5, pp. 386–390, 2011.

[31] H. B. Heersche, P. Jarillo-Herrero, J. B. Oostinga, L. M. K. Vandersypen, and A. F. Morpurgo, "Bipolar supercurrent in graphene," *Nature*, vol. 446, pp. 56–59, Mar. 2007.

[32] X. Du, I. Skachko, and E. Y. Andrei, "Josephson current and multiple Andreev reflections in graphene SNS junctions," *Physical Review B*, vol. 77, p. 184507, May 2008.

[33] J.-H. Choi, H.-J. Lee, and Y.-J. Doh, "Above-gap conductance anomaly studied in superconductor-graphene-superconductor Josephson junctions," *Journal of the Korean Physical Society*, vol. 57, pp. 149–155, July 2010.

[34] J. Voutilainen, A. Fay, P. Häkkinen, J. K. Viljas, T. T. Heikkilä, and P. J. Hakonen, "Energy relaxation in graphene and its measurement with supercurrent," *Physical Review B*, vol. 84, p. 045419, July 2011.

[35] Ç. Girit, V. Bouchiat, O. Naaman, Y. Zhang, M. F. Crommie, A. Zettl, and I. Siddiqi, "Tunable graphene dc superconducting quantum interference device," *Nano Lett.*, vol. 9, no. 1, pp. 198–199, 2008.

[36] F. Miao, S. Wijeratne, Y. Zhang, U. C. Coskun, W. Bao, and C. N. Lau, "Phase-coherent transport in graphene quantum billiards," *Science*, vol. 317, pp. 1530–1533, Sept. 2007.

[37] C. Ojeda-Aristizabal, M. Ferrier, S. Guéron, and H. Bouchiat, "Tuning the proximity effect in a superconductor-graphene-superconductor junction," *Physical Review B*, vol. 79, p. 165436, Apr. 2009.

[38] U. C. Coskun, M. Brenner, T. Hymel, V. Vakaryuk, A. Levchenko, and A. Bezryadin, "Distribution of supercurrent switching in graphene under the proximity effect," *Physical Review Letters*, vol. 108, p. 097003, Feb. 2012.

[39] I. V. Borzenets, U. C. Coskun, S. J. Jones, and G. Finkelstein, "Phase diffusion in graphene-based Josephson junctions," *Physical Review Letters*, vol. 107, no. 13, p. 137005, 2011.

[40] D. Jeong, J.-H. Choi, G.-H. Lee, S. Jo, Y.-J. Doh, and H.-J. Lee, "Observation of supercurrent in PbIn-graphene-PbIn Josephson junction," *Physical Review B*, vol. 83, p. 094503, Mar. 2011.

[41] G.-H. Lee, D. Jeong, J.-H. Choi, Y.-J. Doh, and H.-J. Lee, "Electrically tunable macroscopic quantum tunneling in a graphene-based Josephson junction," *Physical Review Letters*, vol. 107, no. 14, p. 146605, 2011.

[42] K. Komatsu, C. Li, S. Autier-Laurent, H. Bouchiat, and S. Gueron, "Superconducting proximity effect through graphene from zero field to the quantum Hall regime," *arXiv:1202.1690*, Feb. 2012.

[43] M. Popinciuc, V. E. Calado, X. L. Liu, A. R. Akhmerov, T. M. Klapwijk, and L. M. K. Vandersypen, "Zero-bias conductance peak and Josephson effect in graphene-NbTiN junctions," *Physical Review B*, vol. 85, p. 205404, May 2012.

[44] A. Shailos, W. Nativel, A. Kasumov, C. Collet, M. Ferrier, S. Guéron, R. Deblock, and H. Bouchiat, "Proximity effect and multiple Andreev reflections in few-layer graphene," *Europhysics Letters (EPL)*, vol. 79, p. 57008, Sept. 2007.

[45] B. Josephson, "Possible new effects in superconductive tunnelling," *Physics Letters*, vol. 1, pp. 251–253, July 1962.

[46] V. V. Schmidt, *The Physics of Superconductors: Introduction to Fundamentals and Applications*. Springer, July 1997.

[47] P. Rickhaus, M. Weiss, L. Marot, and C. Schönenberger, "Quantum Hall effect in graphene with superconducting electrodes," *Nano Lett.*, vol. 12, no. 4, pp. 1942–1945, 2012.

[48] K. Grove-Rasmussen, H. I. Jørgensen, B. M. Andersen, J. Paaske, T. S. Jespersen, J. Nygård, K. Flensberg, and P. E. Lindelof, "Superconductivity-enhanced bias spectroscopy in carbon nanotube quantum dots," *Physical Review B*, vol. 79, p. 134518, Apr. 2009.

[49] J. Haruyama, K. Takazawa, S. Miyadai, A. Takeda, N. Hori, I. Takesue, Y. Kanda, T. Akazaki, and H. Takayanagi, "Supercurrent in diffusive multi-walled carbon nanotubes," *Physica C: Superconductivity*, vol. 408–410, pp. 85–87, Aug. 2004.

[50] L. Lechner, M. Gaaß, A. Paila, M. A. Sillanpää, C. Strunk, and P. J. Hakonen, "Microwave reflection measurement of critical currents in a nanotube Josephson transistor with a resistive environment," *Nanotechnology*, vol. 22, p. 125203, Mar. 2011.

[51] A. Tselev, Y. Yang, J. Zhang, P. Barbara, and S. E. Shafranjuk, "Carbon nanotubes as nanoscale probes of the superconducting proximity effect in Pd-Nb junctions," *Physical Review B*, vol. 80, no. 5, p. 054504, 2009.

[52] J. Zhang, A. Tselev, Y. Yang, K. Hatton, P. Barbara, and S. Shafraniuk, "Zero-bias anomaly and possible superconductivity in single-walled carbon nanotubes," *Physical Review B*, vol. 74, p. 155414, Oct. 2006.

[53] M. I. Katsnelson, *Graphene: Carbon in Two Dimensions*. Cambridge University Press, 1 ed., Apr. 2012.

[54] J. Robertson, "Amorphous carbon," *Advances in Physics*, vol. 35, no. 4, pp. 317–374, 1986.

[55] S. Reich, J. Maultzsch, C. Thomsen, and P. Ordejón, "Tight-binding description of graphene," *Physical Review B*, vol. 66, p. 035412, July 2002.

[56] M. I. Katsnelson, K. S. Novoselov, and A. K. Geim, "Chiral tunnelling and the klein paradox in graphene," *Nature Physics*, vol. 2, no. 9, pp. 620–625, 2006.

[57] A. K. Geim, "Nobel lecture: Random walk to graphene," *Reviews of Modern Physics*, vol. 83, pp. 851–862, Aug. 2011.

[58] G. D. Wilk, R. M. Wallace, and J. M. Anthony, "High-k gate dielectrics: Current status and materials properties considerations," *Journal of Applied Physics*, vol. 89, p. 5243, 2001.

[59] S. V. Morozov, K. S. Novoselov, M. I. Katsnelson, F. Schedin, D. C. Elias, J. A. Jaszczak, and A. K. Geim, "Giant intrinsic carrier mobilities in graphene and its bilayer," *Physical Review Letters*, vol. 100, p. 016602, Jan. 2008.

[60] J. Singleton, *Band Theory and Electronic Properties of Solids*. OUP Oxford, Aug. 2001.

[61] K. S. Novoselov, D. Jiang, F. Schedin, T. J. Booth, V. V. Khotkevich, S. V. Morozov, and A. K. Geim, "Two-dimensional atomic crystals," *Proceedings of the National Academy of Sciences of the United States of America*, vol. 102, pp. 10451–10453, July 2005.

[62] K. S. Novoselov, Z. Jiang, Y. Zhang, S. V. Morozov, H. L. Stormer, U. Zeitler, J. C. Maan, G. S. Boebinger, P. Kim, and A. K. Geim, "Room-temperature quantum Hall effect in graphene," *Science*, vol. 315, p. 1379, Mar. 2007.

[63] A. Ferrari, "Raman spectroscopy of graphene and graphite: Disorder, electron-phonon coupling, doping and nonadiabatic effects," *Solid State Communications*, vol. 143, no. 1-2, pp. 47–57, 2007.

[64] J. Röhrl, M. Hundhausen, K. V. Emtsev, T. Seyller, R. Graupner, and L. Ley, "Raman spectra of epitaxial graphene on SiC(0001)," *Applied Physics Letters*, vol. 92, pp. 201918–201918–3, May 2008.

[65] J. Yan, Y. Zhang, P. Kim, and A. Pinczuk, "Electric field effect tuning of electron-phonon coupling in graphene," *Physical Review Letters*, vol. 98, p. 166802, Apr. 2007.

[66] N. B. Colthup, L. H. Daly, and S. E. Wiberley, *Introduction to Infrared and Raman Spectroscopy, Third Edition*. Academic Press, 3 ed., Sept. 1990.

[67] C. V. Raman and K. S. Krishnan, "A new type of secondary radiation," *Nature*, vol. 121, pp. 501–502, June 1928.

[68] E. Smith and G. Dent, *Modern Raman Spectroscopy: A Practical Approach*. Wiley-Blackwell, Dec. 2004.

[69] R. Saito, M. Hofmann, G. Dresselhaus, A. Jorio, and M. S. Dresselhaus, "Raman spectroscopy of graphene and carbon nanotubes," *Advances in Physics*, vol. 60, no. 3, pp. 413–550, 2011.

[70] A. C. Ferrari, J. C. Meyer, V. Scardaci, C. Casiraghi, M. Lazzeri, F. Mauri, S. Piscanec, D. Jiang, K. S. Novoselov, S. Roth, and A. K. Geim, "Raman spectrum of graphene and graphene layers," *Physical Review Letters*, vol. 97, p. 187401, Oct. 2006.

[71] L. Malard, M. Pimenta, G. Dresselhaus, and M. Dresselhaus, "Raman spectroscopy in graphene," *Physics Reports*, vol. 473, pp. 51–87, Apr. 2009.

[72] M. Tinkham, *Introduction to Superconductivity: v. 1: Vol i*. Dover Publications Inc., 2nd revised edition ed., June 2004.

[73] J. F. Annett, *Superconductivity, Superfluids and Condensates*. OUP Oxford, Mar. 2004.

[74] W. Buckel and R. Kleiner, *Superconductivity: Fundamentals and Applications*. Wiley VCH, 2nd, revised and enlarged edition ed., Aug. 2004.

[75] T. V. Duzer and C. W. Turner, *Principles of Superconductive Devices and Circuits*. Prentice Hall, 2 ed., Dec. 1998.

[76] N. W. Ashcroft and N. D. Mermin, *Solid State Physics*. Brooks/Cole, Jan. 1976.

[77] J. Bardeen, L. N. Cooper, and J. R. Schrieffer, "Microscopic theory of superconductivity," *Physical Review*, vol. 106, pp. 162–164, Apr. 1957.

[78] A. A. Golubov, M. Y. Kupriyanov, and E. Il'ichev, "The current-phase relation in Josephson junctions," *Reviews of Modern Physics*, vol. 76, pp. 411–469, Apr. 2004.

[79] J. Moser, A. Barreiro, and A. Bachtold, "Current-induced cleaning of graphene," *Applied Physics Letters*, vol. 91, p. 163513, 2007.

[80] P. Dubos, H. Courtois, B. Pannetier, F. K. Wilhelm, A. D. Zaikin, and G. Schön, "Josephson critical current in a long mesoscopic s-n-s junction," *Physical Review B*, vol. 63, p. 064502, Jan. 2001.

[81] J. C. Hammer, J. C. Cuevas, F. S. Bergeret, and W. Belzig, "Density of states and supercurrent in diffusive SNS junctions: Roles of nonideal interfaces and spin-flip scattering," *Physical Review B*, vol. 76, no. 6, p. 064514, 2007.

[82] J. Martin, N. Akerman, G. Ulbricht, T. Lohmann, J. H. Smet, K. v. Klitzing, and A. Yacoby, "Observation of electron–hole puddles in graphene using a scanning single-electron transistor," *Nature Physics*, vol. 4, no. 2, pp. 144–148, 2008.

[83] C. Berger, Z. Song, X. Li, X. Wu, N. Brown, C. Naud, D. Mayou, T. Li, J. Hass, A. N. Marchenkov, E. H. Conrad, P. N. First, and W. A. de Heer, "Electronic confinement and coherence in patterned epitaxial graphene," *Science*, vol. 312, pp. 1191–1196, May 2006.

[84] Z. Sun, Z. Yan, J. Yao, E. Beitler, Y. Zhu, and J. M. Tour, "Growth of graphene from solid carbon sources," *Nature*, vol. 468, pp. 549–552, Nov. 2010.

[85] W. Li, Y. He, L. Wang, G. Ding, Z.-Q. Zhang, R. W. Lortz, P. Sheng, and N. Wang, "Electron localization in metal-decorated graphene," *Physical Review B*, vol. 84, p. 045431, July 2011.

[86] V. C. Tung, M. J. Allen, Y. Yang, and R. B. Kaner, "High-throughput solution processing of large-scale graphene," *Nature Nanotechnology*, vol. 4, pp. 25–29, Nov. 2008.

[87] D. V. Kosynkin, A. L. Higginbotham, A. Sinitskii, J. R. Lomeda, A. Dimiev, B. K. Price, and J. M. Tour, "Longitudinal unzipping of carbon nanotubes to form graphene nanoribbons," *Nature*, vol. 458, pp. 872–876, Apr. 2009.

[88] M. S. Dresselhaus, G. Dresselhaus, and P. C. Eklund, *Science of Fullerenes and Carbon Nanotubes: Their Properties and Applications*. Academic Press, Mar. 1996.

[89] C. S. Allen, *Structural Characterisation, Fabrication and Electronic Properties of Carbon Nanotube Devices*. PhD thesis, Leeds, Sept. 2009.

[90] M. Ohring, *Materials Science of Thin Films, Second Edition*. Academic Press, 2 ed., Oct. 2001.

[91] N. A. Porter, *Magnetoresistance in n-type Silicon*. PhD thesis, University of Leeds, Nov. 2010.

[92] W. Bao, F. Miao, Z. Chen, H. Zhang, W. Jang, C. Dames, and C. N. Lau, "Controlled ripple texturing of suspended graphene and ultrathin graphite membranes," *Nature Nanotechnology*, vol. 4, pp. 562–566, July 2009.

[93] H. S. Song, S. L. Li, H. Miyazaki, S. Sato, K. Hayashi, A. Yamada, N. Yokoyama, and K. Tsukagoshi, "Origin of the relatively low transport mobility of graphene grown through chemical vapor deposition," *Scientific Reports*, vol. 2, Mar. 2012.

[94] M. I. Katsnelson and A. K. Geim, "Electron scattering on microscopic corrugations in graphene," *Philosophical Transactions of the Royal Society A: Mathematical, Physical and Engineering Sciences*, vol. 366, pp. 195–204, Jan. 2008.

[95] A. Newaz, Y. S. Puzyrev, B. Wang, S. T. Pantelides, and K. I. Bolotin, "Probing charge scattering mechanisms in suspended graphene by varying its dielectric environment," *Nature Communications*, vol. 3, p. 734, Mar. 2012.

[96] W. Gannett, W. Regan, K. Watanabe, T. Taniguchi, M. F. Crommie, and A. Zettl, "Boron nitride substrates for high mobility chemical vapor deposited graphene," *Applied Physics Letters*, vol. 98, pp. 242105–242105–3, June 2011.

[97] Y.-C. Lin, C.-C. Lu, C.-H. Yeh, C. Jin, K. Suenaga, and P.-W. Chiu, "Graphene annealing: How clean can it be?," *Nano Letters*, vol. 12, no. 1, pp. 414–419, 2011.

[98] M. Ishigami, J. H. Chen, W. G. Cullen, M. S. Fuhrer, and E. D. Williams, "Atomic structure of graphene on SiO_2," *Nano Letters*, vol. 7, no. 6, pp. 1643–1648, 2007.

[99] T. Haruyama and R. Yoshizaki, "Thin-film platinum resistance thermometer for use at low temperatures and in high magnetic fields," *Cryogenics*, vol. 26, pp. 536–538, Oct. 1986.

[100] R. M. Tennent, *Science Data*. Oliver & Boyd, 1 ed., Nov. 1971.

[101] D. Briand, F. Beaudoin, J. Courbat, N. de Rooij, R. Desplats, and P. Perdu, "Failure analysis of micro-heating elements suspended on thin membranes," *Microelectronics Reliability*, vol. 45, pp. 1786–1789, Sept. 2005.

[102] J. Courbat, D. Briand, and N. de Rooij, "Reliability improvement of suspended platinum-based micro-heating elements," *Sensors and Actuators A: Physical*, vol. 142, pp. 284–291, Mar. 2008.

[103] J. Puigcorb, D. Vogel, B. Michel, A. Vil, I. Gr cia, C. Can, and J. R. Morante, "Thermal and mechanical analysis of micromachined gas sensors," *Journal of Micromechanics and Microengineering*, vol. 13, pp. 548–556, Sept. 2003.

[104] A. Delan, M. Rennau, S. Schulz, and T. Gessner, "Thermal conductivity of ultra low-k dielectrics," *Microelectronic Engineering*, vol. 70, pp. 280–284, Nov. 2003.

[105] H.-Y. Chiu, V. Perebeinos, Y.-M. Lin, and P. Avouris, "Controllable p-n junction formation in monolayer graphene using electrostatic substrate engineering," *Nano Lett.*, vol. 10, no. 11, pp. 4634–4639, 2010.

[106] B. Özyilmaz, P. Jarillo-Herrero, D. Efetov, D. A. Abanin, L. S. Levitov, and P. Kim, "Electronic transport and quantum Hall effect in bipolar graphene p-n-p junctions," *Physical Review Letters*, vol. 99, p. 166804, Oct. 2007.

[107] J. R. Williams, L. DiCarlo, and C. M. Marcus, "Quantum Hall effect in a gate-controlled p-n junction of graphene," *Science*, vol. 317, pp. 638–641, Aug. 2007.

[108] E. C. Peters, E. J. H. Lee, M. Burghard, and K. Kern, "Gate dependent photocurrents at a graphene p-n junction," *Applied Physics Letters*, vol. 97, pp. 193102–193102–3, Nov. 2010.

[109] D. Sun, G. Aivazian, A. M. Jones, J. S. Ross, W. Yao, D. Cobden, and X. Xu, "Ultrafast hot-carrier-dominated photocurrent in graphene," *Nature Nanotechnology*, vol. 7, pp. 114–118, Jan. 2012.

[110] N. M. Gabor, J. C. W. Song, Q. Ma, N. L. Nair, T. Taychatanapat, K. Watanabe, T. Taniguchi, L. S. Levitov, and P. Jarillo-Herrero, "Hot Carrier–Assisted intrinsic photoresponse in graphene," *Science*, vol. 334, pp. 648–652, Nov. 2011.

[111] M. C. Lemme, F. H. L. Koppens, A. L. Falk, M. S. Rudner, H. Park, L. S. Levitov, and C. M. Marcus, "Gate-activated photoresponse in a graphene p–n junction," *Nano Lett.*, vol. 11, no. 10, pp. 4134–4137, 2011.

[112] Y.-J. Yu, Y. Zhao, S. Ryu, L. E. Brus, K. S. Kim, and P. Kim, "Tuning the graphene work function by electric field effect," *Nano Lett.*, vol. 9, no. 10, pp. 3430–3434, 2009.

[113] G. Giovannetti, P. A. Khomyakov, G. Brocks, V. M. Karpan, J. van den Brink, and P. J. Kelly, "Doping graphene with metal contacts," *Physical Review Letters*, vol. 101, p. 026803, July 2008.

[114] K. Pi, K. M. McCreary, W. Bao, W. Han, Y. F. Chiang, Y. Li, S.-W. Tsai, C. N. Lau, and R. K. Kawakami, "Electronic doping and scattering by transition metals on graphene," *Physical Review B*, vol. 80, no. 7, p. 075406, 2009.

[115] J.-H. Chen, C. Jang, S. Adam, M. S. Fuhrer, E. D. Williams, and M. Ishigami, "Charged-impurity scattering in graphene," *Nature Physics*, vol. 4, pp. 377–381, Apr. 2008.

[116] D. B. Farmer, Y.-M. Lin, A. Afzali-Ardakani, and P. Avouris, "Behavior of a chemically doped graphene junction," *Applied Physics Letters*, vol. 94, pp. 213106–213106–3, May 2009.

[117] P. Blake, R. Yang, S. Morozov, F. Schedin, L. Ponomarenko, A. Zhukov, R. Nair, I. Grigorieva, K. Novoselov, and A. Geim, "Influence of metal contacts and charge inhomogeneity on transport properties of graphene near the neutrality point," *Solid State Communications*, vol. 149, pp. 1068–1071, July 2009.

[118] P. Joshi, H. E. Romero, A. T. Neal, V. K. Toutam, and S. A. Tadigadapa, "Intrinsic doping and gate hysteresis in graphene field effect devices fabricated on SiO2 substrates," *Journal of Physics: Condensed Matter*, vol. 22, p. 334214, Aug. 2010.

[119] H. Wang, Y. Wu, C. Cong, J. Shang, and T. Yu, "Hysteresis of electronic transport in graphene transistors," *ACS Nano*, vol. 4, no. 12, pp. 7221–7228, 2010.

[120] M. Lafkioti, B. Krauss, T. Lohmann, U. Zschieschang, H. Klauk, K. v. Klitzing, and J. H. Smet, "Graphene on a hydrophobic substrate: Doping reduction and hysteresis suppression under ambient conditions," *Nano Lett.*, vol. 10, no. 4, pp. 1149–1153, 2010.

[121] B. Krauss, T. Lohmann, D.-H. Chae, M. Haluska, K. von Klitzing, and J. H. Smet, "Laser-induced disassembly of a graphene single crystal into a nanocrystalline network," *Physical Review B*, vol. 79, p. 165428, Apr. 2009.

[122] S. Berciaud, M. Y. Han, K. F. Mak, L. E. Brus, P. Kim, and T. F. Heinz, "Electron and optical phonon temperatures in electrically biased graphene," *Physical Review Letters*, vol. 104, p. 227401, June 2010.

[123] E. H. Martins Ferreira, M. V. O. Moutinho, F. Stavale, M. M. Lucchese, R. B. Capaz, C. A. Achete, and A. Jorio, "Evolution of the Raman spectra from single-, few-, and many-layer graphene with increasing disorder," *Physical Review B*, vol. 82, no. 12, p. 125429, 2010.

[124] I. Calizo, A. A. Balandin, W. Bao, F. Miao, and C. N. Lau, "Temperature dependence of the raman spectra of graphene and graphene multilayers," *Nano Lett.*, vol. 7, no. 9, pp. 2645–2649, 2007.

[125] I. Calizo, S. Ghosh, W. Bao, F. Miao, C. N. Lau, and A. A. Balandin, "Raman nanometrology of graphene: Temperature and substrate effects," *Solid State Communications*, vol. 149, pp. 1132–1135, July 2009.

[126] Y. M. Zuev, W. Chang, and P. Kim, "Thermoelectric and magnetothermoelectric transport measurements of graphene," *Physical Review Letters*, vol. 102, p. 096807, Mar. 2009.

[127] K. M. McCreary, K. Pi, and R. K. Kawakami, "Metallic and insulating adsorbates on graphene," *Applied Physics Letters*, vol. 98, pp. 192101–192101–3, May 2011.

[128] K. M. McCreary, K. Pi, A. G. Swartz, W. Han, W. Bao, C. N. Lau, F. Guinea, M. I. Katsnelson, and R. K. Kawakami, "Effect of cluster formation on graphene mobility," *Physical Review B*, vol. 81, p. 115453, Mar. 2010.

[129] J. S. Bunch, S. S. Verbridge, J. S. Alden, A. M. van der Zande, J. M. Parpia, H. G. Craighead, and P. L. McEuen, "Impermeable atomic membranes from graphene sheets," *Nano Lett.*, vol. 8, no. 8, pp. 2458–2462, 2008.

[130] Z. Jiang, E. A. Henriksen, L. C. Tung, Y.-J. Wang, M. E. Schwartz, M. Y. Han, P. Kim, and H. L. Stormer, "Infrared spectroscopy of Landau levels of graphene," *Physical Review Letters*, vol. 98, p. 197403, May 2007.

[131] C. H. Yang, F. M. Peeters, and W. Xu, "Landau-level broadening due to electron-impurity interaction in graphene in strong magnetic fields," *Physical Review B*, vol. 82, no. 7, p. 075401, 2010.

[132] Z. Tan, C. Tan, L. Ma, G. T. Liu, L. Lu, and C. L. Yang, "Shubnikov-de Haas oscillations of a single layer graphene under dc current bias," *Physical Review B*, vol. 84, no. 11, p. 115429, 2011.

[133] A. Isihara and L. Smrcka, "Density and magnetic field dependences of the conductivity of two-dimensional electron systems," *Journal of Physics C: Solid State Physics*, vol. 19, pp. 6777–6789, Dec. 1986.

[134] F. Léonard and A. A. Talin, "Electrical contacts to one- and two-dimensional nanomaterials," *Nature Nanotechnology*, vol. 6, pp. 773–783, Nov. 2011.

[135] K. Nagashio, T. Nishimura, K. Kita, and A. Toriumi, "Metal/graphene contact as a performance killer of ultra-high mobility graphene analysis of intrinsic mobility and contact resistance," in *Electron Devices Meeting (IEDM), 2009 IEEE International*, pp. 1 –4, Dec. 2009.

[136] A. Venugopal, L. Colombo, and E. M. Vogel, "Contact resistance in few and multilayer graphene devices," *Applied Physics Letters*, vol. 96, pp. 013512–013512–3, Jan. 2010.

[137] J. A. Robinson, M. LaBella, M. Zhu, M. Hollander, R. Kasarda, Z. Hughes, K. Trumbull, R. Cavalero, and D. Snyder, "Contacting graphene," *Applied Physics Letters*, vol. 98, pp. 053103–053103–3, Feb. 2011.

[138] F. Xia, V. Perebeinos, Y.-m. Lin, Y. Wu, and P. Avouris, "The origins and limits of metal-graphene junction resistance," *Nature Nanotechnology*, vol. 6, pp. 179–184, Feb. 2011.

[139] S. Russo, M. Craciun, M. Yamamoto, A. Morpurgo, and S. Tarucha, "Contact resistance in graphene-based devices," *Physica E: Low-dimensional Systems and Nanostructures*, vol. 42, pp. 677–679, Feb. 2010.

[140] D. K. Schroder, *Semiconductor Material and Device Characterization*. New York ; Chichester: Wiley, 2nd ed ed., 1998.

[141] B. H.H., "Models for contacts to planar devices," *Solid-State Electronics*, vol. 15, pp. 145–158, Feb. 1972.

[142] L. Weber and E. Gmelin, "Transport properties of silicon," *Applied Physics A: Materials Science & Processing*, vol. 53, no. 2, pp. 136–140, 1991.

[143] A. Dimiev, D. V. Kosynkin, A. Sinitskii, A. Slesarev, Z. Sun, and J. M. Tour, "Layer-by-layer removal of graphene for device patterning," *Science*, vol. 331, pp. 1168–1172, Mar. 2011.

[144] S. Marchini, S. Günther, and J. Wintterlin, "Scanning tunneling microscopy of graphene on Ru(0001)," *Physical Review B*, vol. 76, no. 7, p. 075429, 2007.

[145] B. Uchoa, C.-Y. Lin, and A. H. Castro Neto, "Tailoring graphene with metals on top," *Physical Review B*, vol. 77, p. 035420, Jan. 2008.

[146] B. Huard, N. Stander, J. A. Sulpizio, and D. Goldhaber-Gordon, "Evidence of the role of contacts on the observed electron-hole asymmetry in graphene," *Physical Review B*, vol. 78, no. 12, p. 121402, 2008.

[147] P. A. Khomyakov, G. Giovannetti, P. C. Rusu, G. Brocks, J. van den Brink, and P. J. Kelly, "First-principles study of the interaction and charge transfer between graphene and metals," *Physical Review B*, vol. 79, p. 195425, May 2009.

[148] R. Nouchi and K. Tanigaki, "Charge-density depinning at metal contacts of graphene field-effect transistors," *Applied Physics Letters*, vol. 96, pp. 253503–253503–3, June 2010.

[149] P. A. Khomyakov, A. A. Starikov, G. Brocks, and P. J. Kelly, "Nonlinear screening of charges induced in graphene by metal contacts," *Physical Review B*, vol. 82, no. 11, p. 115437, 2010.

[150] C.-H. Lu, G. M. T. Wong, R. Birringer, R. Dauskardt, M. D. Deal, B. M. Clemens, and Y. Nishi, "Bilayer metal gate electrodes with tunable work function: Mechanism and proposed model," *Journal of Applied Physics*, vol. 107, pp. 063710–063710–6, Mar. 2010.

[151] J. Brona and A. Ciszewski, "Ultrathin films of Pd on Nb(111): Intermixing and effect of formation of a surface alloy," *Physical Review B*, vol. 69, p. 115408, Mar. 2004.

[152] F. Tuinstra and J. L. Koenig, "Raman spectrum of graphite," *The Journal of Chemical Physics*, vol. 53, pp. 1126–1130, Aug. 1970.

[153] M. J. Matthews, M. A. Pimenta, G. Dresselhaus, M. S. Dresselhaus, and M. Endo, "Origin of dispersive effects of the Raman d band in carbon materials," *Physical Review B*, vol. 59, pp. R6585–R6588, Mar. 1999.

[154] A. C. Ferrari and J. Robertson, "Interpretation of Raman spectra of disordered and amorphous carbon," *Physical Review B*, vol. 61, pp. 14095–14107, May 2000.

[155] B. Dlubak, P. Seneor, A. Anane, C. Barraud, C. Deranlot, D. Deneuve, B. Servet, R. Mattana, F. Petroff, and A. Fert, "Are al_2o_3 and MgO tunnel barriers suitable for spin injection in graphene?," *Applied Physics Letters*, vol. 97, pp. 092502–092502–3, Aug. 2010.

[156] D. C. Kim, D.-Y. Jeon, H.-J. Chung, Y. Woo, J. K. Shin, and S. Seo, "The structural and electrical evolution of graphene by oxygen plasma-induced disorder," *Nanotechnology*, vol. 20, p. 375703, Sept. 2009.

[157] A. Franklin, S.-J. Han, A. Bol, and W. Haensch, "Effects of nanoscale contacts to graphene," *Electron Device Letters, IEEE*, vol. 32, pp. 1035 –1037, Aug. 2011.

[158] R. Danneau, F. Wu, M. Craciun, S. Russo, M. Tomi, J. Salmilehto, A. Morpurgo, and P. Hakonen, "Evanescent wave transport and shot noise in graphene: Ballistic regime and effect of disorder," *Journal of Low Temperature Physics*, vol. 153, no. 5, pp. 374–392, 2008.

[159] B.-C. Huang, M. Zhang, Y. Wang, and J. Woo, "Contact resistance in top-gated graphene field-effect transistors," *Applied Physics Letters*, vol. 99, pp. 032107–032107–3, July 2011.

[160] W. J. Liu, M. F. Li, S. H. Xu, Q. Zhang, Y. H. Zhu, K. L. Pey, H. L. Hu, Z. X. Shen, X. Zou, J. L. Wang, J. Wei, H. L. Zhu, and H. Y. Yu, "Understanding the contact characteristics in single or multi-layer graphene devices: The impact of defects (carbon vacancies) and the asymmetric transportation behavior," pp. 23.3.1–23.3.4, IEEE, Dec. 2010.

[161] W. J. Liu, H. Y. Yu, J. Wei, and M. F. Li, "Impact of process induced defects on the contact characteristics of Ti/Graphene devices," *Electrochemical and Solid-State Letters*, vol. 14, no. 12, pp. K67–K69, 2011.

[162] C. Malec, B. Elkus, and D. Davidović, "Vacuum-annealed Cu contacts for graphene electronics," *Solid State Communications*, vol. 151, pp. 1791–1793, Dec. 2011.

[163] K. Nagashio, T. Nishimura, K. Kita, and A. Toriumi, "Contact resistivity and current flow path at metal/graphene contact," *Applied Physics Letters*, vol. 97, pp. 143514–143514–3, Oct. 2010.

[164] E. Watanabe, A. Conwill, D. Tsuya, and Y. Koide, "Low contact resistance metals for graphene based devices," *Diamond and Related Materials*, vol. 24, pp. 171–174, Apr. 2012.

[165] L. Bulaevskii, A. Buzdin, M. Kulić, and S. Panjukov, "Coexistence of superconductivity and magnetism theoretical predictions and experimental results," *Advances in Physics*, vol. 34, no. 2, pp. 175–261, 1985.

[166] K. A. Delin and A. W. Kleinsasser, "Stationary properties of high-critical-temperature proximity effect Josephson junctions," *Superconductor Science and Technology*, vol. 9, pp. 227–269, Apr. 1996.

[167] K. K. Likharev, "Superconducting weak links," *Reviews of Modern Physics*, vol. 51, pp. 101–159, Jan. 1979.

[168] M. Freitag, T. Low, F. Xia, and P. Avouris, "Photoconductivity of biased graphene," *arXiv:1202.5342*, Feb. 2012.

[169] E. J. H. Lee, K. Balasubramanian, R. T. Weitz, M. Burghard, and K. Kern, "Contact and edge effects in graphene devices," *Nature Nanotechnology*, vol. 3, no. 8, pp. 486–490, 2008.

[170] F. Xia, T. Mueller, R. Golizadeh-Mojarad, M. Freitag, Y.-m. Lin, J. Tsang, V. Perebeinos, and P. Avouris, "Photocurrent imaging and efficient photon detection in a graphene transistor," *Nano Letters*, vol. 9, pp. 1039–1044, Mar. 2009.

[171] X. Xu, N. M. Gabor, J. S. Alden, A. M. van der Zande, and P. L. McEuen, "Photo-thermoelectric effect at a graphene interface junction," *Nano Letters*, vol. 10, pp. 562–566, Feb. 2010.

[172] J. Park, Y. H. Ahn, and C. Ruiz-Vargas, "Imaging of photocurrent generation and collection in single-layer graphene," *Nano Letters*, vol. 9, pp. 1742–1746, May 2009.

[173] M. Kim, H. Ang Yoon, S. Woo, D. Yoon, S. Wook Lee, and H. Cheong, "Polarization dependence of photocurrent in a metal-graphene-metal device," *Applied Physics Letters*, vol. 101, pp. 073103–073103–3, Aug. 2012.

[174] T. Mueller, F. Xia, and P. Avouris, "Graphene photodetectors for high-speed optical communications," *Nature Photonics*, vol. 4, no. 5, pp. 297–301, 2010.

[175] Z. H. Ni, H. M. Wang, Z. Q. Luo, Y. Y. Wang, T. Yu, Y. H. Wu, and Z. X. Shen, "The effect of vacuum annealing on graphene," *Journal of Raman Spectroscopy*, vol. 41, no. 5, p. 479–483, 2010.

[176] R. Nouchi, T. Saito, and K. Tanigaki, "Determination of carrier type doped from metal contacts to graphene by channel-length-dependent shift of charge neutrality points," *Applied Physics Express*, vol. 4, p. 035101, 2011.

[177] Y. Ren, C. Zhu, W. Cai, H. Li, H. Ji, I. Kholmanov, Y. Wu, R. D. Piner, and R. S. Ruoff, "Detection of sulfur dioxide gas with graphene field effect transistor," *Applied Physics Letters*, vol. 100, pp. 163114–163114–4, Apr. 2012.

[178] R. Nouchi, T. Saito, and K. Tanigaki, "Observation of negative contact resistances in graphene field-effect transistors," *Journal of Applied Physics*, vol. 111, pp. 084314–084314–7, Apr. 2012.

[179] L. Prechtel, L. Song, D. Schuh, P. Ajayan, W. Wegscheider, and A. W. Holleitner, "Time-resolved ultrafast photocurrents and terahertz generation in freely suspended graphene," *Nature Communications*, vol. 3, Jan. 2012.

[180] L. Vicarelli, M. S. Vitiello, D. Coquillat, A. Lombardo, A. C. Ferrari, W. Knap, M. Polini, V. Pellegrini, and A. Tredicucci, "Graphene field-effect transistors as room-temperature terahertz detectors," *Nature Materials*, vol. 11, no. 10, pp. 865–871, 2012.